MULTI-SCALE ANALYSES OF GRANULAR FLOWS FOR DISASTER RESILIENCE ENHANCEMENT

A Dissertation
Presented to
The Academic Faculty

by

Fangzhou Liu

In Partial Fulfillment
of the Requirements for the Degree
of Doctor of Philosophy in the
School of Civil and Environmental Engineering

Georgia Institute of Technology
December 2019

MULTI-SCALE ANALYSES OF GRANULAR FLOWS FOR DISASTER RESILIENCE ENHANCEMENT

Approved by:

Dr. J. David Frost, Advisor
School of Civil and Environmental Engineering
Georgia Institute of Technology

Dr. Susan E. Burns
School of Civil and Environmental Engineering
Georgia Institute of Technology

Dr. Sheng Dai
School of Civil and Environmental Engineering
Georgia Institute of Technology

Dr. Steven P. French
School of City & Regional Planning
College of Design
Georgia Institute of Technology

Dr. Qiang Xu
State Key Laboratory of Geohazard Prevention and Geoenvironment Protection
Chengdu University of Technology

Dr. Mesut Turel
Chubb

Date Approved: November 6, 2019

To Minzhi and Colin

&

To the memory of my loving parents

ACKNOWLEDGEMENTS

There are many people who deserve recognition and thanks for their time and efforts in leading to the completion of this thesis. Professor J. David Frost in his capacity as advisor, mentor, and friend has provided me with support, guidance, encouragement, and equally importantly, an environment of high degree of autonomy to explore novel ideas and topics, and for conducting quality research. It is truly a privilege to spend these years observing and learning from such an exceptional researcher, mentor, and leader.

The advice, guidance, and generous support of Professor Qiang Xu lies the platform for me to pursue some of the most interesting questions in my research. The advice and support of Professor Susan E. Burns, Professor Steven P. French, Professor Sheng Dai, and Dr. Mesut Turel is gratefully acknowledged. Professor Burns served as a role model for me in teaching and understanding the needs of students. The insights of Professor French inspired me to pursue a better understanding on the impact of recovery after disasters. Dr. Turel showed me the real-world applications of computational science and engineering at an early stage. Special thanks to Professor Dai for his continued encouragement, support, and discussions.

I acknowledge the members of the Sustainable Geotechnical Systems Laboratory for enriching my life: Alejandro Martinez, Mahdi Roozbahani, Jiaxing Su, Andres Peralta, Jie Cao, Fikret Atalay, Mengmeng Liu, Tianlong Xu, Sangy Hanumasagar, Seth Mallett, Yuzhi Guo, Nick Sianta, Rodrigo Borela, Nimisha Roy, Karie Yamamoto, Ariel Siegel, Yue Xu, Jiaojun Liu, Elliot Nichols, and John Huntoon. I also acknowledge the members of the Geo-society and the friends I have made in Atlanta; special thanks to Longde Jin, Bo Wang, Josh Smith, Jong Muk Won, Xenia Wirth, Jongchan Kim, Yue Zhao, Ming Liu, Fernando Patino, Wilson Espinoza, Boyoung Jeong, Lynnae Luettich, and Sean Tyndale.

Field trips with the members and friends at the State Key Laboratory of Geohazard Prevention and Geoenvironment Protection had made this journey very rewarding; special thanks to Professor Runqiu Huang, Professor Xiangjun Pei, Professor Da Zheng, Professor Yusheng Li, Professor Xiujun Dong, Dr. Xing Zhu, Tiantao Li, Xing Qi, Dalei Peng, Kuanyao Zhao, Yuanzhen Ju, Yixi Zhang, and Dehao Xiu.

Financial support provided by the School of Civil and Environmental Engineering and the School of Computational Science and Engineering at Georgia Tech, the National Science Foundation, the Elizabeth and Bill Higginbotham Foundation, the Future Faculty Fellowship, the National Natural Science Foundation of China (Grant No.41630640), and the Open Research Fund (SKLGP2017K002) in the form of assistantships, scholarships, and operational costs is acknowledged.

I would also like to extend my gratitude to the following people who have helped in various ways:

- to Professor Runqiu Huang for providing tremendous support and incredible research opportunities throughout my Ph.D. studies.
- to Mahdi Roozbahani (my Persian brother) for the relentless encouragement on the pursuit of knowledge in Computational Science and Engineering.
- to Seth Mallett (my American brother) for the uncompromising reminders whenever my priorities becoming sidetracked.
- to Rodrigo Borela for teaching me the arts of espresso.

- to Yue Zhao for friendship and stimulating discussions of many ideas.
- to Longde Jin for steering the Geotechnical Society in the dark times.
- to Eric So for unreserved help and support throughout my study.
- to Yixi Zhang for sampling and assisting the triaxial tests.
- to Jongchan Kim for teaching me wave characterization and sensor manufacturing.
- to Xenia Wirth for teaching me the PSA and SEM-EDS analysis.
- to Robert Simon for patience and support as the graduate program manager.

Finally, and most importantly, I want to thank my wife, Minzhi, who has helped in so many ways that are simply beyond words. I want to thank my son, Colin, for being such a joy in our life. I want to thank my father, Ming, and my mother, Haiyan, for everything; their vision, aspiration, courage, and tenacious characters continuous to inspire me in life. This would not have been possible without their unconditional love, patience, support, and sacrifices.

TABLE OF CONTENTS

LIST OF TABLES

LIST OF FIGURES

SUMMARY

A study that overlaps the fundamentals of granular flows with human responses to disasters at the community or regional scale is considered to be a strategic approach that advances existing methods in natural and human-induced hazard research in light of global-scale changes in earth systems. This study aims to improve the understanding: 1) on the mechanical behaviors of fluidized loess flowslide using centrifuge modeling as well as in-house designed laboratory testing and elastic wave characterization techniques (i.e. natural systems), and 2) on the cascading impacts of geohazards on local communities, assessing disaster resilience associated with reconstruction strategies and the performance of debris flow mitigation systems (i.e. natural-human systems interactions).

The current work reveals the state-dependent effects of structure on flow behavior of loess and proposes modified criteria to predict the flow behavior. Laboratory tests show the changes in the mechanical behavior due to decementation of loess and indicate the needs to study loess within the scope of geotechnical analysis. The failure mechanism of loess flowslide is better understood from the study on the deformation process that shows the compounding effects of increasing pore-water pressure and reducing confining stresses on static liquefaction. The earthquake and post-earthquake impacts are documented after the 2008 Wenchuan earthquake, which permits a pilot study on quantifying the recovery processes of two communities of different reconstruction modes in light of Bayesian-based learning method. The design and performance of post-earthquake debris flow mitigation systems are reviewed; it offers a simple and robust data-driven approach to evaluate the effectiveness of debris flow mitigation systems at the regional scale.

CHAPTER 1. INTRODUCTION

1.1 Overview and objectives

The resilience of society can be tested when natural or human-induced geophysical hazards, which represent the ultimate experiment on nature-human system interactions. Long-runout mass movements of granular solids, fluid, and air in a multi-phase system are typically highly mobile with 'flow-like' motions (Hungr *et al.*, 2014; McDougall, 2016). Flowslides and debris flows commonly cause severe and far-reaching destruction to downstream communities. With an increasing land use expansion at the global scale, predicting, preventing, and mitigating the damage from flow-like landslides, relies on resilient infrastructure solutions that are attained through improved understanding of the fundamental behaviors of granular materials, both during the pre-failure deformation and post-failure propagation stages. In adding capacity to develop resilience in a community, hazard susceptibility and runout analyses, failure mechanisms, and mitigation systems of granular flows are intertwined with land use and, in some cases, post-disaster reconstruction. The undertaking of a study that overlaps the fundamentals of flow-like landslides (i.e. nature systems), as well as the mitigation, risk analysis and resilience strategies (i.e. nature-human system interactions) is thus considered to be a critical component that can advance the existing dimensions of natural and human-induced hazard research associated with the planetary-scale changes in the Earth system.

This work amasses a set of studies with the aims of: 1) advancing the understanding of the fundamentals of long-runout flowslides in natural cemented soils by decomposing site-scale observations into meso-scale physical modeling and particle-scale interactions;

2) evaluating the performance of mitigation systems to better mitigate the impacts of post-earthquake debris flows; and 3) exploring the applications of Bayesian-based statistical approaches in predicting landslide runout and quantifying disaster resilience.

1.2 Background and significance

Landslide denotes the movement of a mass of rock, debris, or earth down a slope, as defined and classified by Cruden (1991) and Varnes (1978), and subsequently updated by Hungr *et al.* (2014) to emphasize a landslide type termed ‘flow-like landslide’ due to its distinct characteristics, i.e. rapid movement (0.5-5000 mm/s) with long runout. Flow-like landslides impose great risks to the local community as well as the communities that are away from the source, often with little or no early warnings; for example, the 2010 Mount Meager rockslide-debris flow (Guthrie *et al.*, 2012; Allstadt, 2013), the 2014 Oso landslide (Keaton *et al.*, 2014; Iverson & George, 2015; Wartman *et al.*, 2016), the 2015 Shenzhen landfill flowslide (Ouyang *et al.*, 2016; Xu *et al.*, 2017; Zhan *et al.*, 2018), and the 1983 Saleshan loess flowslide (Derbyshire *et al.*, 1994; Dijkstra *et al.*, 1994; Derbyshire, 2001).

Flow-like landslides represent a collection of diverse and complex phenomena with no unanimous agreement on the mechanism of the long-runout behavior. The major challenges in advancing the understanding of long runout behavior can be attributed to the varying location, frequency of occurrence, and failure characteristics, including materials, fluids, shear rate, pressure, and temperature. Therefore, the mechanism tends to be more tailored for a single event and can rarely be validated at the field scale under the same or similar conditions, and the failure analyses are largely constrained in the format of forensic-style back-analysis of previous events (McDougall, 2016).

To circumvent the predicament of replicating long-runout behavior at the full scale as a means to better understand the failure mechanisms, this work identifies two study areas that are subject to continual impacts of flow-like landslides. Study Area I is the Heifangtai terrace in the loess plateau of China, where agricultural irrigation on the surface of the terrace has resulted in more than 200 loess-related landslides (Peng *et al.*, 2018; Qi *et al.*, 2018). Study Area II is the region impacted by the 2008 Wenchuan earthquake in southwestern China, where a large amount of loose and unsorted sediments was deposited by co-seismic landslides and subsequently became the source materials for debris flow, representing a typical post-earthquake instability process (Huang & Fan, 2013; Fan *et al.*, 2019). A key advantage of analyzing failures in the selected study areas is the pronounced similarity of the observed long runout behaviors. As a result, the postulated failure mechanism can be calibrated and validated by groups of events, and thus more readily be applied to better monitor and mitigate future events, turning back-analyses into forward-analyses.

The following items summarize the key knowledge gaps and challenges that need to be addressed in this work:

- The mechanism of flowslides in loess, as a natural cemented soil, are commonly studied within the scope of geology and/or engineering geology, which lack geomechanical analysis with limited interests in the particle interactions. Within the scope of geotechnical practice, the existing soil classification system and landslide classification system also fail to capture the behavior of cemented soils due to the ignored bonding properties. The effects of cementation on the large strain behavior of loess are not well understood, and its small strain behavior remains largely unclear.

There is a vast knowledge gap in understanding the fundamental behaviors of loess, and thus the failure mechanism of loess-related landslides.

- The understanding of the physics of debris flows has been greatly improved over the past two decades (Jakob *et al.*, 2005), and a large number and variety of mitigation measures has been designed to control runoff, erosion, discharge, and/or sediments (Huebl & Fiebiger, 2005). There is no quantitative method to assess the performance of the mitigation system at the site scale; most studies are conducted with the foci of hazard and risk mapping (Berti & Simoni, 2007; Fuchs *et al.*, 2007) or numerical and experimental impact analyses of a particular mitigation technique (e.g. Canelli *et al.*, 2012; Li & Zhao, 2018; Cucchiaro *et al.*, 2019).
- The resilience of different communities to the same disaster can vary significantly depending on the land-use planning (Saunders & Becker, 2015). In the case of post-earthquake reconstruction, the development of a recovery plan is commonly not supported by any quantitative estimation on the resilience of the adopted plan, which can ultimately lead to the ineffectiveness of the reconstruction mode and the lack of a proactive pre-event recovery plan for future disruptive events.
- It is not always possible to stabilize the landslide source areas so methods are needed to predict runout behavior to provide useful context for disaster recovery. Empirical-statistical methods for runout analyses are used heavily for quantitative risk assessment, as no universal constitutive laws governing landslide runout are readily available (Pastor *et al.*, 2012). Model calibration remains as the key challenge in runout analyses, which can be benefited from group calibration (Ayotte & Hungr, 2000; Revellino *et al.*, 2004) and uncertainty characterization.

1.3 Thesis overview and organization

This work is envisaged with themes of Natural Systems and Natural-Human System Interactions. The key research tasks are summarized as follows:

Theme I – Nature Systems:

- *Site-scale* field investigation to characterize loess-related landslide in HFT to better understand the deformation process and failure characteristics.
- *Macro-scale* centrifuge modeling to investigate flow liquefaction as the failure mechanism of long runout flowslide using both intact and reconstituted loess.
- *Meso-scale* laboratory testing using conventional undrained triaxial tests to analyze the shearing behavior of intact and reconstituted loess under the framework of the Critical State Soil Mechanics (CSSM).
- *Micro-scale* laboratory characterization in instrumented 1-D compression test using compression and shear waves to study the contact-level deformation of loess during decementation process.

Theme II – Nature-Human Systems Interactions:

- *Regional-scale* review on the earthquake impact and reconstruction process after the 2008 Wenchuan earthquake.
- *Local-scale* quantification of the recovery curves for the adopted post-earthquake reconstruction strategies using Bayesian Neural Network (BNN) with uncertainty characterization.

- *Local-scale* evaluation on the performance of debris flow mitigation systems using pre-/post-mitigation rainfall thresholds.

This thesis consists of eight chapters; CHAPTER 2 reviews the material and study areas and CHAPTER 8 summarizes the conclusions and recommendations for future work.

- CHAPTER 3 describes laboratory tests on intact and reconstituted loess and reports the effects of cementation and grading on flow instabilities and liquefaction.
- CHAPTER 4 analyzes the effects of decementation processes in loess induced by physical and chemical alterations using wave measurements.
- CHAPTER 5 reports the field investigation of loess flowslides in HFT followed by centrifuge model tests on the flowslide deformation and failure process.
- CHAPTER 6 documents the seismic impacts and reconstruction process after the 2008 Wenchuan earthquake, through which the disaster resilience recovery curve was explored by applying Bayesian-based learning uncertainty characterization.
- CHAPTER 7 reviews the design of a novel debris flow mitigation system and evaluates the performance of debris flow mitigation systems at different sites using pre-/post-mitigation rainfall thresholds.

CHAPTER 2. MATERIAL AND STUDY AREAS

This chapter summarizes the key characteristics of the Chinese loess that is used in this work, and it reports the geological settings of the study areas. Field investigations in the study areas were conducted through the collaborative work between the Sustainable Geotechnical Systems Laboratory (SGSL) at the Georgia Institute of Technology and the State Key Laboratory of Geohazard Prevention and Geoenvironment Protection (SKLGP) at the Chengdu University of Technology.

2.1 Loess

2.1.1 Distribution and formation

Loess is an aeolian deposit which experienced diagenesis in certain ecological environments. Loess can be found in North and South America, Europe, Russia, central Asia, and China with varying thickness of accumulation (Figure 2.1a); they cover about 10%-15% of the land area of the Earth (Pésci, 1990; Langroudi, 2014). Loess contains predominately silt-sized quartz grains that are bonded by various cementation agents, such as salt (Fan *et al.*, 2017), water-film (Derbyshire & Mellors, 1988; Pye, 1995), carbonate (Milodowski *et al.*, 2015), and clay (Smalley *et al.*, 2006), however researchers are not unanimous about the origins of the interparticle bonds (e.g. Barden *et al.*, 1973; Derbyshire *et al.*, 1995; Delage *et al.*, 1996; Jiang *et al.*, 2012). The formation of loess represents a complex cycle within the sedimentary system. Silt is product of quartz size particle reduction, which takes place at different spatial and temporal locations in a natural process. To be brief, quartz is part of a coarse eutectic mixture of quartz and feldspar, in which two phases are delivered, known as the ‘high quartz (β-quartz)’ and ‘low quartz (α-quartz)’, as the temperature of magmas reduce. This causes contraction in the crystal and tensile stresses (in the crystal), and in turn, facilitates the separation of grains from the material matrix when cracks caused by the weathering agents/actions (Smalley, 1966).

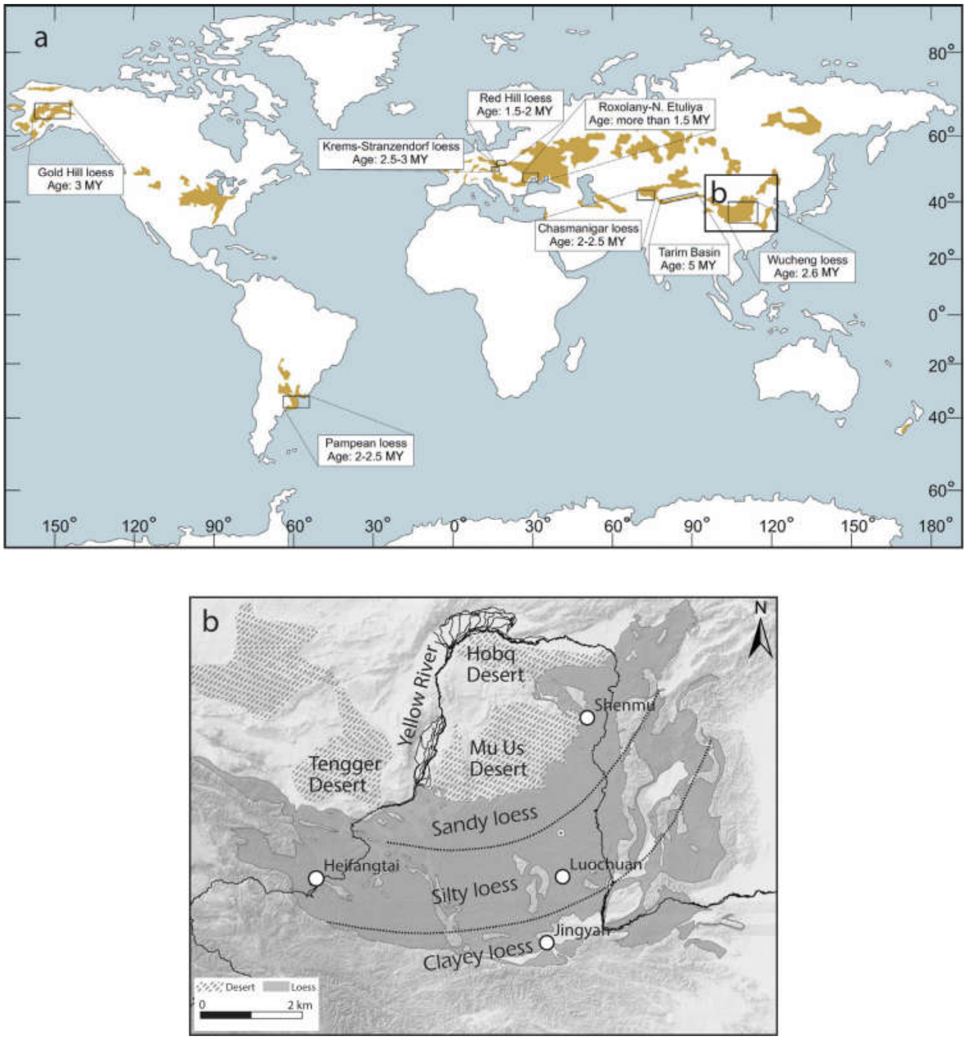

Figure 2.1 – Schematic map of the distribution of loess deposits. (a) global distribution after the Scheidig 1934 map (after Pésci, 1990; Muhs *et al.*, 2003; Smalley *et al.*, 2011); it is re-printed in Varga (2011) showing the confirmed loess area illustrated in Pésci (1990); (b) the loess plateau of China (Liu, 1985) and the sampling locations for this work. Loess samples were retrieved from SM for sandy loess, HFT and LC for silty loess, and JY for clayey loess.

Glacial grinding is widely accepted as the main source of present-day silt in Britain and Europe (Smalley *et al.*, 2006; Langroudi, 2014). Pye (1995) and Smith *et al.* (2002) argued that chemical and salt weathering with seasonal temperature and wetting/drying cycles are the main causes for peridesert silt that are transported by wind action.

The formation of loess is believed to be influenced by the sequence of the generation of the loess constituents, the transportation, the emplacement, and post-depositional events. Smalley *et al.* (2011) devised four present-day 'attitudes' to loess, including the 'soil science' attitude, sedimentological attitude, stratigraphical attitude, and geotechnical attitude. The latter two tend not to focus on the basic problem of loess formation. Despite the ongoing research on the ultimate source of silt-sized particles found in present-day loess, the disagreements between the 'soil science' attitude, as devised by Berg (1916) and Pésci (1990), and the sedimentological attitude, as represented by Smalley (1990), emerged from the debate, which in essence is "what made the loess into loess". Berg (1916) proposed that loess is formed '*in situ*' through the process of weathering and soil formation, i.e. loessification (non-loess ground turn into loess). Smalley (2011) argued that the key characteristics of loess, i.e. porous and metastable structures, highlight the occurrence of aeolian transportation, which ultimately put a defining mark on the argument.

2.1.2 Collapse in loess

Collapsibility is arguably the most discussed phenomenon that is associated with loess as a form of natural cemented soil. The term collapse in granular materials is used, by implication, to describe the sudden and significant deformation; it is not the immediate settlement, nor primary (or secondary) consolidation settlement (Mackechnie, 1989). The typical features of collapsible soils are: open structure, high void ratio (and porosity), low dry density, high sensitivity, low inter-particle bond strength, and geologically young or recently altered deposit (Rogers, 1995).

Loess is considered as the most eminent example of silt-sized collapsible soil; it is problematic upon wetting as its metastable structure can rapidly transform from a cemented solid body to a fluidized material, and as a result, subject to sudden particle rearrangement when grain-cement connections are comprised under loading and/or wetting. A large number and variety of geological hazards in loess is associated with the collapse behavior, including land subsidence (Derbyshire, 2001), differential settlement of building and pipeline (Phien-Wej *et al.*, 1992; Derbyshire *et al.*, 1995), failure of earth structure, e.g. Teton Dam (Smalley, 1992) and landslide (Derbyshire & Mellors, 1988). Thereby, geotechnical research in loess has centered on understanding the mechanism of collapse to improve mitigation techniques.

The study of collapse mechanism in loess can be loosely categorized into three approaches, including the traditional approach, microstructure approach, and unsaturated soil mechanics approach (Li *et al.*, 2016). The traditional approach views the collapse from the standpoint of one or several single soil properties, such as density, clay content, and/or grain size distribution (Fuller & Clapp, 1924; Sun, 1957; Feda, 1966, 1988; Feda *et al.*, 1993). With the application of scanning electron microscope (SEM) and X-ray tomography image technique, the collapse is widely being studied from the aspects of microstructure and fabric changes using 2-D/3-D image processing (Derbyshire & Mellors, 1988; Rogers *et al.*, 1994; Delage *et al.*, 1996; Jang *et al.*, 1999; Wang *et al.*, 2003, 2004a); but such an approach lacks a quantitative descriptor for real-time estimation on collapse.

Without relying on SEM-based techniques, Assallay *et al*. (1997) provides valuable insights to collapse and open structures through an 'airfall geometrical model'. The model suggests that the mode of sedimentation, and consequentially, the open fabric, and the interparticle bonds of loess are both important factors to the collapse mechanism. Such an argument underlines the differences in the observed collapse behaviors between loess and soils cemented by Portland cements (Yun & Santamarina, 2005; Trhlíková *et al.*, 2012) or soils mixed with soluble particles (Truong *et al.*, 2010)

The more recent developments in studying collapse mechanisms lie upon the framework of unsaturated soil mechanics (Chen *et al.*, 1999; Muñoz-Castelblanco *et al.*, 2011; Munoz-Castelblanco *et al.*, 2012; Langroudi, 2014); it attributes the loss of strength during collapse to suction reduction due to wetting (Alonso *et al.*, 1990; Fredlund & Gan, 1995; Cui & Delage, 1996). Some elastoplastic constitutive models have been proposed to study the collapse mechanism of loess; many of them represent some variations of the Barcelona Basic Model (BBM) approach (Alonso *et al.*, 1990; Li *et al.*, 2016). The sophisticated constitutive models offer means to predict the collapse behaviour more accurately; but they have not been widely adopted.

2.1.3 The Chinese loess

The Chinese loess is a wind-blown silt-sized deposit distributed in the arid regions of the loess plateau of China, with an increasing fines content from northwest to southeast of that area at locations further away from the desert source area, and thus classified as sandy, silty, and clayey loess (Liu, 1985), as shown in Figure 2.1b. The loess-paleosol sequences of China have provided rare and valuable information to study the Quaternary climate change, as they represent the most complete and well-known record of non-marine sedimentation (Gallet *et al.*, 1996). As a result, the composition varies with depth and location, reflecting the changes in the characteristics of the source area(s) and/or wind (Ding *et al.*, 1999). The loess found in the loess plateau of China are typically normally consolidated (Shao *et al.*, 2011). The research on the mechanical properties of the Chinese loess has largely eluded the non-Chinese readers in the past, as most of them appear only in the literature in Chinese, including some widely used references in China (e.g. Liu, 1985, 1997). However, study of the Chinese loess has sustained its popularity globally within the scope of geological hazards (Derbyshire *et al.*, 1994, 1995; Dijkstra *et al.*, 1994; Meng & Derbyshire, 1998; Derbyshire, 2001).

The problem of flowslides induced by static liquefaction remain largely unexplored in general, and much less so for natural cemented soils like the Chinese loess. The lack of study on the instability process of loess under undrained (and possibly drained) conditions, with respect to decementation, has resulted in challenges in understanding the onset of static liquefaction and the initiation for flow failure in loess for constitutive models. The recent studies by Xu & Coop (2016, 2017) and Xu *et al.* (2018) presented a more systematic analysis on the effects of structure on the large strain behaviors of clayey and silty Chinese loess within the CSSM framework. The results have shown that the structure of intact loess is able to sustain large stress under k_0 loading, and it can considerably alter the compressive and shear behaviors.

To better understand the instability of intact and reconstituted loess and the initiation process of flowslides, four sampling locations were selected to represent all three types of the Chinese loess, as shown in Figure 2.1b. The specifics of the test specimens are discussed in detail in the corresponding sections in CHAPTER 3 and CHAPTER 4.

2.1.4 Structure of soils

The unique behaviors of loess are largely attributed to the meta-stable structure. The term ‘structure’ refers to the combination of ‘fabric’ and ‘bonding’ in soils (Lambe & Whitman, 1969; Mitchell & Soga, 2005). Fabric is the arrangement of the particles and the resultant inhomogeneity, whereas bonding is the combination of forces that connects the particles (Gasparre, 2005). Leroueil *et al.* (1984) introduced the concept of ‘state of structure’ to characterize four different states of structure of a soil, depending on the process the soil has undergone, and thereby, any soil is to be considered to have a ‘structure’. The ‘intact’ state occurs in natural deposits, which reflects complex geological processes. The ‘deconstructed’ state denotes to the state in which the initially intact soil undergoes sufficient volumetric or shear deformations that the original structure is broken. The ‘remolded’ state is reached when sufficient mechanical energy is imparted to a clay mass to reduce its strength to a minimum. The ‘resedimented’ state is obtained by the deposition of remolded clay particles in slurry prior to self-weight consolidation of increasing thickness. The ‘destructed’ state is often assumed to be same as the ‘reconstituted’ state in which the soil has been mixed at a water content between w_L and $1.5w_L$, without drying prior to mixing, and then consolidated under 1-D conditions (Burland, 1990). Such a remolding process cannot fully remove the micro-fabric (Fearon & Coop, 2000), and it may produce a sedimentation structure that is different from that of the natural deposit (Cotecchia & Chandler, 1997).

2.2 Study Area I: the Heifangtai terrace

The work conducted in CHAPTER 3, CHAPTER 4, and CHAPTER 5 are based on Study Area I.

2.2.1 Geological setting

Heifangtai (HFT) is an arid loess terrace (area: ~12 km^2) of the Yellow River in the loess plateau of China (Figure 2.2); it consists of four layers in the sequence of the Malan silty loess (thickness: 30-50 m), clay (3-20 m), gravel (1-10 m), and bedrock comprises sandstone with mudstone partings and the bedding plane dipping 135°∠11°. The thickness of the exposed rock stratum is greater than 70 m. The average annual precipitation and evaporation are 287.6 mm and 1600 mm, respectively (Zhou, 2012). Local inhabitants were re-settled in the terrace since the 1960s due to the nearby construction of a hydropower station. Agricultural irrigation was started on the terrace surface by pumping water from the adjacent Yellow River, covering an area of 7.5 km^2 (exceeding 83% of terrace surface), with an annual consumption of water varying from $6\times10^6 - 8\times10^6$ m^3 (Lin *et al.*, 2014). The groundwater level has increased by 20 m at an average rate of 0.18 m/yr. There is no prior knowledge of the groundwater status before irrigation.

Sub-vertical joints are observed in the loess layer and provide preferential conduits for groundwater recharge. The apparent spring lines are visible at the bedrock slope along the edge of the terrace, with seepage of groundwater at or near the bottom of the loess layer. More than 200 loess-related landslides have occurred since the irrigation began. Land subsidence (> 1 m) was found at several locations in the early 1980s (Derbyshire *et al.*, 1995).

Figure 2.2 – Landslide distribution along the margin of HFT; landslide sections (S1 – S7) are discussed in Peng *et al.* (2018) and details are summarized in Table 1.

2.2.2 Loess-related landslides

Peng *et al.* (2018) reconstructed the landslides in HFT by using Unmanned Aerial Vehicles (UAVs) and 3-D Laser Scanning to create the Digital Elevation Model (DEM) of the terrace at a resolution of 10 cm. A typical UAV mission involves 35 flights spanning over one week. Each image is processed in high precision 3-D point clouds constrained by 15 primary control points and 146 Ground Control Points. The basic geometrical characters and failure modes are summarized in Table 1. Landslides in loess provide a unique collection of landforms and failure mechanisms that are often undervalued in global classification systems; but they have often been generalized as a single type of landslide based on the material composition, such as loess flow by Varnes (1978) and loess flowslide by Hungr *et al.* (2014), under the class of earth flow.

Table 1 – A summary of the landslides in HFT.

Section	Site	L	H	V	Φ_1	Φ_2	Φ_3	Type	Legend
		m	m	10^4 m^3	°	°	°		
S1	XY#1	173.96	43	73.02	13.88	62.23	10.48	**1**	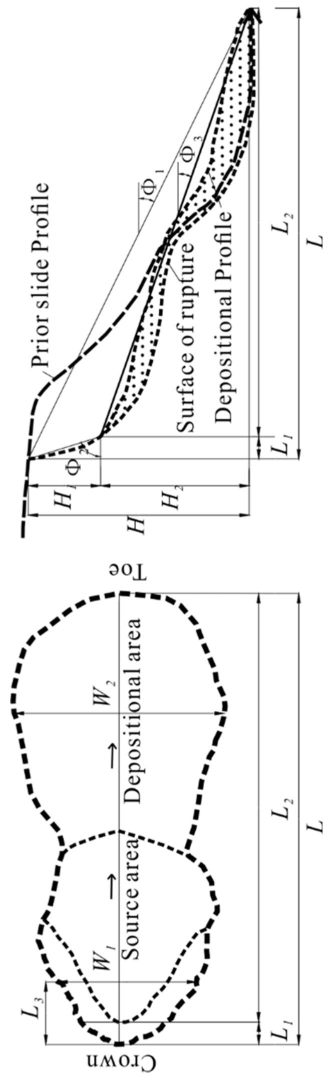
	XY#2	282.75	85	223.73	16.73	58.68	13.51		
	XY#3	345.55	70	523.68	11.45	53.85	10.62		
S2	DC#1	318.9	111	531.61	19.19	51.64	18.12		
	DC#2	346.09	106	32.03	17.03	32.65	14.78	**2**	
	DC#3	293.48	104	77.32	19.51	51.84	17.25		
	DC#4	99.48	75	3.11	37.01	32.13	37.33	**3**	
	DC#5	61.14	43	2.73	35.12	57.62	33.25		
	DC#6	156.37	101	19.15	32.86	46.78	31.88		
	DC#7	204.03	97	19.11	25.43	25.26	25.44		
	DC#8	132.26	90	7.9	34.23	58.09	31.18		
	DC#9	-	-	-	-	-	-		
S3	HC#1	244.32	101	77.04	22.46	32.44	19.92	**1**	
	HC#2	386.18	104	553.05	15.07	32.83	11.96		
	HC#3	376.44	101	610.36	15.02	23.5	12.57		
	HC#4	130.4	58.7	6.2	24.24	41.07	22.29		
	HC#5	212.16	107	18.24	26.76	37.38	25.23		
S4	JY#1	226.15	132	28.68	30.27	30.01	30.39	**4**	
	JY#2	181.41	121	7.05	33.7	35.48	33.15		
	JY#3	217.7	133	8.16	31.42	37.57	29.23		
	JY#4	163.31	108	5.26	33.48	41.95	32.55		
	JY#5	201.36	92	7.32	24.56	26.8	24.51		
	JY#6	342.2	113	8.69	18.27	65.63	16.96		
	JY#7	56.58	43	0.41	37.23	38.83	36.99		
	JY#8	88.26	57	0.94	32.86	56.74	28.17		
S5	JJ#1	353.43	121	34.38	18.9	55.64	16.18	**2**	
	JJ#2	425.66	120	88.99	15.74	42.85	13.4		
	JJ#3	515.48	124	92.88	13.53	52.44	10.32		
	JJ#4	609.55	119	333.81	11.05	35.22	9.3		
	JJ#5	468.73	120	152.65	14.36	41.89	12.53		
	JJ#6	326.17	108	33.2	18.32	42.36	15.02		
	JJ#7	322.83	100	10.55	17.21	46.39	14.89		
	JJ#8	390.97	101	52.86	14.48	37.48	12.52		
	JJ#9	98.81	53	2.43	28.21	44.56	13.3	**3**	
S6	JJ#10	190.56	91	6.89	25.53	42.58	24.79	**1**	
	JJ#11	178.63	70	6.17	21.4	48.77	19.66		
	JJ#12	175.27	91	7.55	27.44	60.1	25.34		
	JJ#13	45	50	2.08	48.01	44.22	49.04	**3**	
S7	CJ#1	175.02	72	2.34	22.36	55.52	20.46		
	CJ#2	91.13	52	1.77	29.71	46.03	28.81		
	CJ#3	283.86	104	55.65	20.12	48.1	17.1	**2**	
	CJ#4	164.11	99	17.75	31.1	64.36	28.99	**3**	
	CJ#5	207.58	79	15.77	20.84	52.65	18.66		
	CJ#6	199.53	64	29.92	17.78	48.11	14.53	**2**	
	CJ#7	129.12	54	5.99	22.69	72.59	16.25	**3**	
	CJ#8	154.97	40	15.91	14.47	59.27	7.96	**2**	
	CJ#9	80.23	31	3.36	21.13	35.09	16.26	**3**	**Note:** Type 1 – loess-bedrock slide Type 2 – loess flowslide Type 3 – loess slide Type 4 – loess flow
	CJ#10	-	-	-	-	-	-		
	CJ#11	62.43	38	0.82	31.33	49.1	13.56		
	CJ#12	57.28	39	0.55	34.25	34.94	33.87		
	CJ#13	40.84	40	0.16	44.4	54.38	39.72		
	MS#1	41.18	36	0.69	41.16	57.11	39.66		
	MS#2	21.43	12	0.36	29.24	61.93	20.46	**2**	
	MS#3	57.57	28	1.59	25.94	74.2	17.34		
	MS#4	32.93	13	0.24	21.54	38.44	18.93		
	MS#5	48.3	21	0.94	23.5	55.48	14.87	**3**	
	MS#6	78.69	43	2.78	28.65	53.91	26.07		
	MS#7	81.66	33	3.67	22	50.7	16.85		
	MS#8	185.66	34	8.46	10.38	49.44	5.67	**2**	
	MS#9	250.81	59	25.87	13.24	48.4	10.69		
	MS#10	76.99	43	4.05	29.18	73.77	19.21	**3**	
	MS#11	22.8	25	0.81	47.64	54.89	45.19		

Within the context of loess landslide classification, the definitions and descriptions in different systems were formulated by using case studies from different parts of the loess plateau. The usage of the terms for the landslide type can be ambiguous or misleading and often contradicts with other systems even for the same study area. There is no unanimous agreement on the types of loess-related landslides in HFT, or the loess-related slope failures in general.

Table 2 summarizes the landslide classifications that have been proposed or used for loess-related slope failures in the loess plateau of China; it classifies them into loess landslides or loess-bedrock landslides based on the material composition, and divides them into five types (Peng *et al.*, 2018). The proposed types are readily incorporated in the Varnes classification (Varnes, 1978) in consideration of the engineering properties of loess, and they provide backward compatibility for HFT and potentially other regions in the loess plateau of China. A more complete classification system for loess slopes was recently proposed by Li & Mo (2019).

Table 2 – Landslide classifications for loess-related slope failures in HFT and the loess plateau of China.

Type of landslides		Descriptions and definitions (if provided)
Material	Movement	
Loess	landslide	• A board definition for landslide involves primarily loess and a common type of landslide in HFT and other loess regions in China. • Landslide develops within loess and/or contains fractions of mudstones (Wu & Wang, 2002). • Landslide develops in loess and it is typically accompanied by fluidization and liquefaction (Wang, 1992; Wang *et al.*, 2004b). • *Asequent landslides* (Meng & Derbyshire, 1998): landslides developed exclusively in loess. **(LP)**
	slide	• In general, such type of failure has small scale and short runout. • *Collapse-sliding* (Lu, 1984; Zhou *et al.*, 2002): collapse with subsequent sliding motion. • *Tan-ta* (Meng & Derbyshire, 1998): small adjustment failures due to localized changes with no clear failure plane. • *Loess slide* (Wu & Wang, 2002): failure develops in loess containing layers formed at different ages, sliding surface is governed by vertical joints. **(LP)** • *Loess slide-fall* (Xu et al., 2009a) or *loess slide* (Xu et al., 2008, 2014): failure develops in the un-saturated portion of the loess slope with shallow thickness, small scale, short runout, and uniform color of deposit. **(HFT)**

	flow	• Most of the failures exhibit fluidized movement with long runout and high speed. • *High-speed collapsing landslide* (Zhao *et al.*, 1995): failures with catastrophic fall and slide, with smooth scarp after numerous failures. **(LP)** • *Loess earthflow* (Xu *et al.*, 2008) or *loess flow* (Xu *et al.*, 2009a, 2014): failure initiates at the contact between loess and the underlying clay layer in HFT. Surface seepage can be seen at the failure site with steep scarp (ave. 35 m). The movement lasts for <1 min, exhibiting liquefaction and fluidization with high-speed and long runout. **(HFT)**	
Loess-Bedrock†	interface landslide*	• *Bedrock contact landslide* (Meng & Derbyshire, 1998): sliding of loess along the bedrock surface, often due to a saturated base with progressively decreasing strength by groundwater stagnation at the interface. • *Loess interface landslide* (Wu & Wang, 2002): common at slopes with an average gradient of 10°-20°, strain-softening occurs between loess and bedrock forming sliding surface. **(LP)** • *Loess-mudrock interface landslide* (Xu *et al.*, 2008): the principal sliding direction aligns with the bedrock dip causing the sliding surface to develop along the mudstone parting and causing low-velocity failure, it is often recurring and forms step-shaped head of deposits. **(HFT)**	
	plane landslide	• *Low-speed landslide along weak structural belt* (Zhao *et al.*, 1995): groundwater flow along joints and bedding plane reduces strength and resistance to deformation, and eventually causes creeping-like low-velocity landslide. • *Loess-mudstone plane landslide* (Wu & Wang, 2002): occurs in bedding plane with mild dip (10°-20°) under long-term gravitational deformation causing shear failure along bedding plane. • *Loess-bedrock landslide* (Wang *et al.*, 2004b): long-term deformation in the bedding plane due to strength reduction caused by groundwater, commonly has short runout and low velocity. **(LP)** • *Loess-mudrock bedding landslide* (Xu *et al.*, 2008) or *Combined loess and bedrock along bedding planes* (Xu *et al.*, 2014): failure along the bedding plane with a runout of 30-60 m at a speed of 0.002-0.005 m/s. **(HFT)**	*Mixed landslide* (Meng & Derbyshire, 1998): ingress of groundwater through joints into the underlying bedrock, causes slope to failure, with no evidence of movement in the overlying loess layer. **(LP)**
	cutting landslide	• *Terrace landslide* (Meng & Derbyshire, 1998)**: it denotes to a special type of failure occurs along terrace margins, with slip surface develops within the loess, resulting in catastrophic failure under the impact of groundwater movements. • *Loess-mudstone cutting landslide*: The sliding body is mainly composed of loess and Middle Cenozoic strata. The main scarp is steep with size >1×10^6 m^3. **(LP)** • *Loess-bedrock incising landslide* or *Combined loess and bedrock across bedding planes*: Slip surface cuts bedding planes with a high angle. Field survey shows that the difference between bedding plane dip and the sliding direction is 60°-90°. **(HFT)**	

†A board definition for landslide with failure surface develops in the overlaying loess layer and propagates into the underlying bedrocks.

*Loess-bedrock interface landslide is sometimes classified as a type of loess landslide as the deposit consists of mainly loess; we categorized such failure into the loess-bedrock landslide group because the deposit still contains other material, commonly clay and gravel.

**The concept of terrace landslide was formulated to generalize the large-scale and high-speed landslide occur at the loess terrace margin; but the definition and character descriptor of terrace landslide are similar to the loess-bedrock cutting landslide.

Note: **LP** denotes to the loess plateau of China.

2.2.3 Loess flowslides

The loess flowslides in HFT are multi-staged retrogressive failures induced by irrigation, with failure surfaces developing entirely within the overlying loess layer; they are medium- to large-scale slope failures with rapid movement and long runout exhibiting liquefied and fluidized flow behavior. Qi *et al.* (2018) showed that flowslides in HFT have exhibited pronounced retrogressive behaviors, where new landslides develop on the scarp of the previous ones, causing slope retreat at the margin of the terrace at an average rate of 0.024 km^2/yr (about 3% annual depletion). As the end of 2017, 18 loess flowslides were observed in HFT (see Table 1), with the reach angle, defined as $\varphi_{\alpha} = \tan^{-1}(H/L)$, ranging from 10°-37° (average 22.8°), where H and L are the vertical drop and the horizontal projection of the runout distance, respectively (Corominas, 1996).

The flowslides typically form a semi-circular scarp, with conchoidal tensile cracks near the crest due to unloading following a landslide event. Field data indicated that the openings of the tensile cracks range from 1 cm to over 100 cm as they approach the crown of the landslide; the openings typically exceed 20 cm within 3 m of the crown, with evidence of vertical surface offsets.

There is no unanimous agreement on the mechanism of the long-runout behaviors in flow-like landslides; they have been largely ascribed as flow instability in soils, e.g. sand-fine mixtures (Eckersley, 1990; Zhu & Anderson, 1998; Olson *et al.*, 2000; Wang & Sassa, 2001; Lade & Yamamuro, 2011; Bedin *et al.*, 2012) or loess (Derbyshire *et al.*, 1994; Derbyshire, 2001; Zhang *et al.*, 2017). The more widely accepted hypothesis for such an instability process involves pore pressure response (Iverson, 1997, 2012; Hungr & Evans, 2004; Xu *et al.*, 2012b); others include lubrication and fluidization by ice (Delaney & Evans, 2014), by heat (Lucas *et al.*, 2014; Hu *et al.*, 2018; Wang *et al.*, 2018), by trapped air or dust (Hsu, 1975), by acoustic vibration (Johnson *et al.*, 2016), or by dynamic rock fragmentation (Bowman *et al.*, 2012). Many have argued that the metastable structure of loess facilitates the onset of flow liquefaction; yet the degree and micromechanics of such effects remain unclear (Leng *et al.*, 2018; Zhang & Wang, 2018).

2.3 Study Area II: the 2008 Wenchuan earthquake

The work conducted in CHAPTER 6 and CHAPTER 7 are based on Study Area II.

2.3.1 Geological setting

The 2008 Wenchuan Earthquake (M_W 7.9) occurred in Sichuan province, China on May 12, 2008; it released significant energy at a shallow focal depth with long-lasting ground motion (Huang & Fan, 2013). The earthquake resulted in 87,145 fatalities (17,923 missing) and 374,643 injures (National Development and Reform Commission, 2008). The co-seismic surface rupture was along the middle segment of the Longmen Mountain Fault zone, with a length of 270 km, between the Sichuan Basin and the eastern margin of the Tibetan Plateau (Xu *et al.*, 2008; Hubbard & Shaw, 2009), as shown in Figure 2.3. The fault zone was formed due to the oblique collision between the Indian Plate and the Eurasian Plate, which resulted in the extrusion of the Tibetan Plateau moving against the Sichuan Basin at rates of 15-20 mm/yr (Tapponnier *et al.*, 2001).

The steep margin of the Tibetan Plateau is intensely dissected by the tributaries of the Yangtze River (Ouimet *et al.*, 2007), accompanied by drastic elevation change of 3500-5500 m within 50 km (Fu *et al.*, 2011), shaping one of the most mountainous regions for human settlement in China. Eight historical mega earthquakes (M_W 7.0 or greater) occurred within 200 km of the epicenter of the Wenchuan earthquake, including the 1933 Sichuan Earthquake (M_W 7.5) (Qi *et al.*, 2010). A survey of the literature shows that at least 66 large earthquakes ($4.7 < M_W < 7.0$) can be attributed to the Longmen Mountain Fault zone since 638 AD (Li *et al.*, 2008b; Dai *et al.*, 2011; Gorum *et al.*, 2011).

The main surface rupture was caused by the simultaneous ruptures of the Yingxiu-Beichuan Fault (YBF) and the Pengguan Fault (PF) that form an imbricate thrust belt; these two northeast-striking fault zones are connected by a short northwest-striking rupture zone (Parsons *et al.*, 2008; Xu *et al.*, 2009c). The earthquake initiated close to the base of the YBF and its ability to link these various fault segments enabled the earthquake to become such a large seismic event (Xu *et al.*, 2009c). The impacts of the mainshock and aftershocks have caused extremely severe damage to the regions along the fault zone with an intensity of XI (extreme) on the Mercalli Intensity scale.

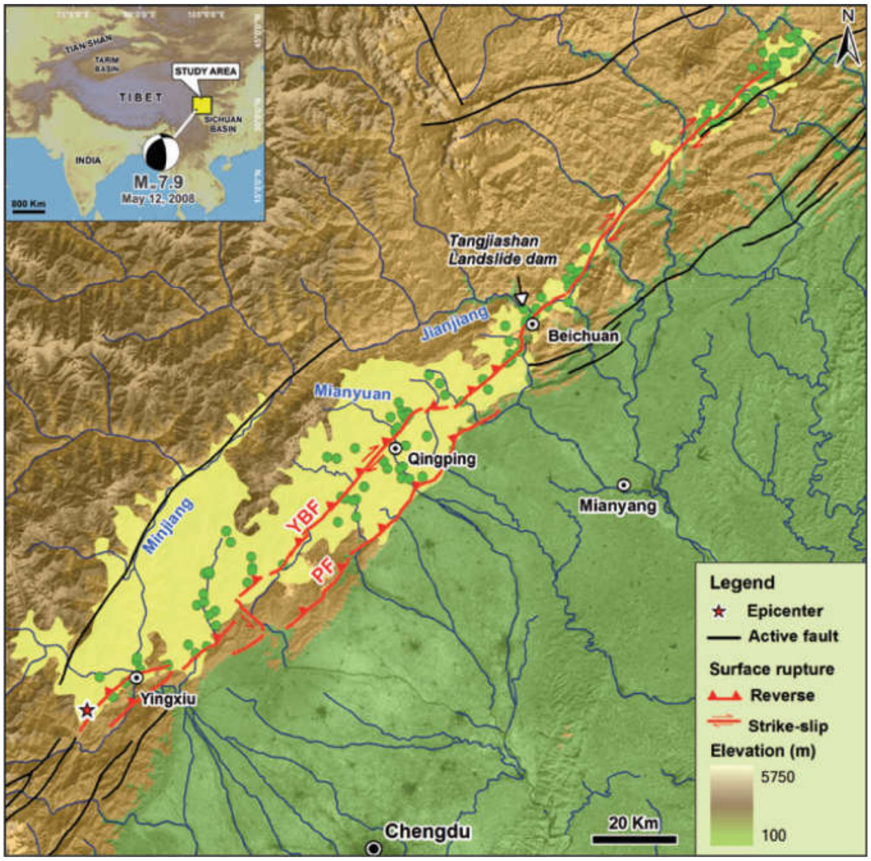

Figure 2.3 – Tectonic and geomorphic setting of the 2008 Wenchuan earthquake in China, where each green dot represents a large scale co-seismic landslide (displaced surface area > 50,000 m^2), and the region with more than 0.1% of the area impacted by landslides are shown in yellow (after Huang & Fan, 2013).

2.3.2 *Co-seismic landslides*

Over 50,000 co-seismic geohazards were reported (Huang, 2009b; Huang & Li, 2009; Dai *et al.*, 2011; Parker *et al.*, 2011), including 30 extremely large scale landslides (vol. > 10 million m^3). Gorum *et al.* (2011) mapped nearly 60,000 post-earthquake landslide scraps in the study area. More than 1,200 landslides were posing direct risks to the communities in Sichuan (Huang & Li, 2009). The number of co-seismic landslides has greatly exceeded those triggered by other recent earthquakes, including the 1999 Chi-Chi earthquake, the 2005 Kashmir earthquake, and the 2015 Nepal earthquake.

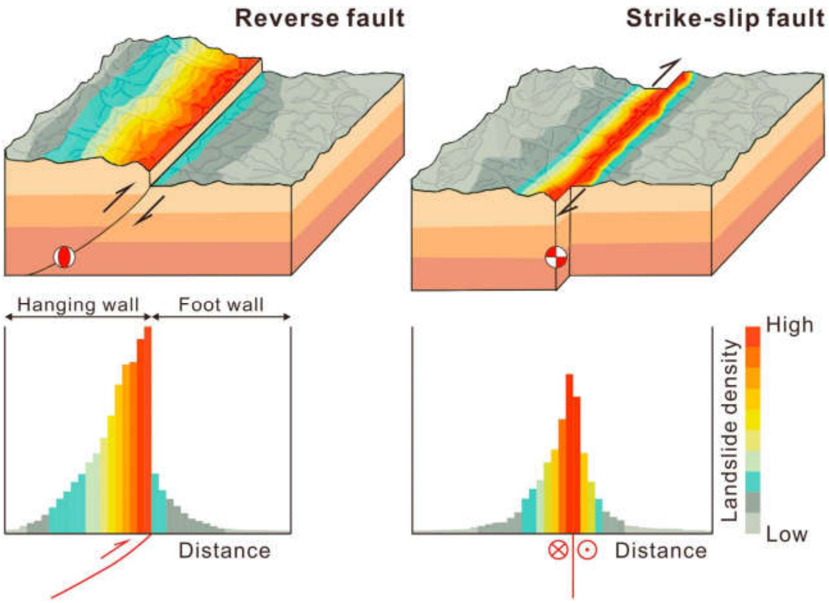

Figure 2.4 – Schematic representation of the co-seismic landslide distribution of the 2008 Wenchuan earthquake due to the effect of faulting (Fan *et al.*, 2019).

The slip in the southwest of the earthquake region was dominantly vertical, thrusting motion, whereas the slip in the northeast was oblique, with the maximum slip lower in magnitude (Xu *et al.*, 2009c; Ouimet, 2010). Keefer (1984) and Rodriguez *et al.* (1999) provided global reviews on earthquake-induced landslides, and identified the positive correlation of the earthquake magnitude to the maximum distance between landslides and co-seismic faults. Fan *et al*. (2019) suggested that co-seismic landslides were clustered over a much wider corridor along the southwest part of the fault (Figure 2.4) due to the strong vertical and horizontal motion caused by the reverse faulting.

2.3.3 Post-earthquake debris flows and impacts

Debris flows are the sudden downward surge of saturated and poorly sorted sediments under gravitational forces (Iverson, 1997; Iverson *et al.*, 1997); they behave as a flow-like landslide and pose significant risks to the downstream communities with their far-reaching impacts. A significant increase in debris flow events was observed after the Wenchuan earthquake, which can be attributed to the increase in sediment flux caused by the co-seismic landslides (Huang & Fan, 2013; Guo *et al.*, 2016), as a large amount of landslide deposit material becomes the source material for rainfall-induced debris flow, which can increase the magnitude through progressive entrainment during the movement (Iverson *et al.*, 2011; Cui *et al.*, 2013). The mobilized materials of the debris flows typically contain a wide range of particle sizes. For example, the percentage of gravel (4.75 mm – 75 mm) in the co-seismic landslide deposits in the Wenjia gully ranges from 30% - 95% depending on the location in the gully, and nearly 50% of the deposits are gravels in the August 2010 debris flow (Yu *et al.*, 2013).

The co-seismic landslides and the subsequent debris flows represent a post-earthquake instability process (Zhang *et al.*, 2014b). Such changes in debris flow occurrences can be reflected by the drastic variations in pre-/post-earthquake rainfall thresholds of the region. A rainfall threshold represents the minimum precipitation required to trigger a debris flow, or shallow landslide, which is typically expressed as the rainfall intensity-duration relation, $I = aD^{-b}$, where a and b are empirical coefficients, I is the mean rainfall intensity, and D is the rainfall duration (Caine, 1980).

Numerous destructive debris flows occurred immediately after the earthquake during the monsoon seasons of 2008, 2009 and 2010. Many debris-flow mitigation systems that were implemented at the time followed the conventional design specifications which later proved to be insufficient for debris flows after an earthquake due to high sediment flux (Xu *et al.*, 2012c). As a result, the design of mitigation systems has been upgraded to alleviate the cascading impacts of debris flows on the downstream community. However, there is a lack of a performance evaluation framework for the mitigation systems at the site-scale.

The region of interest for the debris flow studies in this work includes the watersheds of Qingping, Yingxiu, and Dujiangyan; these areas contain more detailed records of pre-/post-earthquake as well as pre-/post-mitigation precipitation and debris flow occurrences.

CHAPTER 3. VOLUME-STRESS STATE AND FLOW BEHAVIOR OF LOESS UNDER UNDRAINED CONDITIONS

This chapter presents an analysis of the effects of structure and grading on the large strain behavior of saturated Chinese loess, with the objective of understanding the shearing response under the undrained loading conditions.

3.1 Introduction

The mechanism of loess flowslides, as discussed in Section 2.2.3, has been largely ascribed to the flow instability and flow liquefaction of loess, which is characterized by the sudden loss of strength with the development of large strains, accompanied by increasing pore pressure under monotonic loading.

There are some ambiguities about the definition of liquefaction; it is common to cite the definition of liquefaction as '*a phenomenon wherein the shear resistance of a mass of soil decreases when subjected to monotonic, cyclic, or dynamic loading at constant volume*' (Poulos *et al.*, 1985), or '*the stage in a cyclic load test when 100% pore pressure develops momentarily, irrespective of the shear strength that remains after that stage is reached*'(Seed & Lee, 1966). Sometimes it simply indicates strain softening so that sample would fail uncontrollably at $q_{\max}$ (Sladen *et al.*, 1985). In other cases, it indicates that soil has reached a liquefied state with zero effective stress and zero strength (Yamamuro & Covert, 2001). Carrera *et al.* (2011) defined that a 'true' liquefaction occurs when a specimen visibly appears to liquefy as pore pressure equals confining pressure (with $q \approx 0$ and $p' \approx 0$), which incorporates the definitions given by many researchers (e.g. Seed & Lee, 1966; Poulos *et al.*, 1985; Yamamuro & Covert, 2001), and thereby is adopted here despite the fact that intact loess may not achieve such a state due to its structure.

Many have argued that the metastable structure of loess facilitates the onset of flow liquefaction; for example, strong contractive responses with rapid decrease in strength can be observed for both intact and reconstituted silty loess (Zhou *et al.*, 2014b; Qi *et al.*, 2018). However, the influence of structure on such instability processes remains unclear, especially from the micromechanics standpoint (Leng *et al.*, 2018; Zhang & Wang, 2018). The need for better understanding of such effects are also highlighted by the increasing activities for the land creation project in the loess plateau of China (Li *et al.*, 2014), in which typically intact loess is disturbed or remolded during excavation (and transportation) before being re-deposited to fill valleys to create flatter land due to urbanization. Hence, understanding the relative position between the state of a loess (as the result of structure) and its CSL in the volumetric plane aids in analyzing the susceptibility to flow liquefaction and flowslides. This is emphasized by the most recent report on a loess mudflow occurred in a ‘bulldozed’ mountain area near Lanzhou city (Zhang *et al.*, 2019).

The grading of loess is of significant interest to the study of the mechanical properties of loess, because while loess flowslides are observed at many locations in the loess plateau, including HFT and JY terrace, they are not usually found in sandy loess regions, despite the common aeolian origin with typical open structures at a highly porous state. The fines content (FC) is the ratio between the volume of fine particles and the volume of the soil (Ni *et al.*, 2004). The evolution of the shape and location of CSL with changing FC of a soil remains unclear, and often the findings appear to be contradictory. Been & Jefferies (1985) indicated that the CSL of the Kogyuk sand became steeper with increasing FC. On the other hand, Coop & Atkinson (1993) indicated that the CSL of the Dog's Bay sand became flatter as fines increase under high confining pressures. Such differences may be ascribed to the stress level of the tests, depending on whether the role of particle breakage is pronounced (Carrera *et al.*, 2011). Andrianopoulos *et al.* (2001) proposed that the CSL may even 'rotate' around a pivot point in the $e: \ln(p')$ plane. Thevanayagam *et al*. (2002) reported that the CSL's of the F55 Foundry sand exhibited a subparallel downward shift with increasing FC, while maintaining a similar shape; however they reversed direction to move upwards as FC increases. The grading at the lowest location was defined as the 'threshold fine content' (FC_{th}).

In this chapter, a series of conventional isotropically consolidated undrained (CIU) tests are conducted on the intact and reconstituted specimens of the Chinese loess to better characterize the influence of structure and grading on the undrained flow instability.

3.2 Materials and experimental method

Loess typically contains a silt fraction of 70%-100%, depending on the geological origins during deposition. The clayey loess is sampled from a slope on the JY terrace. The silty loess is sampled at the scarp of a flowslide in HFT. The sandy loess is sampled from a slope along a highway in SM. Block samples were retrieved and stored in the split PVC containers. All samples are retrieved from a depth of about 20 m. The index properties of the samples are listed in Table 3. All three samples are slightly above the A-line on the plasticity chart and classified as CL.

Table 3 – Index properties of the natural loess samples.

Sample	G_s	e_0	ρ_d (kg/m^3)	w (%)	w_P (%)	w_L (%)	PI (%)
JY	2.71	0.87-0.90	1540	12.6	18.35	32.45	14.1
HFT	2.69	0.86-0.89	1380	8.0	17.53	26.83	9.30
SM	2.70	0.84-0.87	1470	13.0	20.82	26.13	5.31

3.2.1 Sample preparation

Test specimens are trimmed with average dimensions of 50 mm diameter and 100 mm height. The particle size distribution of the test specimen is discussed in Section 3.2.2, and the detailed test program is discussed in Section 3.2.3. The JY and HFT loess are used to assess the influence of structure on flow instability. The intact specimens are trimmed from the block sample by sandpapering on a hand lathe. The reconstituted specimens are derived from abrading the oven-dried block samples and prepared by wet compaction at the *in situ* water content with different layers depending on the targeted initial void ratio. The reconstituted test specimens of JY loess and HFT loess are prepared with e_0 = 0.81-0.91 and e_0 = 0.77-0.98, respectively.

The SM loess is used to study the influence of grading on flow instability. The reconstituted specimens are created from the block sample of sandy loess by using the same approach as described for JY and HFT loess samples. The sand content is altered by adding or removing sand particles through sieve analysis, while retaining a constant FC. In this fashion, grading of the fines in the natural sandy loess samples are preserved. Five groups of test specimen are produced with sands contents (by weight) of 9.87%, 17.75%, 20.55%, 40.56%, and 60.65%, respectively. The results are presented in terms of equivalent fines content to better compare with other datasets from in previous literature. All specimens are prepared with an e_0 of 0.83-0.87.

3.2.2 Particle size distribution

The particle size distribution of the natural loess samples was determined by using a laser diffraction particle size analyzer (Malvern Panalytical Mastersizer 300E) and the conventional hydrometer test (ASTM D7928). As shown in Figure 3.1, the volume of clay fractions (< 0.005 mm) are 12.2%, 7.9%, and 4.3% for JY, HFT, and SM loess specimens, respectively. The natural volume of fines fractions (< 0.075 mm) are 87.3%, 82.3%, and 73.5% for JY, HFT, and SM loess samples, respectively. The hydrometer tests produced similar trends, showing good agreements with the laser diffraction method, especially for the finer region of the curves.

The clay content of JY loess samples was found to be over 30% by Xu & Coop (2016) at the depths of 20 m and 50 m; however a low clay content (5.2%) was reported for JY loess by Leng *et al*. (2018) at the depth of 60 m. The difference in clay content of JY loess may be ascribed to the sampling locations. The soil profile of JY terrace consists of loess-paleosol layers in an alternating sequence; it is postulated that the loess sampled by Xu & Coop (2016) is more clay-rich as the sampling location was in close proximity to a paleosol layer.

The particle size distribution of SM test specimens is determined by laser diffraction method (Figure 3.1) to provide more accurate and direct measurements on the volume of fines fractions. The FC for the reconstituted SM loess samples are 87.9% (group #1), 78.0% (group #2), 73.5% (group #3), 55.5% (group #4), and 34.6% (group #5). Group #3 contains the natural grading of the SM loess and group #1 represents a FC similar to the natural FC of JY loess sample.

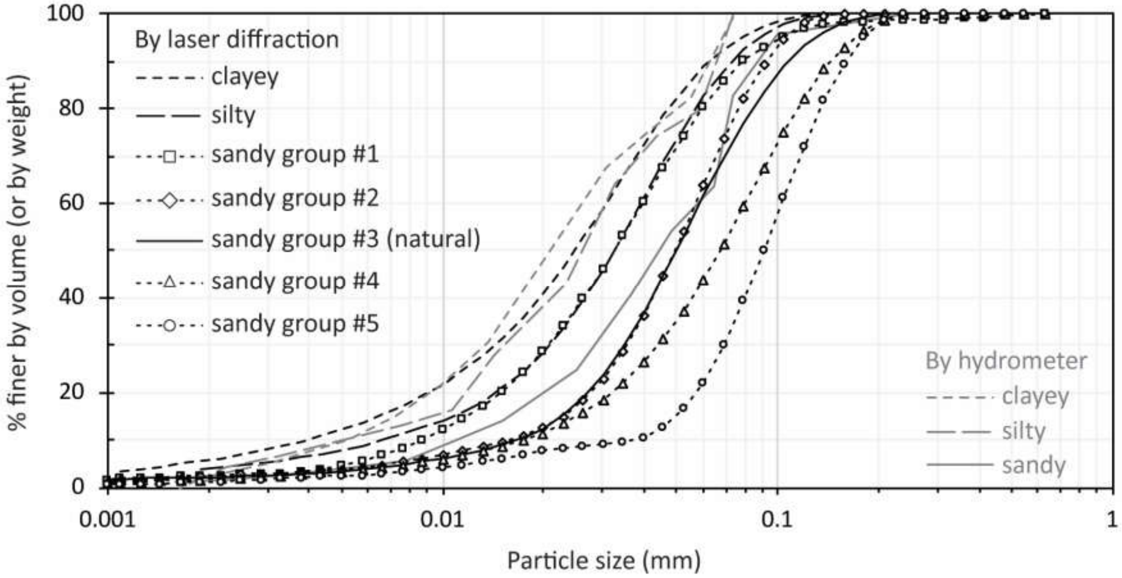

Figure 3.1 – Particle size distributions of the natural clayey (JY), silty (HFT), and sandy (SM) loess samples (with natural and modified sand content), measured by hydrometer test (by weight) and laser diffraction analyzer (by volume).

3.2.3 *Test procedures*

In the CIU tests, specimens are saturated by a low-pressure flow pump until $B > 0.96$ was achieved, followed by isotropic consolidation and shearing under undrained condition at a displacement rate of 0.1 mm/min. A direct comparison between the shearing behavior of the intact and reconstituted specimens at the exact same initial condition is implausible; but the tests are conducted at the same stress levels, and at similar void ratio to offer some insights into the differences on the onset of flow instability under the influences of structure and grading in loess. A total of 46 tests were performed. A summary of the tests is presented in Table 4.

Table 4 – Summary of the CIU test program on JY and HFT loess samples.

Test	FC	p'_0 (kPa)	e_0	e_c	p'_{CS} (kPa)	q_{CS} (kPa)	ψ	ψ_m
J_i50	-	51	0.910	0.841	29.36	46.86	0.210	0.102
J_i100		101	0.886	0.805	31.11	47.00	0.242	0.136
J_i310		311	0.796	0.743	57.87	72.40	0.291	0.176
J_i510		511	0.871	0.652	129.35	154.32	0.249	0.116
J_i800		801	0.908	0.625	176.64	196.40	0.266	0.126
J_r50	-	51	0.911	0.815	10.28	16.73	0.118	0.068
J_r100		101	0.900	0.689	27.71	36.99	0.092	0.041
J_r310		311	0.809	0.661	88.47	109.23	0.144	0.073
J_r510		511	0.879	0.603	178.55	226.30	0.134	0.060
J_r800		801	0.881	0.558	318.50	406.01	0.125	0.049
H_i50	-	51	0.889	0.842	5.17	12.40	0.059	0.044
H_i60		61	0.880	0.836	12.47	24.55	0.070	0.048
H_i100		101	0.878	0.828	25.25	28.98	0.123	0.077
H_i300		301	0.881	0.776	54.27	74.85	0.194	0.123
H_i500		501	0.891	0.647	168.91	215.12	0.123	0.053
H_r15	-	16	0.982	0.851	3.82	7.94	0.029	0.023
H_r35		36	0.967	0.841	7.53	10.52	0.085	0.067
H_r50_1		51	0.771	0.634	92.63	135.29	-0.083	-0.057
H_r50_2		51	0.959	0.827	5.544	13.54	0.110	0.073
H_r100		101	0.784	0.729	51.57	70.06	0.089	0.035
H_r300		301	0.865	0.673	77.49	100.36	0.157	0.079
H_r500		501	0.856	0.605	152.74	194.71	0.146	0.064
S1_50	87.9%	51	0.855	0.822	9.91	12.82	0.086	0.057
S1_100		101	0.857	0.778	20.83	26.56	0.077	0.047
S1_310		311	0.853	0.727	81.45	97.47	0.085	0.050
S1_510		511	0.845	0.674	164.61	202.64	0.058	0.026
S1_800		801	0.858	0.642	291.72	361.77	0.049	0.020
S2_50	78.0%	51	0.860	0.747	12.28	12.68	0.044	0.023
S2_100		101	0.868	0.735	24.66	27.66	0.055	0.032
S2_310		311	0.873	0.708	86.39	98.50	0.066	0.040
S2_510		511	0.859	0.674	162.76	189.80	0.049	0.024
S2_800		801	0.860	0.647	271.73	332.73	0.037	0.015
S3_50	73.5% (natural)	51	0.846	0.760	15.10	17.60	0.048	0.027
S3_100		101	0.841	0.747	23.84	30.50	0.058	0.035
S3_310		311	0.875	0.704	116.40	138.50	0.053	0.029
S3_510		511	0.858	0.662	190.50	231.40	0.028	0.009
S4_50	55.5%	51	0.829	0.782	4.13	8.20	0.089	0.064
S4_100		101	0.861	0.720	19.27	25.10	0.050	0.027
S4_310		311	0.868	0.701	63.56	75.15	0.069	0.041
S4_510		511	0.856	0.657	157.14	190.03	0.041	0.018
S4_800		801	0.854	0.648	283.71	346.80	0.047	0.022
S2_50	34.6%	51	0.848	0.822	9.91	12.82	0.011	0.003
S2_100		101	0.857	0.778	20.83	26.56	0.004	0.0004
S2_310		311	0.852	0.727	81.45	97.47	0.027	0.011
S2_510		511	0.835	0.674	164.61	202.64	0.027	0.012
S2_800		801	0.829	0.642	291.72	361.77	0.017	0.005

Note. J and H represent JY and HFT loess samples, respectively. S represents SM loess samples with the suffix denotes to the group number. The test designators *i* and *r* represent intact and reconstituted samples, respectively. The p'_0, e_0, e_c, p'_{CS}, q_{CS} are the initial confining stress, initial void ratio, void ratio after consolidation, and mean effective stress and deviatoric stress at the critical state, respectively. ψ is the state parameter and ψ_m is the modified state parameter.

3.3 Influence of structure on the undrained behavior

3.3.1 Stress-strain behavior

The undrained stress-strain responses of the intact and reconstituted silty loess (HFT) reveal a strong contractive tendency with intense strain-softening behavior, with peak strengths reached at $\varepsilon_\mathrm{a} < 2\%$ and sharp increases of pore pressure (Figure 3.2a). The initial stiffness, defined by the initial tangent elastic modulus, increases with increasing confining stresses; however, no distinctly stiffer responses were found for the intact silty samples as compared to the reconstituted samples at similar stress levels, implying a possibly more significant effect of void ratio over structure on the initial stiffness (Figure 3.2b). The change of pore pressure is normalized by p'_0, which highlights an increasing excess pore pressure related to the flow instability (Figure 3.2c); such tendency can be suppressed by an increasing p'_0 and a decreasing e_c.

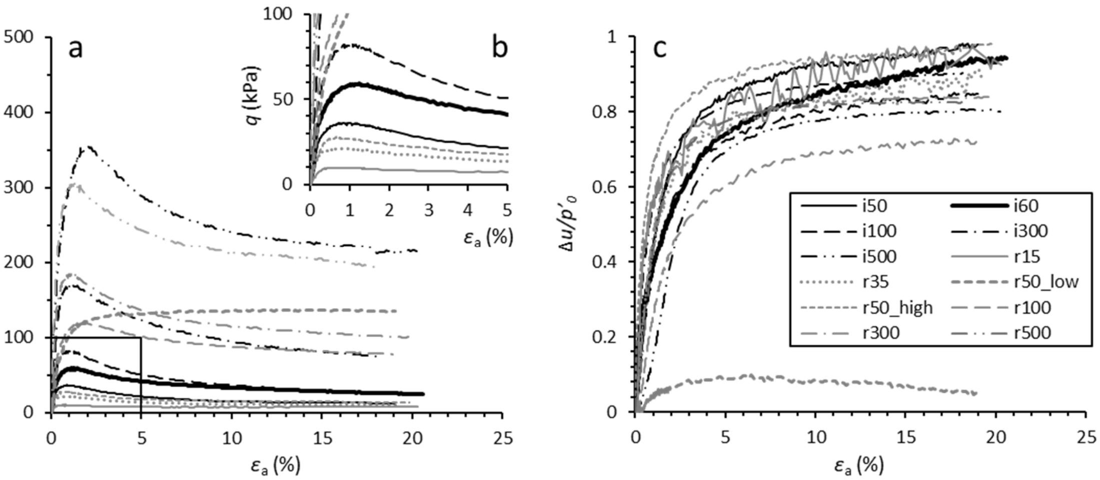

Figure 3.2 – CIU results of the intact and reconstituted silty loess (HFT) samples. (a) undrained shear stress and axial strain responses for all the tests; (b) enlargement for axial strain below than 5%; (c) pore-water pressure responses during the tests (normalized).

The undrained stress-strain responses of the intact and reconstituted clayey loess (JY) exhibit similar intense strain-softening behavior, with peak strengths reached also at $\varepsilon_\mathrm{a} <$ 2% and sharp increases of pore pressure (Figure 3.3a). The void ratio at the beginning of shearing appears to have a more prominent effect than the influence of structure on the initial stiffness (Figure 3.3b). The development of excess pore pressure is also normalized by p'_0, as shown in Figure 3.3; but it appears to be visibly less intense as compared to the HFT specimens.

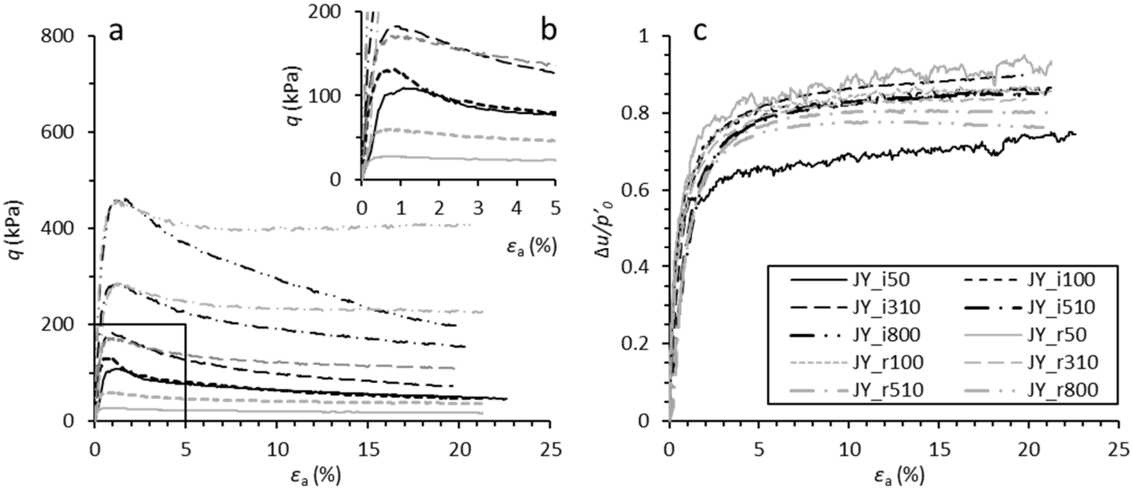

Figure 3.3 – CIU results of the intact and reconstituted clayey loess (JY) samples. (a) undrained shear stress and axial strain responses for all the tests; (b) enlargement for axial strain below than 5%; (c) pore-water pressure responses during the tests (normalized).

Although critical states have not been fully established for several tests in this series of CIU tests, as shown in Figure 3.4, it can be assumed that an $\varepsilon_\mathrm{a} \approx 18\%$ is sufficient for most tests to reach the critical state. The final stress ratios M and the corresponding critical state friction angles for clayey and silty loess samples are 1.29 (ϕ'_CS = 30.4°) and 1.36 (ϕ'_CS = 33.7°), respectively. The differences in M of the samples may be associated with the insufficient strain to establish critical state due to the limited displacement range of the triaxial instrument; such inconsistency appears to be more pronounced in clayey samples. No identifiable plane of rupture was observed for the JY and HFT specimens.

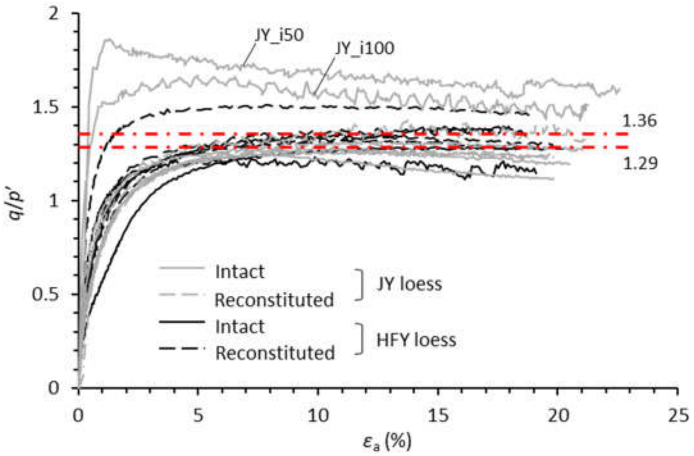

Figure 3.4 – Development of the stress ratios of the intact and reconstituted clayey and silty loess samples.

3.3.2 Critical states

Severe strain-softening behaviors were observed for intact and reconstituted HFT samples from the undrained stress paths in the $q\colon p'$ plane (Figure 3.5a); but no test has reached the 'true' liquefied state ($q \approx 0$ and $p' \approx 0$). A dilative tendency observed for test H_r15 (Figure 3.5b) is analogous to the typical temporary instability behavior for silty sand (Yamamuro & Lade, 1998). In Figure 3.5, inflection points appear along the instability lines for intact (IL_i) and reconstituted (IL_r) samples at $p' \approx 300$ kPa, showing a concave curvature as the $q_{\max}$ moves towards the CSL with a decreasing p'_c, highlighting the possibility of non-linear, non-unique ILs (Figure 3.5b); similar to the observation on the state-dependent ILs of loose sands (Yang, 2002). The concept of instability line (or instability locus, IL) provides a practical view of the instability region based on the trends observed in undrained tests.

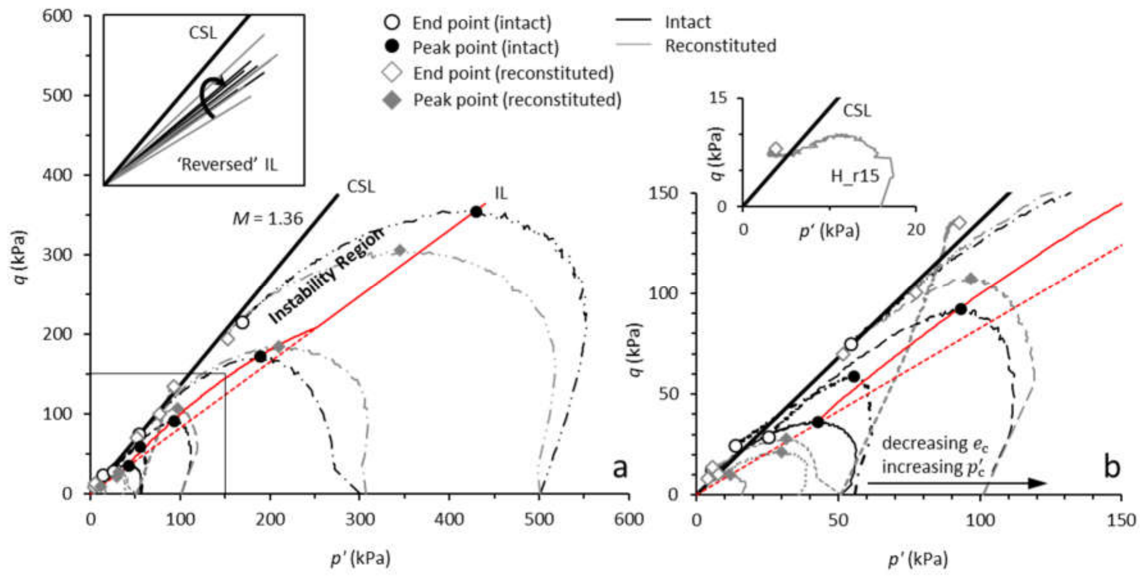

Figure 3.5 – Undrained stress paths of intact and reconstituted silty loess (HFT) samples. (a) the varying instability lines and region for intact samples with similar initial void ratio; (b) enlargement on stresses less than 150 kPa, with dilative tendency showing temporary flow instability for the reconstituted sample at confining stress of 15 kPa.

The IL connects the origin and locus of peak points that are assumed to be the instability points regardless of the occurrence of flow liquefaction (Lade, 1993). Although IL was an extension of the steady-state concept (i.e. collapse surface or line), it follows the principles of CSSM in many respects (Schofield & Wroth, 1968; Sladen *et al.*, 1985; Yang, 2002). The IL was originally assumed to be unique (Kramer, 1996), in an attempt to provide a more sound guidance to explain the nature of instability in stress path space; but larger dataset of test results have suggested that IL is not a soil property and it changes with state parameter the soil and its mechanical properties (Jefferies & Been, 2015). The offset between IL_r and IL_i in Figure 3.5b suggests a larger instability region for intact samples. The possible concave IL_i and IL_r for silty loess differs from the convex IL for silty sands that represents a temporary liquefaction region, as reported by Yamamuro & Lade (1997), indicating an increasing stability in silty loess with a decreasing confining stress. The q_{CS} of the stress paths in the more 'stable' region appears to be substantially lower than that in the less 'stable' region separated by the ILs, indicating a stronger contractive response.

Intense strain-softening responses were also observed for intact and reconstituted JY samples (Figure 3.6a), with no test reaching the 'true' liquefied state. A minor dilative tendency can be observed for test J_i800; but no dilatancy was found for reconstituted JY samples, possibly due to the smaller range of e_0 as compared to the HFT samples. The locus of $q_{\max}$ of the reconstituted JY samples forms a fairly straight instability line (Figure 3.6a), which differs from the concave IL_r of the silty samples. However, a more evident inflection point appears along IL_i, as demonstrated by the trend line in Figure 3.6a, in an attempt to connect the locus and the origin. While the stress paths for test J_i50 and J_i100 highlight the severe strain-softening responses, the $q_{\max}$ are located above the CSL which limited the illustrative capacity of the instability line (Figure 3.6b). The shearing responses of test J_i50 and J_100 may be attributed to the more pronounced effects of structure on JY loess under low confining stresses.

The comparison of the data for the JY and HFT samples provides a broader view on the large strain behavior under the influence of structure on the consistent strain-softening of the intact samples for both clayey and silty loess. The M of JY and HFT samples in this work are lower than the M of JY sample (1.35 ± 0.5) and HFT sample (1.38 ± 0.5) reported by Xu & Coop (2016) and Xu *et al.* (2018); the sampling depths are about 20 m and 30 m for JY and HFT samples, respectively. Such a difference may be associated with the more localized variations in the layer due to different sampling locations.

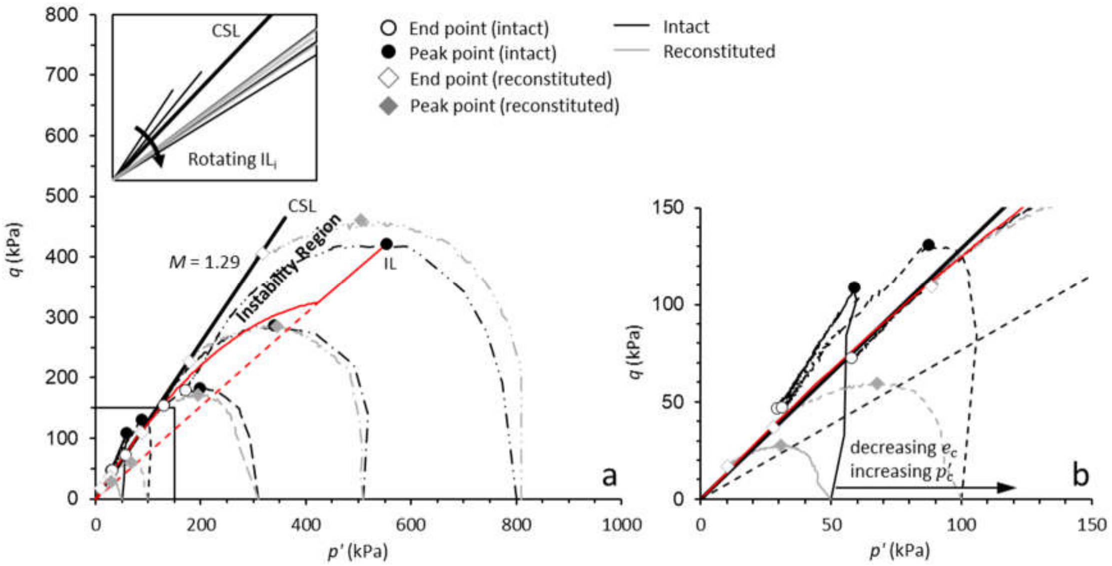

Figure 3.6 – Undrained stress paths of intact and reconstituted clayey loess (JY) samples. (a) the varying instability lines and region for intact samples with similar initial void ratio; (b) enlargement on stresses less than 150 kPa.

The critical states and the start-and-end points of both series of tests are presented in the e: lnp' plane in Figure 3.7, in which two distinct CSL's are observed for the intact (CSL$_i$) and reconstituted (CSL$_r$) specimen for both JY and HFT samples. Difficulties emerged when integrating the CS at the lower confining stresses by a straight CSL in HFT specimens (Figure 3.7a). The intact specimens typically located further right of the CSL than the reconstituted specimens at the same stress level with similar e_0, which can be attributed to the effect of structure that resulted in a more robust compressive responses during consolidation, and thus a higher e_c for intact samples. A linear CSL cannot be established for the range of stresses in the e: lnp' plane; curved CSL's for HFT specimens were also reported by Xu *et al*. (2018) and presented for comparison. The offset between CSL$_i$ and CSL$_r$ reduces from high (Δe = 0.065) to low (Δe = 0.01) stress levels, if straight CSL's are assumed and connected by a curved 'transition' region.

Similar to the CS of silty loess specimens, offsets in the CSL's are observed for intact and reconstituted clayey loess (JY) specimens (Figure 3.7b); however the pair appears to be straight in the volumetric plane. The intact specimens are located further right to the CS as compared to the reconstituted form.

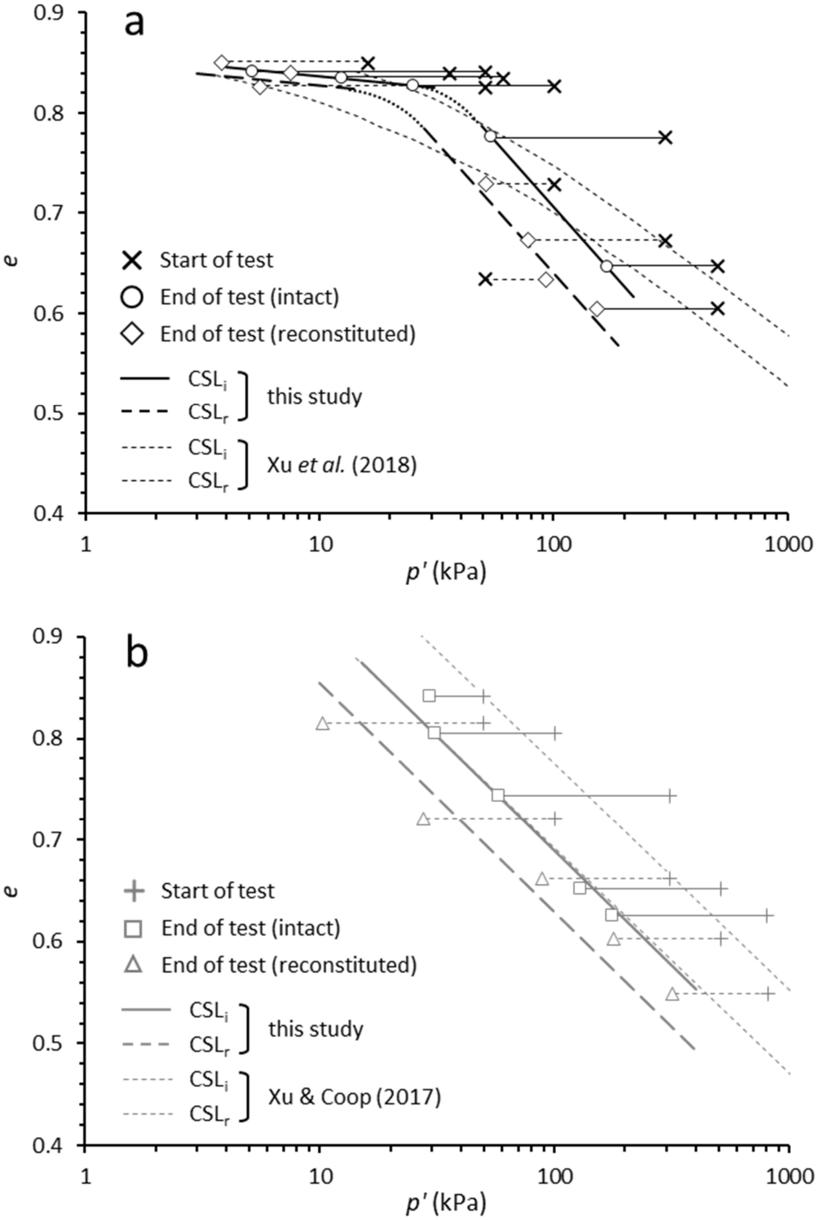

Figure 3.7 – The critical states in the volumetric plane. (a) CSL$_i$ and CSL$_r$ for silty loess (HFT) sample. (b) CSL$_i$ and CSL$_r$ for clayey loess (JY) samples.

For the CSL at high stress levels in JY and HFT specimens, the effect of structure is likely to cause a large offset in e_c between the intact and reconstituted specimens with the same e_0, which results in a higher susceptibility to flow instability for intact loess due to higher state parameters, as illustrated by Figure 3.8. For low stress levels in HFT specimens, a smaller offset in e_c may not be sufficient to cause a distinctly different ψ with the same e_0 along the CSL. Although no data in this series of tests can effectively confirm such a 'reversed' trend, the two sets of CSL's have clearly shown that the effect of structure on flow instability of loess is, at least, stress-dependent.

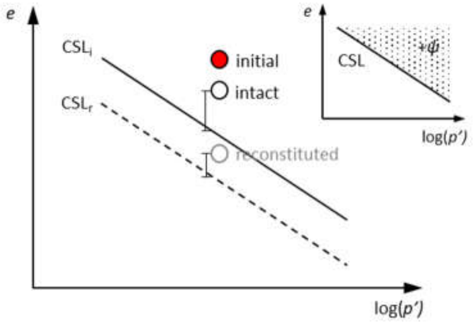

Figure 3.8 – Schematic representation of the difference in the resultant state parameters due to the structure of the Chinese loess. The state parameter concept provides criterion for flow liquefaction susceptibility (Been & Jefferies, 1985); regions that are susceptible to liquefaction are highlighted.

3.4 Influence of grading on the undrained behavior

3.4.1 Stress-strain behavior

The general trend of the undrained stress paths of reconstituted sandy loess (SM) samples indicates a 'shift' from the strain-softening behavior to strain-hardening behavior with a decreasing FC at a similar e_0, with peak strengths reached at $\varepsilon_a < 2\%$ and sharp increases of pore pressure (Figure 3.9).

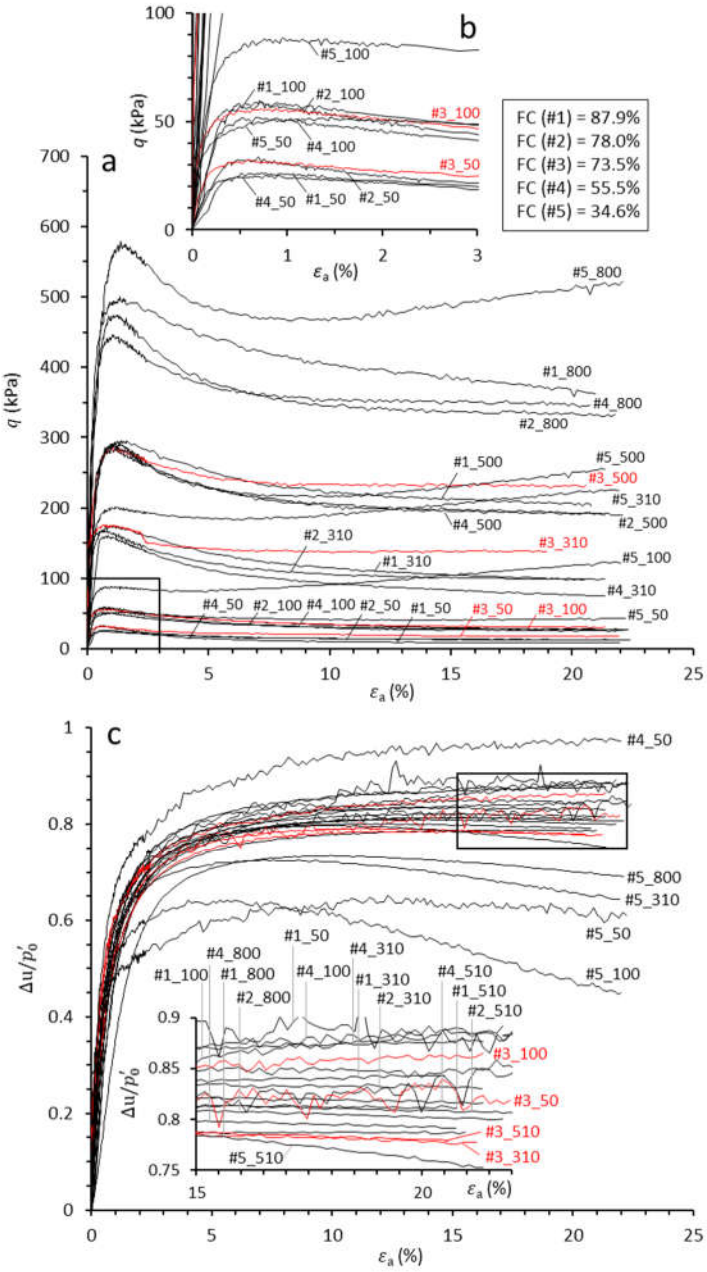

Figure 3.9 – Undrained stress paths of reconstituted sandy loess (SM) samples with various FC. The stress-strain responses of group #3 is highlighted since they represent the natural grading of SM loess. (a) overview of the stress paths; (b) enlargement of stresses less than 100 kPa; (c) pore pressure responses for undrained tests enlarging the end of the tests.

The evident dilative tendency emerges for group #5, with the lowest FC in this series of tests. Within the higher FC groups, the peak strength appears to increase with an increasing FC; but such a trend is less pronounced at p_0' lower than 100 kPa. Nonetheless, the changes in the peak strength imply the presence of a 'reversed' pattern when FC is reduced below 59.4% in the sandy loess sample. The changes of pore pressures are normalized by p_0', and most of the normalized pore-pressure responses are within about 0.82 ± 0.05, despite the varying FC at different stress levels (Figure 3.9c). The pore-pressure responses confirm the dilative tendency in group #5. Most of the tests have reached the CS at the end with axial strain of at least 18%, although some tests continued to change in the stress-volume state.

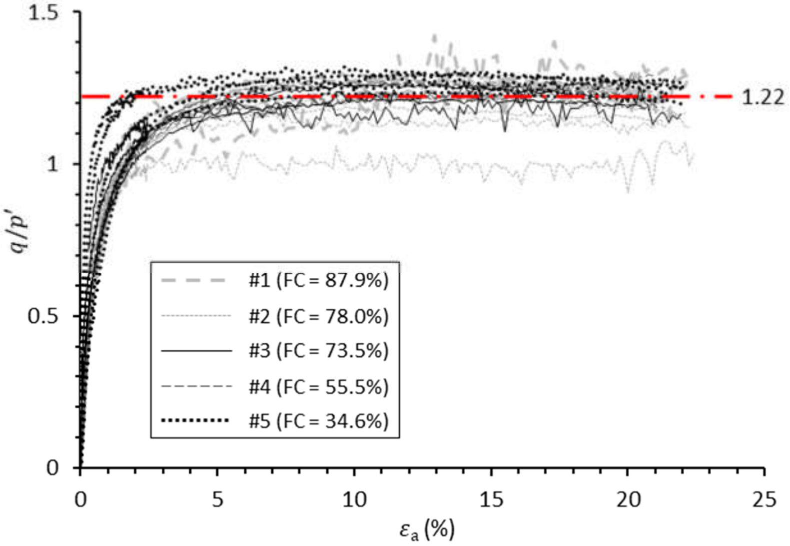

Figure 3.10 – Development of the stress ratios of reconstituted sandy loess (SM) samples with varying FC.

The stress-strain data are represented by stress ratio q/p' in Figure 3.10, in which specimens in group #1 and #5 appeared to be stiffer for the loading conditions. Although the stress ratio varies slightly due to different FC, the majority of the tests converge towards a final stress ratio M of about 1.22 ± 0.05, corresponding to the shearing resistance of ϕ_{CS}' = 29.0°. Such M of reconstituted sandy loess is not consistent with the lower plasticity as compared with intact JY and HFT samples, which further suggests the effects of structure on the undrained behavior of loess.

3.4.2 Critical states

Severe strain-softening behaviors were observed for the reconstituted SM samples at different FC in the $q\colon p'$ plane (Figure 3.11a). Although no test has reached the 'true' liquefied state, the stresses at the end of the test are visibly low (q and p' less than 20 kPa), especially for tests with lower initial confining stresses. Dilative tendency can be observed for specimens in group #5 with the lowest FC, which represent the temporary instability behavior for silty sand (Yamamuro & Lade, 1998).

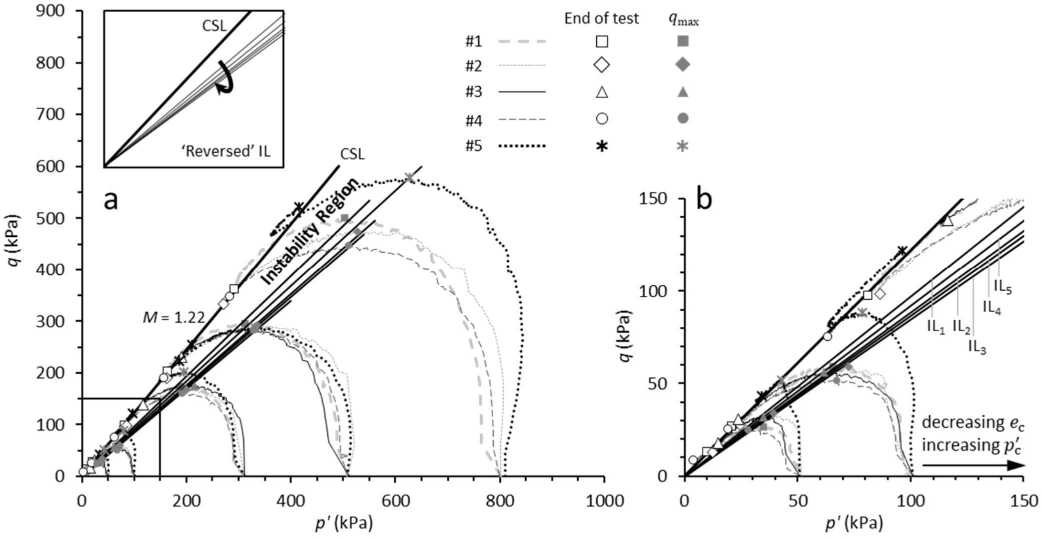

Figure 3.11 – Undrained stress paths of the sandy loess (SM) samples with varying FC. (a) the instability lines and region for specimen with different FC but similar initial void ratio; (b) enlargement on stresses less than 150 kPa showing the 'reversed' trend of IL caused by grading, with peak strength of tests in group #5 lie above the IL.

The locus of peak strengths is connected by a trend line representing each group, which forms the instability line for SM samples at different FC. While the trend lines can sufficiently ($R^2 > 0.99$) characterize the instability region as shown in Figure 3.11a, some clear inflections can be found at the lower confining stresses, especially for specimens in group #5. A ‘reversed’ trend in IL’s is observed; the IL moves away from the CSL with a decreasing FC from IL_1 to IL_3 before ‘rotating’ back towards the CSL as seen in IL_4 and IL_5 as FC continued to decrease (Figure 3.11b). However, such a trend is far less prominent as compared to JY and HFT samples, implying: 1) a strong influence of structure on IL, and thus the flow liquefaction behavior as ‘instability region’ expands at higher stress levels, and 2) the effects of e_c may be stronger than grading on IL, and thus the flow liquefaction behavior of the Chinese loess.

The critical states and stress paths of SM loess samples are shown in Figure 3.12, in which the CSL of group #5 (i.e. CSL_5) is located far right to the rest of the specimens. The CSL’s of group #2, #3, and #4 are clustered with a small offset in void ratio, with CSL_4 being at the lowest point, implying a sharp downward shift from CSL_5 due to an increasing FC. It was postulated that CSL_3 would be located below CSL_2 in light of the increasing FC; but the results may be affected by the limited data points given the very close proximity of the end points of the tests in group #2 and #3.

The continued increasing of FC resulted the ‘rotation’ of CSL_1 with steeper gradient at a FC similar to the natural FC of JY loess, which implies an increasing state parameter at higher stresses as compared to other groups, with everything else being equal. Following the same line of reasoning, the low FC in group #5 results in a stronger shear strength and dilative behaviors. The observed CSL remained, by and large, a straight line at all grading in the $e{:}\ln p'$ plane.

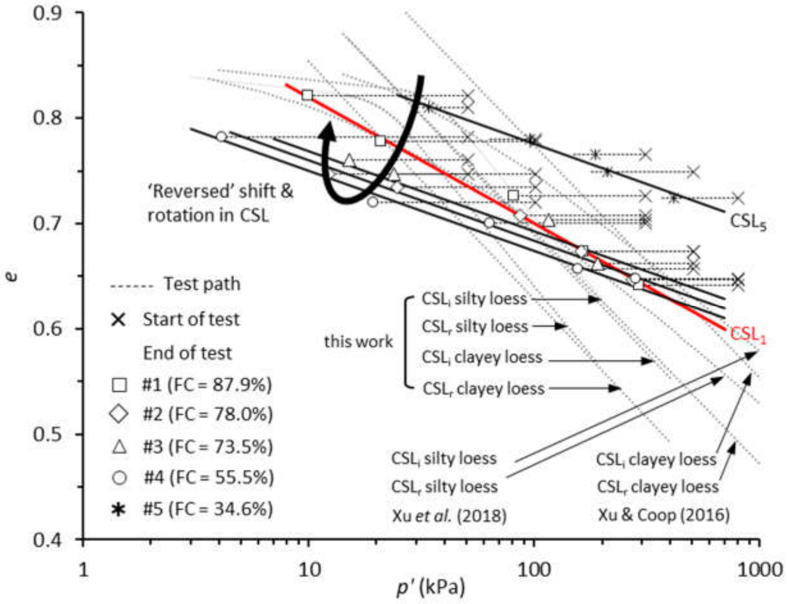

Figure 3.12 – The critical states of sandy loess (SM) samples in the volumetric plane. The CSLs of JY and HFT loess samples are shown for better comparisons.

Thevanayagam *et al*. (2002) proposed an intergranular soil mix classification system, in which the equivalent interfine void ratio, $(e_\mathrm{f})_\mathrm{eq}$ is suggested to better characterize the mechanical behavior of a mix soil system with a FC that is higher than the $\mathrm{FC_{th}}$ but lower than the limiting fines content, $\mathrm{FC_L}$ ($\mathrm{FC_{th}} < \mathrm{FC} < \mathrm{FC_L}$), in addition to the interfine void ratio, e_f that is used when the coarse grains are fully dispersed by the fine particles ($\mathrm{FC_L} <$ FC). The e_f and $(e_\mathrm{f})_\mathrm{eq}$ can be expressed as:

$$e_\mathrm{f} = \frac{e}{\mathrm{FC}} \tag{1}$$

$$(e_\mathrm{f})_\mathrm{eq} = \frac{e}{\mathrm{FC} + (1 - \mathrm{FC})/R_d^m} \tag{2}$$

where e is the global void ratio, FC is the fines content, R_d is the particle size disparity ratio, and m is a fitting parameter depends on grain characteristics and fine grain packing. However, no clear approaches of determining $\mathrm{FC_{th}}$ or $\mathrm{FC_L}$ were given in Thevanayagam *et*

al. (2002), and little information was provided for estimating R_d and m. The e_f is only applied in the case of FC = 100% in Thevanayagam *et al*. (2002) and $(e_\mathrm{f})_\mathrm{eq}$ is used for mixed soils with FC > 40%.

Difficulties emerged when integrating the CS in terms of $(e_\mathrm{f})_\mathrm{eq}$ in a straight line for all groups (Figure 3.13). The CS's of group #1 - #4 lie reasonably on a straight CSL, as the phenomena of a 'rotated' CSL_1 becomes far less pronounced. The CSL_5 is still located significant higher in the $(e_\mathrm{f})_\mathrm{eq}$:$p'$ plane, which suggests that the undrained behaviors of loess are more complex than the sand-fines mixtures.

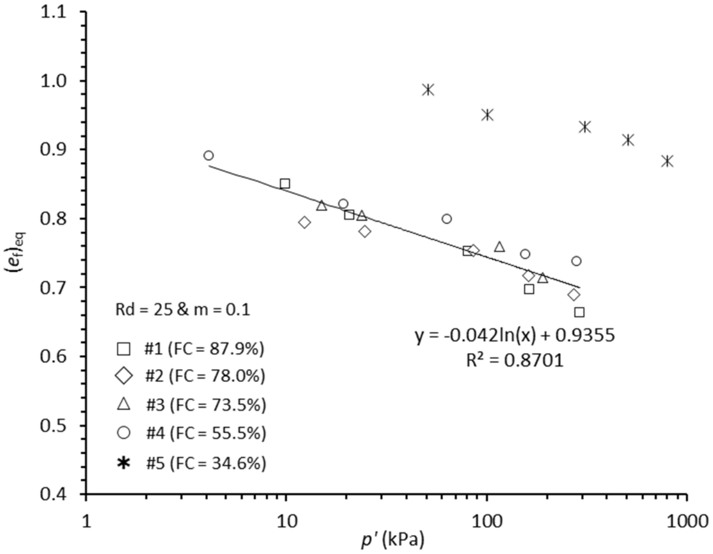

Figure 3.13 – The critical states of sandy loess (SM) samples in $(e_\mathrm{f})_\mathrm{eq}$:$p'$ plane. The results of group #1 - #4 are connected by a trend line.

3.5 Predication of the undrained behavior

The state parameter has been used to assess liquefaction susceptibility; however little discussion can be found on whether it should be used for curved (or bilinear) CSLs (Carrera *et al*., 2011). Curved CSLs have been reported at low confining stresses in sand-fines mixture (Verdugo & Ishihara, 1996; Bobei *et al.*, 2009) and often found in tailings materials (Bedin *et al.*, 2012; Li & Coop, 2018). The curvature of CSL has been largely ascribed to particle breakage (Konrad, 1998). However, such a mechanism cannot necessarily explain the curved CSLs of intact and reconstituted HFT loess (Liu *et al.*, 2018) or the Stava tailing materials (Carrera *et al.*, 2011).

A modified state parameter for characterizing flow instability was proposed by Bobei *et al.* (2009) for sand-fine mixtures; it incorporated the state parameter (Been & Jefferies, 1985) and the state pressure index (Wang *et al.*, 2002) and is expressed as:

$$\psi_m = \psi \left| \frac{\Delta p'}{p'} \right| e \tag{3}$$

where ψ is the state parameter, defined by the relative position of e with respect to the CSL, and $\Delta p'$ is the relative position of p' with respect to the CSL. The definition of ψ_m can be illustrated in Figure 3.14. The e_c and p' are the void ratio after consolidation and the mean effective mean stress, respectively.

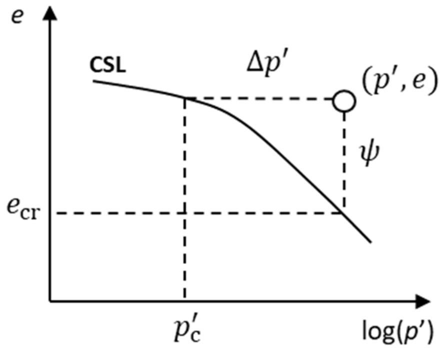

Figure 3.14 – The definition of the modified state parameter (after Bobei *et al.*, 2009).

The ψ_m of the CIU tests are listed in Table 4, and they are plotted in the volumetric plane in Figure 3.15. For HFT loess samples, the ψ_m increases with increasing confining stress until 300 kPa in the intact specimens, followed by a reduced ψ_{m} at p'_0 = 500 kPa. As the intact specimens had similar e_0, the compression responses are expected to roughly follow the same compression curve above the intrinsic compression line (Burland, 1990), assuming no transitional behavior for fine silty loess (Xu & Coop, 2017). This suggests that the effect of structure on flow instability is stress-dependent for a given e_0, and thus the flow instability of intact loess is state-dependent under the net effect of structure.

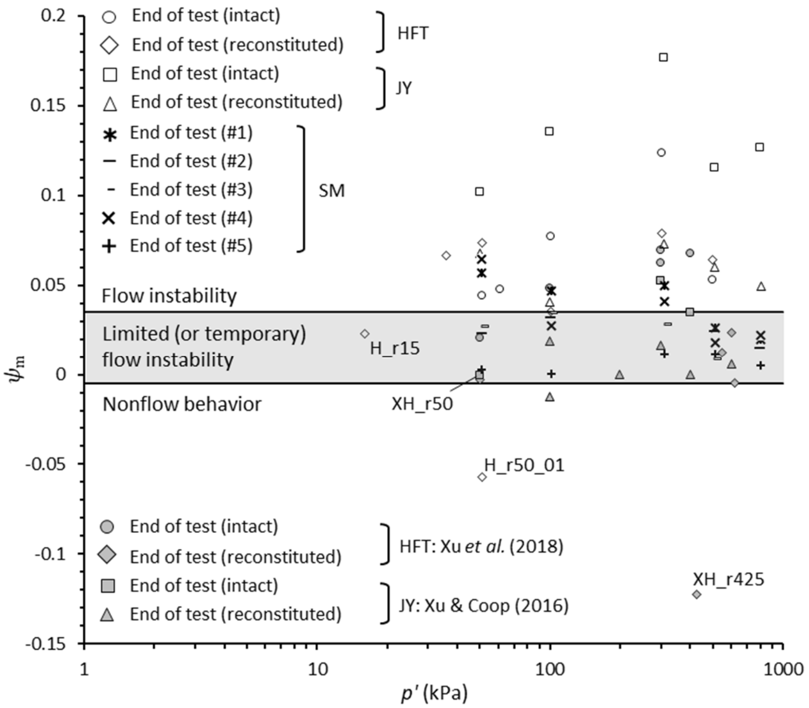

Figure 3.15 – The modified state parameter of this series of CIU tests. Additional dataset on JY and HFT loess are added for validation and better comparison.

The non-unique $\mathrm{IL_i}$ is the result of such an effect. For the reconstituted samples which were prepared with e_0 = 0.771-0.982, and potentially precluded from the effects of structure of an intact sample, the changing ψ_{m} clearly indicates the effect of e_0 on the flow behavior. CIU data on reconstituted HFT samples by Xu *et al.* (2018) also confirmed the changing ψ_{m} with different e_0 at similar stress levels. Similar state-dependent changes in

ψ_{m} is observed for the intact JY samples, which is confirmed by additional data reported by (Xu & Coop, 2016). By reducing the influence of structures while maintaining a similar e_0, an increasing FC of SM loess appears to increase flow liquefaction susceptibility; such a trend is demonstrated by the overall upward movements of the end-points in the $\psi_{\mathrm{m}}: p'$ plane. Bobei *et al.* (2009) originally defined the ranges of ψ_{m} to describe flow behavior of sand-fine mixtures; they are revised here in an attempt to characterize the undrained behavior for the Chinese loess as follows:

- Flow instability (flow behavior in Bobei *et al*. (2009)): $\psi_{\mathrm{m}} \geq 0.035$
- Limited or temporary flow instability: $-0.005 \leq \psi_{\mathrm{m}} < 0.035$
- Nonflow behavior: $\psi_{\mathrm{m}} < -0.005$

The subtle temporary flow instability in H_r15 from this study as well as the more intense temporary flow instability in XH_r550, XH_r600, and XH_i50 (Xu *et al.*, 2018) are captured by the proposed criteria incorporating the state of soil and the net effect of structure for HFT silty loess Following the same line of reasoning, the proposed criterion is capable of characterizing the undrained behaviors of JY and SM samples, and especially with the tendency of temporary flow instability observed in some SM specimens. The $q_{\mathrm{CS}}/q_{\max}$ ratio of the tests in the region of 'flow instability' can reflect the magnitude of ψ_{m}, and thereby the intensity of the flow instability.

3.6 Concluding Remarks

The critical states of intact and reconstituted loess can be either linear or non-linear, and flow behaviors appear to be state-dependent with non-unique instability lines. While a larger strain level is more desirable to further verify the locations of the CSLs, especially for the intact samples, the $\mathrm{CSL_i}$ would be closer to the $\mathrm{CSL_r}$ should the current strain level be sufficient to establish the critical state, which implies a more pronounced state-dependency of the Chinese loess.

The effect of structure of intact samples can either impede or facilitate the onset of flow instability depending on the state of the soil, whereas increasing fines content can largely increase the flow liquefaction susceptibility at the similar initial void ratio, as reflected in the changes in the modified state parameter.

The ψ_m serves as a good predictor of the flow behavior of silty loess, providing a sound basis to identify the susceptibility to flow instability with the proposed flow behavior criteria. Despite the intense flow instability, no flow liquefaction ($q \approx 0$ and $p' \approx 0$) was observed in silty loess, which may be attributed in part to the high fine content. Further, use of stress control as opposed to strain control could facilitate demonstration of flow liquefaction. More experimental data of high quality are required to further investigate the proposed flow behavior criteria and the possibility of flow liquefaction in silty loess.

The substantially reduced stresses and excess pore pressures indicate that a ‘flow-like’ movement of loess can be associated with flow instability, as rapid development of large strains is required for maintaining equilibrium when the shear strength required is greater than can be mobilized in the soil.

CHAPTER 4. DECEMENTATION AND MICROSTRUCTURE OF LOESS UNDER 1-D COMPRESSION

This chapter monitors the wetting-induced decementation process of intact Luochuan (LC) silty loess using elastic waves, with the objectives of analyzing the change of internal structure and small-strain stiffness due to decementation and fabric rearrangement.

4.1 Introduction

The small-strain stiffness reflects the contact-level deformation of granular materials. Stiffness is affected by soil structure in the range from very small to large strains (Burland, 1989). At very small strain (< 0.001%), shear modulus, G_0 is independent of shear strain; the stiffness decreases significantly after exceeding 1% of strain and continues to decrease as the soil approaches the failure state (Viggiani & Atkinson, 1995).

The small-strain stiffness of uncemented soils is controlled by the state of stress, whereas cementation can dramatically increase the stiffness by increasing contact area and bonding neighboring particles (Yun & Santamarina, 2005); observations are reported on coarse-grained (Clough *et al.*, 1981; Sharma & Fahey, 2004; Escribano & Nash, 2015) and fine-grained (Pennington *et al.*, 1997; Hird & Chan, 2008) materials. Cementation of sands governs G_0 at low stress level (i.e. cementation-controlled region) until a 'threshold' stress is reached (i.e. stress-controlled region) with the onset of structure degradation (Fernandez & Santamarina, 2001). Cementation of clays appears to be effective on G_0 only up to the isotropic or vertical yield stress (Jovičić *et al.*, 2006; Trhlíková *et al.*, 2012). Following the same line of reasoning, G_0 is affected by structural degradation due to decementation and fabric rearrangement. Decementation is reported to cause G_0 to decrease after yielding with an increasing mean effective stress (Cuccovillo & Coop, 1997). Yun & Santamarina (2005) reported a collapse-induced 'temporary' reduction in V_S of cemented sands before the stress is sufficiently large to increase the stiffness again.

The investigation of the time-dependent increases in the stiffness and strength of soils (Leonards & Altschaeffl, 1964; Mesri & Godlewski, 1977; Schmertmann, 1991) motivated the use of measurements with mechanical and electromagnetic waves to assess change in the structure of nature soils (Nakagawa *et al.*, 1995; Shibuya *et al.*, 1997) and cemented soils (Fam & Santamarina, 1996; Fernandez & Santamarina, 2001) under 1-D compression.

The collapse behavior and changes in microstructure of loess are discussed in Section 2.1.2. While some studies on loess attempted to address the effects of water content and pressure on small-strain stiffness (Song *et al.*, 2017), or the changes in structure during decementation (Rinaldi *et al.*, 2001; Rinaldi & Santamarina, 2008) in light of shear-wave velocity, most studies are equipped with limited means to monitor ongoing decementation in real-time. The current approach to interpret wetting-induced collapse still heavily image-based (Liu *et al.*, 2015; Li *et al.*, 2019; Wang *et al.*, 2019a; Wei *et al.*, 2019), even when incorporated with laboratory tests for large-strain behaviors (Wang *et al.*, 2019b; Yuan *et al.*, 2019). Such a lack of understanding on the decementation process limits the global observation on the collapse behavior of loess at micro-scale.

In this chapter, a series of compression tests are conducted on intact and reconstituted specimens of Luochuan (LC) silty loess under zero lateral strain loading conditions using instrumented oedometric cell with elastic wave sensors. The objectives are: 1) to assess the effects of wetting-induced and mechanical-induced decementation on small-strain stiffness of LC loess at low stress level, 2) to monitor the evolution of internal structure of LC loess during wetting, and 3) to explore the effects of structure and grading on the ‘transitional’ behavior of dry LC loess.

4.2 Materials and experimental method

The as-received samples of loess in this work are retrieved from the Luochuan (LC) loess-paleosol sequence in the layers of L1, L2, and L3 at the depths of 4 m, 10 m, and 19 m, respectively; the sampling work was conducted by the Northwest University in China. The Luochuan section is often regarded as the most complete and best studied loess section in China, with more than 30 loess-paleosol alternations providing a long record of climatic change for the last 2.5 Ma (Gallet *et al.*, 1996). The location of the study area is shown in Figure 2.1b. The index properties of the samples are listed in Table 5. The samples are above the A-line on the plasticity chart and classified as CL.

Table 5 – Index properties of the as-received LC silty loess samples.

Sample	G_s	e_0	ρ_d (kg/m^3)	w_P (%)	w_L (%)	PI (%)
L1	2.70	1.11-1.24	1.26	12.48	24.88	12.40
L2	2.71	0.92-1.16	1.38	13.56	26.67	13.11
L3	2.71	1.09-1.22	1.43	13.94	27.91	13.97

4.2.1 Instrumented oedometric cell

A low-stress and a high-stress oedometric cells are used in this work. The low-stress oedometric cell resembles the apparatus described in Fam & Santamarina (1997); it is modified to implement piezoelectric disk element (PDE) for compressional wave (p-wave) and bender elements (BE) for shear wave (s-wave), as shown in Figure 3.1a. Both sensors are made in-house so that the intrusion of the sensors is sufficiently small to ensure contact with the test specimen, while not causing significant stress concentration during loading. The intrusions are 1.80 mm and 4.02 mm for p- and s-wave sensors (both transmitters and receivers), respectively. The high-stress oedometric cell is a fixed-ring setup that was originally designed to explore the effects of microbial activity on soil behaviors under high stress (Rebata-Landa, 2007), as shown in Figure 3.1b. The low-stress cell is used to access the internal structure changes of loess at dry to unsaturated state, whereas the high-stress cell is used to evaluate the 'transitional' behavior of silty loess at dry state.

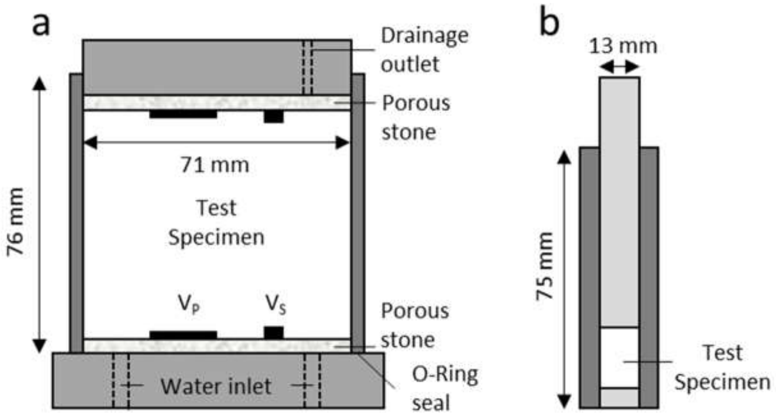

Figure 4.1 – A schematic illustration of the experimental setup for the low- and high-stress compression cell. (a) low-stress cell permits inflow and drainage of water; (b) high-stress cell is used only in dry state. The height change during loading/unloading is monitored by a Linear Variable Displacement Transformer (LVDT).

4.2.2 *Sample preparation*

The as-received intact samples are in cylindrical shape and air-dried ($w < 2\%$), with average diameters of 100 mm and heights of 110 mm. Natural water contents are 14.33% and 14.21 % for L1 and L2 LC loess, respectively, as reported by Song *et al*. (2017). No evidence of prior invasion of groundwater was found. Visible voids and macro-scale pores, probably of biogenic origin, can be seen for the samples and appear to be more pronounced for L1 samples. The intact test specimens are trimmed by using sandpaper with extreme care. Typical intact specimens are shown in Figure 4.2; diameters and heights of intact specimens for low-stress tests of 71 mm and 50 mm, respectively, and the corresponding values for high-stress tests are 12.5 mm and 10 mm, respectively. The clearance between the inner diameter of the loading cell and intact specimen is of significant importance to ensure the test reflects the 1-D loading condition; any trimmed sample with clearance greater than 0.8 mm is discarded to ensure a radial strain less than 0.01.

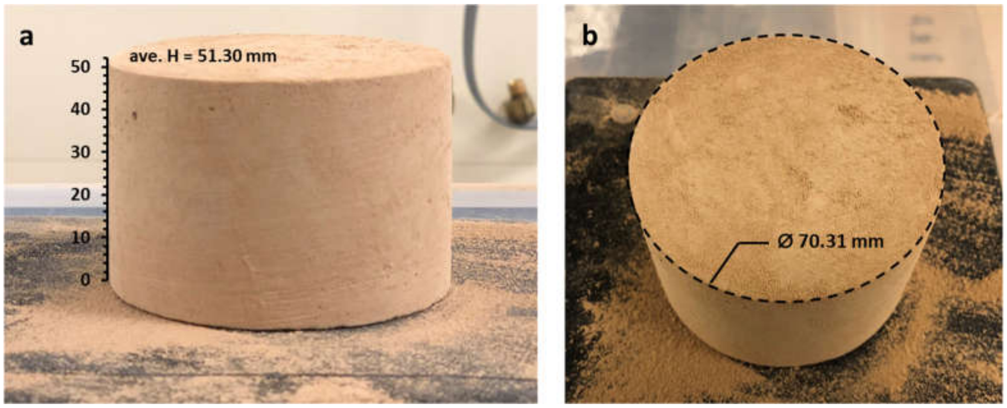

Figure 4.2 – Intact specimen (for test L1i_w) trimmed for low-stress 1-D compression test.

As discussed in Section 2.1.4, Burland (1990) provided a practical guide on how to create a ‘destructed’ state of a sedimentary clay, from which the parameters determined reflect the ‘intrinsic’ state of the soil, and thus can be used as the reference material for that type of soil. Many ambiguities and discussions have been circulating since the concept of ‘intrinsic’ property were originally suggested, as such a state appears to be highly dependent on the preparation method (Fearon & Coop, 2000). Notwithstanding the complex cross-scale influence of structure on soil behaviors, the immediate challenge in producing a reconstituted loess specimen is that the process, according to Burland (1990), cannot be executed in a dry state. With a high susceptibility to wetting-induced collapse of intact loess, introducing water and consolidation may simply produce a 'sedimentation' structure that is different from that of the natural loess, rather than the 'unstructured' loess specimen; a similar finding is reported by Cotecchia & Chandler (1997) for a Pleistocene stiff clay.

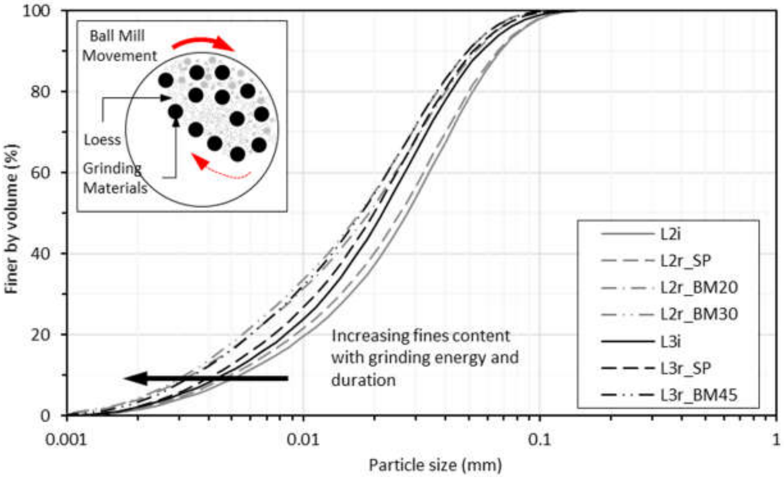

Figure 4.3 – Particle size distribution of intact and reconstituted LC specimens measured by laser diffraction analyzer (see also Section 3.2.2). The terms 'i' and 'r' represent 'intact' and 'reconstituted' samples, respectively; 'SP' and 'BM' denote to 'sandpaper' and 'ball mill' methods, respectively. The number following 'BM' represent the grinding duration. The concept of ball mill method is illustrated.

To circumvent the predicament of applying Burland's method on loess, reconstituted specimens are derived from abrading the intact samples by sandpaper and followed by mechanical grinding in a Retsch© Planetary Ball Mill (PM 100CM) for varying durations for further particle size reduction. The sample that is prepared in such a manner preserves the chemical characteristics of the intact form; yet still remolded by breaking down particle associations and producing a more homogeneous fabric at the macro-scale. The particle size distribution of pre-test specimens is shown in Figure 4.3. The ‘reconstituted’ samples created in such a fashion are mechanically decemented (termed ‘mechanical-decemented’ in this work). The mechanical-decemented samples are prepared in the oedometric cell by funneling and tamping methods to attain certain loose or dense states.

4.2.3 Test procedures

The as-received specimens are air-dried before the test. A summary of 1-D compression tests is presented in Table 6. The compression behavior is discussed in Section 4.3, whereas Section 4.4 and 4.5 focuses on characterizing structure changes using wave data. The initial void ratio of both tests are calculated using two methods given in Equation (4) and Equation (5), as suggested by Li & Coop (2018) to ensure accuracy:

$$e_0 = \frac{G_S \gamma_w}{\gamma_{di}} - 1 \tag{4}$$

$$e_0 = \frac{G_S \gamma_w (1 + w_i)}{\gamma_{bi}} - 1 \tag{5}$$

where G_S is the specific gravity, w_i is the initial water content, γ_w is the unit weight of water, γ_{di} is the initial dry unit weight, and γ_{bi} is the initial bulk unit weight.

In low-stress tests (apparatus in Figure 4.1a), p- and s-wave velocities are measured at each loading step up to $\sigma'_v \approx 2$ MPa; each loading sequence is conducted at the intervals of 6 hrs and 24 hours for dry and wet specimens, respectively. Wetting is only conducted on intact specimens and starts at $\sigma'_v \approx 1$ MPa. De-ionized water is introduced into the system by gravitational flow with a falling-head setup at an initial head, h_0 = 0.2 m. After the wetting process is completed, the test specimen is subsequently loaded to $\sigma'_v \approx 2$ MPa. The evolution of vertical strain and wave velocities are monitored throughout the test.

Wave velocities are measured at the end of the loading period before changing the load. The first arrival time, $t_{1\mathrm{st}}$ of the wave is chosen from the stored time series, the travel distance, L_{t} (tip-to-tip length between sensors) is measured by an LVDT, and thus velocity can be computed as $V_{\mathrm{wave}} = L_{\mathrm{t}}/t_{1\mathrm{st}}$. In high-stress tests (apparatus in Figure 4.1b), dry specimens are loaded up to $\sigma_{\mathrm{v}}' \approx 60$ MPa at an interval of 30-60 min at each loading sequence. No wave data is collected for high-stress tests.

Table 6 – Summary of 1-D compression tests on LC loess samples.

Sample	Test	Preparation method	e_0	$e_{\min}$	Maximum σ_{v}'
L1	L1i_w	-	1.105	0.317	2027.46
	L1i_1	-	1.241	0.234	58306.82
	L1i_2	-	1.158	0.266	59613.74
	L1r_1	SP	1.130	0.245	58306.82
	L1r_2	BM (5 min)	1.367	0.258	56175.78
	L1r_3	BM (5 min)	1.357	0.679	2131.62
L2	L2i_w	-	0.925	0.359	2022.66
	L2i_1	-	1.161	0.186	58136.45
	L2i_2	-	1.115	0.229	58136.45
	L2r_1	SP	1.069	0.196	58136.45
	L2r_2	BM (20 min)	0.859	0.236	58306.82
	L2r_3	BM (20 min)	1.052	0.183	58306.82
	L2r_4	BM (10 min)	0.831	0.223	58306.82
	L2r_5	BM (8 min)	1.461	0.645	2131.62
L3	L3i_w	-	0.793	0.358	2062.55
	L3i_2	-	0.947	0.303	58318.18
	L3i_3	-	1.024	0.311	58490.87
	L3i_4	-	0.929	0.325	58306.82
	L3r_1	SP	1.146	0.814	1393.80
	L3r_2	SP	1.277	0.763	2004.93
	L3r_3	BM (45 min)	1.060	0.604	2053.66
	L3r_4	BM (60 min)	1.155	0.724	1129.70
	L3r_5	BM (95 min)	1.334	0.642	2053.66
	L3r_7	BM (45 min)	0.806	0.187	58136.45
	L3r_8	BM (45 min)	1.070	0.239	58306.82
	L3r_9	BM (45 min)	1.307	0.289	58306.82

4.3 Compressibility and collapse

4.3.1 Vertical strain

The stress-volume responses reflect the evolution of decementation and collapse. The vertical strain responses of the L1, L2, and L3 intact specimens are similar before wetting, with smaller vertical strain increments than the mechanical-decemented specimens (Figure 4.4). The wetting-induced vertical strain decreases with sampling depth, of which L1 specimen exhibits the highest vertical strain. The collapse potential is defined as the changes in vertical strain and is expressed as:

$$\mathrm{P_C} = \frac{\Delta \mathrm{H}}{\mathrm{H_0}} = \frac{\Delta e}{1 + e_0} \times 100 \tag{6}$$

where ΔH and Δe represent the changes in height and in void ratio, respectively. $\mathrm{H_0}$ and e_0 are the initial height at the inundation stress, respectively.

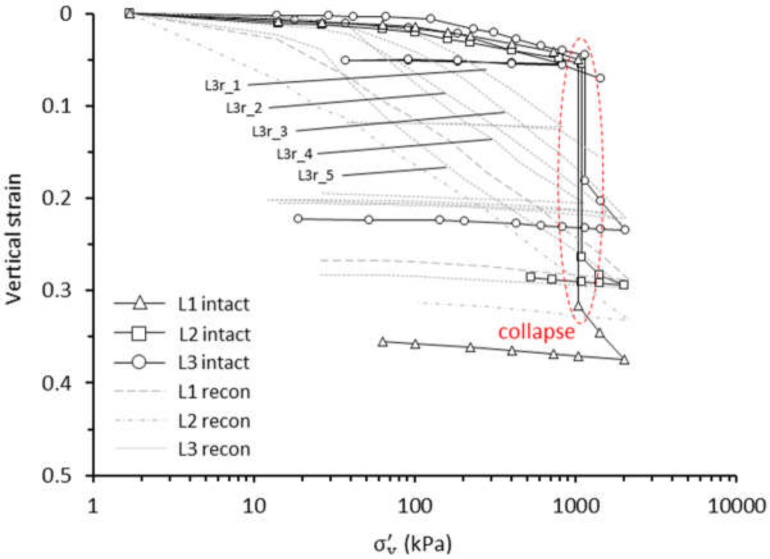

Figure 4.4 – Changes in vertical strain with effective stress of intact and mechanical-decemented LC loess in low-stress 1-D compression test.

The collapse potentials for L1, L2, and L3 specimens are 26.7%, 20.9%, and 14.2%, respectively. The increment of vertical strain for the wetting-decemented specimens is similar to mechanical-decemented specimens, indicating a compromised structure. It also appears that mechanical-decemented specimens with lower FC are accompanied by more robust vertical strain responses.

4.3.2 Void ratio

The compression curves of intact LC loess and wetting-/mechanical-decemented LC loess are compared in the $e\colon \log\sigma'_{\mathrm{v}}$ plane (Figure 4.5). The compression curves of intact specimens are above the reconstituted (i.e. mechanical-decemented) ones and outside their post-yield compression curves; such a response is typical for natural structured soils and can be ascribed to the effects of structure (Feda *et al.*, 1993; Burland *et al.*, 1996). The inter-particle cementation of intact specimens contributes to the load bearing at the early stage. The yield vertical stress σ'_{y} is not reached for intact specimens in low-stress tests.

Wetting is conducted for intact specimen at $\sigma'_{\mathrm{v}} \approx 1$ MPa (Figure 4.5); an intact L3 specimen without wetting is shown for comparison. The wetting-decementation results in the void ratio to reduce by 0.562, 0.403, and 0.253 for L1, L2, and L3, respectively. The post-wetting void ratios for intact specimens appear to be similar; but they are clearly lower than that of the reconstituted specimens at the same stress. While no converging tend can be found for pre-wetting intact specimens, the post-wetting compression curves clearly exhibit a higher degree of convergence, indicating that wetting-decementation significantly reduces the effects of structure in LC loess.

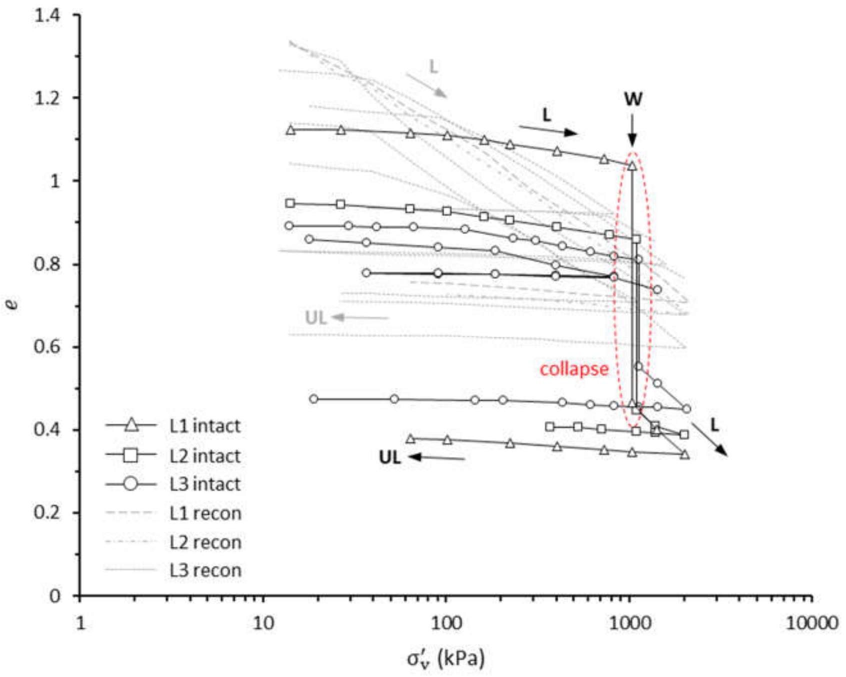

Figure 4.5 – Changes in void ratio with vertical effective stress of intact and mechanical-decemented LC loess in low-stress 1-D compression test.

The void ratio responses of LC loess differ from the responses of soils mixed with dissolvable particles, in which an increasing void ratio can be observed after dissolution due to the overwhelming effects of reduction in the volume of solids (Truong *et al.*, 2010). Such different responses highlight the unique characteristics that pertain to the open structure formed by the constituent particles of loess that is supported by the dissolvable cementation agents, which subsequently permits the sudden reduction in void ratio during wetting (or dissolution). Such an observation supports the conclusion in Assallay *et al.* (1997) that is discussed more in detail in Section 2.1.2.

4.3.3 Compressibility index

The changes in the compressibility of an intact specimen can be reflected by the changes of the compression index C_c that is expressed as:

$$C_c = \frac{\Delta e}{\Delta \log \sigma'_v} \tag{7}$$

where Δe represents the void ratio change and $\Delta \log \sigma'_v$ is the logarithmic stress change. The C_c measured under zero lateral strain is primarily the result of interparticle relative displacement and fabric change. The C_c of reconstituted specimens increase with effective vertical stress, showing a clear converging trend at higher stresses (Figure 4.6). The C_c of intact specimens are similar for all three layers before wetting; but lower than that of reconstituted specimens, implying robust responses of LC loess due to its intact structure.

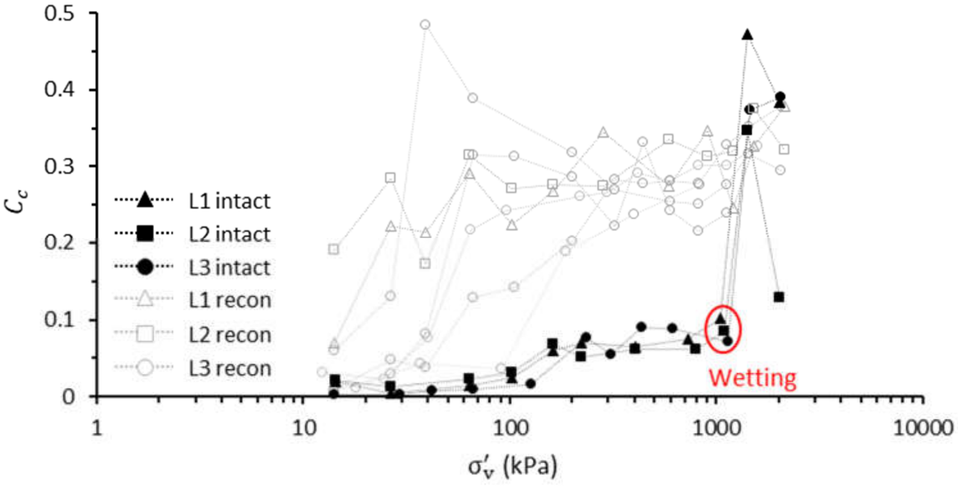

Figure 4.6 – Changes in compression index with vertical effective stress of intact and mechanical-decemented LC loess in a low-stress 1-D compression test.

The C_c of intact specimens are increased significantly after wetting and remained similar to the magnitude of the reconstituted C_c in the subsequent loading steps. The lower post-wetting C_c of L2 sample at $\sigma'_v \approx 2$ MPa may be related to the 'knee' point in the compression curve after $\sigma'_v \approx 1$ MPa (Figure 4.5); such a response may be caused by strain localization during wetting and the subsequent collapse.

4.3.4 *Transitional behavior*

Non-converging trend in compression curves is found for mechanical-decemented specimens (Figure 4.5), implying the possibility of non-unique NCL. A non-unique NCL is not consistent with the CSSM framework, in which a unique NCL may be reached for a soil with different initial density in $e: \log\sigma'_v$ or $v: \ln p'$ space (v: specific volume). Some silty or graded soils are reported to be characterized by non-unique NCLs and CSLs (e.g. Nocilla *et al.*, 2006; Altuhafi *et al.*, 2010; Shipton & Coop, 2012; Xu & Coop, 2017), and were termed as 'transitional' behavior in Martins *et al.* (2001).

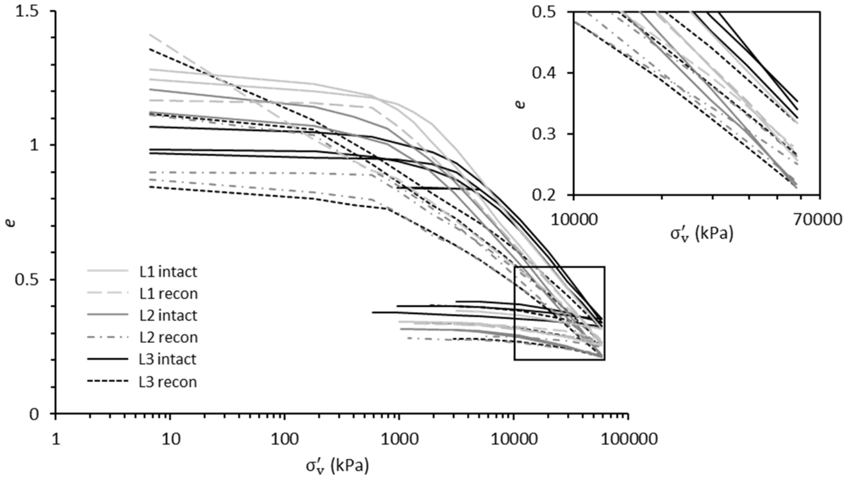

Figure 4.7 – Changes in void ratio with vertical effective stress of intact and mechanical-decemented LC loess in the high-stress test. Enlargement on the final void ratio is presented, with unloading curves omitted for clarity.

Transitional behavior was observed for silty loess samples retrieved at depths of 5 m and 10 m (Xu & Coop, 2017), as non-unique ICLs were observed for samples with different initial void ratio. To further investigate the transitional behavior in silty loess, the intact and mechanical-decemented silty LC loess are compressed to $\sigma'_v \approx 60$ MPa in a fixed ring oedometric setup. Figure 4.7 compares the compression curves of high-stress tests, in which the results demonstrate the lack of convergence for intact as well as mechanical-decemented LC loess. The initial void ratio for intact specimens for high-stress tests are comparatively higher than low-stress tests, which may be ascribed to the magnified effects of localized pores and the less accurate measurements of a smaller intact test specimen for the high-stress tests. However, the sample preparation and measurements for high-stresses test specimens are carried out in the same manner.

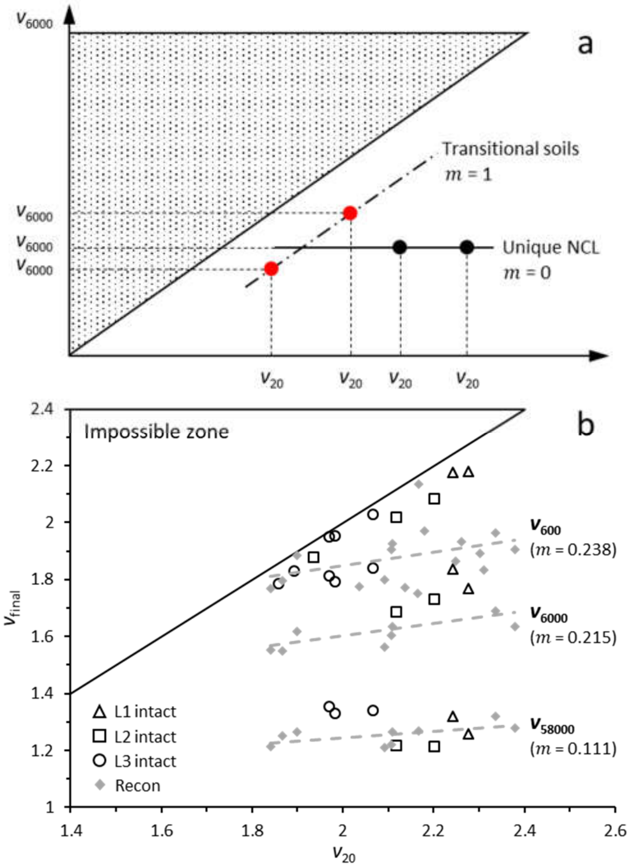

Figure 4.8 – Evolution of m of intact and mechanical-decemented LC loess with increasing v_{final}: (a) definition of m (after Ponzoni *et al.*, 2014); (b) v_{final} at effective vertical stresses of 600 kPa, 6000 kPa, and 58000 kPa (max σ'_v = 56175.78 kPa is used for test L1r_2).

Ponzoni *et al*. (2014) proposed a method to quantify the convergence of compression curves using an m value. As shown in Figure 4.8a, the m value is defined as the gradient in the v_{20}: v_{6000} graph (v_{20}: specific volume at $\sigma_v' = 20$ kPa). The evolution of m is shown in Figure 4.8b, in which m reduces with increasing v_{final} due to the gradual erase of the initial structure. The m of the mechanical-decemented specimens show a continuing decrease with increasing stress, whereas a more drastic changes can be seen from v_{600} to v_{6000} for intact specimens within each layer.

The m of intact specimen is higher than the mechanical-decemented specimen before it approaches 0 and parallel at v_{58000}, suggesting a convergent trend between intact and mechanical-decemented samples at $\sigma_v' \approx 60$ MPa. While m of intact specimens converges for specimens from an individual layer, there is still lack of convergence in intact specimens from different layers, indicating significant effects of the inherent structure of LC loess related to the depositional event and period.

4.4 Small-strain behaviors and decementation

4.4.1 Wave velocity

The p- and s-wave time series evolution of the intact L3 specimen and one of the reconstituted L3 specimens are shown in Figure 4.9. The evolution of wave velocities during wetting is discussed in Section 4.4.3. Slight decrease in $t_{1\text{st}}$ of wave time series are seen for intact specimens before wetting as vertical stress increases, whereas $t_{1\text{st}}$ of mechanical-decemented specimens reduces substantially with an increasing vertical stress. The relative increase in $t_{1\text{st}}$ appears to be similar for wetting- and mechanical-decemented specimens. The initial decrease in $t_{1\text{st}}$ at the onset of wetting (Figure 4.9a) is caused by the rapid decrease in travel distance due to collapse; the velocity is decreased by wetting.

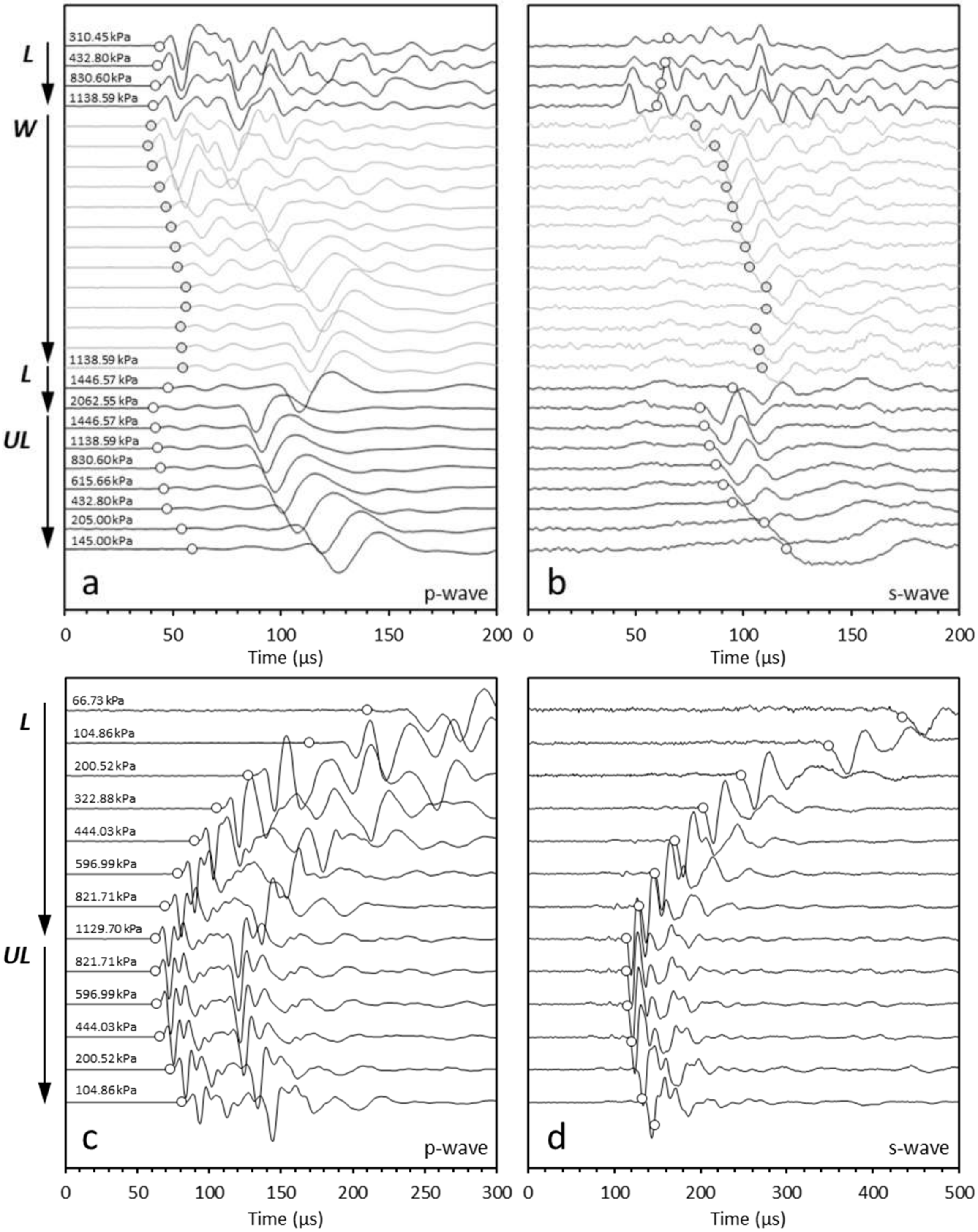

Figure 4.9 – Evolution of wave time series during 1-D compression test. (a) p-wave and (b) s-wave for intact L3 specimen (test L3i_w: e_0 = 0.775); (c) p-wave and (d) s-wave for mechanical-decemented L3 specimen (test L3r_4: e_0 = 1.103). The applied vertical stress is listed for each wave path (*L*: loading; *W*: wetting; *UL*: unloading).

The p-wave velocity measures the bulk stiffness of the soil matrix, and it is primarily controlled by the bulk modulus of the fluid in a saturated soil, and can be expressed as:

$$V_{\mathrm{P}} = \sqrt{\frac{M}{\rho}} = \sqrt{(B + \frac{4}{3}G)/\rho} \tag{8}$$

where M is the constraint modulus, B is the bulk modulus, G is the shear modulus, and ρ is the mass density. The p-wave velocities of intact and mechanical-decemented LC loess are shown in Figure 4.10a. The velocities of intact specimens are significantly higher than that of mechanical-decemented specimens, indicating a governing role of the cementation on V_{P} at the early stage. Small increment in V_{P} is observed as σ'_{v} increases prior to wetting, showing little effects of stress on structure. A distinct reduction in V_{P} can be seen after wetting, and the post-wetting V_{P} of intact specimens are comparable for all three samples, and similar to the mechanical-decemented specimens at the same stress level. Since the specimen is not fully saturated during wetting, the V_{P} of the specimen remains lower than that of water ($V_{\mathrm{P}} \approx 1480$ m/s). The V_{P} during unloading appears to be dependent on the maximum σ'_{v} experienced by the specimen.

The s-wave velocity is determined by the stiffness of the granular skeleton, and thus affected by the state of the effective stress. By assuming an isotropic continuum, the s-wave velocity can be expressed as:

$$V_{\mathrm{S}} = \sqrt{\frac{G}{\rho}} = \alpha\left(\frac{\sigma'_{\mathrm{m}}}{1\ \mathrm{kPa}}\right)^{\beta} \tag{9}$$

where σ'_{m} is the mean effective stress on the shear plane that is computed by $\sigma'_{\mathrm{v}}(1 + k_0)/2$, α factor is the s-wave velocity at $\sigma'_{\mathrm{m}} = 1$ kPa, β exponent reflects the sensitivity of stiffness to the stress (Cha *et al.*, 2014), and ρ is the mass density. Both α factor and β exponent are determined experimentally. The s-wave velocities of intact and reconstituted LC loess are shown in Figure 4.10b. The measurement of s-wave propagation is affected by the contact and coupling of the BE; poor BE-specimen contact at the lower stress level prevents a clear identification of t_{1st}.

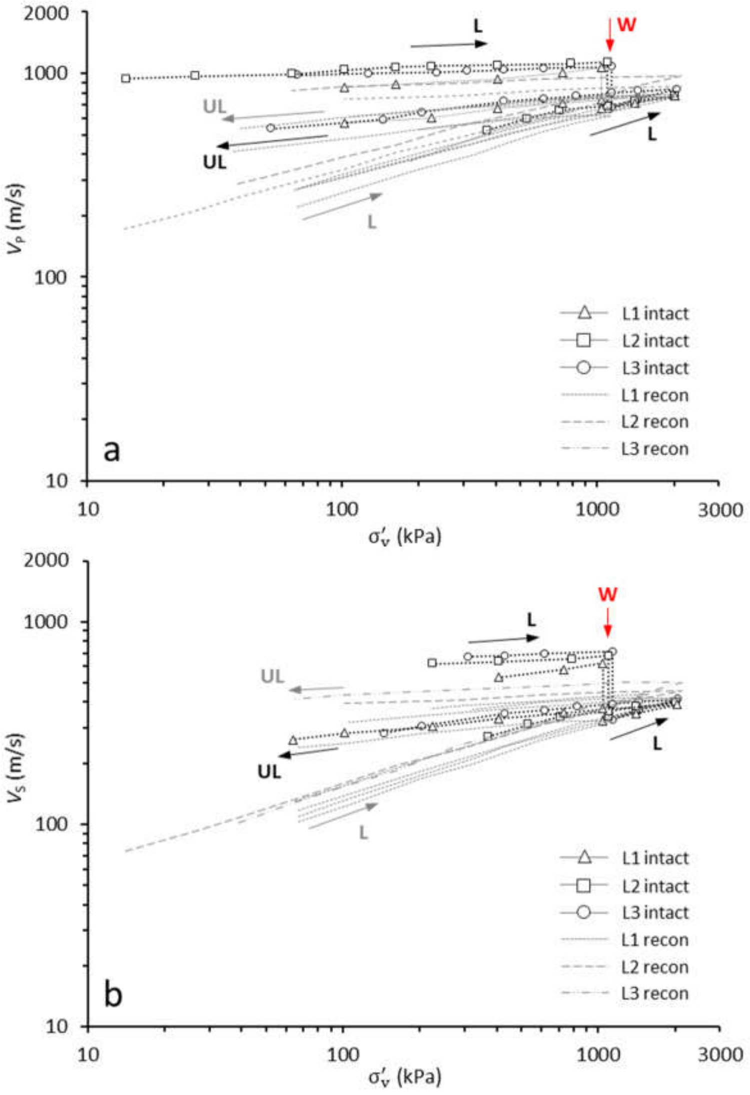

Figure 4.10 – Evolution of velocity-stress relation during 1-D compression test. (a) p-wave and (b) s-wave of intact and mechanical-decemented LC loess (*L*: loading; *W*: wetting; *UL*: unloading).

The initial V_S of intact specimens are higher than the mechanical-decemented ones, indicating a strong effect of cementation on stiffness. With an increasing effective vertical stress, the pre-wetting V_S of the intact L2 and L3 specimens remain fairly constant, with a minor increase is observed for L1 specimen, which may suggest a reduced effect of structure with depth due to the extent of cementation on the small-strain stiffness of LC loess. The V_S of the mechanical-decemented specimens increase with effective vertical stress, showing a converging trend at the higher stress level. A significant decrease in the V_S is found after wetting-decementation, and it increases upon further loading. The post-wetting V_S of intact specimens are marginally lower than the mechanical-decemented ones despite of the higher initial V_S, indicating wetting causes a lower contact-level stiffness.

4.4.2 Small-strain stiffness

The pore compressibility, m_v is defined as the ratio of volumetric strain change to the stress change, which is the inverse of the constrained modulus, M (defined as the ratio of $\Delta\sigma_0/\Delta\varepsilon_\mathrm{v}$ under zero lateral strain conditions) and it is expressed as:

$$m_\mathrm{v} = \frac{1}{M} = \frac{1}{\rho V_\mathrm{P}^2} \tag{10}$$

where ρ is the mass density. As shown in Figure 4.11, the initial m_v of intact specimens is substantially lower than of the mechanical-decemented specimens. Wetting-decementation increases the pore compressibility, suggesting a transition in the system from compressing particle bonds to compressing water- and air-filled voids. No clear pattern emerged from m_v changes of the mechanical-decemented specimens in term of e_0 and grading.

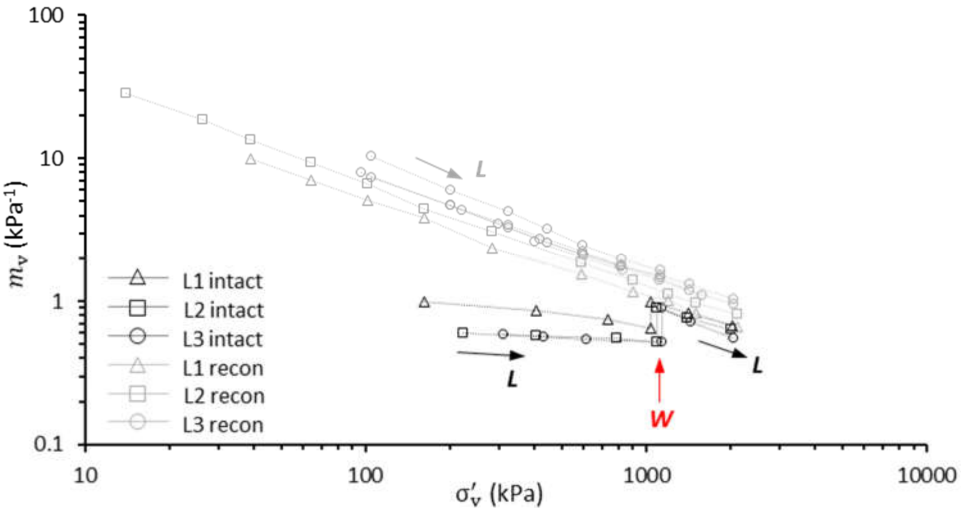

Figure 4.11 – Changes in the pore compressibility with increasing effective vertical stress.

With the measurements of p- and s-wave velocities, the Poisson's ratio, υ_m of the LC loess samples can be computed as:

$$\upsilon_\mathrm{m} = \frac{(V_\mathrm{P}/V_\mathrm{S})^2 - 2}{2(V_\mathrm{P}/V_\mathrm{S})^2 - 2} \tag{11}$$

The changes in υ_m with increasing σ'_v is shown in Figure 4.12. The initial υ_m of intact specimens are lower as compared to the mechanical-decemented specimens, indicating the initial υ_m is controlled by cementation with insignificant responses to vertical stresses. High initial υ_m values are observed for mechanical-decemented specimens with gradual decrease with an increasing σ'_v. Wetting results in a substantial increase in υ_m that surpasses response of the mechanical-decemented specimens, indicating an overwhelming effect of wetting-decementation, as observed from the test results discussed in the previous sections. The unloading stage causes minimum changes for the decemented specimens, suggesting that high stress can result in stress locking within the specimen, and the elastic properties are affected by stress history.

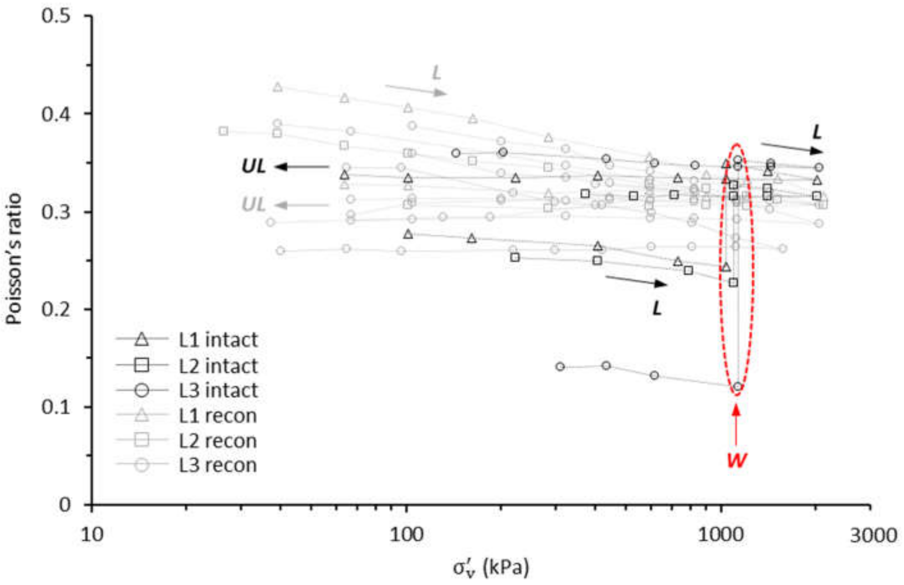

Figure 4.12 – Changes in the Poisson's ratio, v_m with increasing effective vertical stress.

The low initial v_m of the intact LC loess, such as the L3 sample (sampling depth ~ 19 m), may suggest the possibility of a Poisson's ratio approaching 0 or even negative value in the deeper LC layer with a higher extent of diagenetic cementation. A material with negative Poisson' ratio is referred to as auxetic material; for example, a solid with $v_\mathrm{m} \rightarrow -1$ would be highly resistant to shear deformation but easy to deform volumetrically (Ji *et al.*, 2018). Auxetic properties can be found in honeycomb, polymeric foams, or some natural rocks (Lakes, 1987; Evans *et al.*, 1991; Greaves *et al.*, 2011). Man-made auxetic materials are commonly not strong enough due to the honeycomb structure with high anisotropy in mechanical properties. Pasternak & Dyskin (2008, 2009) have shown that a negative v_m can be achieved in an assembly of particles elastically bonded to each other, and thereby further investigations on the deeper LC layer, such as L15 (more than 80 m deep in the LC loess-paleosol sequence), is recommended as it aids in understanding the fundamental principles in condensed matter physics as well as geoscience.

As indicated in Equation (8) and (9), the wave velocities can provide direct insights on the stiffness of a soil. The relative variation in bulk and shear stiffness before and after wetting is reflected by the changes in the ratio of the wave velocities and expressed as:

$$\left(\frac{V_\mathrm{P}}{V_\mathrm{S}}\right)^2 = \frac{B}{G} + \frac{4}{3} \tag{12}$$

where B and G are the small-strain bulk and shear modulus, respectively. As presented in Figure 4.13, $(V_\mathrm{P}/V_\mathrm{S})^2$ implies that wetting-decementation can cause sufficient reduction in the skeletal shear stiffness to produce a global increase in $(V_\mathrm{P}/V_\mathrm{S})^2$, which further confirms the effects of the inherent particle-level cementation of the intact LC loess. The post-wetting $(V_\mathrm{P}/V_\mathrm{S})^2$ is slightly higher than the mechanical-decemented specimens, indicating a more pronounced decemented assemblage in terms of contact-level deformation, as the results of wetting-decementation.

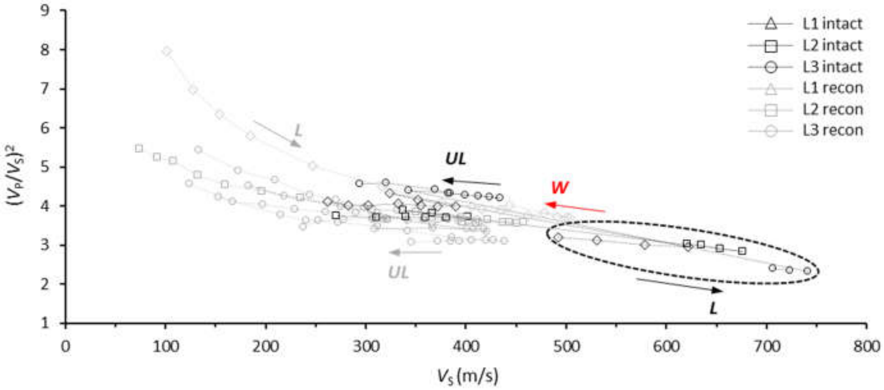

Figure 4.13 – $(V_\mathrm{P}/V_\mathrm{S})^2$ as a function of V_S for intact and decemented specimens.

4.4.3 *Wetting process*

The wetting process is monitored by measuring the evolution of wave velocities as well as vertical displacement with an increasing time interval. The entire wetting process lasted about 90 hrs, 120 hrs, and 24 hrs for L1, L2, and L3 specimens, respectively. The first inflow is permitted with 30 ml of de-ionized water by opening the valve connecting the falling-head setup and the base of the low-stress oedometric cell. The subsequent inflow is permitted with 20 ml of de-ionized water after 48 hrs, 48 hrs, and 4.8 hrs for L1, L2, and L3 samples, respectively. One additional inflow was introduced for L2 and L3 specimens; however less than 1 ml of inflow was found for both cases, which is related to the lack of pressure to overcome the changing air-entry value of the specimen. The vertical strain stays virtually constant with slight changes in the wave velocities. The degree of saturation of the specimen is not measured during the test. The evolution of vertical strain and p- and s-wave velocity during wetting is shown in Figure 4.14.

Each inflow sequence produces large deformation in test specimens (Figure 4.14a). The drop in vertical strain reflects the collapse potential of each test specimen, as discussed in Section 4.3.1. The end-of-wetting void ratios (Figure 4.14b) of L1 and L2 test specimens are similar; however they differed in the subsequent loading which is possibly the result of strain localization (see Section 4.4.3) of L2 specimen or residual cementation.

Immediate reductions are observed for V_P and V_S after wetting (Figure 4.14c), which is related to the combining effects of decementation (contact-level) and shortening of the specimen height (macro-level). A sharp increase is found in $(V_\mathrm{P}/V_\mathrm{S})^2$ after wetting as the results of an overwhelming effect due to the reduction of V_S (and shear stiffness) that is related to decementation (Figure 4.14d). The subsequent drop in $(V_\mathrm{P}/V_\mathrm{S})^2$ may be ascribed to the re-establishment of particle contact due to collapse as void ratio continues to decrease and as the specimen approaching a more equilibrium state; however such an abrupt drop is not observed after in the subsequent wetting events.

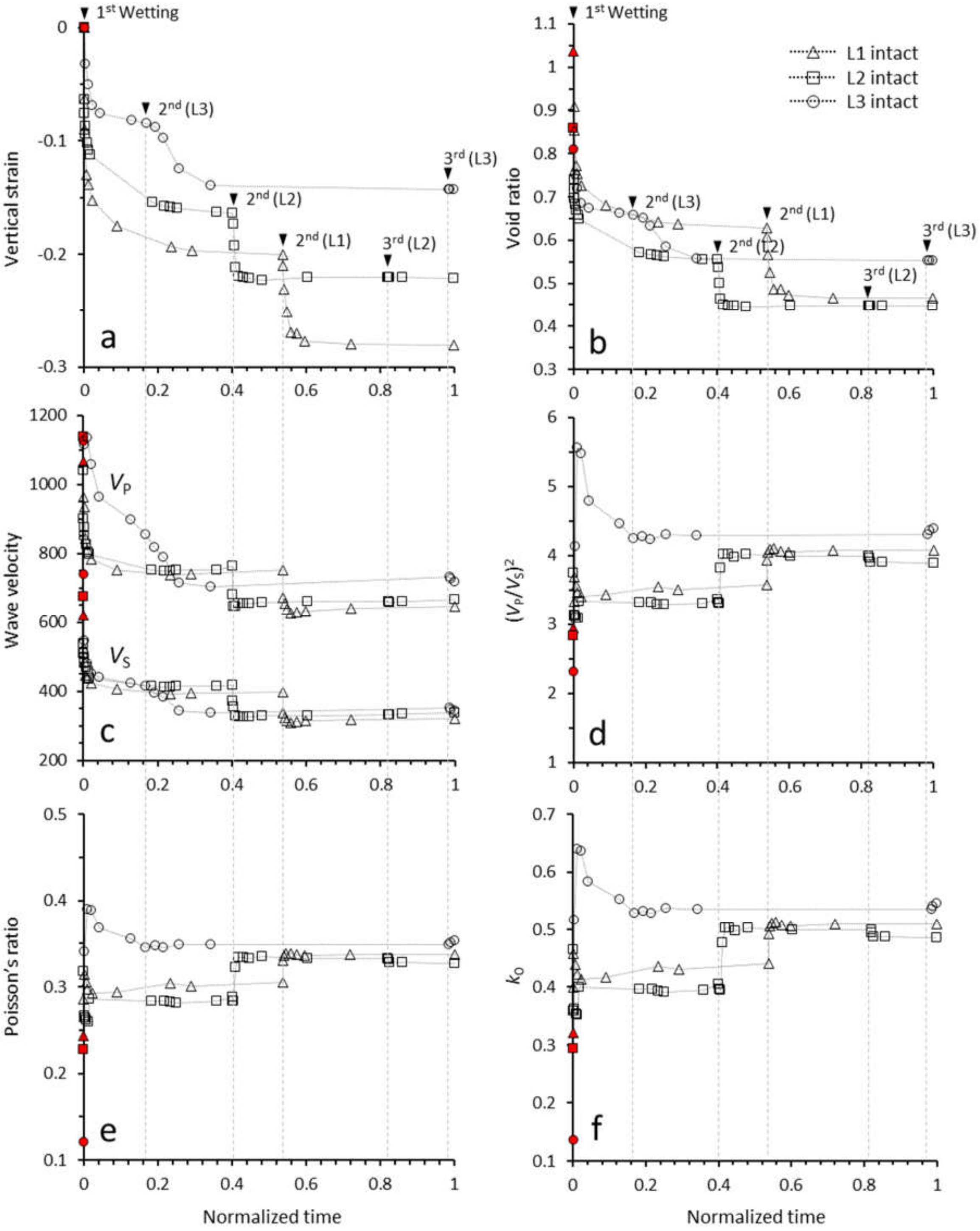

Figure 4.14 – Evolution of collapse and wave velocities of LC loess during the wetting process (constant applied vertical stress) over normalized time: (a) vertical strain; (b) void ratio; (c) V_P and V_S; (d) $(V_\mathrm{P}/V_\mathrm{S})^2$; (e) Poisson's ratio; (f) k_0. Readings at the onset of wetting is highlighted.

Affected by the changes in $(V_\mathrm{P}/V_\mathrm{S})^2$, the evolution of the Poisson's ratio in Figure 4.14e exhibits similar characteristics; however the apparent converging trend of the post-wetting Poisson's ratio requires further investigation. The stress ratio, k_0 characterizes the frictional resistance of the soil (Michalowski, 2005). The evolution of k_0 is presented in Figure 4.14f; it is estimated by using $k_0 = v/(1-v)$ which is derived by Tschebotarioff (1973) based on the elasticity theory. Hence, caution must be exercised in interpreting the results, as the elasticity theory is arguably not applicable in the decementation process.

Notwithstanding the accuracy of estimating k_0 using wave velocities, the immediate increase of k_0 at the beginning of wetting may be attributed to a temporary development of excess pore-water pressure, and hence a momentary drop of σ'_v rather than the increase of σ'_h. The nearly constant k_0 between wetting events suggests that a more permeant increase of σ'_h, which is related to the rearrangement of the granular structure. Such an observation agrees with the general observations on normally-consolidated fine-grained materials, for which k_0 increases with increasing plasticity (Brooker & Ireland, 1965). A higher terminal k_0 is not consistent with the finding on k_0 response to mineral dissolution conducted by Shin & Santamarina (2009); but cementation was not considered in their study.

4.5 Quantification of structure degradation

4.5.1 Wave-stress relation

The observed trend of s-wave velocity and effective vertical stress is summarized in Figure 4.15. As indicated by the changes of V_S presented in Figure 4.10b (Section 4.4.1), wetting triggers a substantial decrease in V_S and results in an end-of-wetting V_S similar to the corresponding mechanical-decemented specimen. The low-stress test cannot assess the changes in V_S beyond the ‘cementation-controlled’ region; but it is postulated that the V_S of the intact specimen can asymptotically approach the decemented specimen under very high stress (Yun & Santamarina, 2005). The transition zone from ‘cementation-controlled’ t0 ‘stress-controlled’ may be subject to the competing effects of cementation and stress as the soil undergoes partial decementation. Additional investigations are needed to better understand such a competing effect on the stiffness.

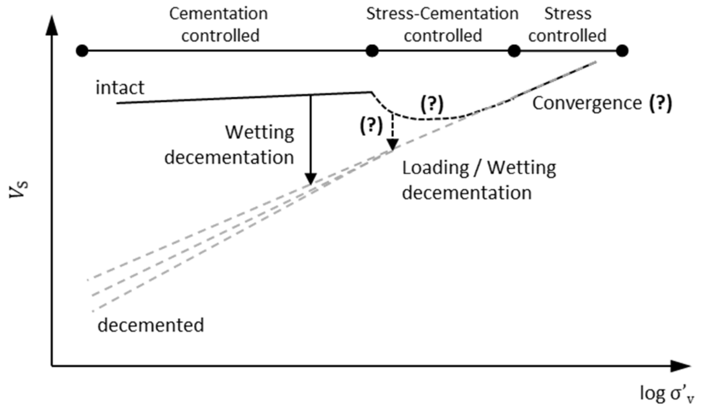

Figure 4.15 – Schematic illustration on the postulated V_S-σ'_v relation for loess.

4.5.2 *α-β relation*

Decementation-induced structure degradation can be reflected by the changes of the α-β relation in Equation (9) can be estimated by assuming k_0 = 0.5 (Figure 4.16). The α factor reflects the grain packing and fabric, and the β exponent reflects both the nature of interparticle contacts and fabric change during loading (Cha *et al.*, 2014). For example, low α and high β imply clay with high plasticity, and β ≈ 0 indicates cemented media. The α-β relation of the intact LC loess behaviors is similar to that of cemented media. The intact

L1 specimen shows a lower degree of diagenetic cementation, as α increases with the extent of cementation. The cluster of the decemented specimens is located in the clay region; the inherent heterogeneity related to the depositional event and depth appear to be removed by decementation. The shift between intact and decemented specimens in the α-β graph again highlights the significant effects of structure; but the empirical relation, as listed in Figure 4.16, is maintained as the soil structure underwent such drastic change.

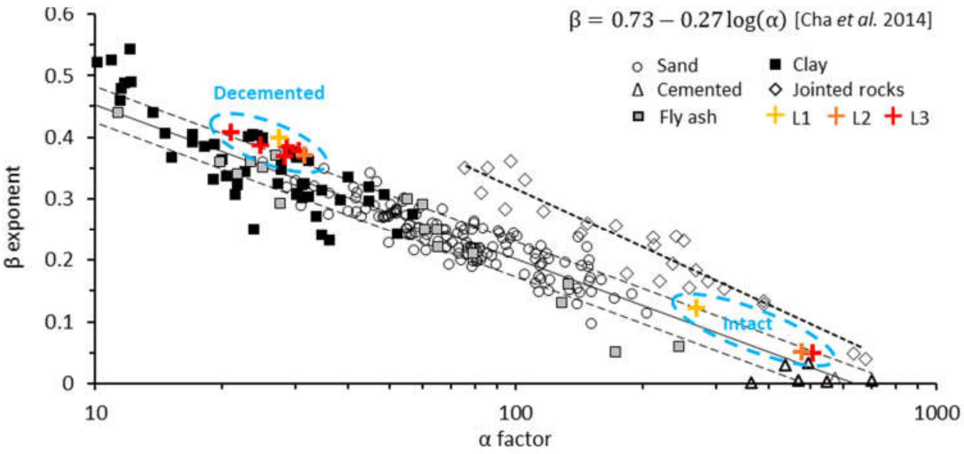

Figure 4.16 – Inverse relation between α factor and β exponent. The α-β relations of sand, clay, jointed rocks, and cemented soils are compiled by Cha *et al*. (2014) (reproduced with permission from Cha) and that of fly ash is included in Bachus *et al*. (Bachus *et al.*, 2019).

4.5.3 Variation of G₀

Viggiani & Atkinson (1995) proposed a relation between G_0 and the effective stress for reconstituted fine-grained materials which can be expressed as:

$$\frac{G_0}{p_\mathrm{r}} = A\left(\frac{p'}{p_\mathrm{r}}\right)^n \left(\frac{p'_\mathrm{P}}{p'}\right)^m \tag{13}$$

where p_r is the reference pressure (1 kPa), p'_P is the yield pressure, and thus p'_P/p' reflects the isotropic overconsolidation ratio. A represents G_0 of the reconstituted soil at p' = 1 kPa,

n relates G_0 and applied stress, and m reflects the effect of the overconsolidation. A, n, and m are dimensionless soil parameters;

To better characterize the effects of structure on G_0, Trhlíková *et al*. (2012) suggested an additional term and modified the Equation (10) to the following form:

$$\frac{G_0}{p_\mathrm{r}} = A\left(\frac{p'}{p_\mathrm{r}}\right)^n \left(\frac{p'_\mathrm{e}}{p'}\right)^m \left(\frac{s}{s_\mathrm{f}}\right)^l \tag{14}$$

where l is a parameter controlling the influence of the structure, and for cemented soils, p'_e/p' is the apparent overconsolidation ratio that is responsible for the higher G_0 at the pre-yield state. The value of s represents the sensitivity of a soil, which is measured by the distance between the sedimentary compression line (SCL) and the normal compression line (NCL). The value of s_f reflects the final value of s as it decreases with the 'destructuction' process and approaches a 'stable' state; $s = s_f = 1$ is considered for reconstituted soils. The more detailed definitions of the parameters are shown in Figure 4.17. Trhlíková *et al.* (2012) provides a useful term for characterizing the effects of structure; but the estimation of s is not elaborated in the study, and the estimation of s_f appears to be unclear.

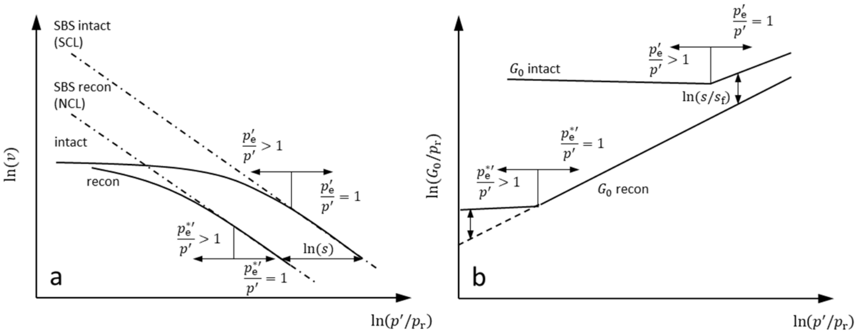

Figure 4.17 – Schematic illustration of the behaviors of intact and reconstituted soil and the defining parameters: (a) compression; (b) small-strain shear modulus (after Trhlíková *et al.*, 2012).

In this work, G_0 is computed for intact and decemented LC loess samples. The effect of overconsolidation, p'_{e}/p' is measured by combing the compression curves in Figure 4.5 and Figure 4.7 and comparing the distance of convergence to SCL and the corresponding NCL; the same approach is used for estimating the s value. The s_{f} value is chosen as 60 for the intact L1 specimen and increased to 120 for L3 specimen to represent the slow-to-no convergence of NCL; it decreases with decreasing sampling depth to reflect the reducing effects of structure. Equation (14) is applied for the intact specimens; but the decemented specimens are considered as reconstituted soils; Equation (13) is applied with $p'_{\mathrm{e}}/p' = 1$. The values of the fitting parameters are summarized in Table 7.

Table 7 – Fitting parameters of G_0 of intact and decemented LC loess

Test	A	n	m	l	s_{f}
L1i_w	1800	0.6	0.65	0.33	80
L1i_w (after wetting)	1000	0.78	-	-	-
L2i_w	2800	0.59	0.62	0.32	90
L2i_w (after wetting)	1100	0.79	-	-	-
L3i_w	3600	0.62	0.36	0.35	120
L3i_w (after wetting)	700	0.84	-	-	-
L1r_3	600	0.85	-	-	-
L2r_5	820	0.79	-	-	-
L3r_2	1000	0.77	-	-	-
L3r_3	580	0.82	-	-	-
L3r_4	440	0.84	-	-	-
L3r_5	800	0.77	-	-	-

As shown in Figure 4.18, the measured data and the estimated values are compared for the LC loess samples. The empirical relation shows a reasonable fit for the decemented samples. The G_0 calculated for the intact specimens are lower than the measured data at low stress levels. Similar errors are observed in Trhlíková *et al*. (2012) which indicated the inherent challenges to predict a nearly constant G_0 before yield point that is associated with strongly cemented soils. Additional challenge of applying this model lies upon the needs of identifying compression lines for both intact and reconstituted samples that are with very similar initial void ratio to provide a more accurate estimation on the value of s; meanwhile these samples must be loaded to a sufficiently high stress to ensure convergence to their corresponding SBSs (or SCL and NCL), which can be difficult for more strongly cemented soils. As discussed in Section 4.3.4, the transitional behavior of the LC loess increases the difficulties in measuring the controlling parameters due to the non-converging trend and the state-dependent SBSs in the $\ln(v):\ln(p'/p_\mathrm{r})$ plane (Figure 4.17).

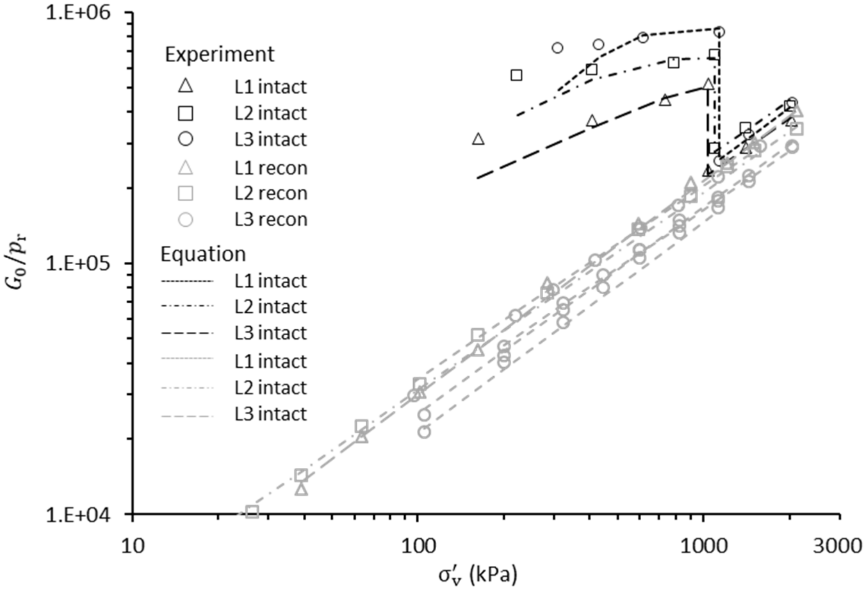

Figure 4.18 – Changes of G_0 with effective vertical stress for intact and decemented LC loess samples. G_0/p_r lower than 10^4 is omitted for clarity.

4.5.4 Cement content and sequence

The cement content (*cc*) is a key parameter in studying cemented soils, and it is often a controlled parameter in many laboratory studies on cemented material, as it affects the overall behavior of the material. The understanding of the potential effects of cc for intact loess is limited, which is largely ascribed to the significant challenges in estimating the volume (or weight) of the bonds. Without any measurement of cc of the LC loess, a set of hypothetical values are used to explore its effects on stiffness in light of analytical approach derived from the simplified Hertzian contact model.

Fernandez & Santamarina (2001) proposed that the sequence of cementation in terms of loading has effects of the small- and large-strain behaviors of granular materials, with the key difference lies upon the contact area for a given cc ($W_{\mathrm{cement}}/W_{\mathrm{particle}}$). The study provides an analytical approach to assess the effects of cc on the contact-particle area ratio based on the Hertzian contact model (Richart et al., 1970), and can be expressed as:

$$\frac{a_{\mathrm{c}}}{R} = \left((cc+1)^{\frac{2}{3}} - 1 + \left(\frac{3(1-v_{\mathrm{m}})\sigma}{2G} \right)^{\frac{2}{3}} \right)^{\frac{1}{2}} \tag{15}$$

$$\frac{a_c}{R} = \left(\frac{3(1-v_{\mathrm{m}})}{2} \left(\frac{2}{3} \frac{G}{1-v_{\mathrm{m}}} \frac{\left((cc+1)^{\frac{2}{3}} - 1 \right)^{\frac{3}{2}}}{(cc+1)^{\frac{1}{3}}} + \sigma \right) / G \right)^{\frac{1}{3}} \tag{16}$$

$$\frac{a}{R} = \left(\frac{3(1-v_{\mathrm{m}})\sigma}{2G} \right)^{\frac{1}{3}} \tag{17}$$

where a_{c} is the contact area, R is the radius of elastic spheres, v is the Poisson's ratio, G is the shear modulus, and σ is the normal vertical stress. Equation (15) represents the case of loading-before-cementation (LbC) for soil particles, which reflects the common sequence of cementation in nature. Equation (16) characterizes the case of cementation-before-loading (CbL) for soil particles, which reflects the common setup of cementation in laboratory tests. Equation (17) is a generalized form for uncemented soil, which is used for the decemented specimens in this work. The derivation of the equations is based on simply cubic packing; Fernandez & Santamarina (2001) argued other packings cause little effects on the results.

Following the same line of assumptions, the ratio of the tangent elastic modulus, E_{T} to the shear modulus can be computed for the cases of LbC, CbL, and uncemented:

$$\frac{E_{\mathrm{T}}}{G}=\frac{1}{1-v_{\mathrm{m}}}\left[(cc+1)^{\frac{2}{3}}-1+\left(\frac{3(1-v_{\mathrm{m}})\sigma}{2G}\right)^{\frac{2}{3}}\right]^{\frac{1}{2}} \tag{18}$$

$$\frac{E_T}{G}=\frac{3}{2}\left(\frac{2}{3(1-v_{\mathrm{m}})}\right)^{\frac{2}{3}}\left[\frac{2}{3(1-v_{\mathrm{m}})}\frac{\left((cc+1)^{\frac{2}{3}}-1\right)^{\frac{2}{3}}}{(cc+1)^{\frac{1}{3}}}+\frac{\sigma}{G}\right]^{\frac{1}{3}} \tag{19}$$

$$\frac{E_T}{G}=\frac{1}{1-v_{\mathrm{m}}}\left(\frac{3(1-v_{\mathrm{m}})\sigma}{2G}\right)^{\frac{1}{3}} \tag{20}$$

where the descriptors are identical to Equation (15)-(17). Equation (18) characterizes the normal stiffness of LbC case, whereas Equation (19) reflects that of CbL case. Equation (20) represents the uncemented (or decemented) skeleton. Since G_0 and v can be estimated by V_{P} and V_{S}, the a/R and E_{T}/G values can be explored under this simplified framework using various cc. Figure 4.19 compares the results of a/R and E_{T}/G for the specimens.

To back-analyze the minimum cc of the LC loess samples, three cc are hypothesized to compute the normal stiffness. The E_{T} of intact loess is higher than the corresponding reconstituted form, as observed in clayey, silty, and sandy loess samples in CHAPTER 3, and also concluded by Xu & Coop (2016, 2017) and Xu *et al.* (2018). To reflect such an observation, the cc value is found to be at least greater than 50% for the case of LbC, which is considerably higher than many reported cemented soils (e.g. Fernandez & Santamarina, 2001; Hird & Chan, 2008; Trhlíková *et al.*, 2012), albeit artificially cemented. However, such a high cc may be misled by the large differences in the small-strain stiffness between intact and decemented samples. The corresponding a/R of LbC indicates that the contact area increases with applied stress, with the contact area higher for intact specimens. The results for the case of CbL are rather confusing with high a/R values that lie within the extrapolated line of the decemented specimens is not consistent with the understanding on the effects of structure.

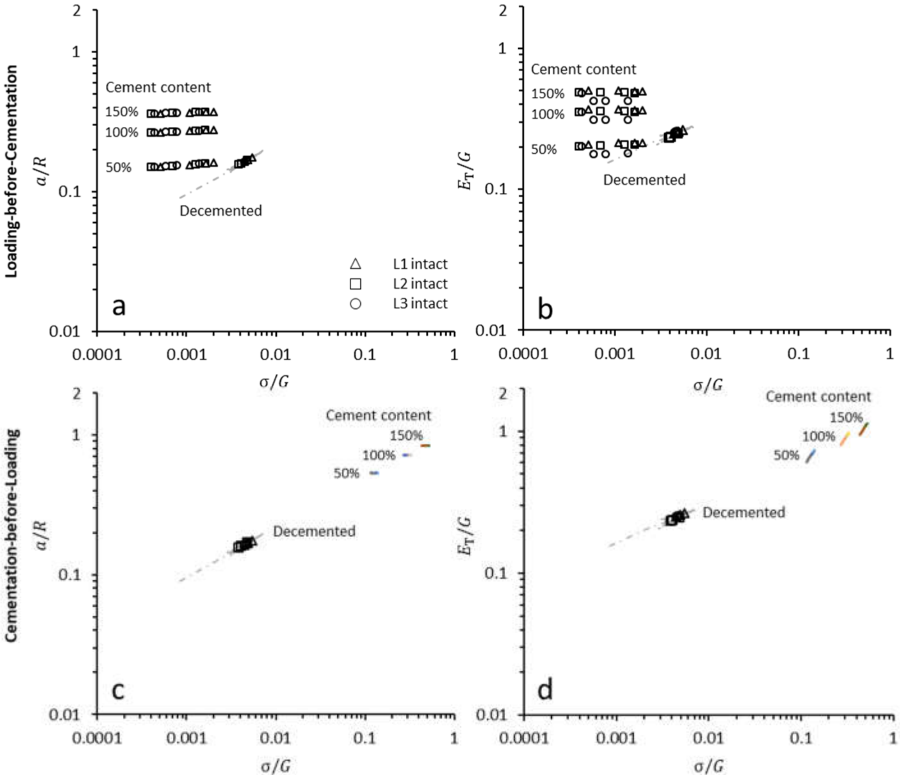

Figure 4.19 – Comparison between intact and decemented LC loess samples for LbC and CbL sequences using micromechanical model. LbC: (a) a/R and (b) E_T/G; CbL: (c) a/R and (d) E_T/G; it is assumed that wetting- and mechanical-decementation both follows the uncemented soil behaviors.

Notwithstanding the difficulties of estimating the cement content of a natural loess specimen with sufficiently high accuracy, the hypothetical cc values in this section serve as an attempt to assess the potential effects of natural cement content on the behavior of loess on both micro- and macro-scales.

4.6 Concluding Remarks

The degree of cementation in LC loess is proportional to the buried depth from L1 to L3, whereas the collapse potential decreases with increasing depth due to the decreasing void ratio. A significant drop in wave velocities can be seen at the onset of wetting, indicating substantial reduction in the small-strain stiffness at the contact level and the decementation of the intact sample.

A decemented LC sample can be produced either by wetting or grinding, of which the inter-particle contact deformation exhibits similar response under 1-D compression, as reflected by the wave velocity variations, of which in particular, the similarities of the s-wave velocity between wetting-decemented and mechanical-decemented LC loess sample. Such an observation can also be reflected by the changes in the α-β relation which is used as a typical indictor to reflect the interplays between soil fabric and interparticle contacts. This observed converging trend in s-wave velocity caused by decementation confirms the concept of the 'cementation-controlled region' in which the s-wave velocity shows little to no changes with increasing stress due to strong inter-particle cementation, until the stress has become sufficiently large to overcome the effects of cementation, and thus the soil enters the 'stress-controlled region'. The results of LC loess suggest the existence of such a threshold stress which may be in the range of 10-20 MPa.

The intact and reconstituted LC loess exhibit clear transitional behavior with non-converging NCL, which may be attributed to grading and interparticle contacts of the soil. The transitional behavior diminishes with increasing vertical stress for reconstituted LC loess, while the intact samples show an indistinct trend of convergence in the m value, suggesting cementation is persistent in affecting the compression behavior of LC loess.

An empirical model was used in an attempt to predict G_0 for intact LC loess; however a nearly constant initial G_0 that pertains to many strongly cemented soils presents great challenges for the model. However, such a model provides good estimation for decemented samples. This work also attempted to back-analyze the cement content by applying a semi-analytical approach developed for Hertzian contact model; while such an assumption may appears to be too ideal for loess particles, the exploration provides a rough estimation on the order of magnitude of the ratio between the weight of cementation agent and that of the particles that have not been explored for loess.

The inherent structure of intact loess is characterized by the extent of cementation, which reflects the depositional event and period that the small- and large-strain behaviors are considerably altered for different layers. Therefore, gaining more understanding of the cementation is crucial to facilitate the study on the diagenetic process and the thixotropic process of the Chinese loess.

CHAPTER 5. DEFORMATION PROCESS AND FAILURE ANALYSIS OF LOESS FLOWSLIDES

This chapter discusses the field investigation on the retrogressive loess flowslides in HFT and the results of the centrifuge model tests on reconstituted loess slopes in response to an increasing phreatic surface, with the objectives of analyzing the deformation process and failure mechanism of loess flowslides caused by surface irrigation. Field investigation is based on the collaborative work with the State Key Laboratory of Geohazard Prevention and Geoenvironment Protection (SKLGP), and results of the fieldwork are published in Qi *et al*. (2018) and Peng *et al*. (2018).

5.1 Introduction

The Heifangtai terrace is located in the arid loess area in northwestern China, where a large number of landslides were induced by agricultural irrigation on the surface of HFT (Figure 5.1). The frequent failures along the margin of the terrace have caused an average slope retreat of 0.036 km^2 between Nov 2014 and May 2016, which corresponds to about 3% annual depletion of the terrace.

As discussed in Section 2.2.2, the alluvial clay layer overlain by the loess layer in HFT has a nearly uniform thickness and low permeability, which results in a saturated base in the overlaying loess layer. The long-term irrigation increased the groundwater level in the terrace by 0.36 m between Jul 2010 and Jul 2012, and by 0.5 m between Sept 2015 and Dec 2016 (Peng *et al.*, 2018). The rising groundwater is postulated as the main reason for the landslides in HFT.

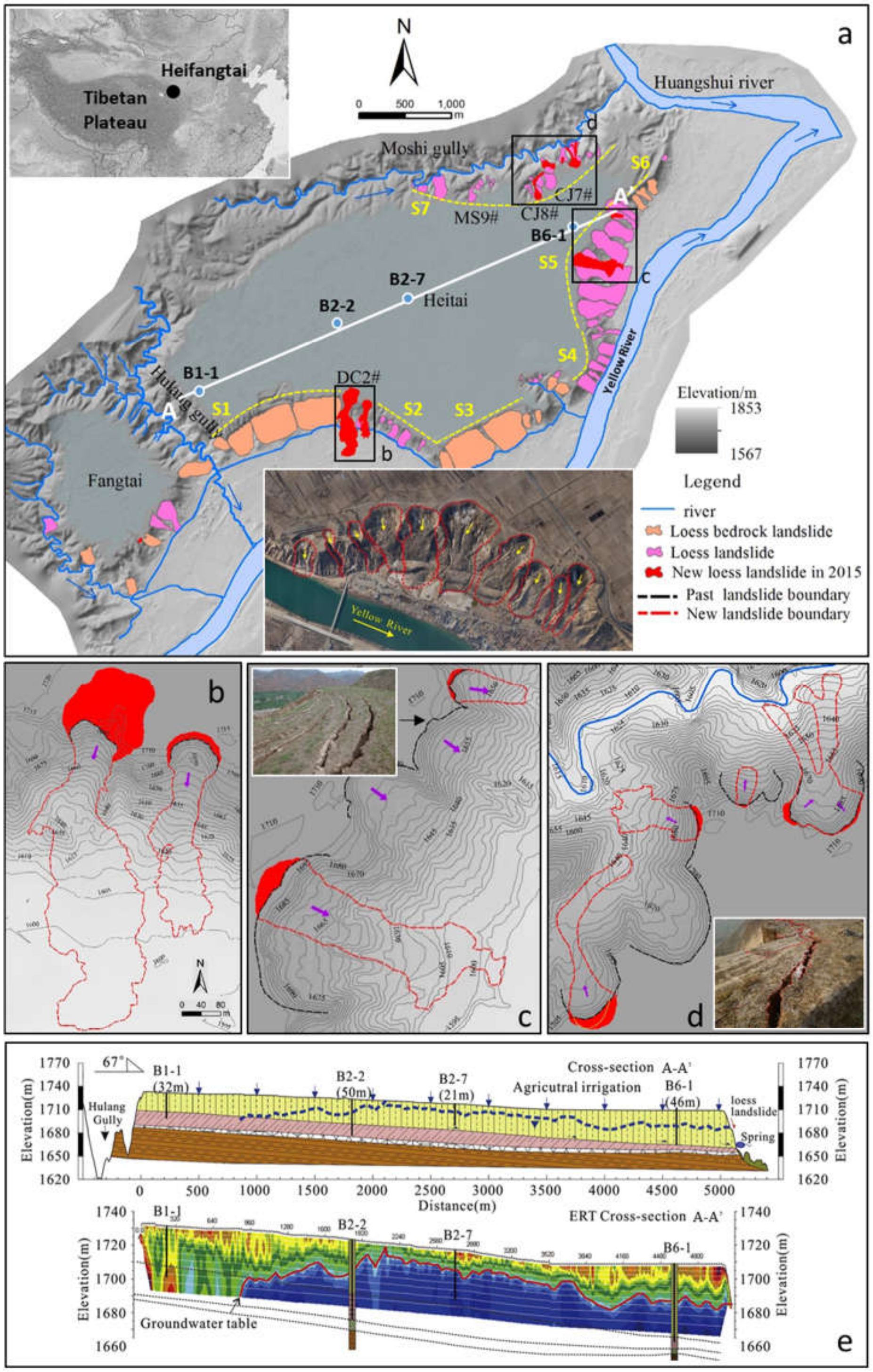

Figure 5.1 – Some flowslides along the margin of HFT as the end of 2015: (a) DEM of the study area (image of S5); (b) DC#2 and DC#3 flowslides; (c) JJY group of flowslides; (d) CJ group of flowslides; (e) geological profile and ERT mapping of groundwater variations of AA' (after Peng *et al.*, 2018; Qi *et al.*, 2018).

Annual variations on the number of landslide events are not well understood and out of the scope of this work; but a strong temporal correlation, with a degree of lag, between landslide events and irrigation activities exists (Peng *et al.*, 2018). The groundwater level in the study site was mapped by using field data from 4 monitoring wells and the electrical resistivity tomography (ERT) results across the longitudinal center of the terrace (Figure 5.1a). The 2-D resistivity map of the water table is produced from a survey line of 5000 m in length that is divided into 25 survey segments with 61 electrodes at 5 m spacing. In consideration of the overall length of the survey lines, effective depth of detection, and accuracy of the results, each consecutive segment has an overlap of 100 m. The coordinates of electrodes were calibrated by ground GPS to ensure a straight line on the same profile with precise elevation. Well monitoring data are used to validate the ERT results, with a margin of error of ± 0.5 m for groundwater level variation. The ERT results show that the groundwater level is higher on the west of the terrace with the maximum elevation difference of 30 m (Figure 5.1e).

Peng *et al.* (2018) divided the terrace into 7 sections (S1-S7) based on the included angle between the principle sliding direction of the landslide and the bedrock dip (Figure 5.1), as the included angle shows a strong effect on the development of the failure surface. The bedrock dips of S2, S4, S5, and S6 are nearly perpendicular to the dominating direction of slope deformation so that it obstructs the potential sliding motion along with the dip of the bedrock bedding.

Field investigation classified the landslides in HFT into 5 types (see Section 2.2.2); in which loess flowslide is defined as a large-to-medium scale failure with failure surface develops entirely within the overlying loess layer; it exhibits rapid movement and long runout with liquefied and fluidized flow behavior. Loess flowslide is typically associated with pronounced retrogressive behavior and appears to be induced by static liquefaction; however the failure mechanism of flowslide and the effects of groundwater variation are not fully understood.

In this chapter, the failure mechanism of loess flowslides is proposed in light of the field investigation results, and further tested by using centrifuge modeling, with the aims of 1) understanding the effects of groundwater dynamics on the slope failure along the margin of the terrace, and 2) analyzing the liquefaction event that accompanies loess flowslides.

5.2 Retrogressive loess flowslide

5.2.1 Field investigation

5.2.1.1 Slope deformation process

The slope retreat at the terrace edge can be demonstrated by the landform changes caused by the MS#9 loess flowslides near the Moshi gully. Satellite images between 2004 and 2013 were obtained for the MS#9 (location see Figure 5.1). No apparent groundwater discharge outlets were seen on the slope surface due to the limited quality of the Google Earth images (Figure 2.3a). With an increasing area of cultivated fields and irrigation, a groundwater dome started to build up, resulting in enhanced flow from the center towards the edge, and in turn the formation of apparent spring line in the loess layer with salt coating at the scarp and the displaced material (Figure 2.3b). Under such a long-term groundwater recharge, the basal zone of the loess layer is likely softened by saturation and migration of the finer particles forming the salt coating as a result of eluviation reported in the previous studies (Gao, 1986; Derbyshire & Mellors, 1988; Assallay *et al.*, 1998; Derbyshire, 2001); such a strain-softening process may contribute to the development of the loess flowslide in early 2013 (Figure 2.3c). Surface discharge can be seen below the apparent spring line at the landslide deposit forming distinct erosion channels. The slope failure was followed by another landslide in Nov 2013, which formed behind the previous scarp and dammed the Moshi gully. The concavity of the scarp extended in both length and size in the latest failure with a slightly gentler slope angle compared to the previous failure (Figure 2.3d). The loess flowslide dammed the Moshi gully with a run-out distance of 250 m and a width of 140 m; the estimated volume of the flowslide was 250,000 m^3.

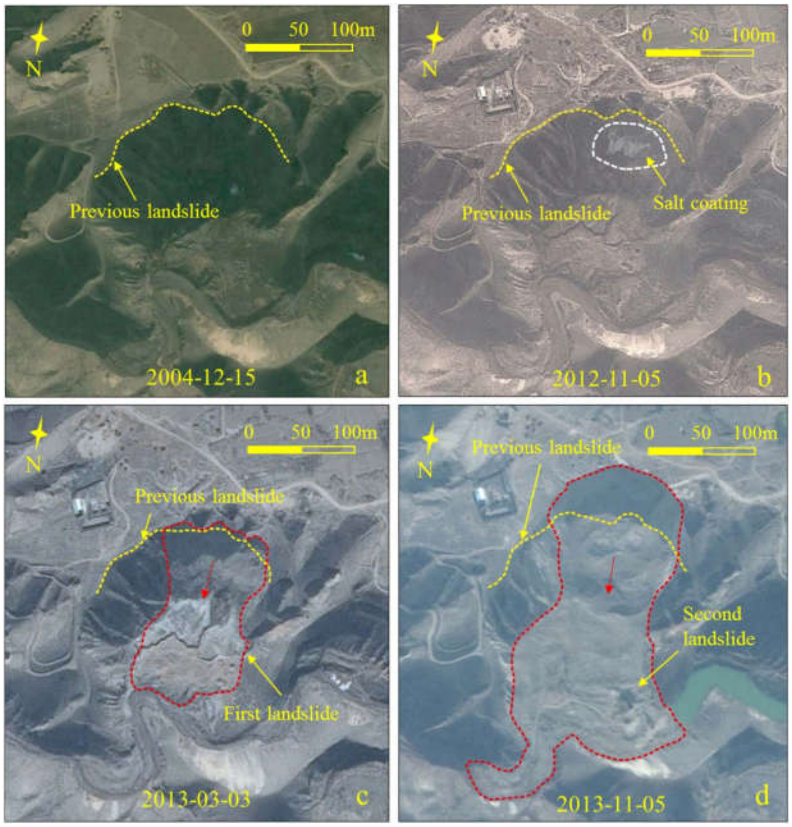

Figure 5.2 – Satellite imageries showing slope evolution due to the retrogressive MS#9 loess flowslides near the Moshi Gully (from Google Earth image).

The slope retreat along the terrace edge continues as new landslides develop on the scarp of the previous ones. The resultant slope retreat is not exactly parallel, because the magnitude and the convexity vary for each case. A prominent retreat can be exemplified by the repetitive sliding that occurred during the DC#2 failure on the south edge of the terrace (Figure 5.1b). The failure occurred in Jul 2012 was small in size with a short runout; but it resulted in a dense distribution of crown cracks (Figure 5.3a). A loess flowslide occurred at the same location in Apr 2015, involving a two-staged failure process, resulted in the recession of the escarpment for more than 150 m (Figure 5.3b).

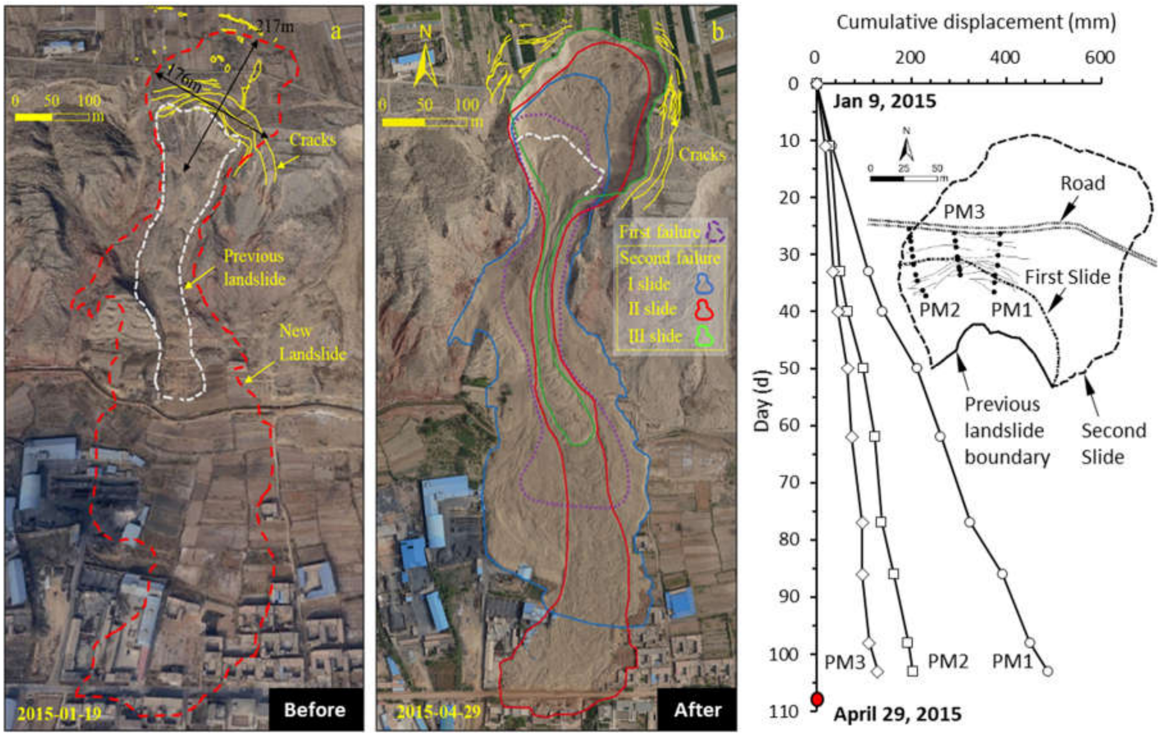

Figure 5.3 – Oblique pre-/post-failure images showing the boundary and displaced material of the DC#2 loess flowslide: (a) pre-failure conchoidal crown cracks coincided with the scarp of the new failure; (b) sliding events and boundaries with newly developed cracks; (c) cumulative displacement before failure based on the monitoring markers placed at the crown of the DC#2, with locations of the markers relative to the boundary.

On Apr 29, 2015, the first failure of the flowslide occurred at approximately 7:50 AM in the direction of 190° with a total volume of 8×10^4 m^3, and the displaced material traveled 437 m in horizontal distance. The second failure occurred approximately 3 hrs later, contained three sliding events as follows:

- The first sliding event occurred at 10:47 AM; it lasted about 3 mins, according to the local inhabitants, with an estimated volume of 32.4×10^4 m^3 and a runout distance of 618 m damaging downstream farmland by forming a fan-shaped deposit with an average thickness of 3 m.
- The second sliding event occurred at 10:51 AM; it travelled over the deposited material of the first sliding, and resulted in a runout distance of 789 m. The sliding destroyed 14 houses, 3 factories and some farmland. The rear boundary of the second sliding was in line with the crown cracks formed by the previous landslide.
- The third sliding event occurred about 20s after the second event, sliding over the displaced material of the previous events with a horizontal runout distance of 474 m.

Ground monitoring markers were placed at the crown of the DC#2 landslide to monitor surface deformation since Nov 2014. Field data were collected at an average 10-day interval by measuring the relative distance between consecutive markers. Surface deformation was found within 40 m behind the scarp. The surface deformation before the first failure on Apr 29, spanned over 3 months, as shown in Figure 5.3c. Field data was obtained 30 mins after the first failure; but more than half of the markers were mobilized during the first failure. Field measurement was conducted after the first failure with the remaining markers, which indicated no deformation for at least 2 hrs prior to the rapid and far-reaching second failure.

5.2.1.2 Groundwater dynamics

With the decreased elevation and increased thickness of the loess cover from the west to the east of the terrace, the resultant hydraulic gradient permits groundwater flow towards the east margin; such a process is enhanced by the seasonal irrigation. An apparent spring line was formed with salt coating at a newly established free face. The spring line can be observed above the head of the displaced material for most of the flowslides, as the original locations of surface discharge are impeded (Figure 5.4), indicating the present groundwater level at the terrace edge. The elevation difference between the apparent spring line at the scarp and flanks of the flowslide can be greater than 10 m.

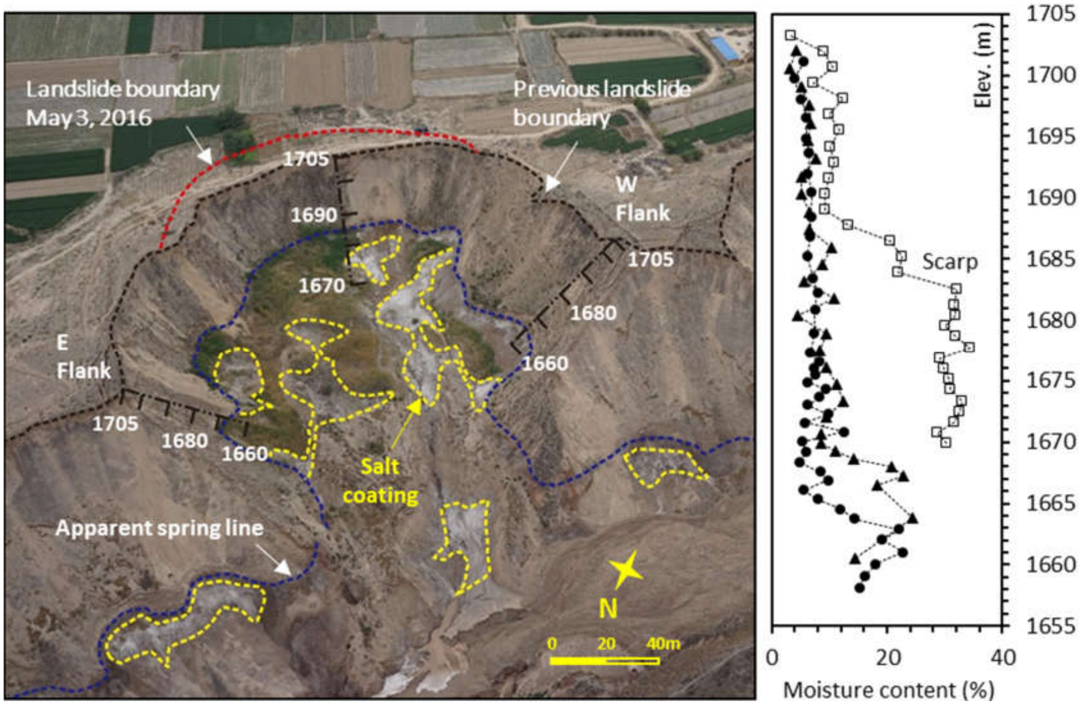

Figure 5.4 – Surface moisture content variations at the CJ#7 landslide, showing elevation difference in the apparent spring line at the scarp and flanks. Spring line was formed above the head of the displaced material due to the rise of groundwater below compared to the flanks. Seepage of groundwater was facilitated by a high hydraulic gradient, which also dissolved soluble particles and resulted in salt coating near the backwall of the landslide.

The observed salt coating at the scarp and flanks shows elevation variations similar to the apparent spring line. The coating was generated by groundwater dissolving soluble salts i.e. leaching (Derbyshire, 2001), which softens the lower part of the loess layer by decementation and redistribution of the particles.

The moisture content of the surface loess was measured at the CJ#7 flowslide (location in Figure 5.1). The apparent spring line is formed at the scarp stretching over both flanks as shown in Figure 5.4. Cubic specimens were collected at the outcrop (~20 cm) at 1 m interval by roping down at the backwall of the landslide. The moisture content increases with depth and consistently greater at the scarp, and particularly below the spring line, indicating a localized hydraulic gradient of over 10 m. Such phenomena are common at newly occurred flowslide sites on the terrace.

5.2.2 Proposed failure mechanism

Field investigation reveals that no or limited re-failure deformation at the crown for loess flowslides in HFT; it is postulated that the failure mechanism involves a localized hydraulic gradient produced by a preceding failure, resulting in groundwater convergence at the newly established scarp, causing strain-softening, decementation, and subsequently a liquefaction-induced flowslide. The failure process is illustrated in the conceptual model in Figure 5.5, hypothetically involving the following steps:

- As groundwater level rises, the basal zone of loess layer is invaded by pore-water and softened by decementation, and become readily to deform under vertical stresses (Figure 5.5a), with seepage on the slope surface forming the apparent spring line. At this stage, cracks and joint systems develop around the crown and provide drainage paths and facilitate groundwater discharge (Xu *et al.*, 2012a; Zeng *et al.*, 2016).

- Gradual crown deformation followed by the 1st failure event which produces a new free face by depositing and impeding the existing surface discharge point (Figure 5.5b). With the groundwater converging to the free face, the deposit obstructs the seepage and increases the localized hydraulic gradient. Surface discharge tends to form at a higher elevation, indicating groundwater level increase (usually reaching the head of the displaced material). Pore-water pressure is built up and the moisture content of loess above the spring line at the scarp may exceed the plastic limit. As pore-water pressure gradually builds up behind the scarp of the first failure, the slope transits from drained to undrained loading condition.
- The upward invasion of groundwater level in the loess layer causes decementation and reduction in strength and stiffness in the lower part of the layer. A small axial displacement may induce liquefaction as deformation continues, and result in a rapid liquefied movement of loess. Groundwater converges after the failure, and thus by its very nature a new flowslide is likely to follow (Figure 5.5c).

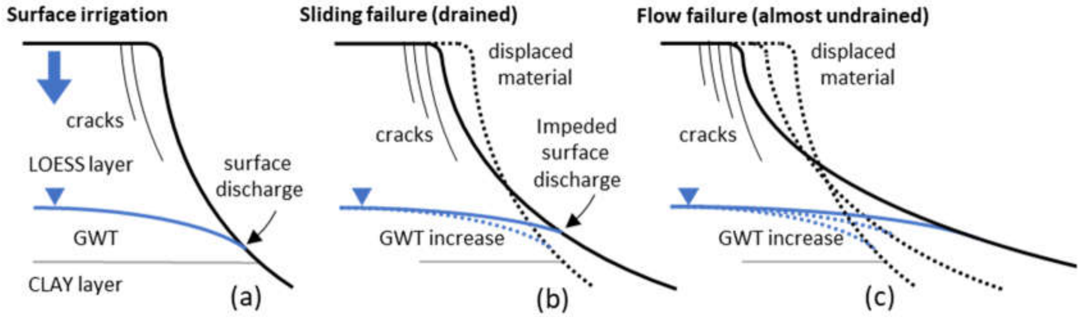

Figure 5.5 – A conceptual model of the multi-staged retrogressive loess flowslides in HFT: (a) pre-failure deformation and surface discharge; (b) sliding failure (first failure) under drained condition; (c) flowslide (second failure) under almost undrained condition.

The results of laboratory tests in CHAPTER 4 have shown that gradual increase of groundwater level in the loess layer causes wetting-induced decementation in the lower part of the layer, and results in large-strain vertical deformation (i.e. collapse), as reflected by the resultant intense development of cracks along the margin of the terrace. The increase of groundwater level reduces the stiffness of loess, which further compromises the stability of the slope. The leaching process results in disaggregation of fabric, which reduces pore size and affects pore distribution by filling the voids. The reduction in strength and leaching may not be sufficient to trigger a long-runout loess flowslide; but as shown in the results of CIU in CHAPTER 3, although a 'true' liquefaction is not observed in HFT loess, the q and p' are reduced to a sufficiently low level under such an undrained condition and lead to a runaway acceleration and high-velocity long-runout failure across a low-relief terrain.

The hypotheses of static liquefaction has been tested as the trigger for rapid and long-runout landslides in coarse granular slopes by a series of physical model studies conducted at Queen's University in Canada (e.g. Take *et al.*, 2004, 2014; Take & Beddoe, 2014; Beddoe & Take, 2016; Wolinsky & Take, 2019). Their studies found that static liquefaction is most likely to occur near the base of a model slope due to seepage impediment, as the results of changing slope geometry; such a finding shed light on the importance of the effects of a natural evolution of slope on creating appropriate conditions to generate static liquefaction, which ultimately aligns with the field observations on the retrogressive loess flowslides in HFT.

Take & Beddoe (2014) argued that for static liquefaction to occur in a landslides, the soil must be: 1) contractive, 2) sufficiently saturated, and 3) subject to monotonic loading to permit the development of excess pore-water pressure. While the failure mechanism proposed in this work appears to be, in principle, consistent with these three criteria to support the argument of static liquefaction as a trigger, the deformation process responding to the resultant pore-water pressure perturbation remains unclear. The proposed failure mechanism is studied by the centrifuge model test at SKLGP centrifuge facility.

5.3 Centrifuge test

Centrifuge modeling has been widely used to investigate failure process of landslides (Lee *et al.*, 2008; Bowman *et al.*, 2010; Ling & Ling, 2012; Milne *et al.*, 2012; Bowman & Take, 2015; Askarinejad *et al.*, 2018), as the mechanical responses of the model slope reflects the prototype at a given stress level during the centrifuge test. However, the scaling nature of centrifuge tests as well as the complexity of structure and size of loess and their associated diffusion events cannot be overcome. The work presented herein is not to predict the temporal evolution and runout distance of a loess flowslide, or to mimic the degradation process of any particular loess slope, the main objectives are 1) to explore the deformation process related to the changing phreatic surface and slope geometry in silty loess, and 2) to analyze the effects of drained-undrained transition and the resultant perturbation of pore-water pressure on slope stability.

5.3.1 Model setup

The centrifuge test in this study is intended to avoid any additional effective gravitational acceleration due to the Coriolis effect (Taylor, 1995). The orientation of the model slope produces the Coriolis acceleration acting against the principle direction of slope movement; otherwise the Coriolis effect can be magnified at the target acceleration for this study (Bryant *et al.*, 2015), and thus physically enhancing the failure phenomena.

5.3.1.1 Model slope and materials

The model setup is illustrated in Figure 5.6. The plane-strain centrifuge model box has a dimension of 1150 (L) × 657 (W) × 1075 (H) in mm, which accommodates an in-house designed reservoir system, an impermeable base, and the model slope. A detachable Perspex window at the front is removed during the construction of the model slope. The base permits water retention to saturate the model slope, which is analogous to the existing clay layer in the HFT. The in-house designed water tank is recharged from an external water intake during the test. Two arrays of small water outlets are located behind the model slope at heights of 65 mm and 115 mm above the base of the slope, respectively (Figure 5.6c). A rectangular porous stone is used to cover the water outlets to ensure uniform and steady water inflow in the slope. An observation window is placed on the front side of the water tank. The geometry of the slope is highlighted in Figure 5.6b.

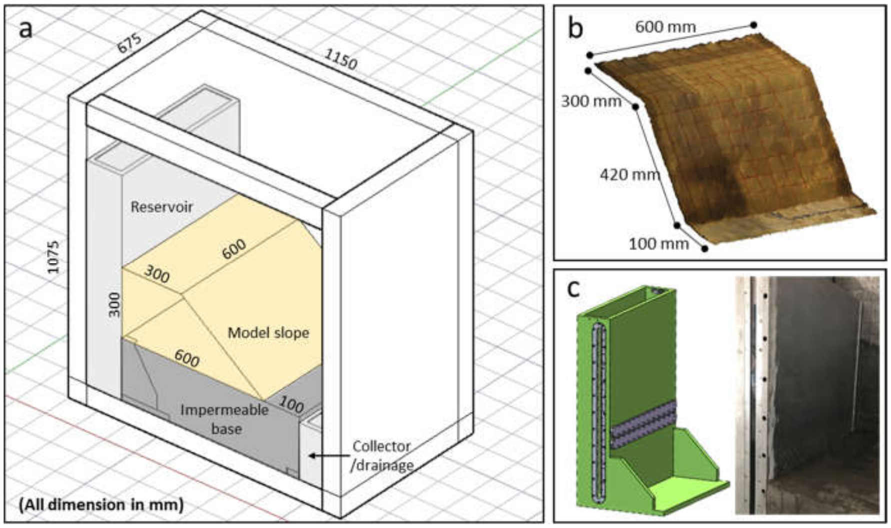

Figure 5.6 – Model setup showing slope geometry and hydraulic boundary conditions: (a) 3-D sketch of the model setup; (b) 3-D scan of the model slope surface after excavation; (3) comparison between the water tank design and the installed reservoir system showing water outflows. The removable Perspex cover of the model box is omitted for clarity.

The mode slope was 300 mm high, which corresponds to a prototype height of 30 m at a test acceleration of $100g$. The model slope was constructed by compacting ten layers of reconstituted HFT silty loess at the water content of 8%. The model box was sealed before the test to reduce changes in the moisture content. The reconstituted sample is prepared by using the same method discussed in CHAPTER 3. A global average of initial void ratio of 0.868 is achieved for the model to ensure a positive state parameter for the soil (see Figure 3.7). The initial void ratio is also similar to the *in situ* void ratio of HFT silty loess of 0.86-0.89 (see Table 3); but such a comparison provides limited information as the internal structure has been altered. The reconstituted loess is compacted by covering the entire impermeable base and the toe drain, and then the sample block is excavated to an inclination angle of 45°, which is higher than the critical state friction angle, ϕ'_{CS} of 33.7° (see Section 3.3.1).

5.3.1.2 Instrumentation

The in-flight instrumentation layout is shown in Figure 5.7a. Three cameras provide continuous data collection on the slope evolution. Two cameras are placed for monitoring the overall operation, and one high-speed camera is to capture the movement of the slope at 20 frames per second (fps). The reservoir level in the water tank needs to be maintained at a designated level for a given period throughout the test. Since the rate of water intake is constant due to system setting in the facility, the reservoir level is monitored by the high-speed camera and controlled by manually opening/closing the intake valve.

A more detailed layout of the model slope is illustrated in Figure 5.7b. Numerous centrifuge studies on slope movement prefer to place pressure transducers at the model-boundary interface, as some have argued that sensors in the model may result in restrictions to movement during shearing. Pressure transducers at the interface may not be sufficient to capture the excess pore-water pressure (PWP) development for a large model slope.

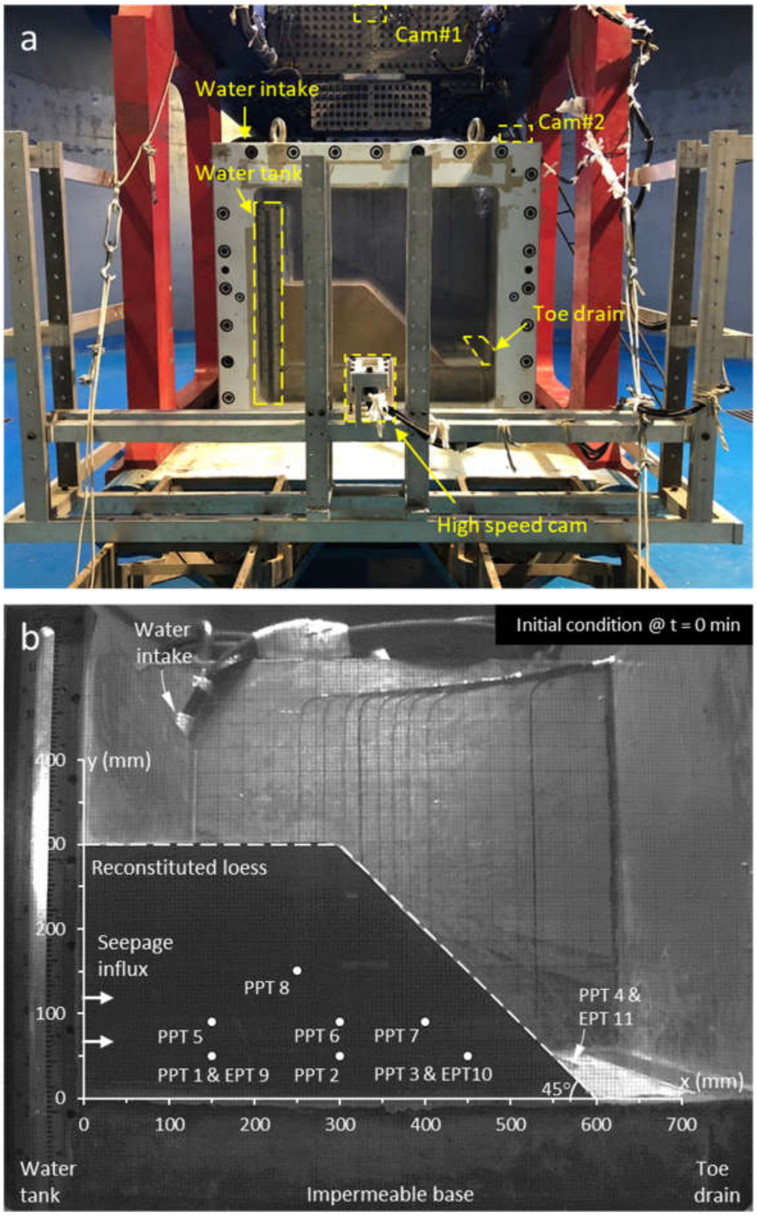

Figure 5.7 – Detailed model setup prior to the test: (a) layout of in-flight instrument for the centrifuge test; (b) model at initial condition (t = 0) illustrating instrumentation layout, slope geometry, hydraulic boundary conditions, and the field of view (FOV) of the high-speed camera (PENTAX 12.5 mm TV LENS).

The responses of PWP at different depth as phreatic surface propagates are of significant interest to this study. Seven pore-water pressure transducers (PPTs) are placed in the model slope at the longitudinal center at various depths, as shown in Figure 5.8. PPT 1 and PPT 3 are paired with separate earth pressure transducers (EPTs) to estimate the effective pressure at the designated location, assuming the paired sensors remain in close proximity throughout the test. The transducer cables are loosely buried in the model slope to reduce potential restrictions by straining. PPT 4 and EPT 11 are placed on the surface of the permeable base adjacent to the toe the slope, with a distance of 50 mm, to provide additional confirmation on the occurrences of slope movement.

5.3.1.3 Hydraulic boundary conditions

As illustrated in Figure 5.5, the hypothesized first failure changes of slope geometry near the base of the slope resulted in a higher hydraulic gradient that favors saturation near the newly established base due to impeded seepage; such a flow constriction may lead to a drained to undrained transition, and subsequently static liquefaction. The localized failure caused by the static liquefaction produces a debutressing effect so that the rest of the displaced materials are being mobilized with potential runaway acceleration.

The test relies on the steady propagation of the phreatic surface in the model to analyze such a complex evolution of slope failure. The model slope is subject to a stepwise increase of water level in the water tank (and by the nature of the test, the acceleration), i.e. water head above the lower inlet (Figure 5.7b). The elevating phreatic surface represents the saturation process of the slope, which in principle, follows the groundwater variations in the HFT, as the groundwater table is increased by seasonal irrigations. A zero-pressure head boundary condition is permitted at the end of the impermeable base, in the form of a gravity drain. The drained water is not re-introduced into the reservoir system due to the high concentration of suspended loess particulates.

5.3.2 Experimental results

5.3.2.1 Phreatic surface and surface subsidence

The model slope is subject to a stepwise increase in centrifugal acceleration. The system is tested and checked during the period (~10 min) of the initial acceleration phase before the seepage flux. The seepage influx is introduced when acceleration is at $20g$, and then gradually increased to $50g$ and maintained at that level for slope saturation process. Difficulties emerged in maintaining a constant water level in the water tank due to seepage influx; however a reasonably steady propagation of phreatic surface is observed during the saturation phase (Figure 5.8).

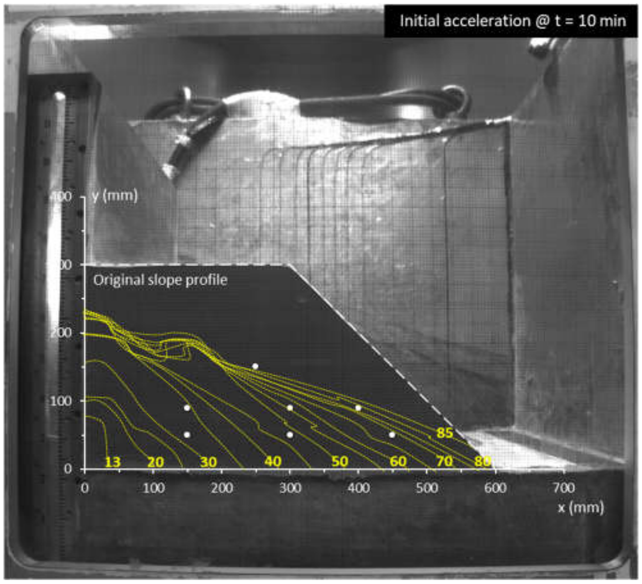

Figure 5.8 – Boundary profile of the phreatic surface during the saturation process (t = 11–80 min), superposing the slope profile at t = 10 min with the corresponding elapsed time.

The phreatic surface reaches the toe of the slope at about t = 80 min, which marks the end of the pre-failure saturation process. As the phreatic surface gradually propagates from the back to the toe of the slope, significant surface subsidence is observed, especially at the Perspex-slope interface near the top of the slope (Figure 5.9). While this particular deformation pattern is attributed to the boundary effect of the smooth Perspex panel, several surface cracks can be seen near the crest of the slope. The large subsidence also appears to affect the shape of the phreatic surface by constricting the propagation underneath the sinkhole, as shown in Figure 5.9a. The locations of the transducers are assumed to be unchanged at this point.

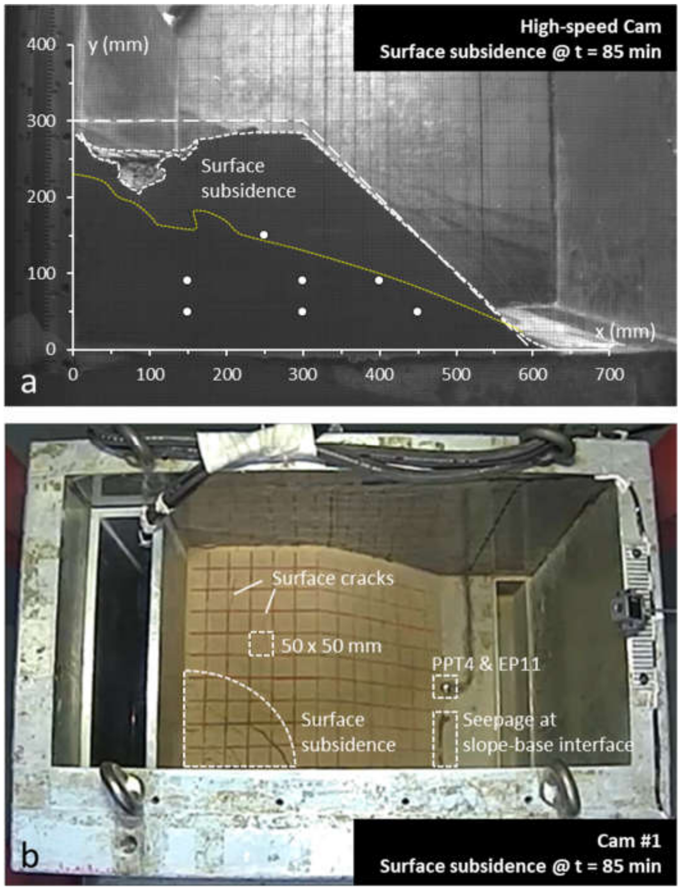

Figure 5.9 – Surface subsidence at the end of the saturation process: (a) FOV of the high-speed cam showing substantial deformation; (b) FOV of cam #1 showing surface cracks.

5.3.2.2 Evolution of failure

Surface subsidence is accompanied by gradual slow-moving slip and followed by a more flow-like failure event. The test lasts for 140 mins, and the investigation focuses on time ranges 0-123 min. Intense surface erosion occurs after t = 125 min, which is caused by the increasing centrifugal acceleration. The model responses to the applied groundwater flow are reflected by the PPTs (Figure 5.10a) and EPTs (Figure 5.10b). The changes of centrifugal acceleration and the applied water pressure during the test are presented in Figure 5.10c and Figure 5.10d, respectively.

The results of PPTs are approximately 0 kPa prior to seepage influx. A slight increase in PPT1 can be seen immediately after the onset of seepage influx due to close proximity. Pronounced increases in PWP are found in PPT 1, PPT 2, and PPT 5 (over 30 kPa) during saturation process, accompanied by some small variations in PPT 6 (up to 5 kPa) after t = 70 min. The PWP of PPT 1, PPT 2, and PPT 5 remain at the same level after about t = 50 min, suggesting the phreatic surface predominately propagates horizontally. Such an observation aligns with the phreatic surface profile (Figure 5.8).

The results of EPT 9 and EPT 10 show a gradual increase in the total stress during the initial acceleration. A slow-moving slip movement can be seen starting around t = 80 mins; this gradual deformation is immediately registered by EPT 11 (at t = 83 mins), suggesting slope movement near the toe area (also see Figure 5.9). As the slope undergoes the initial gradual deformation, the second acceleration is started to reach the target acceleration of $100g$, corresponding to a prototype slope height of 30 m; the steady acceleration causes instant increases in the PPTs and EPT 9 and appears to intensify the slope deformation. The result of EPT 11 confirms the slope movement near the toe area; however it is quickly stabilized and remains at the same level before the subsequent failure.

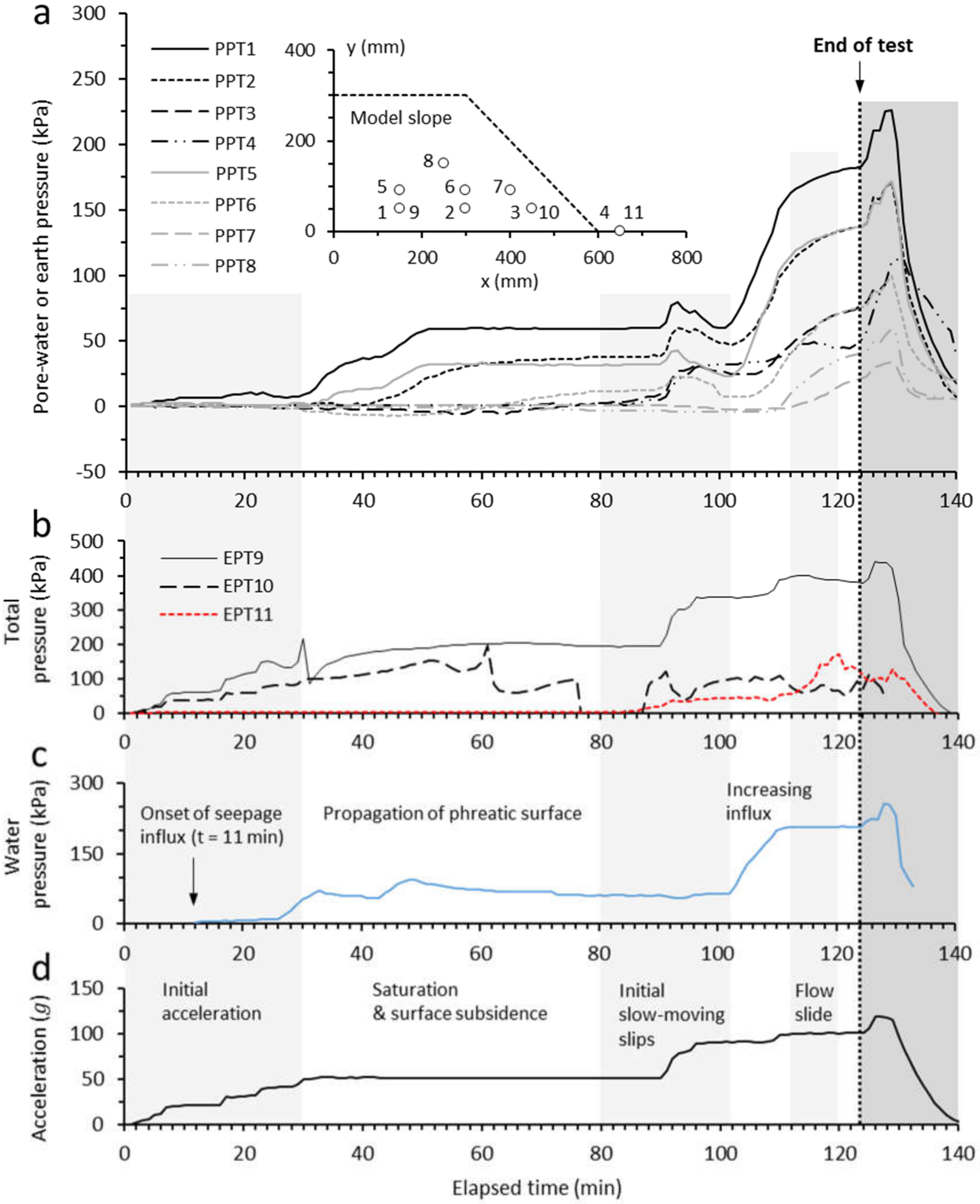

Figure 5.10 – Results of the model slope response during the test (reading at each minute): (a) pore-water pressure responses with locations of the transducers; (b) total pressure responses; (c) water pressure variations; (d) centrifugal acceleration.

Figure 5.11 illustrates the continual deformation of the slow-moving slip during and after the second centrifugal acceleration. The pre-acceleration slope profile can be seen in Figure 5.9 at t = 85 min. While more substantial subsidence is found on the crest of the slope as compared to the pre-acceleration profile, no drastic differences in the deformation pattern can be observed at t = 96-102 min, indicating the second acceleration results in limited impact on the overall deformation process.

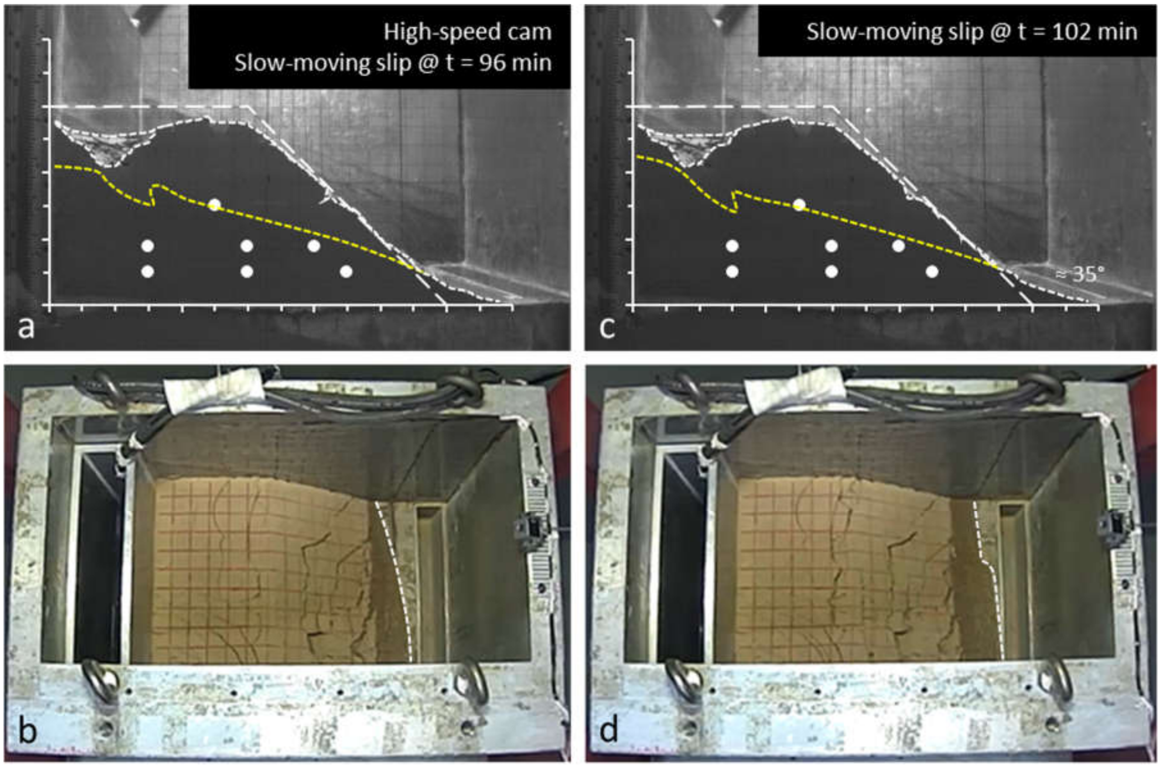

Figure 5.11 – Initial slow-moving slip: (a) slope profile at t = 96 min during the second acceleration and (b) corresponding surface deformation; (c) post-acceleration slope profile at t = 102 min and (d) corresponding surface deformation.

The acceleration causes increases of PWPs in the slope (t = 90-96 min), as shown in Figure 5.10a; but the transient PWPs were gradually stabilized by t = 100 min. Figure 5.11c illustrates the slip movement with the elevated phreatic surface and the variations in the transient PWP, showing flow constriction at the toe with the continuous inclination change as compared to the visible seepage flow near the toe at t = 85 min (Figure 5.9). Such a flow constriction can result in groundwater storage near the toe area, which is found to be a key condition to trigger static liquefaction in centrifuge models (Take & Beddoe, 2014; Beddoe & Take, 2015).

The water level in the tank is increased between t = 102 min and t = 110 min to raise the groundwater level in the slope as flow constriction forms near the toe. A flow-like failure was subsequently observed between t = 113 min and t = 121 min; the transient PWPs and the corresponding changes in EPs at the time of failure are shown in detail in Figure 5.12. Assuming the transducers are being displaced by the slope movement and are traveling in the same principle direction so that they continue to reflect the pressure responses at the same relative position. Substantial increases in the lower PPTs can be seen, including PPT3 near the toe, indicating positive PWP responses to the elevated groundwater level before t = 110 min. The results of EPT11 indicates gradual deformation accompanying the elevated groundwater level.

The PWP at the edge of the newly established toe appears to be unchanged after t = 113 min under increasing seepage influx (see PPT4), implying flow constriction behind the edge of the new slope base, as supported by the increasing PWP in PPT6 and PPT7. A steady decrease in EPT10 is found at the same time, suggesting removal of overlying soils, and thus a reduction in the confining stress. The compounding effect causes the ratio of pore-water pressure to total stress in soil, $\mathrm{r_u} = \mathrm{u}/\sigma$, to increase and reaches upon unity around t = 114 min near the toe (see PPT3 & EPT10 in Figure 5.12c) at $100g$. The $\mathrm{r_u}$ is a useful indicator on the changes of effective stress, as Take & Beddoe (2014) argued that a

r_u approaching unity indicates little to no effective confining stress acting on the soil, and thus suggests liquefaction.

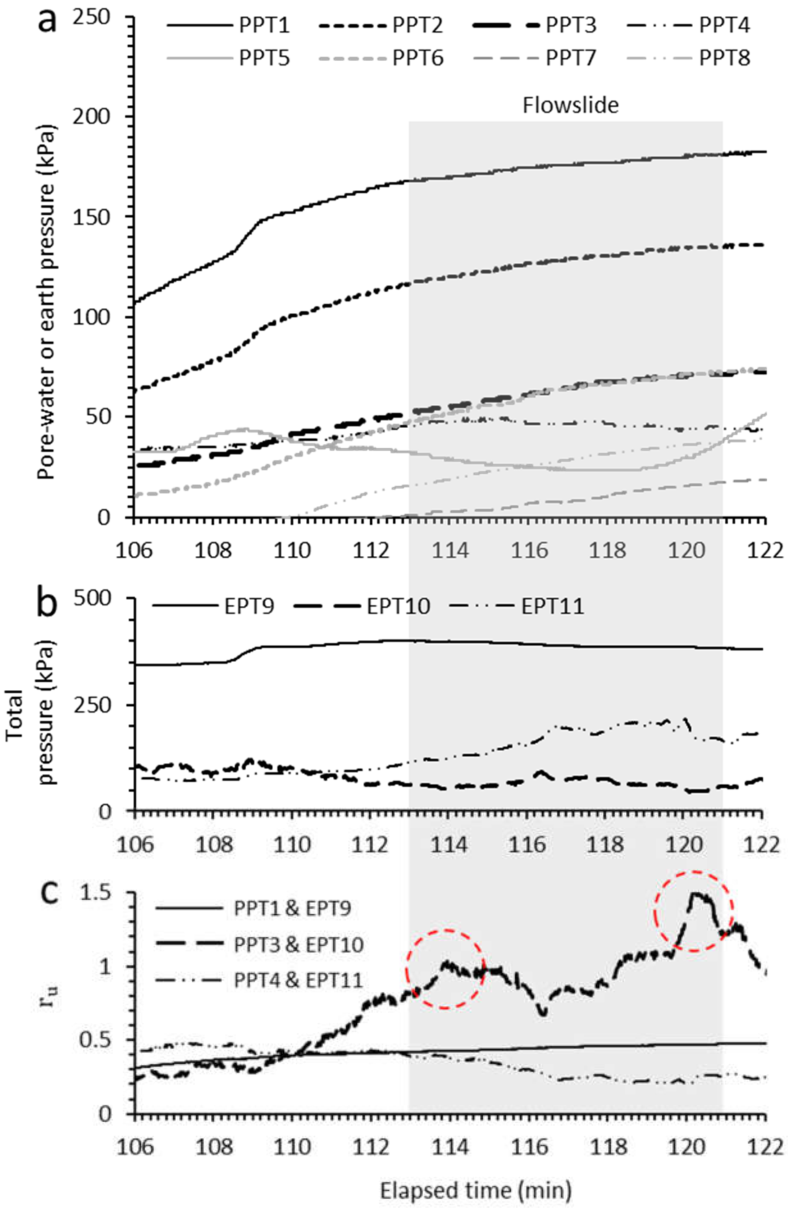

Figure 5.12 – Results of the model slope response during the test (reading at each second): (a) pore-water pressure responses; (b) total pressure responses; (c) r_u responses.

The r_u ratios are calculated for the three paired PPT and EPT locations. The r_u value in the back of the slope (PPT1 & EPT9) remains nearly constant with slight increase, and it is not sufficient to trigger liquefaction ($r_u < 0.5$). In contrast, the r_u value calculated near the toe suggests that the soil has liquefied at t = 113.834 min, and it appears to be followed by another liquefaction event at t = 118.276 min. Figure 5.13 compares the sequential slope profiles for these two apparent liquefaction events at the peak r_u values, in which elevation in phreatic surface is accompanied by pronounced slope movement, exhibiting flow-like motions with reducing inclination of the slope as well as the buried depth of transducers based on their original locations. The surface deformation (cam #1) also shows a more visible retrogressive failure behind the crown of the previous slide.

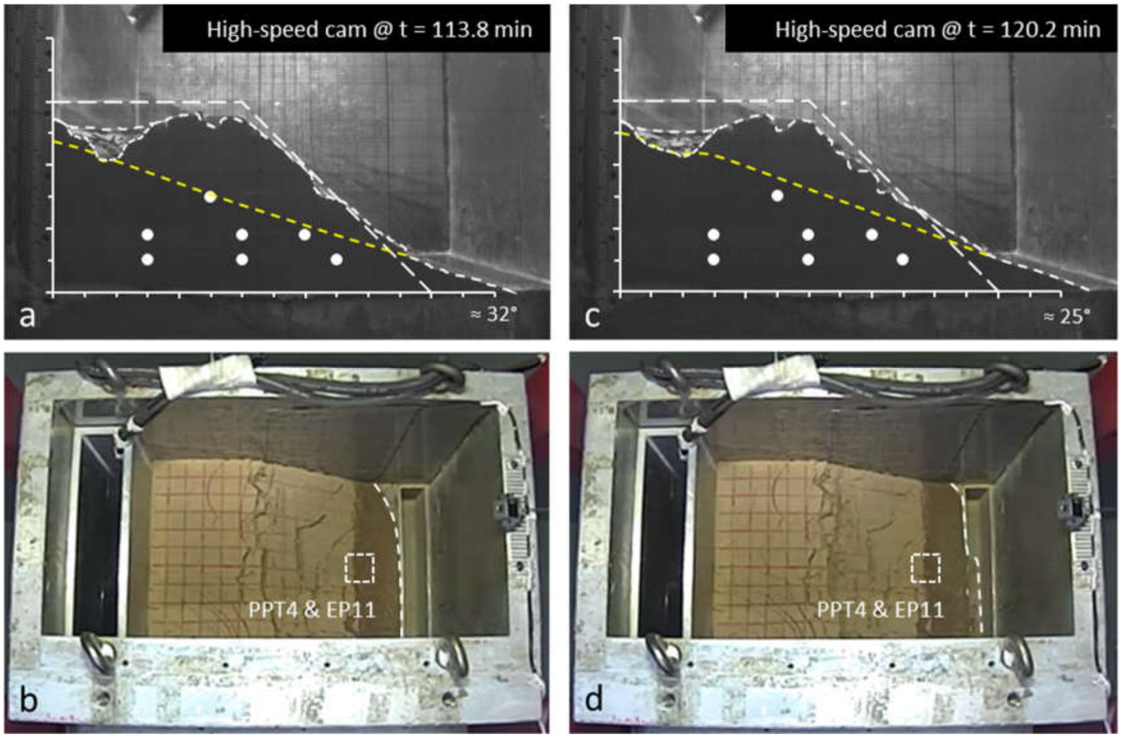

Figure 5.13 – Flow failure: (a) slope profile at t = 113.8 min during first liquefaction and (b) corresponding surface deformation; (c) slope profile at t = 120.2 min during second liquefaction and (d) corresponding surface deformation.

It is perplexing that no spikes in PWPs were found at the time windows correspond to the liquefaction events. This indicates that these apparent liquefaction events may not be entirely caused by shear-induced excess PWP; but also related to the lack of dissipation of excess PWP under the sudden removal of confining stress in the soil due to localized slope failures. During such an event in the field, the shear resistance of the soil can temporarily decrease below the shear stress acting upon the slope, leading to runaway acceleration and rapid development of large strains required for maintaining equilibrium.

5.4 Concluding remarks

A centrifuge test was conducted on an intact HFT slope specimen of the same dimension as the reconstituted specimen discussed here; however considerable difficulties emerged from testing a large intact block specimen, as a fracture was developed during the model preparation process. This produced a preferential channel in the model slope that attracted the water inflow, and resulted in a predominating erosion effect during the test.

The slope deformation process and the evolution of failure of reconstituted loess in this study indicate that a perturbation in groundwater level in loess slope, while the soil is under shearing, can cause a catastrophic impact to the slope stability. A rate of arrival of seepage water exceeding the rate of drainage near the toe serves as the key hydraulic boundary condition to generate seepage impediment at the slope base with a self-reduced inclination changes, and eventually liquefaction under monotonic loading.

The failure process in this study starts with an initial slow-moving slip movement with an increasing phreatic surface that reduces the inclination from 45° to about 35°, which falls within the range of 13°-36° for slope inclination that is reported to be susceptible to static liquefaction (Jefferies & Been, 2015). Such a change of inclination also constricts flows near the toe, producing a drained-to-undrained transition that is captured by the PWP responses in PPT4 with increasing seepage influx. The slip motion is followed by a more flow-like movement that is associated with liquefaction near the toe area. The findings in the centrifuge test are, in essence, resemble the field observation on the loess flowslide in HFT, where the slope base is altered by the displaced material and subsequently delivers the pre-failure conditions that are critical for liquefaction.

As discussed in CHAPTER 3, ‘true’ liquefaction ($q \approx 0$ & $p' \approx 0$) was not observed in either intact or reconstituted loess under the conventional strain-controlled triaxial tests, which results in ample discussions regarding the validity of static liquefaction as the trigger for flowslides in loess. A more popular view on static liquefaction in loess is originated from the ‘brittle collapse’ concept associated with the metastable and the reduction of pore space in the intact loess; however such an argument provides limited applicability to static liquefaction that occurred in uncemented materials. Jefferies & Been (2015) has shown an immediate strength drop upon switching from drained to undrained loading for a silty sand, which indicates that instability is not caused by the metastable collapse of soil fabric but by the change of drainage conditions.

Unlike the proposed failure mechanism discussed in Figure 5.5, the centrifuge test results emphasize the compounding effects of an increasing PWP and a reducing confining stress caused by previous failures on the development of excess PWP, which is often not recognized in the forensic-style field investigations. This remark is of significant value to understanding the relationship between static liquefaction and flowslide in loess. Also the intact loess may be more susceptible to liquefaction should it be used in the centrifuge test, and thus the current observation is based on the external conditions that are arguably less favorable to a liquefaction phenomenon.

CHAPTER 6. POST-EARTHQUAKE RECONSTRUCTION AND RESILIENCE QUANTIFICATION

This chapter reviews the seismic impacts and the reconstruction processes of Yingxiu town and old Beichuan town between 2008 and 2014. A pilot study is presented on characterizing the disaster resilience recovery curve by using Bayesian-based statistical learning approaches.

6.1 Introduction

The 2008 Wenchuan earthquake originated along the Longmen Mountain Fault zone with a length of 300-500 km and a width of 50 km between the Sichuan Basin and the eastern margin of the Tibetan Plateau (Huang & Li, 2009). The regional geomorphology is characterized by drastic transient landscapes with an average 3500-5500 m elevation changes within 50 km (Fu *et al.*, 2011). The steep margin of the Sichuan Basin slope gently towards the Tibetan Plateau while dissected by the tributaries of the Yangtze River, which resulted in one of the most mountainous regions for human settlements in China. The epicenter was in the south of Yingxiu, with YBF passes the downtown area extending NE to the old Beichuan town (Figure 2.3).

A total of 51 counties and cities was classified as ‘extremely-severely damaged’ or ‘severely damaged’, which shaped the area of reconstruction according to the State Overall Plan for Post Wenchuan Earthquake Restoration and Reconstruction (the Overall Plan) (National Development and Reform Commission, 2008). The direct loss was estimated at 100-150 million USD (Chen & Booth, 2011; Zhang *et al.*, 2012), and the seismic impact caused 7,789,100 building structures to collapse and damaged 24,590,000 (Dunford & Li, 2011). The area requires reconstruction is over 132,000 km^2, with floor area of damaged residential buildings exceeding 278 km^2. The damaged infrastructures in the reconstruction area include roadways (> 34,000 km), transmission lines (> 61,500 km) and substations (250), schools (> 7,400), and hospitals (> 11,000) (National Development and Reform Commission, 2008).

The post-earthquake reconstruction typically involves the on-site and reallocated reconstruction. The on-site reconstruction denotes the rebuilding and recovery of the original settlement, i.e. ‘stay and rebuild’, which are commonly adopted after an extreme event (Steinberg, 2007; Gotham & Greenberg, 2008; Yi & Yang, 2014). The reallocated reconstruction refers to the relocation of inhabitants to safer settlements, i.e. ‘relocate and build new’, which potentially improves the livelihoods (Iuchi, 2014). Two timeframes are associated with the post-earthquake reconstruction, as described by Schwab *et al*. (Schwab *et al.*, 1998), including: 1) the first timeframe involves a short-term phase immediately after the disruption (‘response and recovery’), and 2) the second timeframe is a long-term process that incorporates the preparation and adaptation for the demands and challenges of similar disruptions in the future.

Resilience is the ability to prepare for and adapt to changing conditions and withstand and recover rapidly from disruptions (Holling, 1973; The White House, 2013). To a general engineering system, resilience offers the ability to survive failures and to recover from calamities (Yodo & Wang, 2016). Within a disaster context, resilience is defined as the ability to adapt to the demands, challenges, and changes encountered during and after a disaster (Paton & Johnston, 2017). This emphasizes that the system needs to adapt to and evolve to deal with the changing circumstances, rather than ‘bounce back’ to their former state (Saunders & Becker, 2015). A large amount of the displaced materials of co-seismic landslides was transformed into the source materials for debris flows; such a type of cascading geohazard has developed into one of the most challenging issues to the post-earthquake reconstruction in the area impacted by the 2008 Wenchuan earthquake (Liu *et al.*, 2017a). Within the context of reconstruction after the Wenchuan earthquake, different modes yielded different outcomes under the cascading impact of geohazards, which affects the recovery and resilience of the community, and thus quantifying recovery processes under the effects of uncertainties becomes a critical component in quantifying resilience.

In this chapter, the long-term cascading impacts on reconstruction are analyzed for Yingxiu town (on-site) and old Beichuan town (reallocation). The quantification of resilience is analyzed, in the context of reconstruction mode and recovery characterization using Bayesian-based statistical learning. This is to explore uncertainties in the recovery process of post-earthquake communities experiencing continuous disruptive events in the attempt to better evaluate their short- and long-term recovery.

6.2 Seismic impacts of the 2008 Wenchuan earthquake

6.2.1 Earthquake damage in Yingxiu town

Yingxiu town (31.0618°N, 103.4926°E) is located in the south of Wenchuan County in the Ngawa Tibetan and Qiang Autonomous Prefecture in Sichuan Province, southwest of China, with a total area of 115.12 km^2 and population of 6,906 (State Census 2007). The town is at the confluence of the Minjiang River and Yuzixi River (a tributary of Minjiang River), as shown in Figure 5.12; no image of the town was found within 5 years before the earthquake. Area development in Yingxiu resulted in expansion with a major change of land use, where most farmlands were used for building and road constructions since 2005. The regional geological setting is divided along the YBF, of which the north is dominated by the Longmen Mountain crystalline basement consists of mainly diorite, quartz diorite and granite rocks and the south part comprises mainly the Sinian sandstone outcrop with Quaternary alluvium (Xu & Huang, 2008). The regional relief is characterized by deeply dissecting stream networks and steep hillslopes.

Figure 6.1 – Yingxiu town before the earthquake (image: ca. 2000; credit: Government of the Ngawa Tibetan and Qiang Autonomous Prefecture).

The ground peak acceleration (PGA) in Yingxiu was ≥ $0.4g$ (He *et al.*, 2010). The downtown area was destroyed by the intense ground motion associated with the YBF. Aerial images were taken within 48 hours after the mainshock, which showed the rubble and ruins of the downtown area and numerous co-seismic landslides (Figure 6.2). Three major highways which passed through Yingxiu town were severely damaged in the earthquake which posed direct impacts on the arrival of aid and rescue workers. The designed earthquake resistance level for roadways was VII on the Mercalli Intensity scale (Jing, 2007).

Figure 6.2 – Post-earthquake aerial image shows the ruins of Yingxiu town (N-facing), including the Yingxiu Primary School (300 m from YBF) and the Xuankou Middle School (500 m from YBF) (image: May 14, 2008; credit: Xinhua News Agency).

More than 80% of the building structures were destroyed or partially damaged as they underwent vertical and horizontal ground displacements during the earthquake. The vertical vibration resulted in a strong compression, whereas the horizontal vibration resulted in strong shearing effects. The building structures were mainly frame or masonry structures built in the 1990s with reinforced concrete confinement and insufficient seismic design (Zhao *et al.*, 2009; He *et al.*, 2010).

The most catastrophic failure of building structures occurred in the Yingxiu Primary School. The buildings collapsed within 20 sec after the main shock and killed more than 50% of the enrolled students (He *et al.*, 2010). The masonry structure was with some reinforced concrete confinement; but inadequate design at the connections between slabs and columns, which was postulated as the main reason for the poor seismic performance (Ye *et al.*, 2008). Negligible evidence of liquefaction was found. Most buildings in the Xuankou Middle School were four-story masonry structures with RC confinement, where X-shaped cracks were observed on the front and rear walls of buildings due to shearing. The clay brick infill walls collapsed due to inadequate design at the connections between the beam and columns (Ma *et al.*, 2011). Similar observations were made during the 1993 Alaska Earthquake and the 1964 Niigata Earthquake (He *et al.*, 2010).

Two debris flows near Yingxiu town were documented without specific locations before the earthquake (China Institute of Geological Environmental Monitoring, 2009). A large number of geohazards was observed after the earthquake, including surface rupture, landslide, debris flow, and quake-lake, mainly along the highways connecting Yingxiu. 15 landslides were reported after the earthquake, with more than 7 debris flows and 14 quake lakes in the area of Yingxiu (China Institute of Geological Environmental Monitoring, 2009; Cheng *et al.*, 2010). The first debris flow was reported on the Yingxiu-Wolong highway (S303-YW) about 18 hrs after the earthquake (Cheng *et al.*, 2010). Some smallscales debris flows were not included, as they were confined within gullies without posing direct impact to the surrounding areas.

6.2.2 Earthquake damage in old Beichuan town

The pre-/post-earthquake comparison of old Beichuan town is illustrated in Figure 6.3. The old Beichuan town was the county seat of the Beichuan County; the town was combined with Qushan town and a newly developed area that forms the old and new part of the town separated by the Jianjing River. The town is surrounded by hillslopes, as the relief was characterized by the transitional zone between the eastern margin of the Tibetan Plateau and the Sichuan Basin (Wang, 2009; Zhang *et al.*, 2009).

A diverse geological setting can be found in the outcrops, as a result of the YBF that passes through the downtown area. The hanging wall of YBF contains Silurian slate and phyllite, and Cambrian sandstone and siltstone; the footwall contains mainly Carboniferous limestone and shale and Devonian limestone and dolomite (China Institute of Geological Environmental Monitoring, 2009; Wang, 2009; Tang *et al.*, 2011b). The town is located in a subtropical humid monsoon climate zone with an average annual precipitation is about 1400 mm, of which 83% concentrates between June and September (Tang *et al.*, 2009).

The old Beichuan town is located about 90 km NE of the epicenter. The population of the town was less than 20,000 and the death toll was estimated at around 5,500 (Shen *et al.*, 2009), with the maximum PGA reached 0.4-0.5g (Zhang *et al.*, 2009). The average co-seismic vertical surface offset was estimated as 3-4 m, where the maximum vertical offset and dextral displacement were 6.5±0.5 m and 2.5 m, respectively (Xu *et al.*, 2009c). The most catastrophic failure of buildings was caused by two large-scale co-seismic landslides, i.e. the Wangjiayan landslide and the New Beichuan Middle School landslide (Figure 6.4); they were responsible for more than 2,000 deaths (Huang & Li, 2009).

Figure 6.3 – The pre-/post-earthquake old Beichuan town (N-facing): (a) pre-earthquake image (ca. 2007); (b) post-earthquake image (image: August 3, 2008) (China Institute of Geological Environmental Monitoring, 2009).

The seismic design requirements were based on the Design Code GB50011-2001 (Ministry of Construction of China, 2001), with earthquake resistance level of VII on the scale of the Mercalli Intensity (Gao *et al.*, 2009; Zhang *et al.*, 2009). However, the seismic design for most buildings in old Beichuan town was inefficient and a number of buildings were constructed in the absence of any seismic design considerations (Li *et al.*, 2008a; Zhang *et al.*, 2009; Wang *et al.*, 2010; Xu & Liu, 2012).

Figure 6.4 – Post-earthquake aerial image showing the ruins of the old Beichuan town (S-facing) (image: May 27, 2008; credit: Xinhua News Agency).

Most collapsed buildings were located near the YBF; however the failure mode still depended on location of the structure (Figure 6.5). Three typical building types were found, including the RC frame structures (for commercial), masonry structures (for residential), and masonry building with frame structure on the ground floor (combined) (Gao *et al.*, 2009). The seismic impact caused more than 90% of the buildings to collapse (Wang *et al.*, 2010), of which 80% of RC frame structures were destroyed and 60% of masonry structures with inadequate seismic design were destroyed (Expert Group of Science and Technology in Disaster Relief, 2008).

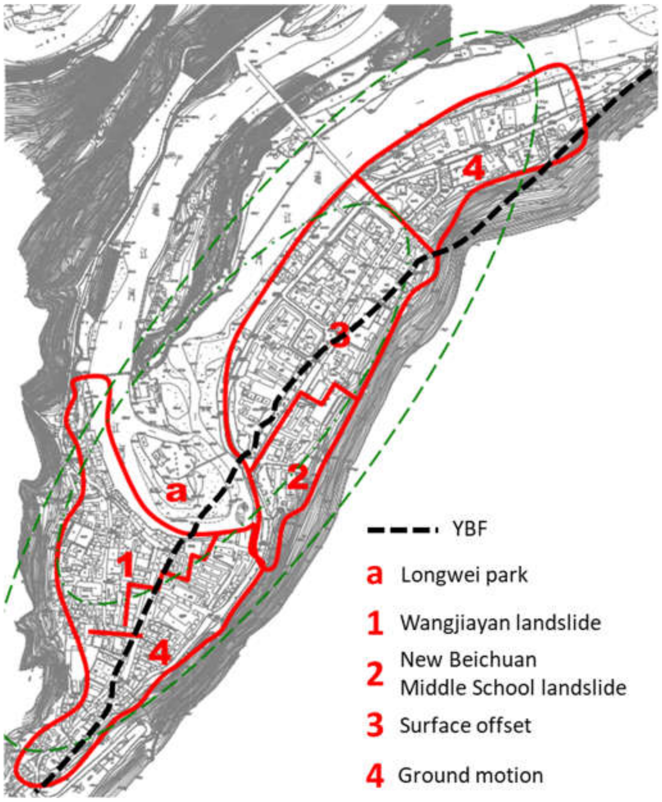

Figure 6.5 – Failure zoning for buildings in the Old Beichuan town, with liquefaction and large ground deformation reported in the Longwei park (after Zhang *et al.*, 2009).

About 75 landslides were reported in the Beichuan County prior to the earthquake (China Institute of Geological Environmental Monitoring, 2009); no report was found for old Beichuan town. The Wangjiayan landslide is located on the hanging wall of the YBF, subject to more violent ground motion (Figure 2.4) and was the most catastrophic co-seismic landslide during the Wenchuan earthquake in terms of impacts on both lives and properties. The landslide had an estimated volume of 7.4 million m^3 and a height of 320 m, with displaced material mainly composed of Cambrian sandstone and siltstone (Xu *et al.*, 2009b; Tang *et al.*, 2011b). The landslide buried more than 1,700 people and destroy about 100 buildings, including the hospital, kindergarten and the elementary school (Xu *et al.*, 2009b; Huang, 2011a; Tang *et al.*, 2011b).

The New Beichuan Middle School landslide was a catastrophic co-seismic landslide that buried more than 700 students in the New Beichuan Middle School (Huang & Li, 2009). The landslide is located on a pre-existing landslide site; the zone of accumulation overlapped the displaced material from previous failure (Huang, 2011a). The height of the landslide is about 300 m, with an estimated total volume of 50 million m^3 (Huang, 2009b). The displaced material contains mainly limestone rock mass triggered by the strong shaking (Xu *et al.*, 2009b).

On the upstream of Jianjiang River, approximately 6.5 km NW of the old Beichuan town, the Tangjiashan landslide dam (height: 82-124 m) caused more than 100 fatalities and formed the largest quake lake, imposing a threat to nearly 2.5 million people downstream (Fan *et al.*, 2012). The estimated volume of impounded water had approached 3×10^8 m^3 as of June 9, 2008 (Liu *et al.*, 2009; Xu *et al.*, 2009b) due to the rapid inflow during the monsoon season. An artificial spillway was under construction immediately after the earthquake for controlled drainage, and completed on June 10, 2018. Several downstream towns were issued mandatory evacuation orders to mitigate damage.

6.3 Post-earthquake reconstruction and cascading impact

A working plan of reconstruction was approved by the State Council on June 9, 2008, (State Council of China, 2008), known as the *Regulations on Post-Wenchuan Earthquake Rehabilitation and Reconstruction*. The *Regulations* provided guidelines for reconstruction of all towns or villages that were damaged during the earthquake. The *Regulations* devised a partner support program, through which the more developed Dongguan city supported the on-site reconstruction of Yingxiu town and the entire Shandong province supported the reallocation reconstruction of old Beichuan town.

The susceptibility to geohazards played a dominant role in the reconstruction mode selection. The selection criteria for reallocated reconstruction were formulated in light of the *Regulations* (Huang, 2009a): (1) towns/villages located on the fault are required to be relocated due to the exposure to future earthquake and co-seismic geohazards, and (2) towns/villages that are not located on the fault with no evident threats from co-seismic geohazards are not recommended for reallocation.

Yingxiu town and the old Beichuan town are the two most damaged administrative units, with similar living standards and culture characteristics prior to the earthquake (Liu *et al.*, 2017b). The fatalities in the old Beichuan town were largely caused by the co-seismic landslides, and that became the main motivation for reallocated reconstruction, as opposite to the on-site reconstruction for Yingxiu. The on-site reconstruction mode was selected for the majority of damaged communities. Although several other smaller communities were relocated, the relocation scheme of the old Beichuan town was by far the largest effort in China.

6.3.1 *On-site reconstruction of Yingxiu town*

The reconstruction process of Yingxiu is illustrated in Figure 6.6 and Figure 6.7. The on-site reconstruction of Yingxiu town started immediately after the earthquake. The *Regulations* divided the reconstruction into two phases, including a three-year short-term reconstruction (2008-2010) and a ten-year long-term development (2011-2020).

Figure 6.6 – Satellite images showing reconstruction process of Yingxiu: (a) earthquake damage; (b) temporary structures; (c) initial phase; (d) final phase (image courtesy of the Center of Earth Observation and Digital Earth, CAS).

The core of the reconstruction plan is to ensure the safety of people and to enable the sustainable development of Yingxiu town (Government of the Ngawa Tibetan and Qiang Autonomous Prefecture, 2010). The plan was approved on May 8, 2009, contained detailed tasks for the first two years with a total investment of over 300 million USD.

Figure 6.7 – Post-earthquake reconstruction process of Yingxiu town: (a) north and center part (credit: SKLGP); (b) center part (credit: SKLGP); (c) south part.

The perimeter of reconstructed buildings must maintain at least 6 m distance from a hillslope, and the distance between adjacent reconstructed buildings is recommended not to be less than the height of the building. Level II structures (public/commercial) are not permitted within 300 m range of the YBF. Level III structures (residential) are not permitted within 200 m range of the YBF (Government of the Ngawa Tibetan and Qiang Autonomous Prefecture, 2010). The restrictive buffer of the YBF has a total land area of 0.64 km^2, covering mostly the north part of the town; it is used for the construction of the Yingxiu park (Xiao & Li, 2009). Ruins of the Xuankou Middle School and the Yingxiu Primary School are preserved as monuments. A memorial museum for the Wenchuan earthquake was built next to the Wenchuan earthquake cemetery in the south part of the town, where more than 6,000 earthquake victims are buried.

6.3.2 Cascading impacts on Yingxiu town

The intense rainstorms during the monsoon seasons have caused a large number of debris flow events near Yingxiu town and disrupted the inbound/outbound traffic as well as the reconstruction process. Immediately after the earthquake, the heavy rainfall on May 17, 2008 resulted in debris flows that further damaged the earthquake-hit lifelines and caused great delays for rescue work. The heavy rainfall on July 23, 2009 and May 29, 2010 caused debris flows and damaged two major highways, which disrupted traffic for about 20 hours affecting the reconstruction process (Gan *et al.*, 2010).

The rainfall event on August 12-14, 2010 caused severe damage to the reconstruction with flood inundation, which was resulted from the blockage of the Minjiang River due to the debris flows that occurred at the immediate upstream (Figure 6.8). The precipitation reached 163 mm in 2 hours on the morning of Aug 14, 2010; it triggered debris flows around 3:00 AM local time and lasted for about 2 hrs (Xu, 2010). The volume of debris flow from the Hongchun gully was estimated as 7.5×10^5 m^3 (Huang & Li, 2014). The flood level in the north part of Yingxiu town was 2-3.5 m (Figure 6.9); the flood remained in that area for more than 7 days (Tang *et al.*, 2011a). The debris flows caused 13 fatalities with 59 missing and evacuation of more than 8000 people in Yingxiu.

Figure 6.8 – A stitched aerial image of the debris flow occurred on August 12-14, 2010 on the upstream of Yingxiu town (image: August 15, 2010) (after Tang *et al.*, 2012b).

Figure 6.9 – Urban flooding in the reconstructed Yingxiu town during debris flow events on August 12-14, 2010 (image: August 15, 2010; credit: SKLGP).

The heavy rainstorm on July 4, 2011 triggered several landslides and debris flows in the area. Even though Yingxiu town was not directly impacted, debris flows damaged roadways connecting the town to the neighboring regions and affecting the reconstruction process. The rainstorm on Aug 21, 2011 triggered debris flows which disrupted inbound/outbound traffic to Yingxiu, with communications cut-off due to flooding of cellular stations.

The heavy rainfall on April 30 and August 18, 2012 triggered debris flows and again disrupted traffic. The rainstorm on July 9, 2013 triggered a large number of debris flows in the region of Yingxiu. The debris flow in Niujuan gully resulted in direct impact on the reconstruction on the south end of the town, where the displaced material blocked the Minjiang River and changed the course of the river. The rainfall events on June 29, 2014 triggered debris flows that damaged roadways connecting Yingxiu town to neighboring regions causing major traffic disruptions.

6.3.3 Reallocated reconstruction of the old Beichuan town

This section documents the reallocated reconstruction of the old Beichuan town. As a result of the severe damage caused by large co-seismic landslides, old Beichuan town was relocated about 25 km SE of the earthquake ruins. The decision for relocation is primarily based on the assessment on safety and suitability of inhabitation (Huang, 2009a).

The assessment concluded that the earthquake-hit Old Beichuan was not suitable for on-site reconstruction under the following reasons (Planning Team of Ministry of Housing and Urban-Rural Development of the People’s Republic of China, 2008):

- The Old Beichuan town is segmented by the YBF, with almost half of the town located on the hanging wall. The reactivation of the YBF imposed future threats in terms of both seismic motions and co-seismic landslides.
- The Old Beichuan town was located in a high geohazard susceptible zone with various types of geohazards reported every year in that area prior to the earthquake. The co-seismic landslide deposits provide high sediment influx, resulting in high debris flow susceptibility in the area (Li & Huang, 2008). The cascading effect of geohazards ispredicted to remain above the pre-quake level for at least another 15 years (Huang & Fan, 2013).
- Many buildings in old Beichuan town were constructed on the poorly graded deposits of historic landslides. Liquefaction and severe differential settlements were reported at various locations after the earthquake.
- Within an urban planning and design context, the development of the Old Beichuan town is spatially constrained by the topographical settings.

The estimated cost of reallocation reconstruction was 2.5 billion USD (Planning Team of Ministry of Housing and Urban-Rural Development of the People's Republic of China, 2008). Five public hearings on the reallocation reconstruction were held for the remaining residents of the Old Beichuan town and the immediate stakeholders from the neighboring communities. Public surveys have shown more than 95% of the residents agreeing with the decision (Sun *et al.*, 2011). The reconstruction is divided into two phases; Phase I is the recovery of the Old Beichuan town by preserving and transforming the ruins into a field-scale memorial museum and research base for seismic impacts (May 22, 2008 to June 2009) and Phase II is the reallocation reconstruction of the new Beichuan town

(May 12, 2009 to January 2011). The site selection for the relocation is a systemic challenge that needs to integrate considerations on seismic zoning, geohazard susceptibility zoning, economic development, sustainability, and societal impacts (Li & Huang, 2008). Various factors were suggested by different researchers for the selection of the site (Chen *et al.*, 2008; Li & Huang, 2008; Mao *et al.*, 2008; Huang, 2009a; Xiang *et al.*, 2010), of which the most considered factors are succinctly summarized as:

- Beichuan County is the only Qiang Autonomous County in China; the ethnic Qiang residents accounts for about 1/4 of the entire Qiang population, and hence the preservation of the traditional mountain people culture of the ethnic group is essential to reconstruction.
- Safety is vital to the final selection. The new site should be situated away from faults and within low geohazard susceptible zone with mild to moderate topographic relief.
- The area of new site needs to be greater than 3 km^2, with basic infrastructure facilities in place and some extra 1-2 km^2 for future development.
- The new site should be located close to the old Beichuan town to minimize societal impact and to avoid changes in the administrative divisions in the Sichuan Province.

Four sites were considered for relocation, including the Leigu town, Yongan town, Sangzao town, and Kaimao-Shunyi village (Figure 6.10). The key characteristics are listed as follows:

- Leigu is located 6 km south of the Old Beichuan town and 1 km away from the YBF. The town is situated on the alluvial basin of the Laochangkou River, and the heights of surrounding hillslopes range 700-910 m (Chen *et al.*, 2008; Zhang *et al.*, 2008)

- Yongan is located 16 km south of the Old Beichuan town near the foreland of the Longmen Mountain. The town is situated between the YBF and PF on the alluvial basin of the Laochangkou River; it is environed by steep hillslope on the south and mild slopes on the east and west (Chen *et al.*, 2008).
- Sangzao is located about 30 km south of the Old Beichuan town and about 2 km south of the PF. The height of the surrounding slopes ranges 20-820 m.
- Kaimao-Shunyi site includes the villages of Kaimao and Shunyi that were within the administrative unit of Anchang; it is about 7 km SE of the Anchang town and 5 km away from the PF (Li & Huang, 2008).

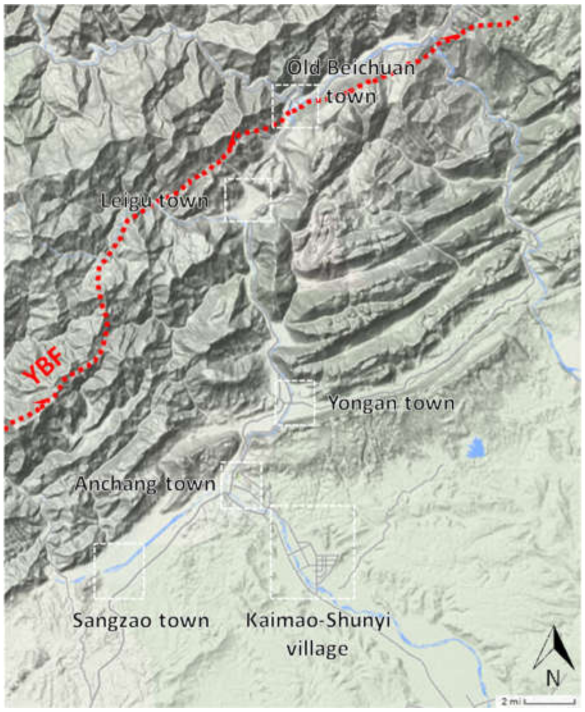

Figure 6.10 – Terrain map of the candidate sites for the reallocated reconstruction of the old Beichuan town (Google Earth image).

The Kaimao-Shunyi village is the final site recommended for the reallocation of the old Beichuan Town, and it was approved by the State Council on February 1, 2009 (China

Academy of Urban Planing and Design, 2008). The new site is located on the confluence of the Anchang River and Laochangkou River with low variance in the local topographic reliefs. The bedrock of this area is stable without known faults. Local lithology contains mainly brown/yellow siltstone and mudstone with mild angle of dip (∠15°~25°) (Li & Huang, 2008). The relocated old Beichuan town incorporates the Anchang town and the Kaimao-Shunyi site, and it serves as the new county seat of Beichuan County; the new town is named as Yongchang.

Figure 6.11 illustrates the land use plan in Yongchang town; the matrix shows the five key categories incorporated in the plan (China Academy of Urban Planing and Design, 2008). The designed seismic resistance of the buildings and lifelines is VIII (Mercalli Intensity scale) and the PGA is $0.2g$, in accordance to the updated Design Code GB50011-2010 (Ministry of Construction of China, 2010). The reconstruction started on May 12, 2009. The area used for reconstruction is about 3 km^2 as of the end of 2010. The relocated residents are more than 40,000 in 2010 and was anticipated to increase to about 70,000 by the end of 2020. More than 11,000 apartments were constructed by the end of 2010. The living conditions are greatly improved in Yongchang town as compared to the old Beichuan town (Liu *et al.*, 2017b). Dunford & Li (2011) discussed the poverty alleviation goal that is featured strongly in the Overall Plan, which attempted to address the poverty issues through resettlement of the rural population. Reflecting that particular consideration, an industrial park was constructed in Yongchang town for short-term employment and long-term economic development. The industrial park occupies nearly 1/3 of the reconstructed area with 28 companies and factories resettled or established by the end of 2011.

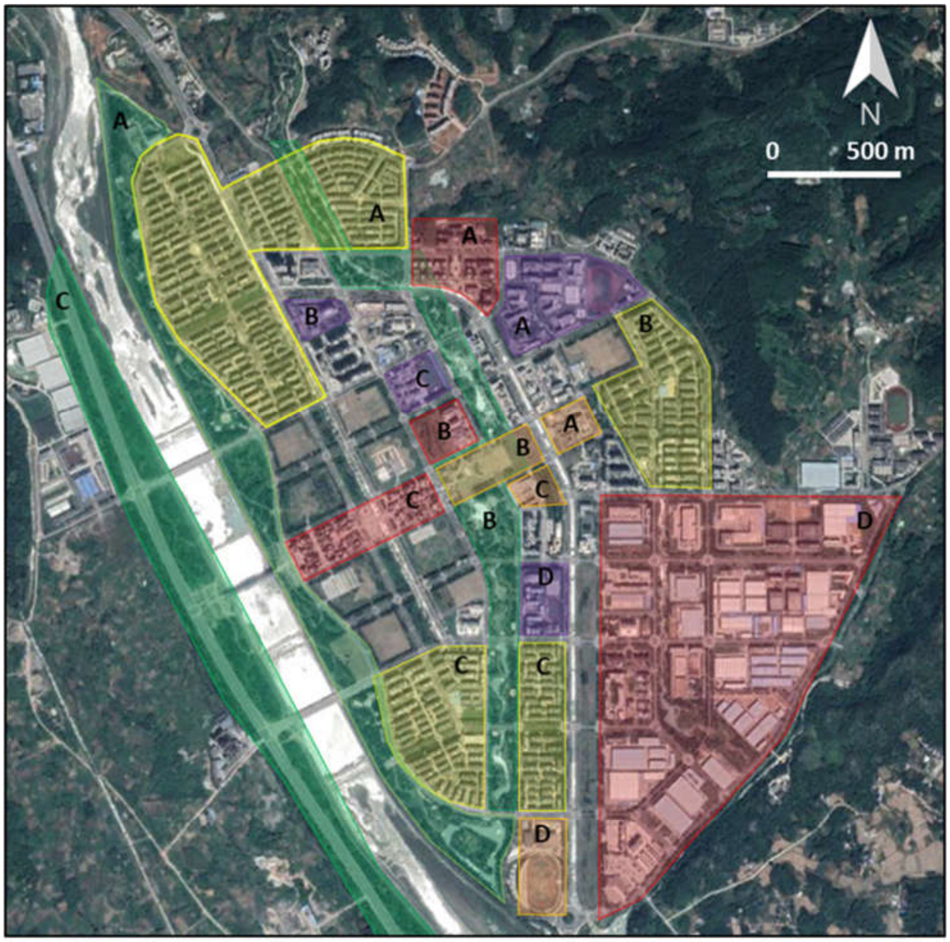

	Business/Public Service	Museums/ Arts Center/Stadium	Residential Areas	Scenic Drive/Byways	Schools/ Hospitals
A	County Hall	Culture Center	Wenquan	Anchang River Scenic Byway	Beichuan Middle School
B	New Beichuan Grand Hotel	Wenchuan Earthquake Museum	Baiyangping	Yongchang River Scenic Byway	Central Hospital
C	Shopping Walkways	Performing Arts Center	Hongqi	Anbei Scenic Drive	No.1 Yongchang Elementary School
D	Shandong Industrial Zone	Stadium			No.2 Yongchang Elementary School

Figure 6.11 – Map of the Yongchang town showing the land use plan superimposed on the satellite image od the town (Google Earth image: September 9, 2016).

6.3.4 Cascading impacts on old Beichuan town

The post-earthquake debris flows are discussed in detail in CHAPTER 7 within the context of debris flow mitigation systems. This section summarizes the impacts of debris flows on the old Beichuan town between 2008 and 2014.

The rain gauge data at the Tangjiashan landslide (6.5 km NW of the old Beichuan town) shows a cumulative precipitation of 173 mm on September 23, and 57.9 mm between 0:00 and 5:00 am and 41 mm between 5:00 and 6:00 am on September 24, 2008 (Tang *et al.*, 2011b). Since a large amount of loose and unsorted displaced materials were deposited in gullies by the co-seismic landslides during the Wenchuan earthquake, they transform into the source materials for debris flows due to the saturation during intense rainfall. A total of 1041 landslides or debris flows was reported on September 23-24, and 169 co-seismic landslides were re-activated in the region of the old Beichuan town; the rainfall-induced geohazards caused 42 fatalities in the region and caused severe damage to the Beichuan County (Tang & Liang, 2008; Tang *et al.*, 2009; Huang & Li, 2014).

The rainstorm on September 23-24 triggered a debris flow by mobilizing the loose deposits of the Wangjiayan landslide (see Section 6.2.2), which caused further damage to the earthquake-hit town. A large-scale debris flow was also triggered in Weijia gully near the south end of the town and deposited more than 340,000 m^3 debris with a length of 900 m, a width of 150-200 m, and a thickness of 5-10 m, as shown in Figure 6.12 (Tang & Liang, 2008; Zhang *et al.*, 2014a). These two debris flows buried about 60% of the ruins and disrupted the preservation work of the ruins of old Beichuan town as part of the Beichuan Earthquake Museum. The debris flows reached the Jianjiang river and increased the riverbed elevation. The debris also changed the course of the river.

The cumulative precipitation in the old Beichuan town reached 275.7 mm on July 15-17, 2009, and the average precipitation was greater than 270 mm in Beichuan County (Huang, 2011b). The rainfall induced landslides and debris flows damaged the roadways, including five bridges that interconnected more than 12 towns in the county.

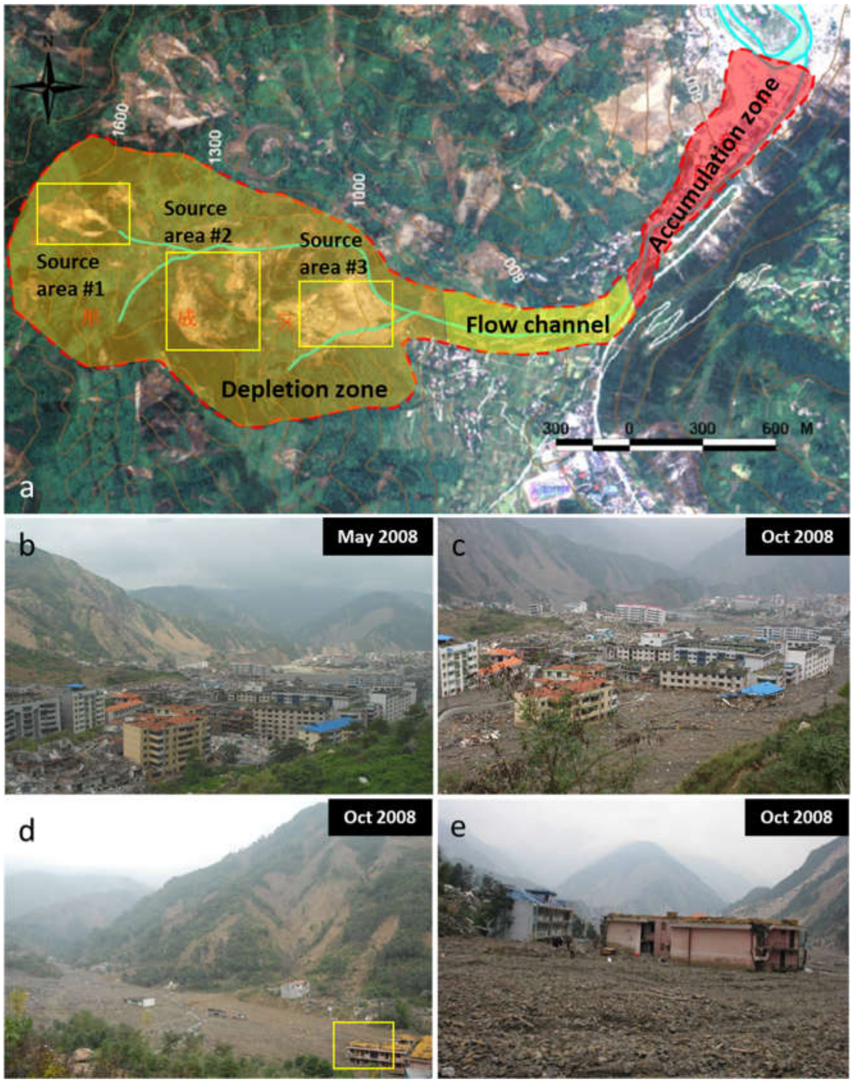

Figure 6.12 – Impact of the debris flows on September 24, 2008 on the old Beichuan town: (a) debris flow occurred in the Weijia gully; (b) seismic impact after the earthquake; (c) buired buildings after the debris flow; (d) exit of the Weijia gully and debris flow deposits; (e) buried earthquake-damaged building with visible top floors.

The cumulative precipitation in old Beichuan town reached 105 mm on August 11, 2010. The strong rainfall event induced several small-scale debris flows in the Weijia gully. A post-earthquake debris flow mitigation system has been implemented at the time, and thus intercepted a large amount of displaced materials and prevented the debris from impacting the preservation work.

The cumulative precipitation in the Tangjiashan Quake Lake reached 251 mm on September 17-18, 2010, followed by an additional 200 mm on September 20-21 (Government of Mianyang City, 2010). The intense rainfall triggered landslides located at the right bank of the quake lake; the volume of displaced material was about 1 million m^3. The landslide blocked the artificial spillway of the quake lake, imposing serious threats to downstream communities. An artificial spillway was re-excavated, with a length of 200 m and a width of 10 m, to avoid dam-breach flood. The old Beichuan town was used as a drainage path so that more than 3,000 workers and infrastructure providers were evacuated.

The heavy rainstorm on August 17, 2011 triggered a number of debris flows in the Shuidongzi Mountain in the south of old Beichuan town. The displaced materials were captured and converged into a debris flow channel near the toe of the slope, and therefore they were diverted from entering the center of old Beichuan Town.

During the heavy rainstorm on July 23, 2012, the water level of Jianjiang River was increased significantly and eventually overtopped the embankment. More than 440 people were evacuated, and the ruins were flooded with the maximum water level of 0.5 m. A number of debris flows were triggered; but no damage was reported for old Beichuan town.

The extreme rainstorm on July 8-9, 2013 inundated 80% of the town, especially the ruins near the river embankment. The cumulative daily precipitation reached 285 mm, which increased the water level of the Tangjiashan Quake Lake by 8 m, which resulted in a peak flood discharge of 5000 m^3/s into the Jianjiang River and flooded old Beichuan town (Figure 6.13). The flooding event caused 1 death and 15 missing. Fan *et al*. (2015) argued that such an extreme rainfall that occurred on July 8-9 can be attributed to human-induced air pollution, as aerosols suppress convection during daytime and allows excess moist air to be transported to the mountainous area during night time, and thus causes heavy rainfall.

Figure 6.13 – Flooded old Beichuan town after the intense rainfall on July 8-9, 2013 (image courtesy of SKLGP).

6.4 Recovery function quantification

6.4.1 The MCEER framework

Within the context of seismic resilience, Bruneau *et al*. (2003) devised a conceptual and measurement framework for disaster resilience, incorporating three key elements in a resilient system which includes the reduced failure probabilities, reduced losses, and reduced time to recovery. Based on this framework, the Multidisciplinary Center of Earthquake Engineering to Extreme Event (MCEER) employs four dimensions to assess resilience, including rapidity, robustness, redundancy, and resourcefulness. A schematic representation of the framework is shown in Figure 6.14, in which performance loss (i.e. the drop in functionality) and resilience (i.e. the area under the curve between $t_{0\mathrm{E}}$ and T_{LC})

is separated by the functionality curve derived from the loss function and recovery function depending on the system. The system does not necessarily return to the same level of functionality prior to the disruptive event.

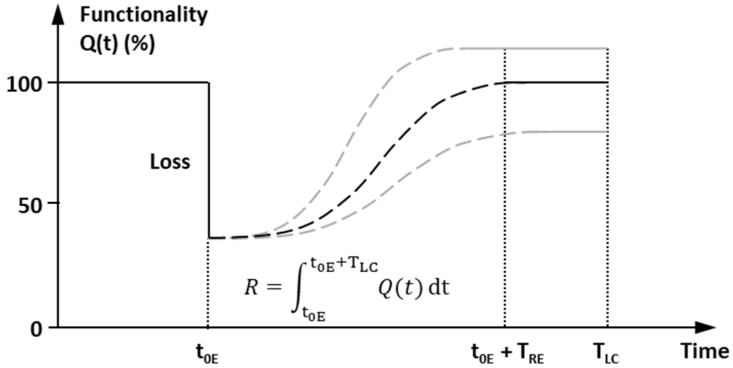

Figure 6.14 – Schematic representation of disaster resilience (after Bruneau *et al.*, 2003).

The *rapidity* is related to the capacity of the system to recover from a disruption (i.e. the average gradient of the recovery curve), and the *robustness* measures the ability to withstand a disruption (Bruneau *et al.*, 2003). The *redundancy* and *resourcefulness* are the interrelated measurements of utilizing principal and alternative resources to permit rapid response to the disruption and facilitate the recovery (Bruneau *et al.*, 2003; Chang & Shinozuka, 2004). The resilience, as a variable, can be expressed as (Bruneau *et al.*, 2003; Tierney & Bruneau, 2007; Cimellaro *et al.*, 2010):

$$R = \int_{t_{0\mathrm{E}}}^{t_{0\mathrm{E}}+T_{\mathrm{LC}}} \frac{Q(t)}{T_{\mathrm{LC}}} dt \tag{21}$$

where R is the value of resilience, $t_{0\mathrm{E}}$ is the time when extreme event E occurs, T_{LC} is the control time for the evaluation of the resilience, and $Q(t)$ is the system functionality as a dimensionless function of time.

In the MCEER framework, the four dimensions are characterized by the loss function and the recovery function. The loss function is typically based on the loss estimation model HAZUS, which is closely related to the community resilience but cannot provide a direct measure of the resilience (Chang & Shinozuka, 2004). The recovery function is system-dependent, as it should reflect the disaster awareness and preparedness as well as resource availability of a community; most common loss models assume everything returns to normal within one year.

6.4.2 Recovery function

In the application of the MCEER framework, Cimellaro *et al.* (2010) listed three common simplified recovery functions as follows:

$$\text{Linear: } f_{\mathrm{REC}}(t) = a(t - t_{0\mathrm{E}})/T_{\mathrm{RE}} + b \tag{22}$$

$$\text{Exponential: } f_{\mathrm{REC}}(t) = a\exp[-b(t - t_{0\mathrm{E}})/T_{\mathrm{RE}}] \tag{23}$$

$$\text{Trigonometric: } f_{\mathrm{REC}}(t) = a/2[1 + \cos(\pi b(t - t_{0\mathrm{E}})/T_{\mathrm{RE}})] \tag{24}$$

where a and b are the constants calculated by using curve fitting to the available dataset, and T_{RE} represents the recovery time needed to return to the pre-earthquake functionality. Notwithstanding the interdependence between the loss function and recovery function for the preparedness and resources of a given community, Cimellaro *et al*. (2010) used these analytical functions to reflect, in general, the recovery processes for different types of communities, as shown in Figure 6.15. A well-prepared community with vast initial inflow of resources followed by rapid recovery is represented by the exponential function. A less-prepared community with limited initial resources and organization depending on external helps to recovery can be represented by the trigonometric function. A linear function is used when no information regarding the preparedness and recourses is known, and hence an average community.

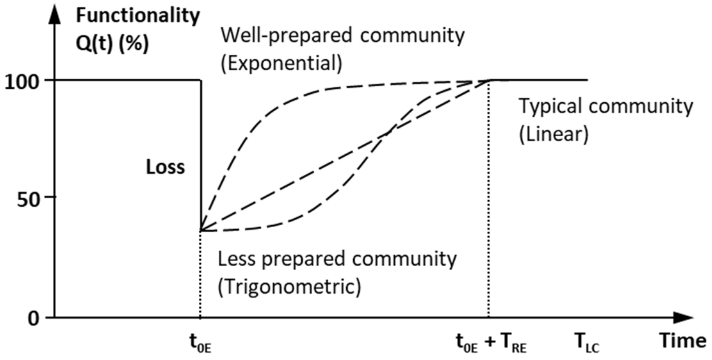

Figure 6.15 – Recovery curves reflecting communities with different level of preparedness and amount of resources under a disruptive event, assuming the community returns to the pre-disaster functionality (after Cimellaro *et al.*, 2010).

Following the same argument made by Cimellaro *et al.* (2010), these three functions can also be used to reflect resilience associated with different reconstruction modes under the impacts of post-earthquake debris flows in the cases of the Wenchuan earthquake. As discussed in Section 6.3, no cascading impacts of geohazards were reported impacting Yongchang town (the relocated old Beichuan town), and thereby the physical reconstruction process was not interrupted by any major form of nature-human disruptive event. On the other hands, the impacts of debris flows have caused substantial damage to the reconstruction, and hence recovery process of Yingxiu town. While the debris flow did not cause direct impact to Yingxiu town for some monsoon seasons, the transportation disruption (see Section 6.3), can accentuate existing social and economic conditions of vulnerability, which leads to a permanent loss in business and forces the transformation of the economic structure of the community. Yingxiu town was considered as a transportation hub and a power substation cluster prior to the earthquake since more than three major hydropower plants are scattered around the town; however the main, and arguably only, post-earthquake economic driver is tourism (Yang *et al.*, 2011). Therefore, the recovery curve of Yingxiu town is considered to be close to the trigonometric function, assuming it returns to the original functionality. A more extreme case of long-term transportation losses was discussed by Chang (2000) for the Port of Kobe.

Notwithstanding the complexity of linking different section, domains, and processes in recovery, as discussed by Miles & Chang (2006), these three simplified models pose 1) limitations on characterizing the complex recovery process due to analytical constraints, and 2) restrictions on predictive capacity on the recovery function with newly available data feed even though the constants can be continuously updated. Miles & Chang (2006) proposed a more complex object-oriented model for recovery estimation using carefully defined attributes and relations; however such a function model cannot fully incorporate uncertainties into the recovery estimation.

6.4.3 Uncertainty characterization for recovery curve

The work in this section is not to devise a new conceptual framework for modelling recovery process; it aims to perform a pilot study on combining Bayesian model and Neural Network, i.e. Bayesian Neural Networks (BNN) to enable uncertainty characterization when predicting the recovery curve with a measured dataset, which is particularly important at the early stage of the recovery process. Such an uncertainty approach can provide an important upgrade to the overall ability of the MCEER framework (Cimellaro *et al.*, 2010). The selection of attributes for datasets for recovery modeling is discussed in detail by Miles & Chang (2006) and outside the scope of this work.

A BNN combines a probabilistic model and neural networks as a universal function approximator (Bishop, 2006). Differ from the classical Artificial Neural Networks (ANN) in which the weight is a constant value, BNN uses a prior distribution, $p(\theta)$ to describe the weights so that the neural network computes the likelihood, $p(x|\theta)$ by comparing with the training data (Blundell *et al.*, 2015), and in turn approximates the posterior distribution, $p(\theta|x)$ through variational inference. The variational inference parameterizes $q(\theta)$ by $\boldsymbol{v}$ to approximate $p(\theta|x)$ through minimization of the Kullback-Leibler (KL) divergence that measures the distance between two distributions and can be expressed as:

$$KL(q||p) = \mathbb{E}_q\left[\log\frac{q(\theta;\boldsymbol{v})}{p(\theta|x)}\right] \tag{25}$$

The BNN is applied here in the attempt to predict the recovery curves of the towns of Yingxiu and Yongchang. The pilot study assumes the loss of functionality due to seismic impact is at 50%, and the community returns to the original level of functionality in five years, as the time framework represents an acceptable duration to be considered as long-term reconstruction, as discussed by Schwab *et al.* (1998). However, the time variable in BNN is dimensionless and not necessarily bounded by the five year constraint.

Synthetic dataset for recovery processes are generated using the discussed analytical functions with random errors, i.e. trigonometric (for Yingxiu town) and exponential (for Yongchang town), which is divided into training and test datasets. The random errors are set to be larger at the beginning of the recovery and diminishing as recovery continues. This reflects the uncertainties that a community may encounter at the earlier stage of reconstruction in the real world scenario. The BNN contains two layers with one single neutron in each layer, which is sufficient for the variables in this one attribute dataset;

however the structure of the BNN has the upscaling potential for multi-dimensional dataset. The implementation starts by assuming a standard normal distribution for the prior $p(\theta)$ and uses the automatic differentiation variational inference (ADVI) to derive an efficient variational inference algorithm to approximate the posterior distribution in light of the training data (Kucukelbir *et al.*, 2017). Sampling θ, and thus weights, yields a collection of neural networks and permits post-processing of the results.

Figure 6.16 illustrates the results for the hypothetic recovery curve of Yingxiu town. The accuracy of BNN prediction increases dramatically with the increase of training data, especially at the early stage. This indicates an improved accuracy of prediction on recovery processes, which is reflected by the best estimate (i.e. mean) and the confidence interval, as more data is measured with time. The results emphasize the importance of data at the early stage to reveal a clear trend, as shown in the difference between Figure 6.16a and Figure 6.16b.

Figure 6.17 shows the results for the hypothetic recovery curve of Yongchang town. The BNN quickly identifies the exponential trend embedded in the synthetic dataset and responds with a reasonable best estimate even with a limited amount of training data at the beginning of the recovery process. Such a performance reveals the importance of founding a clear trend in BNN with the training data, which confirms the merits of applying BNN in predicting the recovery curve as the model can constantly update itself with newly available dataset. The comparison of the results also illustrates the differences in the postulated recovery processes between on-site and reallocation reconstruction, especially under the continual cascading impact of geohazards.

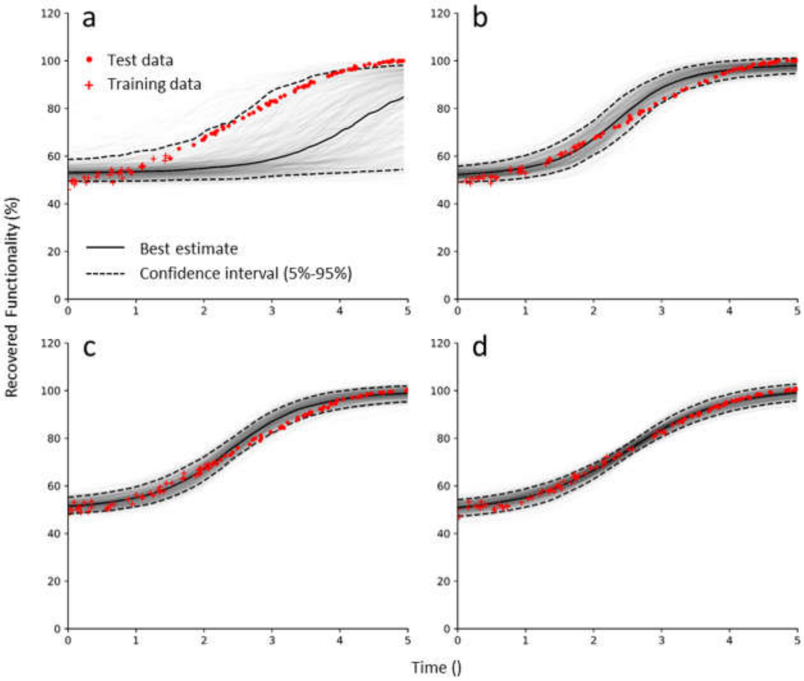

Figure 6.16 – BNN prediction on the hypothetic recovery curve of Yingxiu town, with different percentage of training data in the dataset: (a) 30%; (b) 40%; (c) 50% (d) 60%.

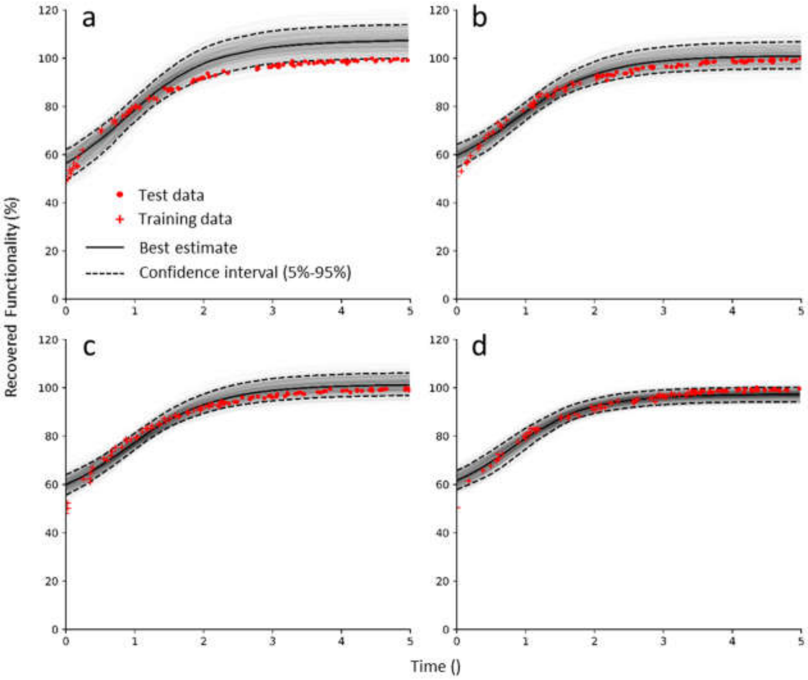

Figure 6.17 – BNN prediction on the hypothetic recovery curve of Yongchang town, with different percentage of training data in the dataset: (a) 30%; (b) 40%; (c) 50% (d) 60%.

Figure 6.18 compares the effects of random errors on the overall effectiveness of the BNN with 40% training data. The results indicate that a small perturbation in the dataset can potentially disguise the trend of the recovery when the training dataset is scarce and cause the prediction to misfit. Such an observation is particularly true in the case of a trigonometric function, or others with similar sharp change in gradient. However, a sudden drop in the functionality may not occur, as adverse impacts on recovery curve are likely to be reflected by the slope gradient of the curve if sufficient number of dimensions are being considered.

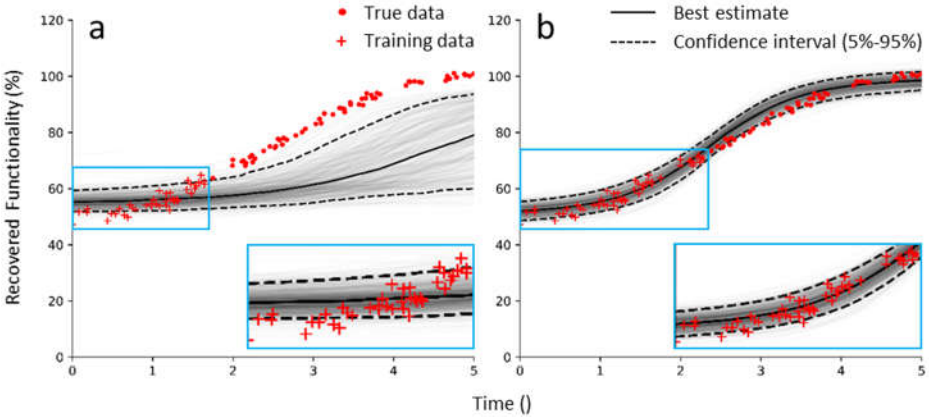

Figure 6.18 – Effects of random error on BNN results: (a) large errors; (b) small errors.

6.5 Concluding remarks

The post-earthquake reconstructions for the counties of Wenchuan and Beichuan are the examples of the top-down approach that is intended to promptly deliver assistance to the impacted communities for rapid recovery (Liu *et al.*, 2014). While discussion on the long-term recovery of economic development and social reconstruction is outside the scope of this work, the recovery process can be swift, in terms of physical reconstruction, under such a political structure (Xin, 2012).

The plan and execution of this reconstruction mode provides an example of a resilient management response to the community recovery process after a mega-earthquake event. If the decision of on-site reconstruction had not been made, the residents of the old Beichuan and many surrounding smaller communities would have been required to choose either to 'stay and rebuild' at the original settlement or to 'immigrate' to other existing communities; both options require them to rely on their own resources and measures to adapt and to recover. The 'immigrate' option for such a large population can cause immediate societal impacts on the destination communities. While the 'stay and rebuild' option may appear to be less of an impact to the community in the short term, it would not be proven to be a resilient and/or sustainable response as discussed in Section 6.3.4.

The pilot study on predicting the recovery curve with uncertainty characterization using BNN provides a useful probabilistic model for resilience quantification. The key improvement is that the recovery curve is no longer subject to a hard constraint by fitting an analytical function to the measured data. However, the synthetic dataset are generated from relatively simple recovery functions that may not be sufficient to represent the complex recovery process. The effectiveness of the proposed BNN approach requires further investigation, especially on the multi-dimensional dataset with different functions of time being considered in the neural network. Additionally, the time resolution of different attributes is not considered in the pilot study.

CHAPTER 7. DESIGN AND PERFORMANCE OF POST-EARTHQUAKE DEBRIS FLOW MITIGATION SYSTEMS

This chapter documents the design of a novel multi-functional debris flow mitigation system in the Wenjia gully after the 2008 Wenchuan earthquake, with the objectives of analyzing the changes of the rainfall thresholds caused by the earthquake and evaluating the site-scale performance of mitigation systems of various gullies in different watersheds, including the regions of Qingping, Yingxiu, and Dujiangyan.

7.1 Introduction

The co-seismic landslides during the 2008 Wenchuan earthquake and the subsequent debris flows represent a post-earthquake instability process (Huang & Fan, 2013; Zhang *et al.*, 2014a). Debris flow poses significant risks to downstream communities as a large amount of landslide deposits becomes the source material for rainfall-induced debris flows, which can increase the magnitude through progressive entrainment during the movement (Iverson *et al.*, 2011; Cui *et al.*, 2013). As discussed in Section 2.3, a significant increase in debris-flow events is observed after the earthquake due to the increase in sediment flux caused by co-seismic landslides (Huang & Fan, 2013; Guo *et al.*, 2016).

The Study Area II includes the regions of Qingping, Yingxiu, and Dujiangyan (see Figure 7.1); these regions contain more detailed collections of pre-/post-earthquake and pre-/post-mitigation records of rainfall and debris flow events to assess the short- and long-term impacts of earthquake as well as the resultant debris flows. The regions are incised by the waterways of the Mianyuan River (Qingping), the Min River (Yingxiu), and the Longxi

River (Dujiangyan), with a drastic elevation change from about 770 to more than 4000 m. The study area comprises a complex lithological assemblage, which primarily include: 1) shale, sandstone, and limestone in Qingping; 2) granite, limestone, and sandstone in Yingxiu; and 3) granite, sandstone, and mudstone in Dujiangyan. The average annual precipitation in Qingping, Yingxiu and Dujiangyan are 1086, 1253, and 1135 mm, respectively. Rainfall concentrates in the monsoon season from June to August, with 60%-80% of the annual precipitation.

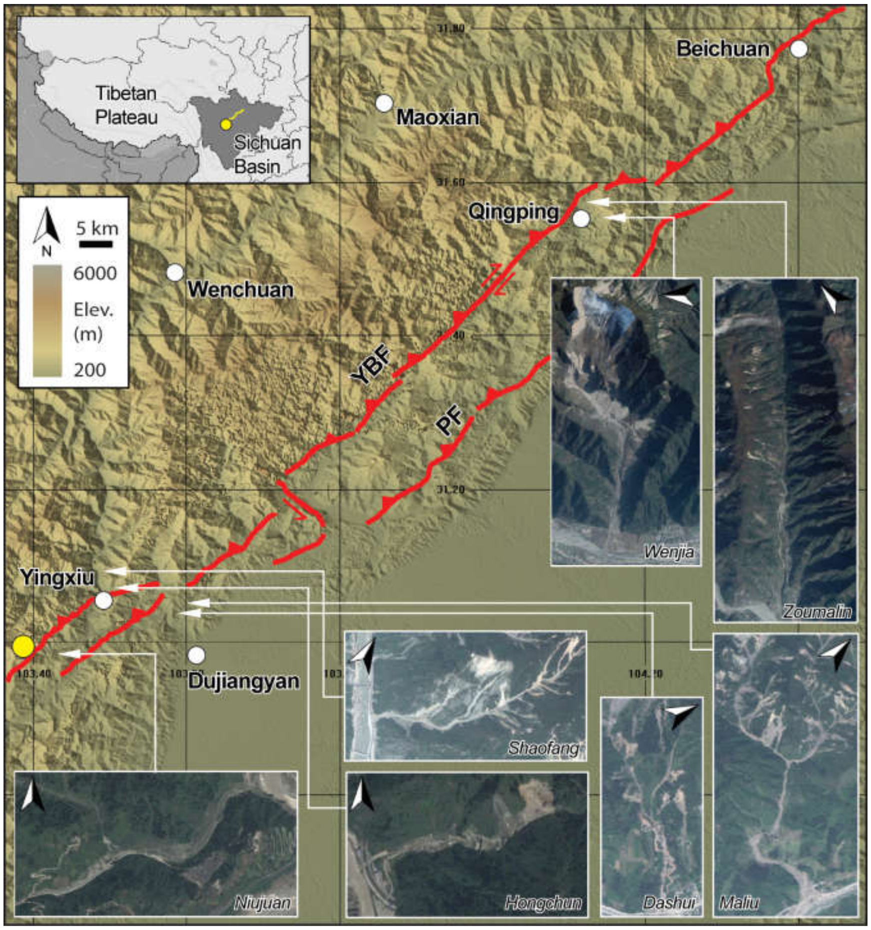

Figure 7.1 – Tectonic and geomorphic settings of the study area (ASTER image). Satellite images of catchment areas and examples of debris flow gullies in the study area are included (Google Earth image). The epicenter and the main ruptures of the earthquake are highlighted (see more details in Section 2.3.1).

There are limited information on the geohazards in the study area before the earthquake; only two debris flows near Yingxiu town were reported without specific locations (China Institute of Geological Environmental Monitoring, 2009). Debris flow events were observed immediately after the earthquake; for example debris flows occurred along the S303-YW highway segment 18 hrs after the earthquake (Cheng *et al.*, 2010). Numerous destructive debris flows occurred during the monsoon seasons of 2008 and 2009, including the debris flows in the Wenjia gully in Qingping and in the Weijia gully that buried part of the ruins of old Beichuan town (Tang & Liang, 2008). The intense rainfall during August 12-13, 2010, triggered debris flows in more than 80 gullies in the study area, which included 20 in Qingping, 21 in Yingxiu, and 44 in Dujiangyan (Huang & Li, 2014), that ultimately became the 'tipping' point for many communities to recognize long-term impact of such a mega-earthquake. The basic characteristics of the studied gullies are shown in Table 8.

Table 8 – The basic geometry of the gully and the estimated amount of the source materials for the debris flow with mitigation system (re-)implemented after August 13, 2010.

Gully	Length (km)	Height (km)	Catchment Area (km^2)	Loose deposit volume (*before Aug 2010*) ($\times 10^6$ m^3)	Loose deposit volume (*after Aug 2010*) ($\times 10^6$ m^3)
Hongchun	3.6	1.29	5.35	3.58	3.1
Shaofang	1.85	1.1	1.5	2.52	2.23
Niujuan	3.9	1.78	10.7	7.89	7.43
Maliu	1.59	0.95	1.98	-	8.14
Dashui	0.88	0.32	0.45	-	2.7
Wenjia	3.25	1.52	4.5	80.6	74.5
Zoumalin	3.5	0.59	5.7	4.37	3.26

Note: estimated volume of source material before August 2010 may not represent the actual total volume of the loose deposit after the Wenchuan earthquake because of the absence of detailed records in literature of debris flows between May 2008 and August 2010.

The cascading debris flows caused significant fatalities and resulted in damage to the post-earthquake reconstruction process (Tang *et al.*, 2012a; Xu *et al.*, 2012c; Huang & Li, 2014). Debris flows destroyed many conventional mitigation systems, especially for the case of the Wenjia gully, which led to the exposure of the shortcomings in the design of the conventional debris flow mitigation systems that are almost exclusively in consist of a large number and variety of concrete check dams and channels. Conventional debris flow mitigation systems are those that typically involved one or more concrete check dams that served to arrest debris as is flowed downwards. Many mitigation systems that were being designed or implemented at that time followed the conventional design specifications that later proved to be insufficient for debris flows after an earthquake due to high sediment flux (Xu *et al.*, 2012c). In this chapter, the focus of the work lies on the design and performance of the debris flow mitigation system in Wenjia gully in Qingping; it documents the design of the system as well as the pre- and post-mitigation debris flow events. Evaluation of the mitigation system is expanded to some mitigated gullies in the regions of Qingping, Yingxiu, and Dujiangyan. The objectives of this work are: 1) to emphasize the importance of a 'paradigm shift' in designing more sustainable and resilient mitigation systems, in particular after a mega-earthquake with high sediment influx; and 2) to evaluate the performance of existing mitigation system at site-scale using quantitative approaches in light of rainfall thresholds and debris flow characterizations.

7.2 Rainfall thresholds and earthquake

Prior to the 2008 Wenchuan earthquake, rainfall data for gullies that were susceptible to debris flows in the study area were typically collected by the nearby rain gauge without the systematic framework of an Early Warning System (EWS) for debris flows. The studies on pre-earthquake debris flows in the study area typically relied on distant rain gauges that may not be at the comparable elevation or the same side of the ridge (Guo *et al.*, 2016).

As noted in Section 2.3.3, the rainfall threshold represents the minimum precipitation required to trigger a debris flow, slope failure, or shallow landslide. The typical approach includes rainfall intensity-duration relationship that can be expressed as:

$$I = aD^{-b} \tag{26}$$

where I is the mean rainfall intensity (mm/hr), D is the rainfall duration (hr), and a and b are empirical coefficients (Caine, 1980). Guo *et al.* (2016) summarized the *I-D* thresholds that triggered debris flows between 2008 and 2013 for the entire region that were impacted by the earthquake. Ma *et al*. (2017) studied the debris flows occurred between 2008 and 2012, and summarized *I-D* thresholds for the regions of Beichuan, Yingxiu, Qingping, and Dujiangyan at the watershed-scale (see Table 9). These rainfall thresholds are plotted and compared with some proposed global or regional thresholds reported in previous literature, as shown in Figure 7.2.

A pre-earthquake *I-D* threshold for the entire region is not available for the Wenchuan Earthquake; but the post-earthquake *I-D* thresholds are significantly lower than the global or regional thresholds included in this study, which implies a possible severe impact caused by the earthquake. The gradual increase in the *I-D* threshold between 2008 and 2013 indicates a decreasing susceptibility to debris flow at the regional scale. Notwithstanding the complex sediment influx caused by the subsequent geohazards after the earthquake (Huang & Fan, 2013; Huang & Li, 2014), the recovery of the *I-D* thresholds can be largely ascribed to the decrease of the overall loose materials, as they were entrained and removed by previous debris flows from the gullies. The watershed *I-D* thresholds are considerably higher than the earthquake regional thresholds (Figure 7.2), which is used as a more direct way to assess the performance of the debris flow mitigation systems in these regions.

Table 9 – Regional *I-D* thresholds for debris flows in some regions that were severely impacted by the Wenchuan earthquake (Tang *et al.*, 2012a; Ma *et al.*, 2017); the lower thresholds denote to the small-scale debris flows.

#	Region	*I-D* threshold	Range
42	Beichuan	$I = 24D^{-0.3}$	1-10*
43		$I = 37D^{-0.6}$	
44	Yingxiu	$I = 15.2D^{-0.8}$	
45		$I = 26D^{-0.7}$	
46	Dujiangyan	$I = 41D^{-0.33}$	
47	Qingping	$I = 31D^{-0.3}$	
48	Qingping (2010)	$I = 25.692D^{-0239}$	1-24
49	Average (2008-2012)	$I = 66.36D^{-0.79}$	2-15

Note: The range of *D* was not specified by Ma *et al.* (2017), and thus assumed to be the maximum value that was presented in that study. The average *I-D* threshold is based on the watersheds of Dashui, Wenjia, Hongchun, and Bayi (Zhou & Tang, 2014).

A single critical rainfall parameter, such as peak rainfall intensity or daily cumulative rainfall, has the tendency to overestimate debris flow occurrence for mitigated gullies (Liu *et al.*, 2017a), and therefore additional rainfall threshold parameters are employed to better characterize the critical conditions and the variations after implementing the mitigation system. The Rainfall Index (*RI*) is defined as R_dI_{max} (Chen *et al.*, 2013), where R_d is the daily cumulative rainfall and I_{max} is the peak rainfall intensity. The Rainfall Triggering Index (*RTI*) is expressed as the product of R_tI_{max}, where R_t is the 7-day antecedent rainfall. The *RTI* has been used to establish the probability of debris flow occurrences in predication models (Jan *et al.*, 2002; Jan & Lee, 2004; Huang *et al.*, 2015b).

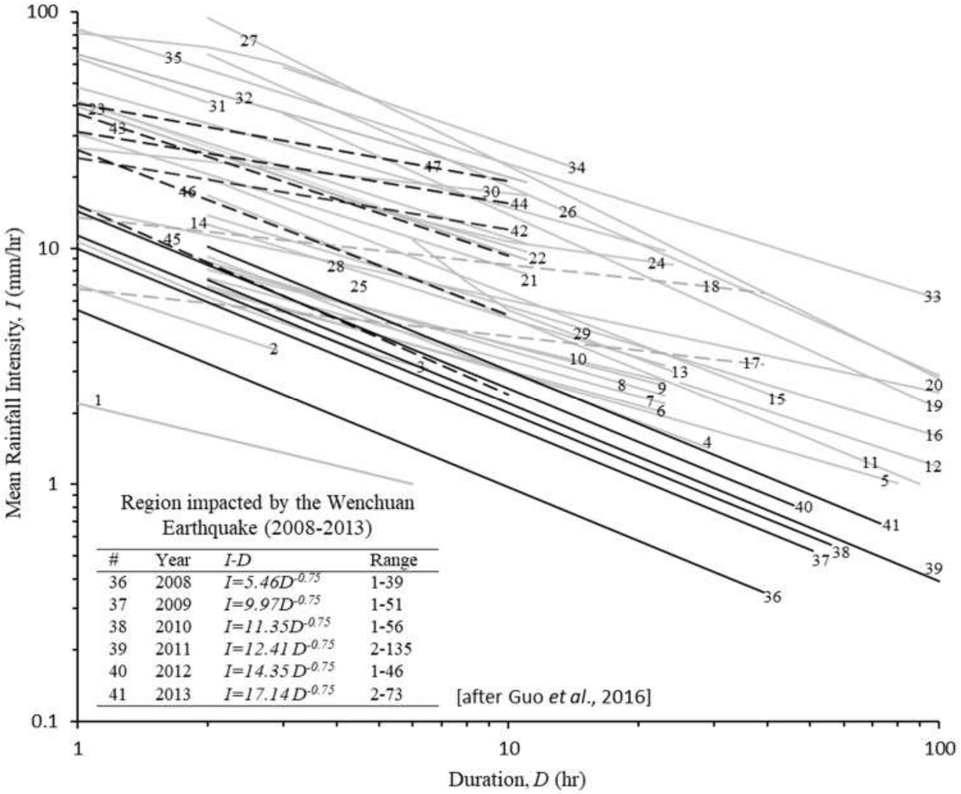

Region impacted by the Wenchuan Earthquake (2008-2013)

#	Year	I-D	Range
36	2008	$I=5.46D^{-0.75}$	1-39
37	2009	$I=9.97D^{-0.75}$	1-51
38	2010	$I=11.35D^{-0.75}$	1-56
39	2011	$I=12.41D^{-0.75}$	2-135
40	2012	$I=14.35D^{-0.75}$	1-46
41	2013	$I=17.14D^{-0.75}$	2-73

[after Guo *et al.*, 2016]

Figure 7.2 – Global and regional mean rainfall *I-D* thresholds for debris flows proposed in previous literatures (references in Table 10). The regional *I-D* thresholds for the Wenchuan earthquake impacted area are highlighted; the watershed *I-D* thresholds are marked by dash lines. The sharp decrease in thresholds #17 and #18 represents the changes after the 1999 Chi-Chi Earthquake.

Table 10 – Some global and regional mean rainfall intensity-duration (*I-D*) thresholds for debris flows.

#	Area	Equation	Reference
1	Global	$I=2.2D^{-0.44}$	(Guzzetti *et al.*, 2008)
2		$I=7.0D^{-6.00}$	(Cannon & Gartner, 2005)
3	USA	$I=1.7+9D^{-1.00}$	(Wieczorek, 1987)
4	Italy	$I=15D^{-7.00}$*	(Marchi *et al.*, 2002)
5	USA	$I=9.9D^{-0.52}$*	(Montgomery *et al.*, 2000)
6	Italy	$I=9.521D^{-0.4955}$	(Bolley & Oliaro, 1999; Calcaterra *et al.*, 2000; Guzzetti *et al.*, 2007)
7		$I=10.67D^{-0.5043}$	
8		$I=12.649D^{-0.5324}$	
9		$I=11.698D^{-0.4783}$	
10		$I=11.0D^{-0.4459}$	

11		I=28.1$D^{-0.74}$*	
12	Japan	I=1.35+55$D^{-1.0}$*	(Hong *et al.*, 2005)
13	USA	I=2.5+300$D^{-2.0}$	(Cannon & Ellen, 1985)
14	Italy	I=18.675$D^{-0.565}$	(Ceriani *et al.*, 1992; Zimmermann, 1997; Guzzetti *et al.*, 2007)
15	Switzerland	I=32$D^{-0.70}$*	
16	Italy	I=20.1$D^{-0.55}$*	
17	Taiwan	I=6.7$D^{-0.2}$**	(Jan & Chen, 2005; Chen, 2011)
18		I=13.5$D^{-0.2}$***	
19	Puerto Rico	I=91.46$D^{-0.82}$	(Larsen & Simon, 1993)
20	Global	I=14.82$D^{-0.39}$	(Caine, 1980)
21		I=30.53$D^{-0.57}$	(Jibson, 1989)
22	Japan	I=39.71$D^{-0.62}$	
23	USA	I=35.23$D^{-0.54}$	
24		I=6.9+30$D^{-1.0}$	
25	China	I=49.11-6.81$D^{1.0}$	
26	Italy	I=176.4$D^{-0.90}$	
27	Taiwan	I=115.47$D^{-0.8}$	(Chen *et al.*, 2005)
28	Hong Kong	I=41.83$D^{-0.58}$	(Jibson, 1989)
29	Italy	I=47.742$D^{-0.507}$	(Paronuzzi *et al.*, 1998)
30	USA	I=26.51$D^{-0.19}$	(Jibson, 1989)
31	Brazil	I=63.38-22.19$D^{1.0}$	
32	Puerto Rico	I=66.18$D^{-0.52}$	
33	Portugal	I=84.3$D^{-0.57}$*	(Jan & Chen, 2005)
34	USA	I=116.48$D^{-0.63}$	(Wieczorek *et al.*, 2000)
35	Indonesia	I=92.06-10.68$D^{1.0}$	(Jibson, 1989)

Note I is the mean rainfall intensity (mm/hr) and D is rainfall duration (hr).
*Applicable to all types of landslide; ***I-D* thresholds after the Chi-Chi Earthquake; ****I-D* thresholds before the Chi-Chi Earthquake.

7.3 Design of debris flow mitigation system in Wenjia gully

A predicament for the Wenjia mitigation system is a large amount of loose material that has been deposited in the gully by the co-seismic landslide, providing abundant source material for debris flows under saturation. A novel design solution was proposed and has exhibited excellent performance and resilience in subsequent debris flows. The design was governed by the idea of controlling water, sediment, and erosion; this solution reduces debris flow energy by combining different mitigation measures.

7.3.1 Co-seismic landslide

Wenjia gully has become one of the most studied geohazard sites in China since the 2008 Wenchuan earthquake. The gully is located on the left bank of the Mianyuan River in the Qingping area near Mianzu County in Sichuan (Figure 7.3a); it is situated less than 4 km SE of the Yingxiu-Beichuan thrust fault and 80 km NE of the epicenter of the 2008 Wenchuan earthquake (Figure 7.3b). The length of the gully is about 3 km (highest elev. 2402 m) with an average gradient of 45° before the earthquake; it had extensive vegetative coverage with an area exceeding 80% of the basin (Wang *et al.*, 2014). The Wenjia gully is situated on the Guanwushan group (Upper Devonian Period) and Qingping group (Cambrian Period) in sequence. The Guanwushan group consists of mainly carboniferous limestone, and the Qingping group comprises primarily sandstone and siltstone, as shown in Figure 7.3f. Loose Quaternary deposits were found in the form of terraces and alluvial fans in the gully (Xu, 2010).

The ground shaking caused a deep-seated co-seismic landslide that initiated at an elevation of 1780-2340 m in the gully. Two main scarps were observed orientating WNW-SEE and NW (Figure 7.3c); it was postulated that the displaced materials originated from the two adjacent limestone rock blocks. The total volume of the rock blocks was 27.5×10^6 m^3, of which nearly 70% remained on the Hanjia Platform, while the rest entered the 1300m Platform (a platform at the elevation of 1300 m), as shown in Figure 7.3d. The landslide transformed into a rock avalanche and entrained a large amount of shallow sand-gravel materials during its movement (Xu *et al.*, 2009b; Xu, 2010). The estimated volume of loose deposits in the 1300m Platform and the Zone of Accumulation II was 30×10^6 m^3 (Figure

7.3d and Figure 7.3e). Based on the characteristics of the deposits, a hypothetical flow trajectory for the landslide was proposed and delineated as shown in Figure 7.3a

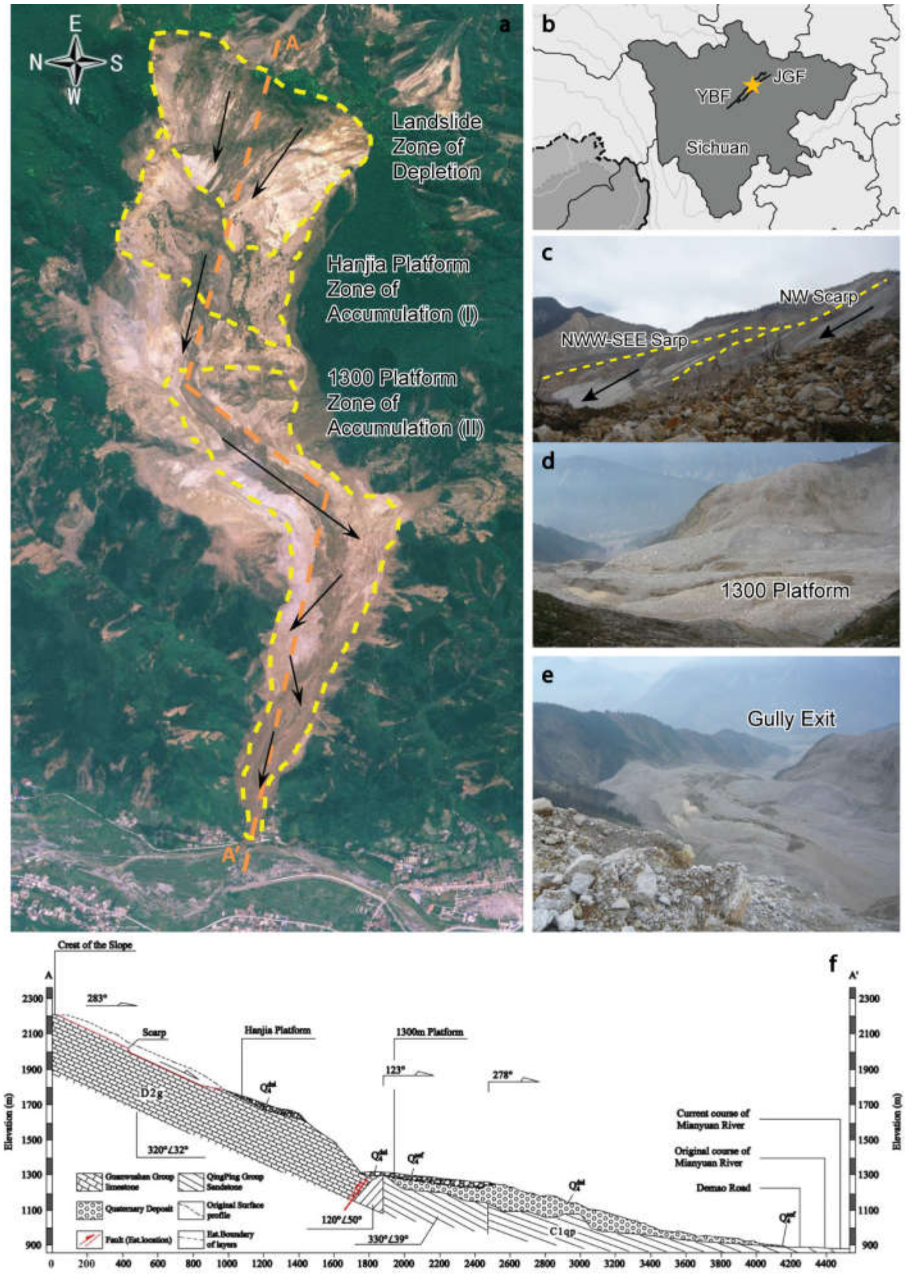

Figure 7.3 – The co-seismic landslide in Wenjia gully: (a) post-earthquake imagery of the gully showing the possible landslide trajectory (Image: May 23, 2008); (b) location of the study area; (c) the co-seismic landslide scarp; (d) the 1300m platform; (e) the Zone of Accumulation II; (f) the geological profile of cross section A-A'.

The study area is in a subtropical monsoon climate zone with rainfall concentrated in the monsoon season that spans from June to September (typically 60% of the annual rainfall). The average annual rainfall is 1086.4 mm with an average temperature of 14.4 °C. No record of debris flow was found before the earthquake; but at least 18 debris flows have occurred in the adjacent gullies in the past two decades.

7.3.2 Pre-mitigation debris flows

In 2008, the monthly precipitation in the Qingping area in Jun, Jul, Aug, and Sept were 113, 167.5, 170, and 350 mm, respectively. Several small-scale debris flows occurred in the Wenjia gully during the rainstorms on Jun 18-21 and Jul 24-25. The first major debris flow occurred on Sept 24, during which the daily rainfall was 88 mm with a peak 10-min rainfall of 11.5 mm. The intense surface run-off mobilized the loose deposits in the Zone of Accumulation I and II, and resulted in channelized erosion and deep incisions (approx. 20 m) in the gully. The volume of the debris flow was estimated as 0.5×10^6 m^3, which is less than 1% of the loose deposit in the gully (Xu *et al.*, 2009b); however it destroyed the infrastructure near the outlet of the gully and part of the Qingping town. The deposit from the debris flow formed a dam and resulted in water impoundment in the Mianyuan River.

Mitigation measures were proposed after the debris flows in 2008, which include a debris basin and a drainage channel with two check dams located at the lower end of the Hanjia Platform and near the exit of the gully. The design of the mitigation measure was modified in the following year by adding 19 additional check dams between 1243-1095 m (elev.), with lengths of 20.5-84 m and an average height of 4.5 m. A diversion dike was constructed in the Zone of Accumulation II with 6 sectional barriers between 1095-1075 m (elev.). Retaining structures were constructed on the hillsides with 35 sectional barriers between 1075-985 m (elev.). A check dam was built near the outlet of the gully (elev. 940 m) spanning 215 m between both sides of the gully, for which the height was 8 m with a large debris basin. The main drainage channel (length: 255 m) contained 12 sectional barriers and retaining structures on both sides. The mitigation measures were completed in early Jul 2010, but were severely damaged by the end of the month; 9 check dams were destroyed and the volume of deposit in the debris basins exceeded the design level.

The debris flow occurred on Aug 13, 2010 has been well studied and presented in the literature (Xu, 2010; Ni *et al.*, 2012; Tang *et al.*, 2012a; Xu *et al.*, 2012c; Yu *et al.*, 2013, 2014; Zhou *et al.*, 2014a), as shown in Figure 7.4. A heavy rainstorm concentrated between 14:00 on Aug 12 and 01:00 on Aug 13 (daily cumulative rainfall R_d = 220 mm; peak rainfall intensity I_{max} = 70 mm/hr). According to eyewitnesses, the debris flow occurred after 01:00 on Aug 13 and lasted for about 2 hours, which coincided with the duration of the rainfall.

The heavy rainfall generated intense surface run-off, and saturated the loose deposit and produced a large erosion channel with a depth of 60 m and a gradient of 60° (Figure 7.4a and Figure 7.4b). The debris flow was intercepted by the check dam at the outlet of the gully until its failure (Figure 7.4c). The estimated debris volume exceeded 4.5×10^6 m^3 and it covered a total area of 635,000 m^2 in Qingping (Xu *et al.*, 2012c). The debris flow deposit has an average thickness of 7 m, with a maximum thickness of over 15 m (Figure 7.4f). The deposits blocked the Mianyuan River (Figure 7.4g) along with compounding debris flows in the area, including a large-scale event in Zoumalin Gully located 4 km upstream of Wenjia gully. The Qingping village was severely damaged and partially buried by the debris flows, which caused 7 casualties, 39 injured and 497 houses buried (Yu *et al.*, 2013). Another debris flow occurred on Aug 19, which interrupted the construction of the rapid-response mitigation measures and deposited an additional 17.6×10^4 m^3 of sediment; the subsequent event also caused severe damage to Qingping village while the community was recovering from the previous event (Figure 7.4d and Figure 7.4e).

Figure 7.4 – The devastating debris flow occurred on Aug 13, 2010: (a) deep incision due to channelized erosion on the 1300m Platform; (b) widened debris flow channel near the exit of the gully; (c) failure of the last check dam (after Tang *et al.*, 2012); (d) a buried house in Qingping village; (e) increase in the thickness of the deposit after a subsequent debris flow; (f) submerged area near the outlet of the gully; (g) aerial image of the debris flow with approximated locations of the images presented herein.

7.3.3 Design and implementation of mitigation measures

The design of the conventional mitigation system which followed the standard design code (Ministry of Land and Resources of China, 2006) underestimated the discharge and volume of the debris flows due to inadequate consideration of the source materials and the rainfall thresholds. Without characterizing the post-earthquake scenario, the estimated volume of debris flow in the Wenjia gully was, on average, 45% less than that observed between 2008 and 2010; the observed volume of the debris flow on Aug 13, 2010 was 12 times greater than the estimate based on the design code.

A design solution for the debris flow mitigation system was proposed by the State Key Laboratory of Geohazard Prevention and Geoenvironment Protection (SKLGP) (cf. Xu, 2010; Xu *et al.*, 2012); it integrates three key elements, e.g. water-sediment segregation (water control), source material stabilization (sediment control), and channelized erosion prevention (erosion control). As a debris flow is a mixture of loose solids and fluid, the aim of the mitigation system is to minimize surface run-off by separating the fluid and solid components. The stabilization of the loose deposit in the Zone of Accumulation II reduces the source material, which in turn, decreases the size of the debris flow. The development of an erosion channel which was typical after debris flows in the gully, indicated a high level of energy from surface run-off. The channelized erosion can easily damage a rigid drainage system, and thereby mobilize additional loose deposits. A novel drainage channel was designed by allowing a certain degree of flexibility in the system, which has proven to be effective in preventing channelized erosion caused by debris flows. Field instruments were deployed in the gully as part of the development of the Early Warning System.

The debris flow mitigation system has a designed seismic resistance level of VII on the Mercalli intensity scale and was completed in May 2011, as shown in Figure 7.5. Reflecting the proposed design, the system has three key sub-systems: 1) a combined sediment basin and debris flow breaker with a drainage tunnel in the upstream section of the gully, 2) a flexible drainage channel in the mid-region of the gully to ‘guide’ the movement of debris flows, and 3) five check dams in the upstream and downstream sections of the gully. A service road was excavated parallel to the flexible drainage channel to allow access by equipment for periodic emptying and maintenance of the debris basins. Accumulation Zone II was excavated for the construction of the drainage channel.

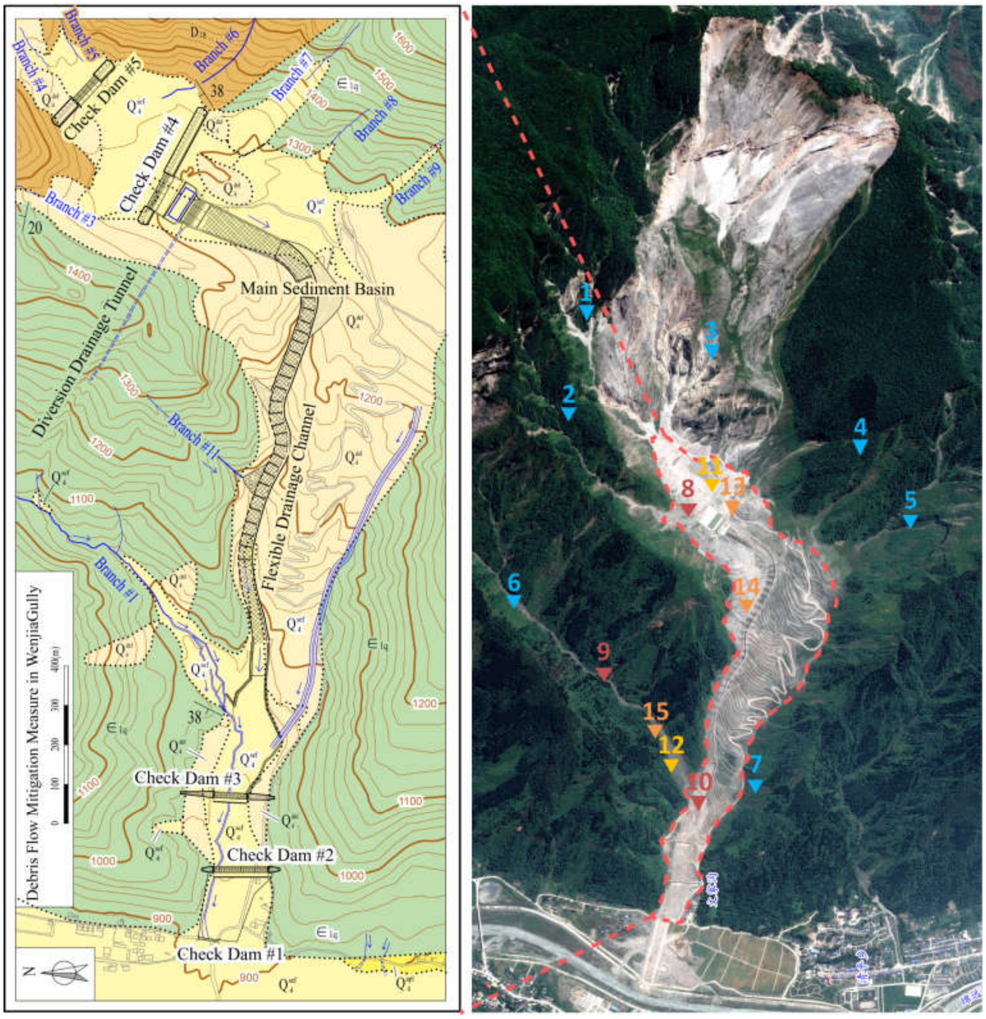

Figure 7.5 – The debris flow mitigation system in Wenjia gully. Check Dams #4 and #5 are located upstream between the Hanjia Platform and 1300m Platform. Three check dams were constructed in the downstream of the gully. A large number and variety of sensors were installed in the gully and/or its catchment, including the rain gauges (1-7), thickness gauges (8-10), piezometers (11-12), and video cameras (13-15).

7.3.3.1 Upstream

The mitigation measures in the upstream section of the gully are shown in Figure 7.6. The primary source materials for debris flows in the upstream region are from the loose deposits in Branches #3, #4, and #5. The landslide deposits in these branches are poorly sorted with an average D_{90} of 1 m; the thickness is 60-80 m and are overlain by 10 m of debris flow deposit. The construction of Check Dam #5 is intended to intercept the loose deposits mobilized from Branches #4 and #5 while reducing the slope gradient below the Hanjia Platform (Figure 7.6a). Check Dam #4 is located downstream of Check Dam #5; its main functions are: 1) to provide additional capacity in the debris basin, and 2) to accommodate the debris-flow breaker and re-route the water of the debris flow into the drainage tunnel. A reflection wall was constructed and connected to Check Dam #4 to prevent the potential impact of the deposits from Branch #3. The design capacities of the debris basins for Check Dams #4 and #5 are 82.6×10^3 m^3 and 57.7×10^3 m^3, respectively.

A sediment basin was constructed downstream of Check Dam #4 integrated with a debris flow breaker system and forms a water-sediment segregation system (Figure 7.6b). The depth of the sediment basin is 4 m with the areas of the top and bottom of 40×10^6 m^2 and 27×85 m^2, respectively. The breaker system consists of four arrays of steel fins (Figure 7.6c) aligned perpendicular to the dominant flow direction of the debris flow surge. The water-sediment segregation system is critical to the entire system. As the catchment area is over 4 km^2, the upstream region of the gully is susceptible to flood and hyperconcentrated flow that may transform into debris flow. In the event of overtopping of Check Dams #4 and #5, the sediment basin slows down the debris flow surge and reduces the dynamic impact by permitting rapid settlement of larger boulders and rocks.

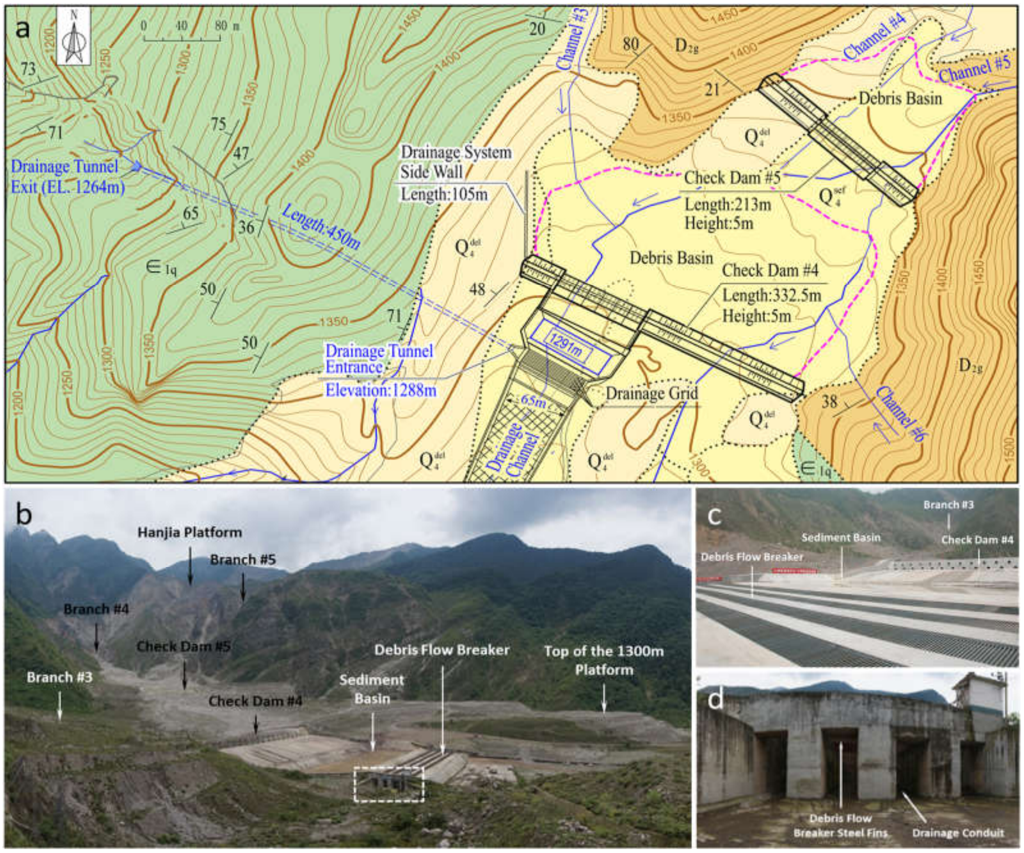

Figure 7.6 – The mitigation measures in the upstream section of the Wenjia gully: (a) plan view of the mitigation structures; (b) an overview of the mitigation structure; (c) the water-sediment segregation system containing a sediment basin and a breaker system; (d) the drainage conduits underneath the steel fins of the debris flow breaker.

The breaker system enables rapid drainage of surface run-off through the drainage tunnel, which in turn, prevents erosion and mobilization of the loose particles at the 1300m Platform and in the rest of the Zone of Accumulation II. The sediment basin optimizes the efficiency of the breaker system by cushioning the impact of surge waves and improves the longevity of the breaker. Fluid and small-scale sediment removed from the bulk of the debris flow is drained through the drainage tunnel (Figure 7.6c) and discharged to Branch #1 (Figure 7.6d). The tunnel has a design discharge capacity of 106.5 m^3/s and a length of 450 m at a gradient of 0.05 with a width and height of 4.5 m and 3.5 m, respectively.

The core of the design is to stabilize the loose deposits at the 1300m Platform by re-routing the fluid component of the debris flow. Check Dams #4 and #5 are considered sufficient to intercept most of the mobilized sediments from Branch #4 and #5, as the amount in these tributary gully branches is comparatively small. Following the same line of reasoning, debris flows in Branch #1 poses a smaller impact even under intense surface run-off from rainfall and the fluid exiting from the drainage tunnel.

7.3.3.2 Midstream

The mitigation structure in the mid-region of the gully is a stepped flexible drainage channel extending from the debris flow breaker system to the outlet of the gully (Figure 7.7a). The channel has a total length of 1290 m containing 25 steps at an average interval of 27m with widths ranging from 45 m (upstream end) to 30 m (downstream end); it aims to reduce the volume of debris flow by minimizing erosion using gabion basket modules (Figure 7.7b). The gabion modules buttress riprap that consists of angular and resistant rocks, which deforms under the impact of a debris flow without a significant reduction of its efficiency (Costa & Wieczorek, 1987). The stepped chute promotes kinematic energy dissipation, which drastically decreases the discharge rate of the debris flow, and in turn, the impact to the midstream and downstream of the gully by minimizing the energy (i.e. discharge control) and reducing the volume of the debris flow (i.e. erosion control).

The upstream end of the channel is connected to the water-sediment segregation system, and a pile system was installed at the downstream end (Figure 7.7b). Retaining structures were constructed on both sides of the channel (Figure 7.7b and Figure 7.7c). A service road was excavated on the hillslope located to the south of the channel, where a large amount of sediment was deposited due to the construction of the channel. The local topography was altered into terraced landscape and additional erosion control methods were applied, including ground seeding, mulching, and small-scale log erosion barriers (LEBs), to stabilize the loose deposits. The LEBs are installed on the road embankments and ground seeding applied in this area (Figure 7.7d). The LEBs are made of bamboos and held in place by steel poles, which serve as mechanical retaining racks and reduce rill erosion while promoting seepage (deWolfe *et al.*, 2008).

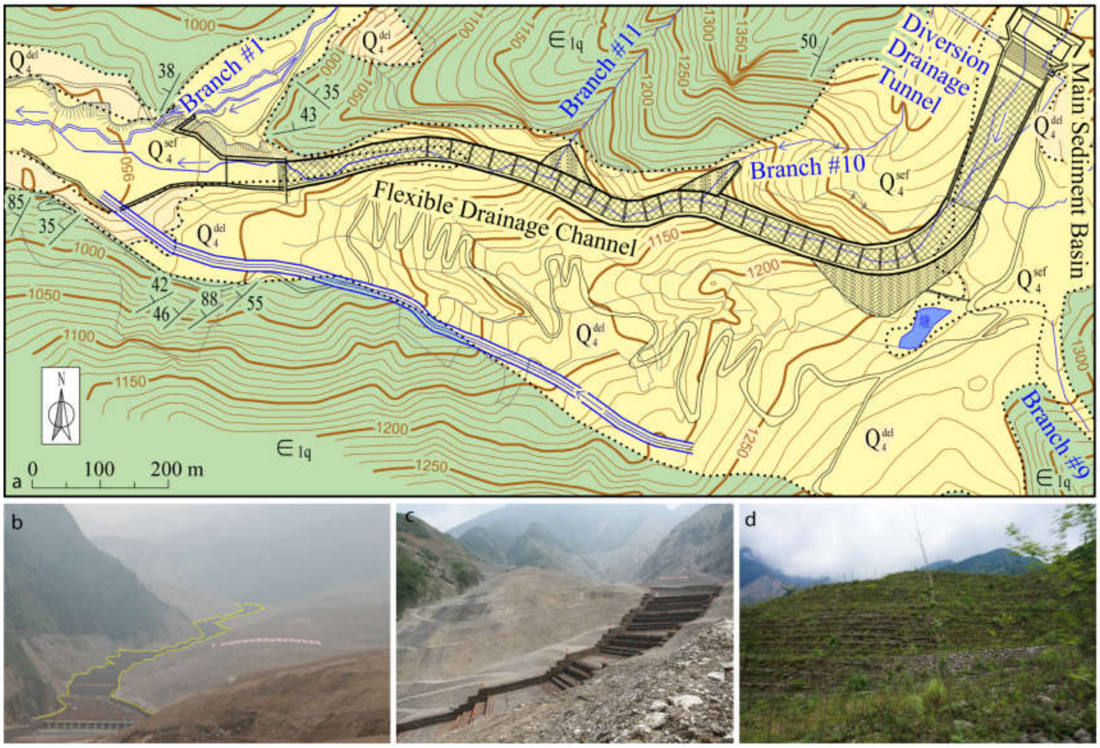

Figure 7.7 – The mitigation measures in the midstream section of the Wenjia gully: (a) the plan view of the mitigation structures; (b) an overview of the flexible drainage channel; (c) a close view on the stepped channel on the 1300m Platform; (d) terraced loose deposits on the south of the channel with ground seeding and LEBs for stabilization.

A smaller drainage channel was constructed parallel to the flexible drainage channel to prevent erosion by surface run-off of the treated hillslope. Three piezometers were installed along the flexible channel to provide real-time monitoring on the groundwater table which may pose risk to the stability of the structure.

7.3.3.3 Downstream

The mitigation system in the downstream section focuses on intercepting the medium and large boulders and rock masses from Branches #1 and #2, and any possible far-reaching sediments that originate from the upstream (Figure 7.8a). The main structures consist of three check dams with sectional barriers and concrete fins (Figure 7.8b and Figure 7.8c). Check Dam #2 has a height of 6 m above ground level with a design width for an overflow of 139 m and a maximum volume of 67.5×10^3 m^3 for the debris basin. Check Dam #3 has a height of 5 m with a design capacity of the basin of 25.6×10^3 m^3. Check Dam #1 was added after the completion of the system, with the primary purpose being pedestrian access while serving as the last barrier for debris flows. Deflection and retaining walls were built to protect and stabilize the hillsides in the downstream.

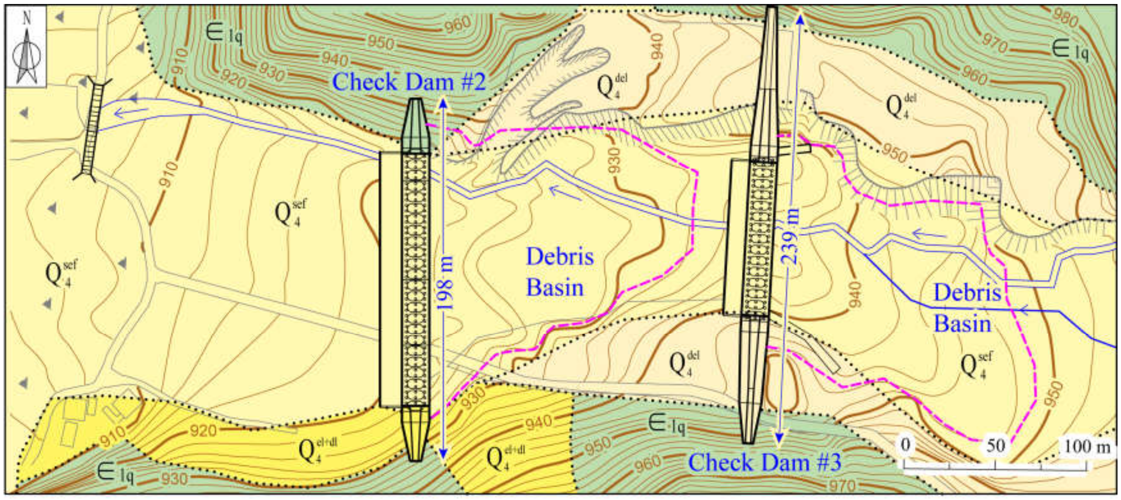

Figure 7.8 – The mitigation measures in the downstream section of the Wenjia gully shows the plan view of Check dam #1 (for pedestrian assess), #2, and #3 with basins.

The design of the check dams is based on the debris flows induced by a peak rainfall intensity of 91.9 mm/hr, which, according to the design code, yields 36.4×10^4 m^3 of sediments (Ministry of Land and Resources of China, 2006). The opening of the fins must be sufficiently small to prevent large sediment from reaching the Qingping area. Since the sediment deposited near the outlet of the gully from the debris flows in Aug 2010 had a maximum particle size of 1.0 m, the first sectional barrier of Check Dam #3 was designed with a fin gap of 1.5 m to intercept the sediment with sizes greater than 0.8 m. Check Dam #2 has a fin gap of 1.0 m to retain the deposits with sizes greater than 0.6 m.

7.3.3.4 Early Warning System

An EWS was implemented for 20 gullies in the region of Qingping that experienced continuous debris flows after the earthquake; it utilizes the real-time data collected by the field instruments. The locations and types of monitoring devices in the Wenjia gully are shown in Figure 7.5. The datasets are acquired, stored, and integrated into a 3-D WebGIS-based platform that consists of a support layer, a service layer, and a client layer. The support layer transmits the monitoring dataset, the service layer integrates data and geospatial information on the publicly available map server, and the client layer provides an end-user interface for data query and visualization. The service layer provides real-time warning based on probabilistic and empirical correlations between rainfall and debris flow occurrences. The EWS issues warning signs representing different danger levels to the registered users. A variety of rainfall-induced debris flow prediction models were tested in the design of the EWS for the Wenjia gully (Glade *et al.*, 2000; Guzzetti *et al.*, 2007, 2008; Cannon *et al.*, 2008). As the occurrence of debris flows has exhibited correlations with $I_{\max}$,

R_d, and the antecedent rainfall P, the EWS monitors and issues alerts based on the designated rainfall thresholds (Zhuang *et al.*, 2014; Huang *et al.*, 2015a, 2015b). Due to limited data availability for debris flows in the Wenjia gully, the thresholds were initially established by using the historical rainfall data, but the model and thresholds are updated annually. Detailed discussion on the EWS is presented by Huang *et al.* (2015a).

7.4 Performance of debris flow mitigation system in Wenjia gully

7.4.1 Post-mitigation debris flows

Three heavy rainstorms occurred in the gully between May and Jun 2011; the first two were on May 9 and Jun 16, respectively. The third rainstorm was the largest and lasted from Jun 30 to Jul 4 with a peak 10-minute rainfall of 10.5 mm and a cumulative rainfall of 387 mm, however no debris flow was observed in the gully. Two large-scale debris flows occurred on Aug 14 and 17.

A rainstorm swept over the study area between 15:00 and 17:10 on Aug 14 (R_d = 138.5 mm; I_{max} = 50 mm/hr) (Figure 7.9a). The debris flow lasted for about 2 hours and mobilized the loose deposits in Branches #4 and #5. The decrease in the surface level of the deposits in the channel was captured by the thickness gauge, indicating a small-scale debris flow (Figure 7.9a); it was followed by two additional ones that possibly originated from Branch #1 and resulted in the spikes at 21:00 and 23:00 (Figure 7.9a). The debris flow was largely blocked by Check Dam #5; however an erosion channel was formed in the basin of Check Dam #4. The estimated volume was over 31,500 m^3 covering a total area of 15,600 m^2.

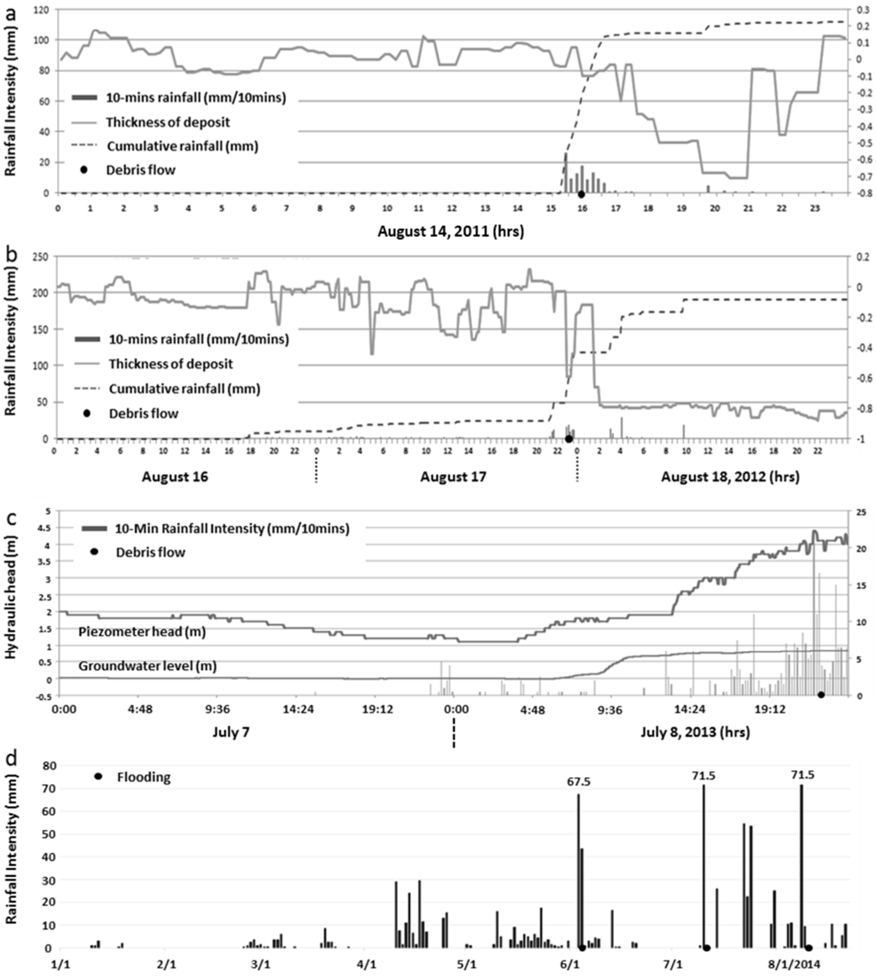

Figure 7.9 – Field data of the post-mitigation debris flows from 2011 to 2014. (a) evident correlations between rainfall and deposit thickness as demonstrated in the debris flow on Aug 24, 2011; (b) rapid decrease in the deposit thickness in Branch #1 was captured indicating the initiation of the debris flow on Aug 17, 2012; (c) field data of the debris flow on Jul 7-11, 2013; and (d) relation between floods and peak rainfall intensity in 2014.

A debris flow was induced by a rainfall event that occurred intermittently between 01:00 on Aug 17 and 05:00 on Aug 18, 2012 (Figure 7.9b). Rainfall started at about 01:10 on Aug 17 and paused for 14 hours before the subsequent rainstorm at 22:50 (R_d = 280 mm; I_{max} = 71.5 mm/hr); it lasted for nearly 5 hours and resulted in debris flows in branches #3, #4, and #5. The increases in the thickness of the deposit in the upstream debris basins became more pronounced before the debris flow event on Aug 17, and eventually the loose deposits overtopped the Check dams #5 and #4 (Figure 7.10).

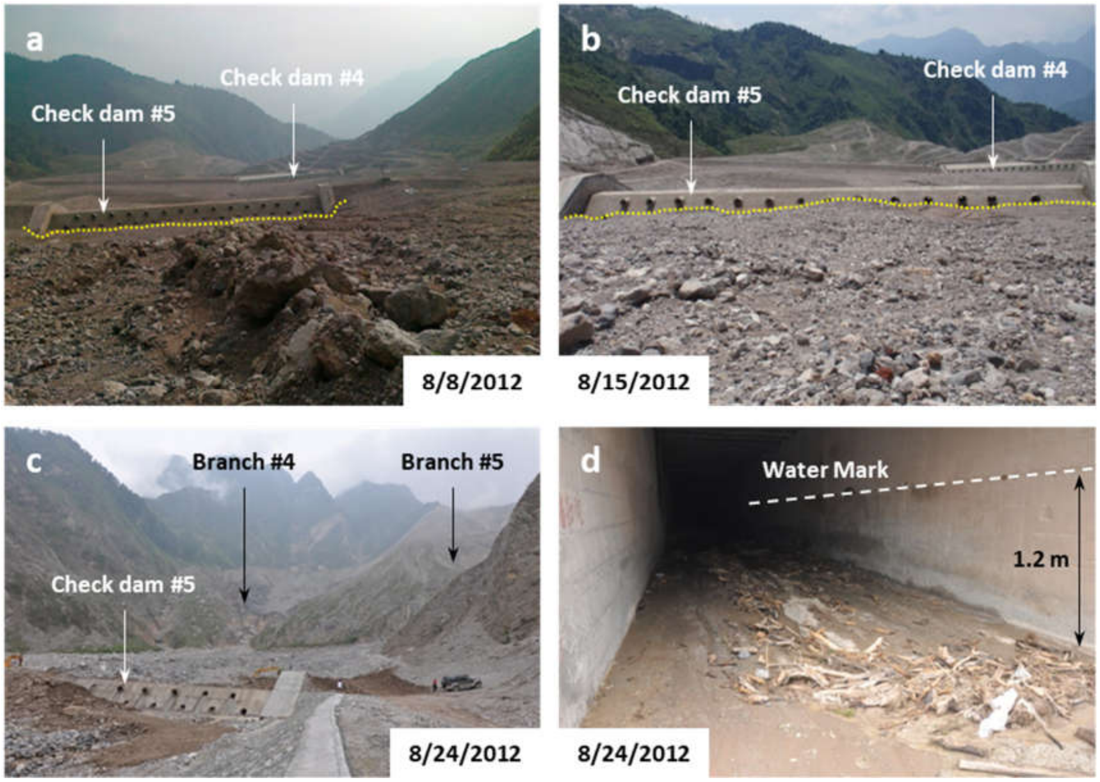

Figure 7.10 – The pre-/post-debris flow images in the monsoon season of 2012: (a) surface profile of the deposit in the debris basin; (b) surface profile of the deposit before the debris flow occurred on Aug 17, showing increased thickness of profile since previous visit which indicates the possible occurrences of some small-scale debris flow events; (c) overtopping of Check dam #5 after the debris flow occurred on Aug 17; and (d) debris basin variations in the Check dams #4 and #5 showing surface erosion caused by loose deposits.

As the debris flow surge reached the breaker on Aug 17, it settled on the steel fins with rapid drainage of fluid. The water mark in the drainage tunnel indicated the height of the flow which was 1.2 m at the entrance with an estimated peak flow discharge of 49.1 m^3/s (Figure 7.10d). The discharge in the drainage tunnel mobilized the loose deposit in Branch #1 (the exit of the tunnel). A considerable amount of sediment was deposited in the debris basins near the outlet of the gully (Figure 7.11a), where the surface run-off eroded and undermined the foundation of Check dam #1. The scouring and erosion caused differential settlement, and ultimately the failure of Check dam #1 (Figure 7.11c), but the debris flow did not cause any damage to the downstream community. The volume of the deposit was estimated as 78,000 m^3 which covers a total area of about 80,000 m^2.

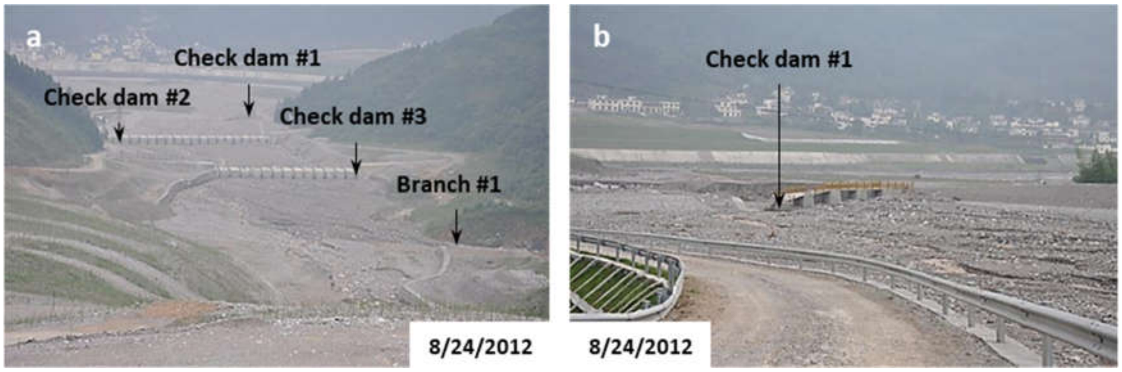

Figure 7.11 – Impact of debris flow occurred on Aug 17 on the Check dams #1, #2, and #3: (a) post-event deposit in the debris basins of Check dams #2 and #3; and (b) damaged dam due to erosion by the debris flow initiated in Branch #1

In 2013, rainstorms were reported in the gully on Jun 18-20, Jun 29, Jul 1, Jul 3-5, and Jul 7-11 (R_d = 836.5 mm; I_{max} = 71 mm/hr). Many of the monitoring instruments were defective due to inadequate maintenance. Field data is summarized and shown in Figure 7.9c. Interviews with local residents confirmed that the debris flow occurred at 22:00-23:00 on Jul 8; the exact time of the occurrence of the debris flow cannot be determined. The loose deposits in Branches #4 and #5 provided the source material, with significant incision and undercutting in both branches. The debris flow reached the debris basin of Check dam #4 and damaged the left flank of the dam. A considerable amount of water entered the drainage tunnel causing minor erosion in Branch #1, which in turn mobilized and deposited some sediments in the debris basin of Check dam #3. The total volume of the debris flow was estimated as 344,000 m^3 based on the changes of the thickness of deposit in the basins. Three small-scale hyperconcentrated flows occurred during the monsoon season on Jun 3, Jul 10, and Aug 8, 2014. The rainfall data were collected and are presented in Figure 7.9d. Two of them are considered as floods because of the small amount of deposit material.

7.4.2 Post-mitigation rainfall thresholds

At least nine large-scale debris flows occurred in Wenjia gully between 2008 and 2015. The associated rainfall parameters, including the peak rainfall intensity I_{max}, the daily cumulative rainfall R_{d}, the 7-day antecedent rainfall R_{t}, Rainfall Index (*RI*), and Rainfall Triggering Index (*RTI*), are computed and summarized in Table 11.

The variations in the number and volume of the debris flows as well as the associated rainfall thresholds are of direct importance in evaluating the performance of the mitigation system. As shown in Figure 7.12, no debris flow event was known before the earthquake, the increased number of debris flows are prominent, and it decreased abruptly with sharp increases in the critical rainfall parameters after implementing the debris flow mitigation system. Notwithstanding the complex and dynamic interplays between rainfall and debris flow, plotting the occurrences in such fashion offers an intuitive representation of the variations in the number of debris flow events and rainfall thresholds. A single critical rainfall parameter (I_{max} or R_{d}) shows a tendency to overestimate debris flow occurrences for the pre-/post-mitigation cases (Figure 7.12a and Figure 7.12b), and therefore *RI* and *RTI* are employed here to better characterize the critical conditions and the variations after implementing the mitigation system (Figure 7.12c and Figure 7.12d).

Table 11 – Major rainfall and debris flow events in the Wenjia gully before and after the Wenchuan earthquake as well as the completion of the debris flow mitigation system. This table includes some of the historical rainfall data from the local metrological stations.

Date	I_{max} (mm/hr)	I (mm/hr)	R_d (mm)	R_t (mm)	RI (cm^2/hr)	RTI (cm^2/hr)	D (hr)	DF	V (10^4 m^3)	A (10^4 m^2)
7/27/92	35.2		232.3	464.6*	57.363	122.69		○		
7/15/93	31.7		233.0	466.0*	25.025	69.615		○		
9/09/94	25.0		56.00	112.0*	36.570	40.015		○		
8/15/95	49.8		496.5	993.0*	36.450	67.770		○		
8/26/96	34.4		221.1	442.2*	24.752	59.378		○		
8/15/97	20.0		110.2	220.4*	25.383	29.110		○		
9/17/98	39.3		290.0	580.0*	81.770	163.54		○		
8/15/99	49.8		100.8	201.6*	73.861	147.72		○		
7/29/00	23.9		148.4	296.8*	14.000	28.000		○		
8/19/01	35.1		258.9	517.8*	247.26	494.51		○		
7/31/02	20.3		104.0	208.0*	76.058	152.12		○		
8/09/03	38.9		227.0	454.0*	22.040	44.080		○		
7/26/04	22.8		58.30	116.6*	113.97	227.94		○		
7/19/05	33.9		126.2	252.4*	50.198	100.40		○		
9/24/08	30.5	7.30	44.00*	88.00	35.468	70.935	12	●	50	12
8/25/09	28.9		43.35*	86.70	90.874	181.75		○		
7/25/10	11.6		44.80*	89.60	21.112	42.224		●		
7/31/10	51.7	17.9	60.20	89.50	88.303	176.61	5	●	60	
8/13/10	70.6	17.2	137.6	227.5	13.292	26.585	7	●	310	63.5
8/19/10	69.0	11.1	122.2	251.0	42.782	85.564	11	●	30	12
9/18/10	29.0	22.5	26.00*	52.00	12.528	25.056	3	●	17.6	8.5
9/22/10	24.5		40.60*	81.20	9.9470	19.894		○		
8/21/11	13.6		38.30*	76.60	5.2088	10.418		○		
8/14/12	73.5	47.2	138.5	138.5	21.503	43.310	3	•	3.16	1.56
8/17/12	71.5	60.3	180.5	280.0	0.7175	2.8525	11	•	7.8	6.4
6/13/13	30.5		70.50	142.0	5.4050	13.685		○		
6/28/13	32.5		176.5	377.5	1.9200	2.7000		×		
7/06/13	59.0	41.5	311.5	858.0	2.1000	8.1000	29	•	34.4	
7/25/13	45.5		55.00	153.0	0.2625	0.7375		×		
8/06/13	26.5		138.0	151.0	5.8125	9.0675		×		
9/01/13	3.50		20.50	81.50	13.420	26.840		○		
9/15/13	11.5		47.00	119.0	5.1968	10.394		○		
5/09/14	12.0		16.00	22.50	31.123	46.272		○		
5/14/14	12.0		17.50	67.50	97.146	160.62		○		
6/03/14	54.0		67.50	125.5	84.318	173.19		×		
7/22/14	45.5		54.40	130.5	7.5400	15.080		×		
8/08/14	35.5		71.50	82.00	101.80	101.80		×		
8/20/14	2.50		10.50	29.50	129.06	200.20		○		
9/20/14	15.5		37.50	58.50	183.79	506.22		○		

Note: I_{max} and I are the peak and mean rainfall intensity, respectively; R_d and R_t are the daily cumulative and 7-day antecedent rainfall, respectively; D is the rainfall duration; and V and A are the estimated volume and covering area of debris flow, respectively. Dash lines represent the earthquake and completion of the new mitigation system.

*assuming $R_d = 1/2R_t$ in case of incomplete rainfall record, as proposed by Yu *et al.* (2013).

●pre-mitigation debris flow; •post-mitigation debris flow; ○No debris flow; ×Hyperconcentrated flow;

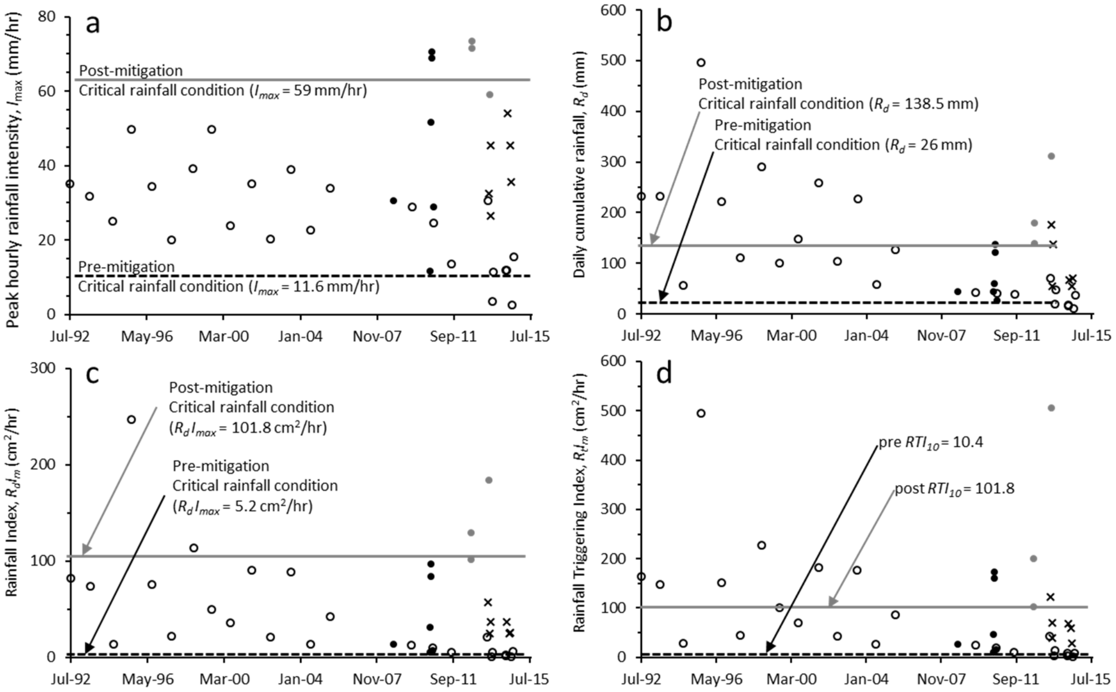

Figure 7.12 – The variations in the rainfall parameters contributing to the pre- and post-mitigation debris flows in Wenjia gully. The rainfall parameters have been significantly modified after implementing the mitigation system. *RI* considers both rainfall intensity and cumulative rainfall. RTI_{10} is the lower critical line which is defined as the lowest value associated with a debris flow.

The *I-D* thresholds are used to further evaluate the performance of the system. The pre-mitigation *I-D* thresholds were established from the five debris flows occurred before implementation of the system ($I = 54.921D^{-0.712}$), and the three events occurring afterwards were used to establish the post-mitigation *I-D* thresholds ($I = 54.07D^{-0.046}$). The mean rainfall intensity decreases linearly as rainfall duration increases on a log-scale before the mitigation system, however it remains almost unchanged with an increasing duration in the post-mitigation scenario (Figure 7.13).

The pre-mitigation *I-D* threshold of Wenjia gully is higher than some reported global and regional thresholds; but the post-mitigation *I-D* threshold is considerably higher than any of the proposed thresholds, indicating a drastic change in the *I-D* relation due to the mitigation system. Reduction in the *I-D* threshold can be expected after strong earthquakes; however changes in the pre-/post-mitigation thresholds of a debris flow gully are rarely assessed. In the pre-/post-mitigation rainfall *I-D* relation on a linear scale (Figure 7.13), rainfall duration shows little correlation with debris flow occurrences after implementation of the system, which implies that loose deposits are more prone to debris flow under intense surface run-off but less affected by the pore-water conditions.

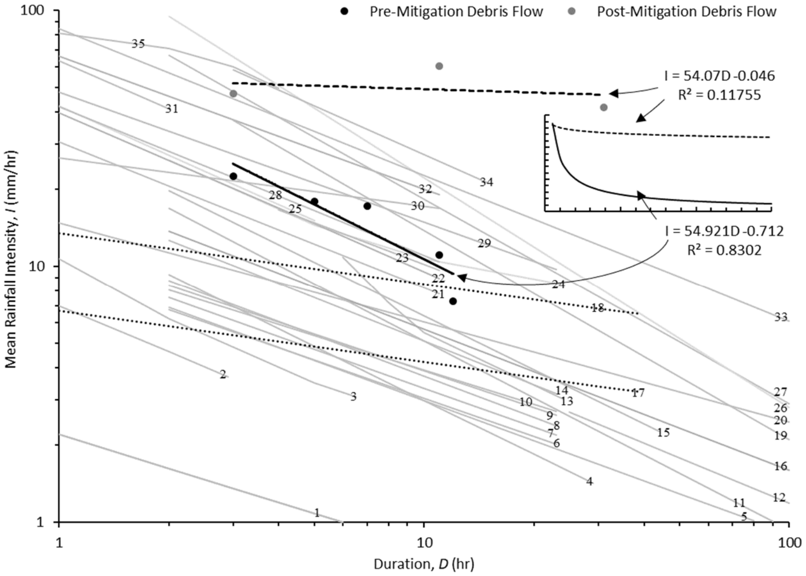

Figure 7.13 – Mean rainfall *I-D* thresholds for pre-/post-mitigation debris flows in Wenjia gully and some global and regional thresholds (reference in Table 10). The poor correlation in the post-mitigation *I-D* threshold can be attributed to the limited data. A sharp escalation in the *I-D* threshold is observed after implementing the system.

The empirical relations between $I_{\max}$, R_d, and debris flow volume, V are presented in Figure 7.14. Strong correlations are found between $I_{\max}$ and post-mitigation V as well as R_{d} and the post-mitigation V, which are noticeably higher than that of the pre-mitigation cases. As presented in Figure 7.14, the ratios between R and pre-mitigation V can be used for a simplified extreme value analysis which estimates the maximum and minimum V for an observed R_d, assuming the absence of the mitigation system, and such estimations are substantially higher than the observed values.

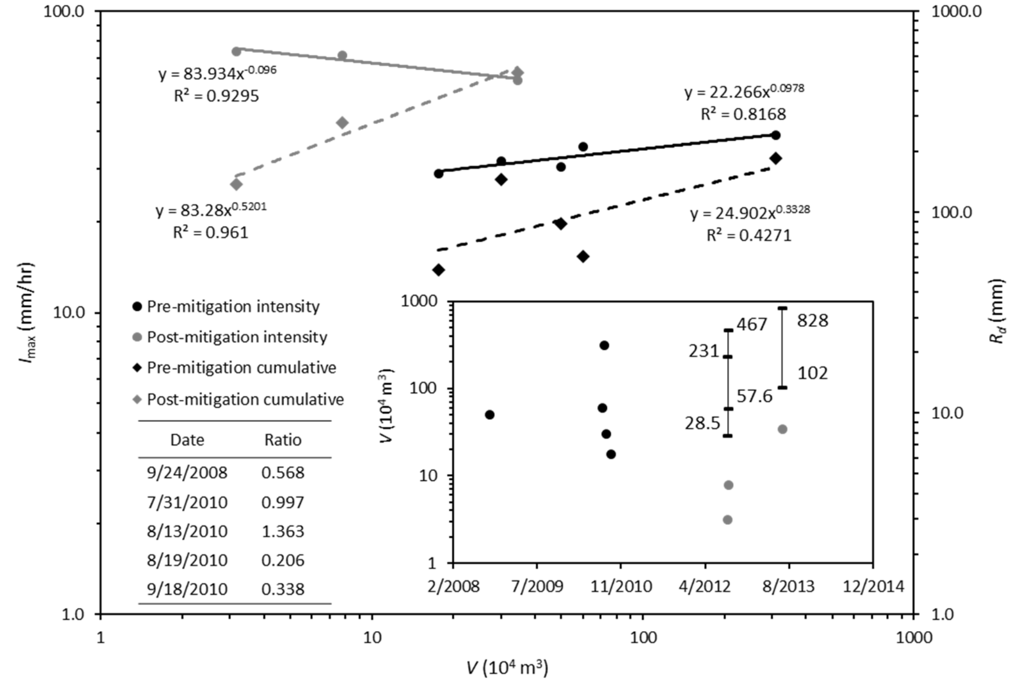

Date	Ratio
9/24/2008	0.568
7/31/2010	0.997
8/13/2010	1.363
8/19/2010	0.206
9/18/2010	0.338

Figure 7.14 – Empirical correlations between I_{max}, R_d and V before and after implementing the mitigation system. Better correlations are shown for the post-mitigation events, with significant changes in the pre-/post-mitigation correlations, indicating modifications on the characteristics of the debris flows due to the mitigation system. Ratios between R_d and pre-mitigation V are used to estimate V_{max} and V_{min} of the potential debris flows, assuming no mitigation system. Comparison of V and the estimations shows substantial differences.

For the case of the debris flow that occurred on Jul 8, 2013, the estimated volume ranges 8×10^6-1×10^6 m^3 (27 to 3 times greater than that observed), indicates catastrophic damage to the downstream community should the debris flow has occurred, assuming the same geologic and topographic environments. The total depletion of the loose deposits in the gully is estimated as 5×10^6 m^3 (about 10% of the overall deposit) after nine large-scale debris flows, assuming no new supplies in the sediment flux. Although the amount of the source material decreases and localized morphological conditions change after each debris flow, a large volume of loose deposit still exists in the gully which would be transformed into source material for subsequent debris flows, so it is logical to anticipate a continuous severe impact to the local community without the new mitigation system.

7.5 Performance of debris flow mitigation system in the regions of Qingping, Yingxiu, and Dujiangyan

This section provides a brief overview of the post-mitigation debris flow events in the regions of Qingping, Yingxiu, and Dujiangyan, and it focuses on the evaluation of the performance of some of the conventional mitigation systems implemented after Aug 2010. Limited datasets are accessible even though EWS framework has been implemented in many of the mitigated gullies. The conventional mitigation systems in these regions are typically deigned with concrete check dams and drainage channels.

7.5.1 Post-mitigation debris flows in Qingping

A large amount of loose sediment was deposited by co-seismic landslides in the Zoumalin gully, with no prior reports of debris flow before the Wenchuan earthquake. The conventional mitigation system consists of 7 large check dams in the main gully, 4 drainage channels in the branches with small sectional barriers, and an additional 3 barriers located between check dam #4 and #5 (Figure 7.15).

The layout of the EWS devices is presented in Figure 7.15, which contains the rain gauges in the main gully and several branches at different elevations. Motion detectors and thickness gauges are deployed to sense surface movements for debris flows, which can also be verified by monitoring cameras at various locations. Details on the EWS framework in Qingping is discussed by Huang *et al*. (2015a). The intense rainfall events on Aug 17, 2012 and Jul 8, 2013 resulted in two large-scale debris flows. The debris flow in 2012 filled most of the basins of the check dams and blocked the drainage channels (Figure 7.15a and Figure 7.15b); the basins were later emptied. The debris flow in 2013 overflowed the check dams (Figure 7.15c) and resulted in severe damage to the building structures near the drainage channel #1 and #2.

Figure 7.15 – The conventional mitigation system and post-mitigation debris flows in the Zoumalin gully: (a) satellite image of the gully and the mitigation system, some small-scale check dams are omitted for clarity (Google Earth image: December 22, 2014); (b) debris flow deposits overflowed check dam #4 (after debris flow on Aug 24, 2012); (c) submerged check dam #6 (after debris flow on Aug 15, 2013).

7.5.2 Post-mitigation debris flows in Yingxiu

The mitigation system in Hongchun gully was completed before the monsoon season of 2011 and was comprised of a large concrete check dam at the exit of the gully with a drainage channel, and 3 small check dams along the gully. The high slope gradient of the Shaofang gully posed challenges to the design of the mitigation system; it consisted of 3 large check dams and a short drainage channel to divert the debris flow into the Minjiang River to reduce damage to the roadway. The epicenter of the Wenchuan Earthquake is located in the Niujuan gully, in which abundant loose materials were deposited by the coseismic landslide. A total of 8 check dams were implemented, of which half is for the branches to prevent sediment supply into the main gully, with a drainage channel to guide the debris flows.

7.5.3 Post-mitigation debris flows in Dujiangyan

The source material in the gullies of Dujiangyan area were mainly deposited by the co-seismic landslides. The peak hourly rainfall on Aug 12-14, 2010 was 75 mm, with a high 2-hr cumulative precipitation of 128.3 mm. A large-scale debris flow occurred in Maliu and Dashui gully on Aug 13 and 18 during intense rainfall, which has collectively mobilized more than 10×10^6 m^3 of loose sediments. The mitigation system in the Maliu gully comprises 7 check dams, as the exit of the gully was close to a temporary settlement for residents of Longchi town that were severely damaged by the earthquake. The volume of the remaining loose materials in the Dashui gully is less compared to other gullies after August 2010, and therefore, the design of the mitigation system was modified to include only 2 larger check dams (height > 13 m) with a drainage channel at the exit of the gully.

7.5.4 Post-mitigation rainfall thresholds

The rainfall parameters associated with the pre-/post-mitigation debris flows in the studied gullies are summarized in Table 12. The volume and covered area of the debris flows in the studied gullies are found not well documented, and thus not included in the analysis. Following the same approach discussed in Section 7.4.2, changes in the rainfall thresholds are evaluating in terms of $I_{\max}$, R_{d}, *RI*, and *RTI* (Figure 7.16).

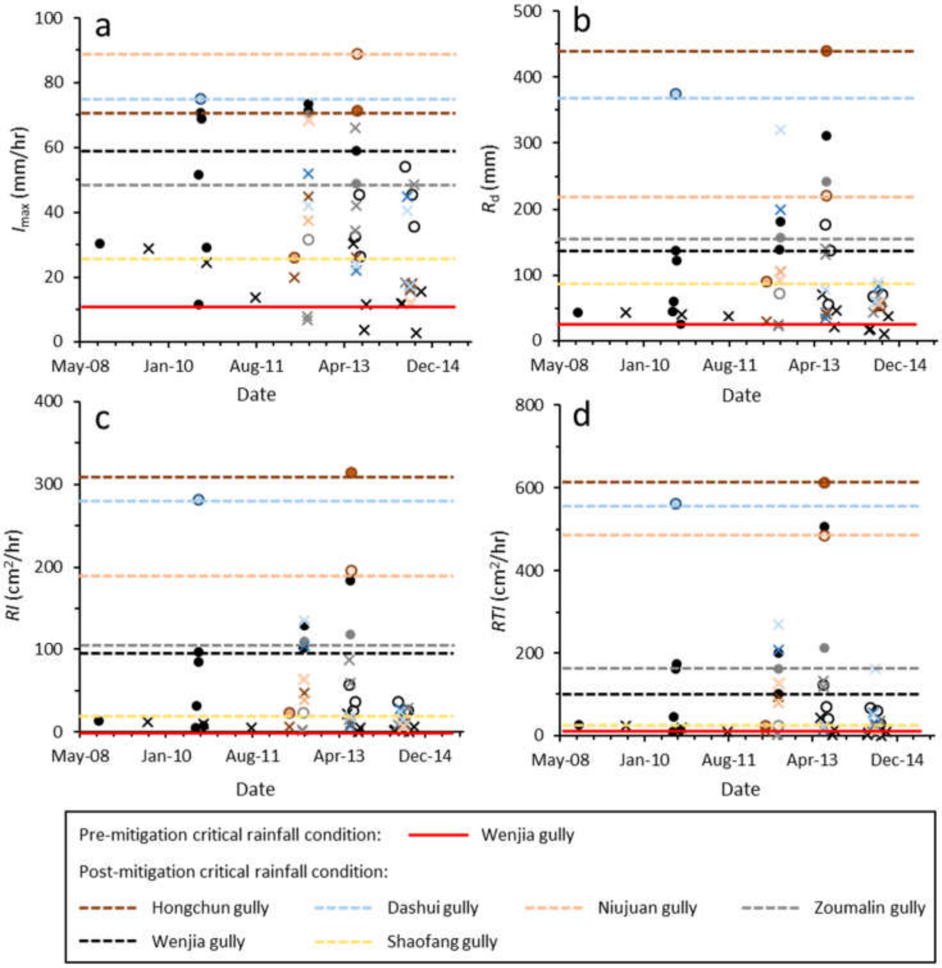

Figure 7.16 – The variations in the rainfall parameters contributing to the pre- and post-mitigation debris flows in the studied gullies. Each circle represents a debris flow event and each cross represents a rainstorm without debris flow (color scheme is identical to the critical rainfall condition).

The major challenge in using this approach is the lack of data in the gullies between the Wenchuan earthquake and the design of the mitigation system, as no systematic data collection was conducted before the long-term impact of debris flows emerged. To facilitate the evaluation, the pre-mitigation critical rainfall conditions of Wenjia gully is used as the baseline lower bounds of the thresholds (Figure 7.16). By comparing the lower bounds of rainfall thresholds, it is evident that mitigation systems in the studied gullies have significantly reduced the susceptibility to debris flows. Without normalizing the characteristics of the gullies, such as geometry or the availability of loose deposits, it is not possible to evaluate the performance between conventional and novel mitigation systems.

Table 12 – Major rainfall and debris flow events in the studied gullies before and after the implementation of mitigation systems.

Gully	Date	I_{max}	R_d	R_t	*RI*	*RTI*	*Duration*	*DF*
Hongchun	5/11/2012	20	30	60*	6	12		×
	8/17/2012	45	105	210*	47.25	94.5		×
	7/8/2013	26	40	80*	10.4	20.8		×
	7/9/2014	16.5	53	106*	8.75	17.49	20	×
	7/24/2014	18	51.5	103*	9.27	18.54	6	×
	7/10/2013	71.5	440	858	314.6	613.47		●
Shaofang	5/11/2012	26	90	90	23.4	23.4	5	●
	8/17/2012	37.5	105	210	39.38	78.75		×
Niujuan	8/17/2012	68.5	92.5	185	63.36	126.73		×
	7/10/2013	89	220	545	195.8	485.05		●
	7/9/2014	12	58	116	6.96	13.92	20	×
Maliu	8/17/2012	52	200	400*	104	208		×
	7/4/2013	22	35	70*	7.7	15.4		×
	6/19/2014	45	61	122*	27.45	54.9	5	×
	7/9/2014	17.5	82.5	165*	14.44	28.88	19	×
Dashui	8/13/2010	75	375	750	281.25	562.5		●
	8/18/2010							●
	8/17/2012	42.2	320	640*	135.04	270.08		×
	7/4/2013	24	78	90	18.72	21.6		×
	6/19/2014	40.5	61	122*	24.71	49.41		×
	7/9/2014	17	89.5	179*	15.215	160.21		×
Zoumalin	7/24/2008							●
	9/22/2008							●
	8/12/2010							●

	9/18/2010							●
	8/5/2012	6.7	22	28	1.47	1.88		×
	8/6/2012	8	25	53	2	4.24		×
	8/14/2012	31.5	72	75	22.68	23.61		○
	8/17/2012	70	157	232	109.9	162.4		●
	6/29/2013	34.48	43.1	46	14.86	15.86		×
	6/30/2013	66	132	178	87.12	117.48		×
	7/4/2013	42	140	318	58.8	133.56		×
	7/8/2013	49	241.2	431.2	118.19	211.29		●
	6/3/2014	18.5	44	76	8.14	14.06	16	×
	7/9/2014	16	70	150	11.2	24	18	×
	8/8/2014	48.4	60.5	72	29.28	34.85		×
Wenjia	9/24/2008	30.5	44	88	13.42	26.84	12	●
	8/25/2009	28.9	43.35	86.7	12.53	25.06		×
	7/25/2010	11.6	44.8	89.6	5.20	10.39		●
	7/31/2010	51.7	60.2	89.5	31.12	46.27	5	●
	8/13/2010	70.6	137.6	227.5	97.15	160.62	7	●
	8/19/2010	69	122.2	251	84.32	173.19	11	●
	9/18/2010	29	26	52	7.54	15.08	3	●
	9/22/2010	24.5	40.6	81.2	9.95	19.89		×
	8/21/2011	13.6	38.3	76.6	5.21	10.42		×
	8/14/2012	73.5	138.5	138.5	101.80	101.80	3	●
	8/17/2012	71.5	180.5	280	129.06	200.2	11	●
	6/13/2013	30.5	70.5	142	21.50	43.31		×
	6/28/2013	32.5	176.5	377.5	57.36	122.69		○
	7/6/2013	59	311.5	858	183.79	506.22	29	●
	7/25/2013	45.5	55	153	25.03	69.62		○
	8/6/2013	26.5	138	151	36.57	40.01		○
	9/1/2013	3.5	20.5	81.5	0.72	2.86		×
	9/15/2013	11.5	47	119	5.41	13.69		×
	5/9/2014	12	16	22.5	1.92	2.7		×
	5/14/2014	12	17.5	67.5	2.1	8.1		×
	6/3/2014	54	67.5	125.5	36.45	67.77		○
	7/22/2014	45.5	54.4	130.5	24.75	59.38		○
	8/8/2014	35.5	71.5	82	25.38	29.11		○
	8/20/2014	2.5	10.5	29.5	0.26	0.74		×
	9/20/2014	15.5	37.5	58.5	5.81	9.07		×

7.6 Concluding remarks

A typical predicament for the design of a debris flow mitigation system in a gully that was impacted by a major seismic event is that a large amount of loose materials has been deposited by, for example co-seismic landslides, and thus debris flows in such a gully is almost inevitable under heavy rainfall. In this chapter, we summarize the debris flow occurred after the 2008 Wenchuan earthquake in the impacted area by focusing three regions, where gullies are implemented with debris flow mitigation systems that are designed in conventional approaches as well as with novel multi-functional solutions. The studied gullies are extremely susceptible to debris flows under rainfall, with significant decreases in the critical rainfall conditions after the earthquake. Discussion focuses on the design and implementation of a novel mitigation systems in Wenjia gully, and subsequently employs rainfall parameters to evaluate the performance of both conventional and novel systems. As demonstrated by the predicament in designing the mitigation system in the Wenjia gully, debris flows are almost inevitable under saturation with such a large catchment area and the amount of loose deposits, and thus the core of the mitigation system needs not just to prevent loose deposits from being mobilized and transformed into debris flows, but also to reduces the frequency and magnitude of events.

The novel mitigation system in the Wenjia gully is not a universal solution that can be replicated and applied to other gullies. The uniqueness of each gully must be carefully considered in the design as the geological environment varies in each case. Each debris flow needs to be viewed as an individual event to understand the evolution of the failure process. The catastrophic damage caused by the debris flows between 2008 and 2011 are the results of failing to understand the characteristics of the gully; it severely under-estimated the volume of the loose deposit after a strong earthquake. The design of any effective debris flow mitigation system, regardless of the size and cost, must start with a deep understanding of the area as well as the creativity of utilizing the nature of the study area as the basis of the design.

CHAPTER 8. CONCLUSIONS AND FUTURE WORK

8.1 Conclusions

The purpose of this work is to develop a renewed understanding on 1) the mechanical behavior of Chinese loess; 2) the failure process and mechanism of long-runout flowslides in loess and other materials; 3) the cascading impacts of natural disasters on community recovery and disaster resilience; and 4) the design and performance of post-earthquake debris flow mitigation systems. The main conclusions are summarized as follows:

Theme I – Nature Systems:

- The structure of the intact Chinese loess can either impede or facilitate the onset of flow instability depending on the state of the soil, whereas increasing fines content can largely increase the flow liquefaction susceptibility at similar initial void ratios.
- The modified state parameter ψ_{m} is particularly useful in predicting flow behavior of the Chinese loess, providing a sound basis to identify the susceptibility to flow instability with the proposed criteria.
- Substantial reduction in the small-strain stiffness at the contact level during wetting, as a result of decementation of intact loess specimen; the reduced stiffness of such a wetting-decemented specimen is similar to that of a mechanical-decemented specimen.
- The converging shear wave velocity after decementation confirms the concept of a 'threshold' stress that can remove the effects of cementation on small-strain stiffness

of loess and produce an extremely similar fabric irrespective to the original fabric (possibly 10-20 MPa for LC loess).

- A compounding effect of an increasing pore-water pressure and a reducing confining stress is observed during the failure process of the centrifuge model, which appears to be vital to the development of excess pore-water pressure as slope continuous to deformation; such a model observed behavior, in principle, agrees with the field observation on loess flowslide.

Theme II – Nature-Human Systems Interactions:

- The on-site reconstruction of Yingxiu town was impacted by the secondary natural disaster of post-earthquake debris flows, whereas the residents of old Beichuan town were proven to be subject to further catastrophic post-seismic damage should the community not to be relocated.
- A Bayesian-based neural network can be effective in predicting the recovery process of the community. Such an approach enables uncertainty characterization which is essential to the decision making process, and it continues to update the prediction of recovery with new measured data, unraveling the trend of recovery at the early stage.
- The debris-flow susceptibility can be significantly increased by a strong earthquake that is accompanied by a large number of co-seismic landslides; such changes in the susceptibility can be reflected by the rainfall thresholds of the impacted area.
- In the design of post-earthquake debris flow mitigation systems, the uniqueness of each gully must be carefully considered as the geological environment varies in each case. The design of any effective mitigation system, regardless of the size and cost, must start with a deep understanding of the area, and it can be benefitted by shifting

from a ‘working-against-nature’ approach to a ‘working-with-nature’ mentality to ensure a resilient and sustainable design for the community.

8.2 Recommendations for future work

Theme I analyzes some of the important issues and challenges in studying cemented soils created by nature, in which a more systematic geotechnical understanding is gained on the mechanical behavior of loess that can aid in the mitigation of loess-related landslide. Theme II documents and explores the cascading impacts of debris flows on the recovery and reconstruction of the earthquake-impacted towns, through which the community resilience is evaluated within the context of reconstruction-dependent recovery estimation and the debris flow mitigation system effectiveness. Some key improvements and future work are recommended to enhance the current work:

Theme I – Nature Systems:

- Despite the intense flow instability, no flow liquefaction ($q \approx 0$ and $p' \approx 0$) was observed in silty loess, which may be attributed in part to the high fine content. Use of stress control as opposite to strain control could facilitate demonstration of flow liquefaction. Insights can be attained by performing constitutive modeling on flow behaviors of loess with a CSSM-based model, such as NorSand model.
- More experimental data of high quality are required to further investigate the proposed flow behavior criteria (both drained and undrained) and the possibility of flow liquefaction in silty loess.
- The grinding duration on producing reconstituted loess under dry condition appears to be affecting the small-strain stiffness, although the degree of such effect appears

to be small. More 1-D compression data on loess samples that are subjected to different durations of mechanical grinding is needed to confirm the magnitude of the effect.

- The auxetic properties discussed in Section 4.4.2, where a negative Poisson ratio is proposed for LC loess that is buried at much greater depths. More experimental data of high quality are required for both wave velocity estimation on intact loess and deeper LC loess to investigate the shear-volumetric deformation interplays of a naturally cemented material.
- A better semi-analytical model is needed to characterize the contact behavior of loess in order to assess the proportion of natural cement content at different depth of loess, as that provides an additional set of information on the depositional event of the constituent particles and the associated paleoclimatic environment.

Theme II – Nature-Human Systems Interactions:

- A single time-dependent function is used to study the prediction of the proposed BNN model, and thus the multi-dimensional dataset at different time resolutions are not considered in the current work.
- A more in-depth investigation is required on the dimension and time resolution before applying the proposed BNN to real-world case histories. In particular, the attributes of the dataset require more detailed definition as they directly affect the characteristics of the measured recovery curve.
- More field data of high quality for debris flows are required to construct a more comprehensive database of debris flows, as it provides important prior probability

on the occurrence of a future event and a useful platform to evaluate and to improve the state-of-art design of debris flow mitigation systems.

- More detailed studies with more sophisticated numerical models are required to investigate the performance of debris flow mitigation systems at a more localized scale. The improvement of the overall performance depends on the effectiveness of all the mitigation measures.

REFERENCES

Allstadt, K. (2013). Extracting source characteristics and dynamics of the August 2010 Mount Meager landslide from broadband seismograms. *J. Geophys. Res. Earth Surf.* **118**, No. 3, 1472–1490.

Alonso, E.E., Gens, A. & Josa, A. (1990). A constitutive model for partially saturated soils. *Géotechnique* **40**, No. 3, 405–430.

Altuhafi, F.N., Baudet, B. & Sammonds, P. (2010). The mechanics of subglacial sediment: an example of new "transitional" behaviour. *Can. Geotech. J.* **790**, 775–790.

Andrianopoulos, K.I., Bouckovalas, G.D. & Papadimitriou, A.G. (2001). A critical state evaluation of fines effect on liquefaction potential. In *Fourth International Conference on Recent Advances in GeotechnicaEarthquakeEngineering, SanDiego, California*.

Askarinejad, A., Zhang, W., de Boorder, M. & van der Zon, J. (2018). Centrifuge and numerical modelling of static liquefaction of fine sandy slopes. In *Physical Modelling in Geotechnics, Volume 2*: 1119–1124. CRC Press.

Assallay, A.M., Jefferson, I., Rogers, C.D.F. & Smalley, I.J. (1998). Fragipan formation in loess soils: Development of the Bryant hydroconsolidation hypothesis. *Geoderma* **83**, No. 1–2, 1–16.

Assallay, A.M., Rogers, C.D.F. & Smalley, I.J. (1997). Formation and collapse of metastable particle packings and open structures in loess deposits. *Eng. Geol.* **48**, No. 1–2, 101–115.

Ayotte, D. & Hungr, O. (2000). Calibration of a runout prediction model for debris-flows and avalanches. In *Debris-flow hazards mitigation: mechanics, prediction, and assessment: proceedings of the Second International Conference on Debris-Flow Hazards Mitigation, Taipei, Taiwan, 16-18 August 2000*: 505–514.

Bachus, R.C., Terzariol, M., Pasten, C., Chong, S.H., Dai, S., Cha, M.S., Kim, S., Jang, J., Papadopoulos, E. & Roshankhah, S. (2019). Characterization and Engineering Properties of Dry and Ponded Class-F Fly Ash. *J. Geotech. Geoenvironmental Eng.* **145**, No. 3, 4019003.

Barden, L., McGown, A. & Collins, K. (1973). The collapse mechanism in partly saturated soil. *Eng. Geol.* **7**, No. 1, 49–60.

Beddoe, R.A. & Take, W.A. (2015). Influence of slope inclination on the triggering and distal reach of hydraulically-induced flow slides. *Eng. Geol.* **187**, 170–182.

Beddoe, R.A. & Take, W.A. (2016). Loss of slope support due to base liquefaction:

comparison of 1g and centrifuge landslide flume experiments. *Soils Found.* **56**, No. 2, 251–264.

Bedin, J., Schnaid, F., Da Fonseca, A.V. & Costa Filho, L.D.M. (2012). Gold tailings liquefaction under critical state soil mechanics. *Géotechnique* **62**, No. 3, 263–267.

Been, K. & Jefferies, M.G. (1985). A state parameter for sands. *Géotechnique* **35**, No. 2, 99–112.

Berg, L.S. (1916). The origin of loess. *Commun. Russ. Geogr. Found.* **11**, 579-646 (in Russian).

Berti, M. & Simoni, A. (2007). Prediction of debris flow inundation areas using empirical mobility relationships. *Geomorphology* **90**, No. 1–2, 144–161.

Bishop, C.M. (2006). *Pattern recognition and machine learning*. springer.

Blundell, C., Cornebise, J., Kavukcuoglu, K. & Wierstra, D. (2015). Weight uncertainty in neural networks. *arXiv Prepr. arXiv1505.05424*.

Bobei, D.C., Lo, S.R., Wanatowski, D., Gnanendran, C.T. & Rahman, M.M. (2009). Modified state parameter for characterizing static liquefaction of sand with fines. *Can. Geotech. J.* **46**, No. 3, 281–295.

Bolley, S. & Oliaro, P. (1999). Analisi dei debris flows in alcuni bacini campione dell'Alta Val Susa. *Geoing. Ambient. e Mineraria, Marzo* 69–74.

Bowman, E.T., Laue, J., Imre, B. & Springman, S.M. (2010). Experimental modelling of debris flow behaviour using a geotechnical centrifuge. *Can. Geotech. J.* **47**, No. 7, 742–762.

Bowman, E.T. & Take, W.A. (2015). The runout of chalk cliff collapses in England and France - case studies and physical model experiments. *Landslides* **12**, No. 2, 225–239.

Bowman, E.T., Take, W.A., Rait, K.L. & Hann, C. (2012). Physical models of rock avalanche spreading behaviour with dynamic fragmentation. *Can. Geotech. J.* **49**, No. 4, 460–476.

Brooker, E.W. & Ireland, H.O. (1965). Earth pressures at rest related to stress history. *Can. Geotech. J.* **2**, No. 1, 1–15.

Bruneau, M., Chang, S.E., Eguchi, R.T., Lee, G.C., O'Rourke, T.D., Reinhorn, A.M., Shinozuka, M., Tierney, K., Wallace, W.A. & von Winterfeldt, D. (2003). A framework to quantitatively assess and enhance the seismic resilience of communities. *Earthq. spectra* **19**, No. 4, 733–752.

Bryant, S.K., Take, W.A., Bowman, E.T. & Millen, M.D.L. (2015). Physical and numerical modelling of dry granular flows under Coriolis conditions. *Géotechnique* **65**, No. 3, 188–200.

Burland, J.B. (1989). “Small is beautiful”—the stiffness of soils at small strains. *Can. Geotech. J.* **26**, No. 4, 499–516.

Burland, J.B. (1990). On the compressibility and shear strength of natural clays. *Géotechnique* **40**, No. 3, 329–378.

Burland, J.B., Rampello, S., Georgiannou, V.N. & Calabresi, G. (1996). A Laboratory Study of Four Stiff Clays. *Géotechnique* **46**, No. 3, 491–514.

Caine, N. (1980). The Rainfall Intensity: Duration Control of Shallow Landslides and Debris Flows. *Phys. Geogr.* **62**, No. Geografiska Annaler. Series A, 23–27.

Calcaterra, D., Parise, M., Palma, B. & Pelella, L. (2000). The influence of meteoric events in triggering shallow landslides in pyroclastic deposits of Campania, Italy. In *Landslides in Research, Theory and Practice: Proceedings of the 8th International Symposium on Landslides held in Cardiff on 26–30 June 2000*: 1–209. Thomas Telford Publishing.

Canelli, L., Ferrero, A.M., Migliazza, M. & Segalini, A. (2012). Debris flow risk mitigation by the means of rigid and flexible barriers-experimental tests and impact analysis. *Nat. Hazards Earth Syst. Sci.* **12**, 1693–1699.

Cannon, S.H. & Ellen, S.D. (1985). Rainfall conditions for abundant debris avalanches, San Francisco Bay region, California. *Calif. Geol.* **38**, No. 12, 267–272.

Cannon, S.H. & Gartner, J.E. (2005). Wildfire-related debris flow from a hazards perspective. In *Debris-flow hazards and related phenomena*: 363–385. Springer.

Cannon, S.H., Gartner, J.E., Wilson, R.C., Bowers, J.C. & Laber, J.L. (2008). Storm rainfall conditions for floods and debris flows from recently burned areas in southwestern Colorado and southern California. *Geomorphology* **96**, No. 3, 250–269.

Carrera, A., Coop, M. & Lancellotta, R. (2011). Influence of grading on the mechanical behaviour of Stava tailings. *Géotechnique* **61**, No. 11, 935–946.

Ceriani, M., Lauzi, S. & Padovan, N. (1992). Rainfalls and landslides in the alpine area of Lombardia region, central Alps, Italy. In *Proc. Int. Symp. Interpraevent*: 9–20.

Cha, M., Ph, D., Asce, a M., Santamarina, J.C., Ph, D., Asce, M., Kim, H., Cho, G. & Ph, D. (2014). Small-strain stiffness , shear-wave velocity , and soil compressibility. *J. Geotech. Geoenvironmental Eng.* **140**, No. 10, 1–4.

Chang, S.E. (2000). Disasters and transport systems: loss, recovery and competition at the Port of Kobe after the 1995 earthquake. *J. Transp. Geogr.* **8**, No. 1, 53–65.

Chang, S.E. & Shinozuka, M. (2004). Measuring improvements in the disaster resilience of communities. *Earthq. Spectra* **20**, No. 3, 739–755.

Chen, C.-Y., Chen, T.-C., Yu, F.-C., Yu, W.-H. & Tseng, C.-C. (2005). Rainfall duration and debris-flow initiated studies for real-time monitoring. *Environ. Geol.* **47**, No. 5, 715–724.

Chen, J.C. (2011). Variability of impact of earthquake on debris-flow triggering conditions: Case study of Chen-Yu-Lan watershed, Taiwan. *Environ. Earth Sci.* **64**, No. 7, 1787–1794.

Chen, J.C., Jan, C.D. & Huang, W.S. (2013). Characteristics of rainfall triggering of debris flows in the Chenyulan watershed, Taiwan. *Nat. Hazards Earth Syst. Sci.* **13**, No. 4, 1015–1023.

Chen, X., Cui, P. & Tang, B. (2008). New site selection for Beichuan County seat after 5.12 earthquake. *J. Mt. Sci.* **5**, No. 26, 524-530 (in Chinese).

Chen, Y. & Booth, D.C. (2011). *The Wenchuan earthquake of 2008: anatomy of a disaster*. Springer.

Chen, Z.-H., Fredlund, D.G. & Gan, J.K.M. (1999). Overall volume change, water volume change, and yield associated with an unsaturated compacted loess. *Can. Geotech. J.* **36**, No. 2, 321–329.

Cheng, Q., Wu, S. & Su, Y. (2010). Geological Hazards due to Wenchuan Earthquake Along Yingxiu to Wolong Highway. *J. Eng. Geol.* **18**, No. 2, 160–167.

China Academy of Urban Planing and Design. (2008). *Work Plan for Reconstruction of County Seat of Beichuan Qiang Autonomous County*. Beijing.

China Institute of Geological Environmental Monitoring. (2009). *An Image-Based Study on Typical Geological Hazards Caused by Wenchuan Earthquake*. Beijing: Geological Publishing House.

Cimellaro, G.P., Reinhorn, A.M. & Bruneau, M. (2010). Framework for analytical quantification of disaster resilience. *Eng. Struct.* **32**, No. 11, 3639–3649.

Clough, G.W., Sitar, N., Bachus, R.C. & Rad, N.S. (1981). Cemented sands under static loading. *J. Geotech. Geoenvironmental Eng.* **107**, No. ASCE 16319 Proceeding.

Coop, M.R. & Atkinson, J.H. (1993). The mechanics of cemented carbonate sands. *Geotechnique* **43**, No. 1, 53–67.

Corominas, J. (1996). The angle of reach as a mobility index for small and large landslides. *Can. Geotech. J.* **33**, No. 2, 260–271.

Costa, J.E. & Wieczorek, G.F. (1987). *Debris flows/avalanches: process, recognition, and mitigation*. Geological Society of America.

Cotecchia, F. & Chandler, R.J. (1997). The influence of structure on the pre-failure behaviour of a natural clay. *Géotechnique* **47**, No. 3, 523–544.

Cruden, D.M. (1991). A Simple Definition of A Landslide. *Bull. Int. Assoc. Eng. Geol.* **43**, No. 1, 27–29.

Cucchiaro, S., Cavalli, M., Vericat, D., Crema, S., Llena, M., Beinat, A., Marchi, L. & Cazorzi, F. (2019). Geomorphic effectiveness of check dams in a debris-flow catchment using multi-temporal topographic surveys. *Catena* **174**, 73–83.

Cuccovillo, T. & Coop, M.R. (1997). Yielding and pre-failure deformation of structured sands. *Geotechnique* **47**, No. 3, 491–508.

Cui, P., Zhou, G.G.D., Zhu, X.H. & Zhang, J.Q. (2013). Scale amplification of natural debris flows caused by cascading landslide dam failures. *Geomorphology* **182**, No. August 2010, 173–189.

Cui, Y.J. & Delage, P. (1996). Yeilding and plastic behaviour of an unsaturated compacted silt. *Géotechnique* **46**, No. 2, 291–311.

Dai, F.C., Tu, X.B., Xu, C., Gong, Q.M. & Yao, X. (2011). Rock avalanches triggered by oblique-thrusting during the 12 May 2008 Ms 8.0 Wenchuan earthquake, China. *Geomorphology* **132**, No. 3–4, 300–318.

Delage, P., Audiguier, M., Cui, Y.-J. & Howat, M.D. (1996). Microstructure of a compacted silt. *Can. Geotech. J.* **33**, No. 1, 150–158.

Delaney, K.B. & Evans, S.G. (2014). The 1997 Mount Munday landslide (British Columbia) and the behaviour of rock avalanches on glacier surfaces. *Landslides* **11**, No. 6, 1019–1036.

Derbyshire, E. (2001). Geological hazards in loess terrain, with particular reference to the loess regions of China. *Earth-Science Rev.* **54**, No. 1–3, 231–260.

Derbyshire, E., Dijkstra, T.A., Smalley, I.J. & Li, Y. (1994). Failure mechanisms in loess and the effects of moisture content changes on remoulded strength. *Quat. Int.* **24**, No. C, 5–15.

Derbyshire, E. & Mellors, T.W. (1988). Geological and geotechnical characteristics of some loess and loessic soils from China and Britain: A comparison. *Eng. Geol.* **25**, No. 2–4, 135–175.

Derbyshire, E., Meng, X., Wang, J., Zhou, Z. & Li., B. (1995). Collapsible loess on the loess plateau of China. In *Genesis and Properties of Collapsible Soils*: 267–293. Springer Netherlands.

deWolfe, V.G., Santi, P.M., Ey, J. & Gartner, J.E. (2008). Effective mitigation of debris flows at Lemon Dam, La Plata County, Colorado. *Geomorphology* **96**, No. 3–4, 366–

377.

Dijkstra, T.A., Rogers, C.D.F., Smalley, I.J., Derbyshire, E., Yong, L. & Min, X. (1994). The loess of north-central China : Geotechnical properties and their relation to slope stability. *Eng. Geol.* **36**, 153–171.

Ding, Z., Sun, J., Rutter, N.W., Rokosh, D. & Liu, T. (1999). Changes in sand content of loess deposits along a north–south transect of the Chinese Loess Plateau and the implications for desert variations. *Quat. Res.* **52**, No. 1, 56–62.

Dunford, M. & Li, L. (2011). Earthquake reconstruction in Wenchuan: Assessing the state overall plan and addressing the “forgotten phase.” *Appl. Geogr.* **31**, No. 3, 998–1009.

Eckersley, D. (1990). Instrumented laboratory flowslides. *Géotechnique* **40**, No. 3, 489–502.

Escribano, D.E. & Nash, D.F.T. (2015). Changing anisotropy of G0 in Hostun sand during drained monotonic and cyclic loading. *Soils Found.* **55**, No. 5, 974–984.

Evans, K.E., Nkansah, M.A., Hutchinson, I.J. & Rogers, S.C. (1991). Molecular network design. *Nature* **353**, No. 6340, 124.

Expert Group of Science and Technology in Disaster Relief. (2008). *Analysis and Assessment of Damage in Wenchuan Earthquake*. Beijing: Science Press.

Fam, M. & Santhamarian, J.C. (1997). A study of consolidation using mechanical and electromagnetic waves. *Géotechnique* **47**, No. 2, 203–219.

Fam, M.A. & Santamarina, J.C. (1996). Study of clay-cement slurries with mechanical and electromagnetic waves. *J. Geotech. Eng.* **122**, No. 5, 365–373.

Fan, J., Rosenfeld, D., Yang, Y., Zhao, C., Leung, L.R. & Li, Z. (2015). Substantial contribution of anthropogenic air pollution to catastrophic floods in Southwest China. *Geophys. Res. Lett.* **42**, No. 14, 6066–6075.

Fan, X., Scaringi, G., Korup, O., West, A.J., Westen, C.J., Tanyas, H., Hovius, N., Hales, T.C., Jibson, R.W., Allstadt, K.E., Zhang, L., Evans, S.G., Xu, C., Li, G., Pei, X., Xu, Q. & Huang, R. (2019). Earthquake-induced chains of geologic hazards: patterns, mechanisms, and impacts. *Rev. Geophys.* 2018RG000626.

Fan, X., Tang, C.X., van Westen, C.J. & Alkema, D. (2012). Simulating dam-breach flood scenarios of the Tangjiashan landslide dam induced by the Wenchuan Earthquake. *Nat. Hazards Earth Syst. Sci.* **12**, No. 10, 3031–3044.

Fan, X., Xu, Q., Scaringi, G., Li, S. & Peng, D. (2017). A chemo-mechanical insight into the failure mechanism of frequently occurred landslides in the Loess Plateau, Gansu Province, China. *Eng. Geol.* **228**, No. June, 337–345.

Fearon, R.E. & Coop, M.R. (2000). Reconstitution: what makes an appropriate reference material? *Géotechnique* **50**, No. 4, 471–477.

Feda, J. (1966). Structural stability of subsident loess soil from Praha-Dejvice. *Eng. Geol.* **1**, No. 3, 201–219.

Feda, J. (1988). Collapse of loess upon wetting. *Eng. Geol.* **25**, No. 2–4, 263–269.

Feda, J., Boháč, J. & Herle, I. (1993). Compression of collapsed loess: Studies on bonded and unbonded soils. *Eng. Geol.* **34**, No. 1–2, 95–103.

Fernandez, A.L. & Santamarina, J.C. (2001). Effect of cementation on the small-strain parameters of sands. *Can. Geotech. J.* **38**, No. 1, 191–199.

Fredlund, D.G. & Gan, J.K.M. (1995). The collapse mechanism of a soil subjected to one-dimensional loading and wetting. In *Genesis and properties of collapsible soils*: 173–205. Springer.

Fu, B., Shi, P., Guo, H., Okuyama, S., Ninomiya, Y. & Wright, S. (2011). Surface deformation related to the 2008 Wenchuan earthquake, and mountain building of the Longmen Shan, eastern Tibetan Plateau. *J. Asian Earth Sci.* **40**, No. 4, 805–824.

Fuchs, S., Heiss, K. & Hübl, J. (2007). Towards an empirical vulnerability function for use in debris flow risk assessment. *Nat. Hazards Earth Syst. Sci.* **7**, No. 5, 495–506.

Fuller, M.L. & Clapp, F.G. (1924). Loess and rock dwellings of Shensi, China. *Geogr. Rev.* **14**, No. 2, 215–226.

Gallet, S., Jahn, B. & Torii, M. (1996). Geochemical characterization of the Luochuan loess-paleosol sequence, China, and paleoclimatic implications. *Chem. Geol.* **133**, No. 1–4, 67–88.

Gan, J., Huang, R., Li, Q., Ye, X. & Gao, W. (2010). Formation Mechanism of Geo-Hazards Triggered by Wenchuan Ms 8.0 Earthquake along Dujiangyan-Wenchuan Highway. *J. Geomech.* **16**, No. 2, 146–158.

Gao, G. (1986). Formation and development of the structure of collapsing loess in China. *Eng. Geol.* **25**, No. 1966, 236–246.

Gao, Z., Tao, X., Kong, J. & Hong, H. (2009). Study on Characteristics and Cause of Damages to the Downtown of Beichuan County due to Wenchuan Earthquake. *J. Disaster-Prevention Mitig. Eng.* **29**, No. 1, 114–118.

Gasparre, A. (2005). *Advanced Laboratory Characterisation of London Clay*. Imperial College London.

Glade, T., Crozier, M. & Smith, P. (2000). Applying probability determination to refine landslide-triggering rainfall thresholds using an empirical "Antecedent Daily Rainfall

Model." *Pure Appl. Geophys.* **157**, No. 6–8, 1059–1079.

Gorum, T., Fan, X., van Westen, C.J., Huang, R.Q., Xu, Q., Tang, C. & Wang, G. (2011). Distribution pattern of earthquake-induced landslides triggered by the 12 May 2008 Wenchuan earthquake. *Geomorphology* **133**, No. 3–4, 152–167.

Gotham, K.F. & Greenberg, M. (2008). Post-disaster recovery and rebuilding in New York and New Orleans. *Soc. Forces* **87**, No. 2, 1–24.

Government of Mianyang City. (2010). Deposit material from debris flows block spillway of Tangjiashan Quake Lake [WWW Document]. URL http://www.my.gov.cn/MYGOV/147211412819673088/20100925/526688.html

Government of the Ngawa Tibetan and Qiang Autonomous Prefecture. (2010). *Regulations on Post-Wenchuan Earthquake Rehabilitation and Reconstruction for Yingxiu Town.*

Greaves, G.N., Greer, A.L., Lakes, R.S. & Rouxel, T. (2011). Poisson's ratio and modern materials. *Nat. Mater.* **10**, No. 11, 823.

Guo, X., Cui, P., Li, Y., Ma, L., Ge, Y. & Mahoney, W.B. (2016). Intensity-duration threshold of rainfall-triggered debris flows in the Wenchuan Earthquake affected area, China. *Geomorphology* **253**, 208–216.

Guthrie, R.H., Friele, P., Allstadt, K., Roberts, N., Evans, S.G., Delaney, K.B., Roche, D., Clague, J.J. & Jakob, M. (2012). The 6 August 2010 Mount Meager rock slide-debris flow, Coast Mountains, British Columbia: characteristics, dynamics, and implications for hazard and risk assessment. *Nat. Hazards Earth Syst. Sci.* **12**, No. 5, 1277–1294.

Guzzetti, F., Peruccacci, S., Rossi, M. & Stark, C.P. (2007). Rainfall thresholds for the initiation of landslides in central and southern Europe. *Meteorol. Atmos. Phys.* **98**, No. 3–4, 239–267.

Guzzetti, F., Peruccacci, S., Rossi, M. & Stark, C.P. (2008). The rainfall intensity–duration control of shallow landslides and debris flows: an update. *Landslides* **5**, No. 1, 3–17.

He, C.-R., Zhang, R., Chen, Q. & Han, S.-L. (2010). Earthquake characteristics and building damage in high-intensity areas of Wenchuan earthquake I: Yingxiu town. *Nat. Hazards* **57**, No. 2, 435–451.

Hird, C. & Chan, C.M. (2008). One-dimensional compression tests on stabilized clays incorporating shear wave velocity measurements. *Geotech. Test. J.* **31**, No. 2, 166–174.

Holling, C.S. (1973). Resilience and stability of ecological systems. *Annu. Rev. Ecol. Syst.* 1–23.

Hong, Y., Hiura, H., Shino, K., Sassa, K., Suemine, A., Fukuoka, H. & Wang, G. (2005). The influence of intense rainfall on the activity of large-scale crystalline schist landslides in Shikoku Island, Japan. *Landslides* **2**, No. 2, 97–105.

Hsu, K.J. (1975). Catastrophic debris streams (sturzstroms) generated by rockfalls. *Geol. Soc. Am. Bull.* **86**, No. 1, 129–140.

Hu, W., Huang, R., McSaveney, M., Zhang, X. hui, Yao, L. & Shimamoto, T. (2018). Mineral changes quantify frictional heating during a large low-friction landslide. *Geology* **46**, No. 3, 223–226.

Huang, J., Huang, R.Q., Ju, N.P., Xu, Q. & He, C.Y. (2015a). 3D WebGIS-based platform for debris flow early warning: A case study. *Eng. Geol.* **197**, 57–66.

Huang, J., Ju, N.P., Liao, Y.J. & Liu, D.D. (2015b). Determination of rainfall thresholds for shallow landslides by a probabilistic and empirical method. *Nat. Hazards Earth Syst. Sci.* **15**, No. 12, 2715–2723.

Huang, R. (2009a). *Geohazard Assessment of the Wenchuan Earthquake*. Beijing: Science Press.

Huang, R. (2011a). Geo-engineering lessons learned from the 2008 Wenchuan earthquake in Sichuan and their significance to reconstruction. *J. Mt. Sci.* **8**, No. 2, 176–189.

Huang, R. & Fan, X. (2013). The landslide story. *Nat. Geosci.* **6**, No. 5, 325–326.

Huang, R. & Li, W. (2009). Analysis of the geo-hazards triggered by the 12 May 2008 Wenchuan Earthquake, China. *Bull. Eng. Geol. Environ.* **68**, No. 3, 363–371.

Huang, R. & Li, W. (2014). Post-earthquake landsliding and long-term impacts in the Wenchuan earthquake area, China. *Eng. Geol.* **182**, 111–120.

Huang, R.Q. (2009b). Some catastrophic landslides since the twentieth century in the southwest of China. *Landslides* **6**, No. 1, 69–81.

Huang, X. (2011b). *Beichuan Qiang Autonomous County Yearbook 2009*.

Hubbard, J. & Shaw, J.H. (2009). Uplift of the Longmen Shan and Tibetan plateau, and the 2008 Wenchuan (M = 7.9) earthquake. *Nature* **458**, No. 7235, 194.

Huebl, J. & Fiebiger, G. (2005). Debris-flow mitigation measures. In *Debris-flow hazards and related phenomena*: 445–487. Springer.

Hungr, O. & Evans, S.G. (2004). Entrainment of debris in rock avalanches: an analysis of a long run-out mechanism. *Geol. Soc. Am. Bull.* **116**, No. 9–10, 1240–1252.

Hungr, O., Leroueil, S. & Picarelli, L. (2014). The Varnes classification of landslide types, an update. *Landslides* **11**, No. 2, 167–194.

Iuchi, K. (2014). Planning resettlement after disasters. *J. Am. Plan. Assoc.* **80**, No. 4, 413–425.

Iverson, R.M. (1997). The Physics of Debris Flows. *Rev. Geophys.* **35**, No. 3, 245–296.

Iverson, R.M. (2012). Elementary theory of bed-sediment entrainment by debris flows and avalanches. *J. Geophys. Res. Earth Surf.* **117**, No. F3.

Iverson, R.M. & George, D.L. (2015). Modelling landslide liquefaction, mobility bifurcation and the dynamics of the 2014 Oso disaster. *Géotechnique* **66**, No. 3, 175–187.

Iverson, R.M., Reid, M.E. & LaHusen, R.G. (1997). Debris-flow mobilization from landslides. *Annu. Rev. Earth Planet. Sci.* **25**, No. 1, 85–138.

Iverson, R.M., Reid, M.E., Logan, M., LaHusen, R.G., Godt, J.W. & Griswold, J.P. (2011). Positive feedback and momentum growth during debris-flow entrainment of wet bed sediment. *Nat. Geosci.* **4**, No. 2, 116–121.

Jakob, M., Hungr, O. & Jakob, D.M. (2005). *Debris-flow hazards and related phenomena*. Springer.

Jan, C. & Chen, C. (2005). Debris flows caused by Typhoon Herb in Taiwan. In *Debris-Flow Hazards and Related Phenomena*: 539–563. Springer.

Jan, C., Lee, M. & Huang, T. (2002). Rainfall Threshold Criterion for Debris-Flow Initiation. *Natl. Cheng K. Univ.* 9104-9112 (in Chinese).

Jan, C.D. & Lee, M.H. (2004). A debris-flow rainfall-based warning model. *J Chin Soil Water Conserv* **35**, No. 3, 275–285.

Jang, D.-J., Frost, J.D. & Park, J.-Y. (1999). Preparation of epoxy impregnated sand coupons for image analysis. *Geotech. Test. J.* **22**, No. 2, 153–164.

Jefferies, M. & Been, K. (2015). *Soil liquefaction: a critical state approach*. 2nd edn. CRC press.

Ji, S., Li, L., Motra, H.B., Wuttke, F., Sun, S., Michibayashi, K. & Salisbury, M.H. (2018). Poisson's ratio and auxetic properties of natural rocks. *J. Geophys. Res. Solid Earth* **123**, No. 2, 1161–1185.

Jiang, M., Hu, H. & Liu, F. (2012). Summary of collapsible behaviour of artificially structured loess in oedometer and triaxial wetting tests. *Can. Geotech. J.* **49**, No. 10, 1147–1157.

Jibson, R.W. (1989). Debris flows in southern Puerto Rico. *Geol. Soc. Am. Spec. Pap.* **236**, 29–56.

Jing, L. (2007). *Beichuan Qiang Autonomous County Yearbook 2007*. Qushan Town: Beichuan County Government.

Johnson, B.C., Campbell, C.S. & Melosh, H.J. (2016). The reduction of friction in long runout landslides as an emergent phenomenon. *J. Geophys. Res. Earth Surf.* **121**, No. 5, 881–889.

Jovičić, V., Coop, M. & Simpson, B. (2006). Interpretation and modelling of deformation characteristics of a stiff North Sea clay. *Can. Geotech. J.* **43**, No. 4, 341–354.

Keaton, J.R., Wartman, J. & Montgomery, D.R. (2014). *The 22 March 2014 Oso Landslide, Snohomish County, Washington*. GEER.

Keefer, D.K. (1984). Landslides caused by earthquakes. *Geol. Soc. Am. Bull.* **95**, No. 4, 406–421.

Konrad, J.-M. (1998). Sand state from cone penetrometer tests: a framework considering grain crushing stress. *Géotechnique* **48**, No. 2, 201–215.

Kramer, S.L. (1996). *Geotechnical Earthquake Engineering*. 1st edn. Englewood Cliffs, NJ: Prentice Hall.

Kucukelbir, A., Tran, D., Ranganath, R., Gelman, A. & Blei, D.M. (2017). Automatic differentiation variational inference. *J. Mach. Learn. Res.* **18**, No. 1, 430–474.

Lade, P. V. & Yamamuro, J.A. (2011). Evaluation of static liquefaction potential of silty sand slopes. *Can. Geotech. J.* **48**, No. 2, 247–264.

Lade, P. V. (1993). Initiation of static instability in the submarine Nerlerk berm. *Can. Geotech. J.* **30**, No. 6, 895–904.

Lakes, R. (1987). Foam structures with a negative Poisson's ratio. *Science (80-.).* **235**, 1038–1041.

Lambe, T.W. & Whitman, R. V. (1969). Soil mechanics, series in soil engineering. *Jhon Wiley Sons*.

Langroudi, A.A. (2014). *Micromechanics of collapse in loess*. University of Birmingham.

Larsen, M.C. & Simon, A. (1993). A rainfall intensity-duration threshold for landslides in a humid-tropical environment, Puerto Rico. *Geogr. Ann. Ser. A. Phys. Geogr.* 13–23.

Lee, Y.S., Cheuk, C.Y. & Bolton, M.D. (2008). Instability caused by a seepage impediment in layered fill slopes. *Can. Geotech. J.* **45**, No. 10, 1410–1425.

Leng, Y., Peng, J., Wang, Q., Meng, Z. & Huang, W. (2018). A fluidized landslide occurred in the Loess Plateau: A study on loess landslide in South Jingyang tableland. *Eng. Geol.* **236**, No. 4, 129–136.

Leonards, G.A. & Altschaeffl, A.G. (1964). Compressibility of clay. *J. Soil Mech. Found. Div.* **90**, No. 5, 133–156.

Leroueil, S., Tavenas, F. & Locat, J. (1984). Discussion: Correlations between index tests and the properties of remoulded clays. *Géotechnique* **35**, No. 2, 223–226.

Li, P., Qian, H. & Wu, J. (2014). Accelerate research on land creation. *Nature* 5-29–31.

Li, P., Vanapalli, S. & Li, T. (2016). Review of collapse triggering mechanism of collapsible soils due to wetting. *J. Rock Mech. Geotech. Eng.* **8**, No. 2, 256–274.

Li, P., Xie, W., Pak, R.Y.S. & Vanapalli, S.K. (2019). Microstructural evolution of loess soils from the Loess Plateau of China. *Catena* **173**, 276–288.

Li, W. & Coop, M.R. (2018). Mechanical behaviour of Panzhihua iron tailings. *Can. Geotech. J.* **56**, No. 3, 420–435.

Li, X., Yu, A., Gan, P., Li, M. & Liu, L. (2008a). Survey and analysis of the diaster and engineering damage of Beichuan County Seat in Ms8.0 Wenchuan Earthquake. *Technol. Earthq. Disaster Prev.* **3**, No. 4, 352–362.

Li, X. & Zhao, J. (2018). A unified CFD-DEM approach for modeling of debris flow impacts on flexible barriers. *Int. J. Numer. Anal. Methods Geomech.* **42**, No. 14, 1643–1670.

Li, X., Zhou, Z., Yu, H., Wen, R., Lu, D., Huang, M., Zhou, Y. & Cu, J. (2008b). Strong motion observations and recordings from the great Wenchuan Earthquake. *Earthq. Eng. Eng. Vib.* **7**, No. 3, 235–246.

Li, Y. & Huang, R. (2008). Engineering Geological Assessments of Reconstruction Sites for Cities and Towns Destoryed by Wenchuan Earthquake. *J. Engingeering Geol.* **16**, No. 6, 764–773.

Li, Y. & Mo, P. (2019). A unified landslide classification system for loess slopes: A critical review. *Geomorphology*.

Lin, X., Li, T., Zhao, J., Wang, H. & Li, P. (2014). Permeability characteristics of loess under different consolidation pressures in the Heifangtai platform. *Hydrogeol. Eng. Geol.* **41**, No. 1, 41-47 (in Chinese).

Ling, H. & Ling, H.I. (2012). Centrifuge model simulations of rainfall-induced slope instability. *J. Geotech. geoenvironmental Eng.* **138**, No. 9, 1151–1157.

Liu, D. (1985). *Loess and the Environment*. Beijing (in Chinese): Science Press.

Liu, F., Xu, Q., Zhang, Y., Frost, J.D. & Zhang, X. (2018). State-dependent flow instability of a silty loess. *Géotechnique Lett.* 1–19.

Liu, F.Z., Xu, Q., Dong, X.J., Yu, B., Frost, J.D. & Li, H.J. (2017a). Design and performance of a novel multi-function debris flow mitigation system in Wenjia Gully, Sichuan. *Landslides* **14**, No. 6, 2089–2104.

Liu, H., Zhang, D., Wei, Q. & Guo, Z. (2017b). Comparison study on two post-earthquake rehabilitation and reconstruction modes in China. *Int. J. Disaster Risk Reduct.* **23**, No. October 2016, 109–118.

Liu, L., Lin, Y. & Wang, S. (2014). Urban design for post-earthquake reconstruction: A case study of Wenchuan County, China. *Habitat Int.* **41**, 290–299.

Liu, N., Zhang, J., Lin, W., Cheng, W. & Chen, Z. (2009). Draining Tangjiashan Barrier Lake after Wenchuan Earthquake and the flood propagation after the dam break. *Sci. China Ser. E Technol. Sci.* **52**, No. 4, 801–809.

Liu, Z. (1997). *Mechanics and Engineering of Loess*. Beijing (in Chinese).

Liu, Z., Liu, F., Ma, F., Wang, M., Bai, X., Zheng, Y., Yin, H. & Zhang, G. (2015). Collapsibility, composition, and microstructure of loess in China. *Can. Geotech. J.* **53**, No. 4, 673–686.

Lu, Z. (1984). Basic charateristics of landslide distribution and main types landslides in China. In *International Symposium on Landslides. Toronto,(5)*: 411–418.

Lucas, A., Mangeney, A. & Ampuero, J.P. (2014). Frictional velocity-weakening in landslides on Earth and on other planetary bodies. *Nat. Commun.* **5**, 3417.

Ma, C., Wang, Y., Hu, K., Du, C. & Yang, W. (2017). Rainfall intensity–duration threshold and erosion competence of debris flows in four areas affected by the 2008 Wenchuan earthquake. *Geomorphology* **282**, 85–95.

Ma, Y., Lu, X., Ye, L., Tang, D. & Li, Y. (2011). Seismic Danage Simulation and Analysis of Typical RC Frames of Xuankou School. *Eng. Mech.* **28**, No. 5, 71–77.

Mackechnie, W.R. (1989). Collapsible and swelling soils - Part 1 : Collapsible soils. In *12th International Conference on Soil Mechanics and Foundational Engineering*: 2485–2490. Rio de Janeiro.

Mao, F., Ma, J. & Zhou, W. (2008). Site Selection for Wenchuan Earthquake after the Earthquake and Historical Anti-seismic Experience in Beijing. *Geo-Information Sci.* **10**, No. 4, 503–510.

Marchi, L., Arattano, M. & Deganutti, A.M. (2002). Ten years of debris-flow monitoring in the Moscardo Torrent (Italian Alps). *Geomorphology* **46**, No. 1, 1–17.

Martins, F.B., Bressani, L.A., Coop, M.R. & Bica, A.V.D. (2001). Some aspects of the compressibility behaviour of a clayey sand. *Can. Geotech. J.* **38**, No. 6, 1177–1186.

McDougall, S. (2016). 2014 Canadian Geotechnical Colloquium: Landslide runout analysis - current practice and challenges. *Can. Geotech. J.* **54**, No. 5, 605–620.

Meng, X. & Derbyshire, E. (1998). Landslides and their control in the Chinese Loess

Plateau: models and case studies from Gansu Province, China. *Geol. Soc. London, Eng. Geol. Spec. Publ.* **15**, No. 1, 141–153.

Mesri, G. & Godlewski, P.M. (1977). Time and stress-compressibility interrelationship. *ASCE J Geotech Eng Div* **103**, No. 5, 417–430.

Michalowski, R.L. (2005). Coefficient of earth pressure at rest. *J. Geotech. geoenvironmental Eng.* **131**, No. 11, 1429–1433.

Miles, S.B. & Chang, S.E. (2006). Modeling community recovery from earthquakes. *Earthq. Spectra* **22**, No. 2, 439–458.

Milne, F.D., Brown, M.J., Knappett, J.A. & Davies, M.C.R. (2012). Centrifuge modelling of hillslope debris flow initiation. *Catena* **92**, 162–171.

Milodowski, A.E., Northmore, K.J., Kemp, S.J., Entwisle, D.C., Gunn, D.A., Jackson, P.D., Boardman, D.I., Zoumpakis, A., Rogers, C.D.F., Dixon, N., Jefferson, I., Smalley, I.J. & Clarke, M. (2015). The mineralogy and fabric of 'Brickearths' in Kent, UK and their relationship to engineering behaviour. *Bull. Eng. Geol. Environ.* **74**, No. 4, 1187–1211.

Ministry of Construction of China. (2001). *Code for Seismic Design of Buildings, GB 50011-2001*. China Architecture & Building Press.

Ministry of Construction of China. (2010). *Code for Seismic Design of Buildings, GB 50011-2010*. China Architecture & Building Press.

Ministry of Land and Resources of China. (2006). *Specification of Geological Investigation for Debris Flow Stabilization (DZ/T0020)*.

Mitchell, J.K. & Soga, K. (2005). *Fundamentals of soil behavior*. John Wiley & Sons New York.

Montgomery, D.R., Schmidt, K.M., Greenberg, H.M. & Dietrich, W.E. (2000). Forest clearing and regional landsliding. *Geology* **28**, No. 4, 311–314.

Muhs, D.R., Bettis, E.A., Chan, M.A. & Archer, A.W. (2003). Quaternary loess-paleosol sequences as examples of climate-driven sedimentary extremes. *Spec. Pap. Soc. Am.* 53–74.

Munoz-Castelblanco, J., Pereira, J.-M., Delage, P. & Cui, Y.-J. (2012). The water retention properties of a natural unsaturated loess from northern France. *Géotechnique* **62**, No. 2, 95–106.

Muñoz-Castelblanco, J., Pereira, J.M., Delage, P. & Cui, Y.J. (2011). Some aspects of the compression and collapse behaviour of an unsaturated natural loess. *Géotechnique Lett.* **1**, No. April-June, 17–22.

Nakagawa, K., Soga, K., Mitchell, J.K. & Sadek, M.S. (1995). Soil structure changes during and after consolidation as indicated by shear wave velocity and electrical conductivity measurements. In *Proceedings of the Symposium on Compression and Consolidation of Clayey Soils (IS-Hiroshima) v. 2*. AA Balkema.

National Development and Reform Commission. (2008). *The state overall planning for post-Wenchuan Earthquake restoration and reconstruction*. Beijing (in Chinese).

Ni, H.Y., Zheng, W.M., Tie, Y.B., Su, P.C., Tang, Y.Q., Xu, R.G., Wang, D.W. & Chen, X.Y. (2012). Formation and characteristics of post-earthquake debris flow: A case study from Wenjia gully in Mianzhu, Sichuan, SW China. *Nat. Hazards* **61**, No. 2, 317–335.

Ni, Q., Tan, T.S., Dasari, G.R. & Hight, D.W. (2004). Contribution of fines to the compressive strength of mixed soils. *Geotechnique* **54**, No. 9, 561–569.

Nocilla, A., Coop, M.R. & Colleselli, F. (2006). The mechanics of an Italian silt: an example of ‘transitional’behaviour. *Géotechnique* **56**, No. 4, 261–271.

Olson, S.M., Stark, T.D. & Castro, G. (2000). 1907 Static liquefaction flow failure of the North Dike of Wachusett Dam. *J. Geotech. Geoenvironmental Eng.* **126**, No. 12, 1184–1193.

Ouimet, W.B. (2010). Landslides associated with the May 12, 2008 Wenchuan earthquake: Implications for the erosion and tectonic evolution of the Longmen Shan. *Tectonophysics* **491**, No. 1–4, 244–252.

Ouimet, W.B., Whipple, K.X., Royden, L.H., Sun, Z. & Chen, Z. (2007). The influence of large landslides on river incision in a transient landscape: Eastern margin of the Tibetan Plateau (Sichuan, China). *Geol. Soc. Am. Bull.* **119**, No. 11–12, 1462–1476.

Ouyang, C., Zhou, K., Xu, Q., Yin, J., Peng, D., Wang, D. & Li, W. (2016). Dynamic analysis and numerical modeling of the 2015 catastrophic landslide of the construction waste landfill at Guangming, Shenzhen, China. *Landslides* **2016**, No. April.

Parker, R.N., Densmore, A.L., Rosser, N.J., de Michele, M., Li, Y., Huang, R., Whadcoat, S. & Petley, D.N. (2011). Mass wasting triggered by the 2008 Wenchuan earthquake is greater than orogenic growth. *Nat. Geosci.* **4**, No. 7, 449–452.

Paronuzzi, P., Coccolo, A. & Garlatti, G. (1998). Eventi meteorici critici e debris flows nei bacini montani del Friuli. *L'Acqua, Sez. I/Memorie* **6**, 39–50.

Parsons, T., Ji, C. & Kirby, E. (2008). Stress changes from the 2008 Wenchuan earthquake and increased hazard in the Sichuan basin. *Nature* **454**, No. 7203, 509.

Pasternak, E. & Dyskin, A. V. (2008). Materials with Poisson’s ratio near -1: Properties and possible realizations. In *Proceeding of XXII International Congress of Theoretical and Applied Mechanics*.

Pasternak, E. & Dyskin, A. V. (2009). *Multiscale hybrid materials with negative Poisson's ratio*. *IUTAM Symp. Scaling Solid Mech.* Springer.

Pastor, M.J., Blanc, T., Manzanal, D., Drempetic, V., Pastor, M.J., Sanchez, M., Crosta, G., Imposimato, S. & Roddeman, D. (2012). Landslide runout: Review of analytical/empirical models for subaerial slides, submarine slides and snow avalanche. *Numer. Model. Softw. tools, Mater. Model. Valid. benchmarking Sel. case Stud. Safel. Deliv.* **1**.

Paton, D. & Johnston, D. (2017). *Disaster resilience: an integrated approach*. Charles C Thomas Publisher.

Peng, D., Xu, Q., Liu, F.Z., He, Y., Zhang, S., Qi, X., Zhao, K. & Zhang, X. (2018). Distribution and failure modes of the landslides in Heitai terrace, China. *Eng. Geol.* **236**, 97–110.

Pennington, D.S., Nash, D.F.T. & Lings, M.L. (1997). Anisotropy of G0 shear stiffness in Gault Clay. *Géotechnique* **47**, No. 3, 391–398.

Pésci, M. (1990). Loess is not just the accumulation of dust. *Quat. Int.* **7/8**, No. X, 1–21.

Phien-Wej, N., Pientong, T. & Balasubramaniam, A.S. (1992). Collapse and strength characteristics of loess in Thailand. *Eng. Geol.* **32**, No. 1–2, 59–72.

Planning Team of Ministry of Housing and Urban-Rural Development of the People's Republic of China. (2008). *Engineering Geology Report on Site Selection for Beichuan Town*. Beijing.

Ponzoni, E., Nocilla, A., Coop, M.R. & Colleselli, F. (2014). Identification and quantification of transitional modes of behaviour in sediments of Venice lagoon. *Geotechnique* **64**, No. 9, 694–708.

Poulos, S.J., Castro, G. & France, J.W. (1985). Liquefaction evaluation procedure. *J. Geotech. Eng.* **111**, No. 6, 772–792.

Pye, K. (1995). The nature, origin and accumulation of loess. *Quat. Sci. Rev.* **14**, No. 7–8, 653–667.

Qi, S., Xu, Q., Lan, H., Zhang, B. & Liu, J. (2010). Spatial distribution analysis of landslides triggered by 2008.5.12 Wenchuan Earthquake, China. *Eng. Geol.* **116**, No. 1–2, 95–108.

Qi, X., Xu, Q. & Liu, F.Z. (2018). Analysis of retrogressive loess flowslides in Heifangtai, China. *Eng. Geol.* **236**, 119–128.

Rebata-Landa, V. (2007). *Microbial activity in sediments: effects on soil behavior*. Georgia Institute of Technology.

Revellino, P., Hungr, O., Guadagno, F.M. & Evans, S.G. (2004). Velocity and runout simulation of destructive debris flows and debris avalanches in pyroclastic deposits, Campania region, Italy. *Environ. Geol.* **45**, No. 3, 295–311.

Richart, F.E., Hall, J.R. & Woods, R.D. (1970). *Vibrations of soils and foundations*.

Rinaldi, V.A., Clariá, J.J. & Santamarina, J.C. (2001). The small-strain shear modulus (Gmax) of Argentinean loess. In *Proceedins of the International Conference on Soil Mechanics and Geotechnical Engineering*: 495–498. AA BALKEMA PUBLISHERS.

Rinaldi, V.A. & Santamarina, J.C. (2008). Cemented soils: small strain stiffness. In *Deformational Characteristics of Geomaterials*: 267–273. Burns, S.E., Mayne, P.W. & Santamarina, J.C. (Eds.). Atlanta: Pro Universitate.

Rodrıguez, C.E., Bommer, J.J. & Chandler, R.J. (1999). Earthquake-induced landslides: 1980–1997. *Soil Dyn. Earthq. Eng.* **18**, No. 5, 325–346.

Rogers, C.D.F. (1995). Types and distribution of collapsible soils. In *Genesis and properties of collapsible soils*: 1–17. Springer.

Rogers, C.D.F., Dijkstra, T.A. & Smalley, I.J. (1994). Hydroconsolidation and subsidence of loess: Studies from China, Russia, North America and Europe. In memory of Jan Sajgalik. *Eng. Geol.* **37**, No. 2, 83–113.

Saunders, W.S.A. & Becker, J.S. (2015). A discussion of resilience and sustainability: Land use planning recovery from the Canterbury earthquake sequence, New Zealand. *Int. J. Disaster Risk Reduct.* **14**, 73–81.

Schmertmann, J.H. (1991). The mechanical aging of soils. *J. Geotech. Eng.* **117**, No. 9, 1288–1330.

Schofield, A. & Wroth, P. (1968). Critical State Soil Mechanics. *Soil Use Manag.* **25**, No. 3, 128–105.

Schwab, J., Topping, K.C., Eadie, C.C., Deyle, R.E. & Smith, R.A. (1998). *Planning for post-disaster recovery and reconstruction*. American Planning Association Chicago, IL.

Seed, B. & Lee, K.L. (1966). Liquefaction of saturated sands during cyclic loading. *J. Soil Mech. Found. Div* **92**, No. ASCE# 4972 Proceeding.

Shao, S., Tao, H. & Xu, P. (2011). Discussion on research of mechanical characteristics of loess considering structural behavior and its application. *Yantu Lixue/Rock Soil Mech.* **32**, No. SUPPL.2, 42-50 (in Chinese).

Sharma, S.S. & Fahey, M. (2004). Deformation characteristics of two cemented calcareous soils. *Can. Geotech. J.* **41**, No. 6, 1139–1151.

Shen, Z.-K., Sun, J., Zhang, P., Wan, Y., Wang, M., Bürgmann, R., Zeng, Y., Gan, W., Liao, H. & Wang, Q. (2009). Slip maxima at fault junctions and rupturing of barriers during the 2008 Wenchuan earthquake. *Nat. Geosci.* **2**, No. 10, 718–724.

Shibuya, S., Hwang, S.C. & Mitachi, T. (1997). Elastic shear modulus of soft clays from shear wave velocity measurement. *Géotechnique* **47**, No. 3, 593–601.

Shin, H. & Santamarina, J.C. (2009). Mineral dissolution and the evolution of k0. *J. Geotech. Geoenvironmental Eng.* **135**, No. 8, 1141–1147.

Shipton, B. & Coop, M.R. (2012). On the compression behaviour of reconstituted soils. *Soils Found.* **52**, No. 4, 668–681.

Sladen, J.A., D'hollander, R.D. & Krahn, J. (1985). The liquefaction of sands, a collapse surface approach. *Can. Geotech. J.* **22**, No. 4, 564–578.

Smalley, I. (1990). Possible formation mechanisms for the modal coarse-silt quartz particles in loess deposits. *Quat. Int.* **7**–**8**, No. C, 23–27.

Smalley, I. (1992). The Teton Dam: rhyolite foundation+ loess core= disaster. *Geol. Today* **8**, No. 1, 19–22.

Smalley, I., Marković, S.B. & Svirčev, Z. (2011). Loess is [almost totally formed by] the accumulation of dust. *Quat. Int.* **240**, No. 1–2, 4–11.

Smalley, I.J. (1966). Formation of Quartz Sand. *Nature* **211**, 476.

Smalley, I.J., Mavlyanova, N.G., Rakhmatullaev, K.L., Shermatov, M.S., Machalett, B., O'Hara Dhand, K. & Jefferson, I.F. (2006). The formation of loess deposits in the Tashkent region and parts of Central Asia; and problems with irrigation, hydrocollapse and soil erosion. *Quat. Int.* **152**, 59–69.

Smith, B.J., Wright, J.S. & Whalley, W.B. (2002). Sources of non-glacial, loess-size quartz silt and the origins of "desert loess." *Earth-Science Rev.* **59**, No. 1–4, 1–26.

Song, B., Tsinaris, A., Anastasiadis, A., Pitilakis, K. & Chen, W. (2017). Small-strain stiffness and damping of Lanzhou loess. *Soil Dyn. Earthq. Eng.* **95**, 96–105.

State Council of China. (2008). *Regulations on Post-Wenchuan Earthquake Rehabilitation and Reconstruction*. Beijing, China.

Steinberg, F. (2007). Housing reconstruction and rehabilitation in Aceh and Nias, Indonesia - Rebuilding lives. *Habitat Int.* **31**, No. 1, 150–166.

Sun, J.Z. (1957). Collapsibility of loess and the relationship with moisture. *Hydrogeol. Eng. Geol.* **11**, 18-21 (in Chinese).

Sun, T., Yin, H. & Zhu, Z. (2011). Experiences in post-earthquake reconstruction of

Beichuan new town. *City Plan. Rev.* **35**, No. S02, 17-36 (in Chinese).

Take, W.A. & Beddoe, R.A. (2014). Base liquefaction: a mechanism for shear-induced failure of loose granular slopes. *Can. Geotech. J.* **51**, No. 5, 496–507.

Take, W.A., Beddoe, R.A., Davoodi-Bilesavar, R. & Phillips, R. (2014). Effect of antecedent groundwater conditions on the triggering of static liquefaction landslides. *Landslides* No. October 2013, 469–479.

Take, W.A., Bolton, M.D., Wong, P.C.P. & Yeung, F.J. (2004). Evaluation of landslide triggering mechanisms in model fill slopes. *Landslides* **1**, No. 3, 173–184.

Tang, C., Van Asch, T.W.J., Chang, M., Chen, G.Q., Zhao, X.H. & Huang, X.C. (2012a). Catastrophic debris flows on 13 August 2010 in the Qingping area, southwestern China: The combined effects of a strong earthquake and subsequent rainstorms. *Geomorphology* **139**–**140**, No. August 2010, 559–576.

Tang, C., Li, W., Ding, J. & Huang, C. (2011a). Field Investigation and Research on Giant Debris Flow on August 14, 2010 in Yingxiu Town, Epicenter of Wenchuan Earthquake. *Earth Sci.* **36**, No. 1, 172-180 (in Chinese).

Tang, C. & Liang, J. (2008). Characteristics of Debris Flows in Beichuan Epicenter of the Wenchuan Earthquake Triggered by Rainstorm on Septermber 24, 2008. *J. Engingeering Geol.* **16**, No. 6, 751-758 (in Chinese).

Tang, C., Zhu, J., Chang, M., Ding, J. & Qi, X. (2012b). An empirical–statistical model for predicting debris-flow runout zones in the Wenchuan earthquake area. *Quat. Int.* **250**, 63–73.

Tang, C., Zhu, J., Li, W.L. & Liang, J.T. (2009). Rainfall-triggered debris flows following the Wenchuan earthquake. *Bull. Eng. Geol. Environ.* **68**, No. 2, 187–194.

Tang, C., Zhu, J., Qi, X. & Ding, J. (2011b). Landslides induced by the Wenchuan earthquake and the subsequent strong rainfall event: A case study in the Beichuan area of China. *Eng. Geol.* **122**, No. 1–2, 22–33.

Tapponnier, P., Zhiqin, X., Roger, F., Meyer, B., Arnaud, N., Wittlinger, G. & Jingsui, Y. (2001). Oblique stepwise rise and growth of the Tibet plateau. *Science* **294**, No. 5547, 1671–7.

Taylor, R.N. ed. (1995). *Geotechnical centrifuge technology*. CRC Press.

The White House. (2013). Critical Infrastructure Security and Resilience [WWW Document]. *Pres. Policy Dir. - 21*.

Thevanayagam, S., Shenthan, T., Mohan, S. & Liang, J. (2002). Undrained fragility of clean sands, silty sands, and sandy silts. *J. Geotech. Geoenvironmental Eng.* **128**, No. 10, 849–859.

Tierney, K. & Bruneau, M. (2007). Conceptualizing and measuring resilience: A key to disaster loss reduction. *TR news* No. 250.

Trhlíková, J., BOHáč, J. & MAšíN, D. (2012). Small-strain behaviour of cemented soils. *Géotechnique* **62**, No. 10, 943.

Truong, Q.H., Eom, Y.H. & Lee, J.-S. (2010). Stiffness characteristics of soluble mixtures. *Geotechnique* **60**, No. 4, 293.

Tschebotarioff, G. (1973). *Soil Mechanics, Foundations, and Earth Structures*. Second Edi. New York: McGraw-Hill Book Company Inc.

Varga, G. (2011). Similarities among the Plio-Pleistocene terrestrial aeolian dust deposits in the World and in Hungary. *Quat. Int.* **234**, No. 1–2, 98–108.

Varnes, D.J. (1978). *Slope movement types and processes*. *Transp. Res. Board Spec. Rep.*

Verdugo, R. & Ishihara, K. (1996). The Steady State of Sandy Soils. *SOILS Found.* **36**, No. 2, 81–91.

Viggiani, G. & Atkinson, J.H. (1995). Stiffness of fine-grained soil at very small strains. *Géotechnique* **45**, No. 2, 249–265.

Wang, G., Liu, H. & Zhang, J. (2010). Analysis on Seismic Hazards in Beichuan County Town Caused by Wenchuan Great Earthquake. *Northwest. Seismol. J.* **32**, No. 2, 173–178.

Wang, G. & Sassa, K. (2001). Factors affecting rainfall-induced flowslides in laboratory flume tests. *Géotechnique* **51**, No. 7, 587–599.

Wang, J.-D., Li, P., Ma, Y., Vanapalli, S.K. & Wang, X.-G. (2019a). Change in pore-size distribution of collapsible loess due to loading and inundating. *Acta Geotech.* 1–14.

Wang, J. (1992). A mechanism of high-speed loess landslides - saturated loess creeping liquefaction. *Geol. Rev.* **38**, No. 6, 532-539 (in Chinese).

Wang, J., Li, P., Gu, Q., Xu, Y. & Gu, T. (2019b). Changes in tensile strength and microstructure of loess due to vibration. *J. Asian Earth Sci.* **169**, 298–307.

Wang, L.B., Frost, J.D. & Lai, J.S. (2004a). Three-dimensional digital representation of granular material microstructure from X-ray tomography imaging. *J. Comput. Civ. Eng.* **18**, No. 1, 28–35.

Wang, L.B., Frost, J.D., Voyiadjis, G.Z. & Harman, T.P. (2003). Quantification of damage parameters using X-ray tomography images. *Mech. Mater.* **35**, No. 8, 777–790.

Wang, Q. (2009). *Sichuan Rural Yearbook 2008*. Chengdu: University of Electronic Science and Technology Press.

Wang, Y., Yin, M., Tang, L., Zhao, M. & Yu, X. (2014). Investigation of Vegetation in Wenjiagou Debris Flow Area. *J. Agric.* **4**, No. 2, 63-67 (in Chinese).

Wang, Y.F., Dong, J.J. & Cheng, Q.G. (2018). Normal stress-dependent frictional weakening of large rock avalanche basal facies: Implications for the rock avalanche volume effect. *J. Geophys. Res. Solid Earth* **123**, No. 4, 3270–3282.

Wang, Z.-L., Dafalias, Y.F., Li, X.-S. & Makdisi, F.I. (2002). State Pressure Index for Modeling Sand Behavior. *J. Geotech. Geoenvironmental Eng.* **128**, No. 6, 511–519.

Wang, Z., Wu, W. & Zhou, Z. (2004b). Landslide induced by over-irrigation in loess platform areas in Gansu Province. *Chinese J. Geol. Hazard Control* **15**, No. 3, 43-54 (in Chinese).

Wartman, J., Montgomery, D.R., Anderson, S.A., Keaton, J.R., Benoît, J., dela Chapelle, J. & Gilbert, R. (2016). The 22 March 2014 Oso landslide, Washington, USA. *Geomorphology* **253**, 275–288.

Wei, T., Fan, W., Yuan, W., Wei, Y. & Yu, B. (2019). Three-dimensional pore network characterization of loess and paleosol stratigraphy from South Jingyang Plateau, China. *Environ. Earth Sci.* **78**, No. 11, 333.

Wieczorek, G.F. (1987). Effect of rainfall intensity and duration on debris flows in central Santa Cruz Mountains. In *Debris flow/avalanches: process, recognition, and mitigation. Geological Society of America, Reviews in Engineering Geology 7*: 93–104.

Wieczorek, G.F., Morgan, B.A. & Campbell, R.H. (2000). Debris-flow hazards in the Blue Ridge of central Virginia. *Environ. Eng. Geosci.* **6**, No. 1, 3–23.

Wolinsky, E. & Take, W.A. (2019). Instability of loose dry granular slopes observed in centrifuge tilting table tests. *Géotechnique Lett.* 1–21.

Wu, W.J. & Wang, N.Q. (2002). Basic types and active features of loess landslide. *Chinese J. Geol. Hazard Control* **13**, No. 2, 36-40 (in Chinese).

Xiang, L., Cui, P. & Fang, H. (2010). Mechanism of Disaster Chain after Earthquake and the Impact to Urban Reconstruction in Wenchuan Earthquake Area. *J. Catastrophology* **25**, No. S0, 278–281.

Xiao, D. & Li, C. (2009). Key points of the reconstruction of Yingxiu town. *Constr. Sci. Technol.* **9**, 37-39 (in Chinese).

Xin, D. (2012). Post-disaster recovery planning and sustainable development—a lesson from the Wenchuan earthquake, China, 2008.

Xu, L. & Coop, M.R. (2016). Influence of structure on the behavior of a saturated clayey loess. *Can. Geotech. J.* **53**, No. 6, 1026–1037.

Xu, L. & Coop, M.R. (2017). The mechanics of a saturated silty loess with a transitional mode. *Géotechnique* **67**, No. 7, 581–596.

Xu, L., Coop, M.R., Zhang, M.S. & Wang, G. (2018). The mechanics of a saturated silty loess and implications for landslides. *Eng. Geol.* **236**, No. 5, 29–42.

Xu, L., Dai, F., Kwong, A.K.L. & Min, H. (2008). Types and characteristics of loess landslides at Heifangtai Loess Plateau, China. *J. Mt. Sci.* **26**, No. 3, 364-371 (in Chinese).

Xu, L., Dai, F.C., Kwong, A.K.L., Min, H. & Xu, C. (2009a). Application of IKONOS image in detection of loess landslide at Heifangtai Loess Plateau, China. *J. Remote Sens.* **13**, No. 4, 723-728 (in Chinese).

Xu, L., Dai, F.C., Tham, L.G., Zhou, Y.F. & Wu, C.X. (2012a). Investigating landslide-related cracks along the edge of two loess platforms in northwest China. *Earth Surf. Process. Landforms* **37**, No. 10, 1023–1033.

Xu, L., Dai, F.C., Tu, X.B., Tham, L.G., Zhou, Y. & Iqbal, J. (2014). Landslides in a loess platform, North-West China. *Landslides* **11**, No. 6, 993–1005.

Xu, Q. (2010). The 13 August 2010 catastrophic debris flows in Sichuan Province: Characteristics, Genetic Mechanism and Suggestions. *J. Eng. Geol.* **18**, 596-608 (in Chinese).

Xu, Q. & Huang, R. (2008). Kinetics Characteristics of Large Landslides Triggered by May 12th Wenchuan Earthquake. *J. Eng. Geol.* **16**, No. 6, 721–729.

Xu, Q., Pei, X. & Huang, R. (2009b). *Large-scale Landslides Induced by the Wenchuan Earthquake*. Beijing (in Chinese): Science Press.

Xu, Q., Peng, D., Li, W., Dong, X., Hu, W., Tang, M. & Liu, F.Z. (2017). The catastrophic landfill flowslide at Hongao dumpsite on 20 December 2015 in Shenzhen, China. *Nat. Hazards Earth Syst. Sci.* **17**, No. 2, 277–290.

Xu, Q., Shang, Y., van Asch, T., Wang, S., Zhang, Z. & Dong, X. (2012b). Observations from the large, rapid Yigong rock slide – debris avalanche, southeast Tibet. *Can. Geotech. J.* **49**, No. 5, 589–606.

Xu, Q., Zhang, S., Li, W.L. & Van Asch, T.W.J. (2012c). The 13 August 2010 catastrophic debris flows after the 2008 Wenchuan earthquake, China. *Nat. Hazards Earth Syst. Sci.* **12**, No. 1, 201–216.

Xu, X., Wen, X., Yu, G., Chen, G., Klinger, Y., Hubbard, J. & Shaw, J. (2009c). Coseismic reverse- and oblique-slip surface faulting generated by the 2008 Mw 7.9 Wenchuan earthquake, China. *Geology* **37**, No. 6, 515–518.

Xu, Z. & Liu, P. (2012). Building damage characeristics of Mianyang City and Beichuan

County in Wenchuan Earthquake. *Shanxi Archit.* **38**, No. 12, 47–48.

Yamamuro, J. a. & Lade, P. V. (1998). Steady-State Concepts and Static Liquefaction of Silty Sands. *J. Geotech. Geoenvironmental Eng.* **124**, No. 9, 868–877.

Yamamuro, J.A. & Covert, K.M. (2001). Monotonic and cyclic liquefaction of very loose sands with high silt content. *J. Geotech. Geoenvironmental Eng.* **127**, No. 4, 314–324.

Yamamuro, J.A. & Lade, P. V. (1997). Static liquefaction of very loose sands. *Can. Geotech. J.* **34**, No. 6, 905–917.

Yang, J. (2002). Non-uniqueness of flow liquefaction line for loose sand. *Géotechnique* **52**, No. 10, 757–760.

Yang, W., Wang, D. & Chen, G. (2011). Reconstruction strategies after the Wenchuan earthquake in Sichuan, China. *Tour. Manag.* **32**, No. 4, 949–956.

Ye, L., Qu, Z., Lu, X. & Feng, P. (2008). Collapse prevention of building structures : a lesson from the W enchuan earthquake. *J. Build. Struct.* **29**, No. 4, 42-50 (in Chinese).

Yi, H. & Yang, J. (2014). Research trends of post disaster reconstruction: The past and the future. *Habitat Int.* **42**, 21–29.

Yodo, N. & Wang, P. (2016). Engineering Resilience Quantification and System Design Implications: A Literature Survey. *J. Mech. Des.* **138**, No. 11, 111408–111413.

Yu, B., Ma, Y. & Wu, Y. (2013). Case study of a giant debris flow in the Wenjia Gully, Sichuan Province, China. *Nat. Hazards* **65**, No. 1, 835–849.

Yu, B., Zhu, Y., Wang, T., Chen, Y., Zhu, Y., Tie, Y. & Lu, K. (2014). A prediction model for debris flows triggered by a runoff-induced mechanism. *Nat. Hazards* **74**, No. 2, 1141–1161.

Yuan, W., Fan, W., Jiang, C. & Peng, X. (2019). Experimental study on the shear behavior of loess and paleosol based on ring shear tests. *Eng. Geol.* **250**, 11–20.

Yun, T.S. & Santamarina, J.C. (2005). Decementation, Softening, and Collapse: Changes in Small-Strain Shear Stiffness in k0 Loading. *J. Geotech. Geoenvironmental Eng.* **131**, No. 3, 350–358.

Zeng, R.Q., Meng, X.M., Zhang, F.Y., Wang, S.Y., Cui, Z.J., Zhang, M.S., Zhang, Y. & Chen, G. (2016). Characterizing hydrological processes on loess slopes using electrical resistivity tomography - A case study of the Heifangtai Terrace, Northwest China. *J. Hydrol.* **541**, 742–753.

Zhan, L. tong, Zhang, Z., Chen, Y. min, Chen, R., Zhang, S., Liu, J. & Li, A. guo. (2018). The 2015 Shenzhen catastrophic landslide in a construction waste dump: Reconstitution of dump structure and failure mechanisms via geotechnical investigations. *Eng. Geol.* **238**, 15–26.

Zhang, F., Kang, C., Chan, D., Zhang, X., Pei, X. & Peng, J. (2017). A study of a flowslide with significant entrainment in loess areas in China. *Earth Surf. Process. Landforms* **42**, No. 14, 2295–2305.

Zhang, F. & Wang, G. (2018). Effect of irrigation-induced densification on the post-failure behavior of loess flowslides occurring on the Heifangtai area, Gansu, China. *Eng. Geol.* **236**, 111–118.

Zhang, F., Yan, B., Feng, X., Lan, H., Kang, C., Lin, X., Zhu, X. & Ma, W. (2019). A rapid loess mudflow triggered by the check dam failure in a bulldoze mountain area, Lanzhou, China. *Landslides* **16**, No. 10, 1981–1992.

Zhang, J., Jiang, F., Guo, X. & Xu, L. (2009). Post-quake consideration of Beichuan County damage investigation and analysis. *J. Disaster-Prevention Sci. Technol.* **11**, No. 1, 48-51 (in Chinese).

Zhang, L., Liu, X., Li, Y., Liu, Y., Liu, Z., Lin, J., Shen, J., Tang, X., Zhang, Y. & Liang, W. (2012). Emergency medical rescue efforts after a major earthquake: Lessons from the 2008 Wenchuan earthquake. *Lancet* **379**, No. 9818, 853–861.

Zhang, L.M., Zhang, S. & Huang, R.Q. (2014a). Multi-hazard scenarios and consequences in Beichuan, China: The first five years after the 2008 Wenchuan earthquake. *Eng. Geol.*

Zhang, Y., Cheng, Y., Yin, Y., Lan, H., Wang, J. & Fu, X. (2014b). High-position debris flow: A long-term active geohazard after the Wenchuan earthquake. *Eng. Geol.*

Zhang, Y., Lei, W., Shi, J., Long, C., Wu, S., Hu, P., Tan, C., Ma, Y., Fang, H. & Li, B. (2008). Crustal stability of the Leigu Basin in Beichuan County, Sichuan Province and its possibility for a new town site. *Acta Geol. Sin.* **82**, No. 12, 1758-1768 (in Chinese).

Zhao, B., Taucer, F. & Rossetto, T. (2009). Field investigation on the performance of building structures during the 12 May 2008 Wenchuan earthquake in China. *Eng. Struct.* **31**, No. 8, 1707–1723.

Zhao, S., Li, H. & Ma, D. (1995). Study on the landslides at the edge of Loess Terrace in Yanguoxia Reservior Region. *Bull. Soil Water Conserv.* **16**, No. 1, 2-6 (in Chinese).

Zhou, G.G.D., Cui, P., Tang, J.B., Chen, H.Y., Zou, Q. & Sun, Q.C. (2014a). Experimental study on the triggering mechanisms and kinematic properties of large debris flows in Wenjia Gully. *Eng. Geol.*

Zhou, J., Zhu, C.-Y., Zheng, J.-M., Wang, X. & Liu, Z. (2002). Landslide disaster in the loess area of China. *J. For. Res.* **13**, No. 2, 157–161.

Zhou, W. & Tang, C. (2014). Rainfall thresholds for debris flow initiation in the Wenchuan earthquake-stricken area, southwestern China. *Landslides* **11**, No. 5, 877–887.

Zhou, Y. (2012). *Study on Landslides in Loess Slope due to Infiltration*. University of Hong Kong.

Zhou, Y.F., Tham, L.G., Yan, W.M., Dai, F.C. & Xu, L. (2014b). Laboratory study on soil behavior in loess slope subjected to infiltration. *Eng. Geol.* **183**, 31–38.

Zhu, J.-H. & Anderson, S.A. (1998). Determination of shear strength of Hawaiian residual soil subjected to rainfall-induced landslides. *Géotechnique* **48**, No. 1, 73–82.

Zhuang, J., Iqbal, J., Peng, J. & Liu, T. (2014). Probability prediction model for landslide occurrences in Xi'an, Shaanxi Province, China. *J. Mt. Sci.* **11**, No. 2, 345–359.

Zimmermann, M. (1997). *Murganggefahr und Klimaänderung-ein GIS-basierter Ansatz*. vdf Hochschulverlag AG.